frontiers | Research Topics

New trends in single photon emission computed tomography (SPECT)

Edited by
Greta Mok and Roberto Massari

Published in
Frontiers in Medicine
Frontiers in Cardiovascular Medicine

ISSN 1664-8714
ISBN 978-2-8325-4246-0
DOI 10.3389/978-2-8325-4246-0

About Frontiers

Frontiers is more than just an open access publisher of scholarly articles: it is a pioneering approach to the world of academia, radically improving the way scholarly research is managed. The grand vision of Frontiers is a world where all people have an equal opportunity to seek, share and generate knowledge. Frontiers provides immediate and permanent online open access to all its publications, but this alone is not enough to realize our grand goals.

Frontiers journal series

The Frontiers journal series is a multi-tier and interdisciplinary set of open-access, online journals, promising a paradigm shift from the current review, selection and dissemination processes in academic publishing. All Frontiers journals are driven by researchers for researchers; therefore, they constitute a service to the scholarly community. At the same time, the *Frontiers journal series* operates on a revolutionary invention, the tiered publishing system, initially addressing specific communities of scholars, and gradually climbing up to broader public understanding, thus serving the interests of the lay society, too.

Dedication to quality

Each Frontiers article is a landmark of the highest quality, thanks to genuinely collaborative interactions between authors and review editors, who include some of the world's best academicians. Research must be certified by peers before entering a stream of knowledge that may eventually reach the public - and shape society; therefore, Frontiers only applies the most rigorous and unbiased reviews. Frontiers revolutionizes research publishing by freely delivering the most outstanding research, evaluated with no bias from both the academic and social point of view. By applying the most advanced information technologies, Frontiers is catapulting scholarly publishing into a new generation.

What are Frontiers Research Topics?

Frontiers Research Topics are very popular trademarks of the *Frontiers journals series*: they are collections of at least ten articles, all centered on a particular subject. With their unique mix of varied contributions from Original Research to Review Articles, Frontiers Research Topics unify the most influential researchers, the latest key findings and historical advances in a hot research area.

Find out more on how to host your own Frontiers Research Topic or contribute to one as an author by contacting the Frontiers editorial office: frontiersin.org/about/contact

New trends in single photon emission computed tomography (SPECT)

Topic editors

Greta Mok — University of Macau, China

Roberto Massari — Institute of Biochemistry and Cell Biology, Department of Biomedical Sciences, National Research Council (CNR), Italy

Citation

Mok, G., Massari, R., eds. (2024). *New trends in single photon emission computed tomography (SPECT)*. Lausanne: Frontiers Media SA.

doi: 10.3389/978-2-8325-4246-0

Table of contents

frontiers | Frontiers in Medicine

TYPE Editorial
PUBLISHED 20 December 2023
DOI 10.3389/fmed.2023.1349877

OPEN ACCESS

EDITED AND REVIEWED BY
Giorgio Treglia,
Ente Ospedaliero Cantonale (EOC), Switzerland

*CORRESPONDENCE
Roberto Massari
roberto.massari@cnr.it

RECEIVED 05 December 2023
ACCEPTED 11 December 2023
PUBLISHED 20 December 2023

CITATION
Massari R and Mok GSP (2023) Editorial: New trends in single photon emission computed tomography (SPECT). *Front. Med.* 10:1349877. doi: 10.3389/fmed.2023.1349877

Editorial: New trends in single photon emission computed tomography (SPECT)

Roberto Massari[1]* and Greta S. P. Mok[2,3,4]

[1]Institute of Biochemistry and Cell Biology, National Research Council of Italy (CNR), Rome, Italy, [2]Biomedical Imaging Laboratory (BIG), Department of Electrical and Computer Engineering, Faculty of Science and Technology, University of Macau, Taipa, Macao SAR, China, [3]Center for Cognitive and Brain Sciences, Institute of Collaborative Innovation, University of Macau, Taipa, Macao SAR, China, [4]Ministry of Education Frontiers Science Center for Precision Oncology, Faculty of Health Science, University of Macau, Taipa, Macao SAR, China

KEYWORDS

single photon emission computed tomography, QSPECT, fast SPECT, artificial intelligence-AI, SPECT/CT

Editorial on the Research Topic
New trends in single photon emission computed tomography (SPECT)

Single photon emission computed tomography (SPECT) is a nuclear imaging technique that provides three-dimensional information about the functional and molecular processes within the patient's body. In SPECT, one or more gamma cameras are used to detect mostly gamma radiation from the administered radioactive tracer. The detectors rotate around the patient, acquiring projections from multiple angles for then three-dimensional reconstruction of the radioactive tracer distribution.

This technique is deeply rooted in the development of nuclear medicine imaging. The very first demonstration of SPECT was carried out by Kuhl and Edwards (1), although it was not until the late 1970s that the first commercial scanner based on rotating gamma camera was developed at Searle Radiographics (2). Nowadays, SPECT imaging is an integrated diagnostic routine in nuclear medicine, where the gamma camera is the workhorse due to its flexibility to perform both planar and tomographic imaging.

However, the development of SPECT imaging has been surpassed in some ways by positron emission tomography (PET) in recent years, which has gained considerable attention in the field of nuclear medicine (3). PET has higher sensitivity, provides high image quality with better spatial resolution as well as more quantitative capability than SPECT. These factors may make PET a more attractive option for certain applications. One factor that has indirectly influenced the rise of PET in past years is the shortage of isotopes in nuclear medicine, a significant issue that has affected the availability of essential medical procedures (4). In recent years, the production of isotopes for nuclear medicine has suffered a series of unplanned interruptions associated with the aging of the medical nuclear reactors, despite all efforts to maintain these infrastructures. These interruptions caused severe shortages of ^{99}Mo, used in ^{99m}Tc generators, resulting in the cancellation of many ^{99m}Tc-based SPECT studies. On the other hand, PET is more reliable as most PET tracers, e.g., ^{18}F, are produced by cyclotron and are less prone to shortages. However, purchasing and maintaining a cyclotron is expensive and requires substantial engineering support, which may not be feasible for most clinical institutions.

Despite the above, SPECT are almost ubiquitous in hospitals and clinics and are more affordable than PET. The SPECT technique uses gamma-emitting radioisotopes, which have longer half-lives than the short-lived β^+ isotopes used in PET. This allows for a longer imaging time to capture the patients' pharmacokinetics. In addition, SPECT is able to perform multi-tracer studies, which can provide more comprehensive information on the biological processes being examined.

Moreover, SPECT can be effectively combined with computed tomography (CT), which offers morphological details and solution of attenuation correction, as an integrated dual-modality scanner known as SPECT/CT (5). This leads to enhanced sensitivity (improved detection of the disease) and specificity (reduction of false positives due to normal uptake of the tracer). In this regard, the first commercial SPECT/CT system was the Hawkeye scanner, introduced in 1999 by GE Healthcare (then known as GE Medical Systems) (6).

Although SPECT is well-established and widely validated, it is still a promising technique that is evolving with ongoing technological advances and research. This Research Topic encompasses several contributions highlighting the most recent progress in SPECT, providing a broad overview of advances in instrumentation, use of artificial intelligence (AI) techniques, quantitative imaging, and exploration of new applications.

In recent years, SPECT detectors have benefited from many technological advances. For instance, new scintillator materials with better properties have been developed and, thanks to advances in solid-state devices, new light transducers such as silicon photomultipliers (SiPM) or new semiconductor-based detectors such as cadmium zinc telluride (CZT) have become available (7). More specifically, these enhanced components facilitate new SPECT system designs by exploiting both enhanced element characteristics and advantageous geometries to achieve high sensitivity as well as a good spatial and energy resolution. In this regard, the first work of this Topic by Besse and Bailly is a case report article describing the use of a new commercial SPECT/CT system equipped with state-of-the-art CZT detectors featuring a ring shaped geometry that enable faster acquisition with better energy resolution. The authors illustrate the use of the StarGuide™ 3D-ring CZT SPECT/CT system (GE Healthcare) in lymphoscintigraphic investigations of lymphoedema. This paper shows a complete SPECT/CT acquisition of the pelvis and limbs with a time reduction of more than 50% compared to a traditional dual-head camera.

The collimator is the component that most influences the image resolution and sensitivity trade-off in a gamma camera. It is an essential component in SPECT to determine the direction of the incident photons, yet posing an upper limit of photon detection. Therefore, novel collimator designs are still actively being pursued to enhance the performance of a SPECT system. In this regard, Wang R. et al. propose a novel cardiac SPECT system without a conventional lead collimator, exploiting with the use of mosaic interval scintillators as collimation to significantly increase sensitivity and reduce scanning time without compromising image resolution. Meanwhile, multi-pinhole collimator is an existing SPECT collimation to improve the sensitivity-resolution trade-off in SPECT particularly for a relatively small field-of-view, e.g., small animals, clinical brain and heart imaging. , In this context, Huang and Mok evaluate the performance of MPH collimator for brain SPECT, exploring its designs along with different number of projection views. They conclude that more number of pinholes are needed for less number of projection views and more complex activity distributions. MPH collimators achieve better spatial resolution and angular sampling than conventional low energy high-resolution (LEHR) and single pinholes in general.

The use of AI is a promising and emerging field that aims to improve the image quality and quantitative accuracy in general medical imaging. The recent advances in machine learning and deep learning techniques are also applied to SPECT, while denoising and attenuation correct are two main applications. In their contribution to this Research Topic, Du et al. compare different deep-learning-based methods of attenuation correction (AC) for ^{99m}Tc-TRODAT-1 brain SPECT, a technique for imaging dopamine transporters in patients with Parkinson's disease. Using a 3D conditional generative adversarial network (cGAN), the authors estimated attenuation maps and attenuation-corrected SPECT images by applying different deep learning training strategies. They conclude that deep learning-based AC methods are feasible and robust for DAT SPECT and can improve quantification of dopamine transporter uptake, and indirectly estimating attenuation maps is superior to direct AC by deep learning. Meanwhile, Sun et al. propose a 3D attention-guided generative adversarial network (AttGAN) for denoising fast myocardial perfusion (MP) SPECT images. This novel method uses an attention mechanism to learn the relationships between different regions of the image and improve the quality of the denoised images. The authors compare their method with two other methods using convolutional neural networks (CNN). The results show that for MP-SPECT, AttGAN-based denoising is superior to conventional CNN-based networks.

One of the main advantages of nuclear medicine imaging is the ability to quantify the amount and distribution of a radiotracer in the body. Recently, SPECT has progressed from using relative and semiquantitative measures to using absolute measures of activity concentration, and even further to using normalized uptake with the standardized uptake value (SUV) (8). Within this context, Kaur et al. evaluate the use of quantitative SPECT/CT (Q-SPECT/CT) with ^{99m}Tc sulfur colloid to assess disease severity, patient outcomes and therapeutic response to granulocyte colony-stimulating factor treatment in patients with decompensated cirrhosis (DC). The study by Lin et al. reports that whole-body ^{99m}Tc methyl-diphosphonate (MDP) bone scans can be used to measure the SUV of bone lesions in patients with lung adenocarcinoma. The paper identifies the maximum SUV as an index that can help identifying bone metastases from benign bone lesions in lung adenocarcinoma patients, especially for those with negative CT findings. The article by Wang X-H et al. show the prognostic value of gated MP SPECT in patients with non-obstructed coronary arteries (INOCA), thus enabling the identification of high-risk groups. The study shows that the long-term predictive efficacy of these data exceeded that of coronary angiography (CAG) data, i.e., the gold standard for detecting

obstructive coronary. Consequently, MP SPECT is an accurate tool for predicting the risk of a major adverse cardiovascular event in INOCA.

Radiopharmaceutical therapy has always been a major component in nuclear medicine development. The recent success of radioligand and radioreceptor-based therapies shield a new light for SPECT development, as many theranostic agents also emit gamma photons. SPECT enables voxel-based dosimetry with high accuracy and reproducibility, which is essential for optimizing the efficacy and safety of radiopharmaceutical therapy, as well as predicting and evaluating treatment outcome. However, SPECT-based dosimetry usually requires sequential SPECT scanning with more than 3 imaging time points, making it a clinically challenging practice for most institutions and patients. In their paper, Chen et al. report the use of based on SPECT images at two imaging time points, to simplify dosimetry protocol in a radioligand therapy with ^{177}Lu prostate-specific-membrane-antigen. Their results show <10% dosimetric error as compared to full 4 time points study in both tumors and kidneys.

With continuous advances in instrumentation and computing techniques that improve its diagnostic, quantitation and dosimetric capabilities, SPECT is still a key tool in nuclear medicine. With a wide spectrum of applications clinically and preclinically, SPECT will still be at the forefront of theranostic medicine for decades to come.

Author contributions

RM: Writing—original draft, Writing—review & editing. GM: Writing—review & editing.

Funding

The author(s) declare that no financial support was received for the research, authorship, and/or publication of this article.

Conflict of interest

The authors declare that the research was conducted in the absence of any commercial or financial relationships that could be construed as a potential conflict of interest.

Publisher's note

References

1. Kuhl DE, Edwards RQ. Image separation radioisotope scanning. *Radiology.* (1963) 80:653–62. doi: 10.1148/80.4.653

2. Jaszczak RJ, Murphy PH, Huard D, Burdine JA. Radionuclide emission computed tomography of the head with 99mTc and a scintillation camera. *J Nucl Med.* (1977) 18:373–80.

3. Chowdhury FU, Scarsbrook AF. The role of hybrid SPECT-CT in oncology: current and emerging clinical applications. *Clin Radiol.* (2008) 63:241–51. doi: 10.1016/j.crad.2007.11.008

4. Thomas JR. The medical isotope crisis: how we got here and where we are going. *J Nucl Med Technol.* (2014) 42:245. doi: 10.2967/jnmt.114.144642

5. Massari R, D'Elia A, Soluri A. Hybrid SPECT/CT. In A. Signore, editor *Nuclear Medicine and Molecular Imaging* (Oxford: Elsevier), 378–389 (2022).

6. Ljungberg M, Pretorius PH. SPECT/CT: an update on technological developments and clinical applications. *Br J Radiol.* (2018) 91:20160402. doi: 10.1259/bjr.20160402

7. Madsen MT. Recent advances in SPECT imaging. *J Nucl Med.* (2007) 48:661–73. doi: 10.2967/jnumed.106.032680

8. Dickson J, Ross J, Vöö S. Quantitative SPECT: the time is now. *EJNMMI Phys.* (2019) 6:4. doi: 10.1186/s40658-019-0241-3

frontiers in Medicine

CASE REPORT
published: 22 March 2022
doi: 10.3389/fmed.2022.866541

Case Report: Potential Applications of Using a 3D-Ring CZT SPECT for Lymphoscintigraphic Exploration of Lower Limb Edema

*Hélène Besse and Matthieu Bailly**

Nuclear Medicine Department, CHR d'Orléans, Orléans, France

Lymphoscintigraphy is still considered the gold standard imaging modality for diagnosing lymphedema, due to ineffective lymphatic transport resulting in edema and skin damage. However, protocol variability and poor image resolution can make the interpretation challenging. Up to now, 99 mTc-labeled colloid lymphatic travel is monitored with dual-head cameras, but single-photon emission CT (SPECT) has proved its interest. Here, we present the case of a 59-year-old-man with bilateral asymmetric lower limb edema which was explored using dual-head and new 3D-ring cadmium -zinc-telluride (CZT) SPECT cameras, confirming bilateral lower limb lymphatic dysfunction. In line with other recently published reports, this case report promotes the use of SPECT/CT in the lymphoscintigraphic exploration of lower limb edema. The recognition of the clinicopathologic features of lower limb edema is required to prevent missed diagnoses, such as compressive disease, tumors, etc., as well as to better influence the management of patients.

Keywords: lymphoscintigraphy, SPECT/CT, 3D-ring CZT, limb edema, scintigraphy and whole-body imaging

OPEN ACCESS

Edited by:
Domenico Albano,
University of Brescia, Italy

Reviewed by:
Luca Camoni,
University of Brescia, Italy
Laetitia Imbert,
Centre Hospitalier Universitaire de Nancy, France

***Correspondence:**
Matthieu Bailly
matthieu.bailly@chr-orleans.fr

Specialty section:
This article was submitted to Nuclear Medicine, a section of the journal Frontiers in Medicine

Received: *31 January 2022*
Accepted: *21 February 2022*
Published: *22 March 2022*

Citation:
Besse H and Bailly M (2022) Case Report: Potential Applications of Using a 3D-Ring CZT SPECT for Lymphoscintigraphic Exploration of Lower Limb Edema. Front. Med. 9:866541. doi: 10.3389/fmed.2022.866541

INTRODUCTION

Lymphoedema is a chronic and evolving disease, caused by an insufficiency of lymph circulation that can cause massive morbidity and takes many forms depending on its origin and localization. Though the diagnosis is based on clinical findings, the lymphoscintigraphic investigation of the superficial lymphatic system remains the gold standard for the diagnosis of lower limb lymphedema (1), especially in the clinically less apparent early stages of lymphatic disease (2). This examination is performed with subcutaneously injected 99mTc-labeled colloids, thus reliably providing information about lymph transport. However, the lack of anatomical localization or information such as fibrotic tissues can be considered a potential limitation (3).

Single-photon emission CT (SPECT)/CT combines functional and anatomic information into fused imaging and creates a more powerful diagnostic tool than the separate SPECT and CT. Few studies focused on the added value of SPECT/CT in lymphoscintigraphy to specify the anatomical correlation of lymphatic disorders (4–6).

New 3D-ring cadmium -zinc-telluride (CZT) SPECT/CT systems are now available [Veriton (Spectrum Dynamics Medical) and StarGuide (GE Healthcare)] and allow fast 3D SPECT/CT acquisitions, leading to PET-like utilization (7). To our knowledge, lymphoscintigraphic explorations have never been reported using such cameras.

CASE REPORT

We report the case of a 59-year-old-man with a history of bilateral asymmetric lower limb edema. He reported a family history of limb edema and an old trauma in their childhood. On the early planar images after subcutaneous injection in the feet of 114 and 110 MBq 99 mTc-labeled colloids, little migration of the radiopharmaceutical was observed on the right calf and thigh, without any inguinal node seen. No migration was visualized on the left side (**Figure 1A**). Then, 4 h after injection, late images were acquired both on a dual-head NaI SPECT/CT system (GE Healthcare, Haifa, Israel) with a planar exploration lasting for 12 min (**Figure 1B**), and on the StarGuide™ 3D-ring CZT SPECT/CT system (GE Healthcare, Haifa, Israel) equipped with 12 swiveling high-resolution CZT detectors. Afterward, 4-bed positions of 3-min uniform SPECT were acquired resulting in 12 min duration SPECT, as well as 40 s of motion and CT (CTDI 2.65 mGy; DLP 312 mGy.cm) (**Figure 2**). SPECT/CT was only acquired on the new system. On the right side, a single lymphatic network was visualized at the level of the right calf, bifid at the level of the right inner thigh, without recruitment of the deep lymphatic network. Minimal extravasation of the radiopharmaceutical was found in the soft tissues of the ankle, as well as hypoplasia of some pelvic and lumbo-aortic nodes compared to the left side. On the left limb, a sparse lymphatic network was visualized, with collaterals and recruitment of the deep lymphatic network and visualization of a popliteal node, normal inguinal, and pelvic nodes. Dermal stasis with clear extravasation of the radiopharmaceutical at the lateral side of the foot and the ankle is seen on the planar images, but better individualized on SPECT/CT. SPECT/CT also confirmed the recruitment of a left popliteal lymph node network (**P** arrow) and global inguinal and right lumbo-aortic hypoplasia without compressive cause on CT. These results confirmed bilateral lower limb lymphatic dysfunction. Appropriate physiotherapy and compression stockings were prescribed by the referring physician (**Figure 3**). The patient began to feel clinical improvement after 3 weeks. Regarding the lymphoscintigraphic acquisitions, the patient did not report any trouble or discomfort when using the new 3D-ring CZT SPECT system.

DISCUSSION

Lymphatic dysfunction may be primary (congenital, praecox, or tarda) or secondary: due to filariasis (8), post-trauma or surgery (9), post-radiation therapy (10), cancer, thyroid disease, obesity, and chronic venous insufficiency. Typical patterns of upper and lower limb lymphedema have been previously described using planar images with dual-head systems (11). Few studies have reported the added value of SPECT/CT to specify the anatomical correlation of lymphatic disorders (2, 4–6).

Different surgical approaches to lymphedema can be considered. Microsurgical treatment of lymphedema, which includes anastomosis between lymphatic vessels and veins or between lymph nodes and veins, requires the identification of functional lymphatic vessels and/or lymph nodes under areas of dermal backflow. Thus, SPECT/CT might be of particular interest (12). Another surgical procedure, liposuction, is used to reduce excess fat deposition in the lymphedematous limb. In this technique, SPECT/CT could be used before surgery to assess the tissue changes related to the lymph stasis, and it could also be used after surgery to understand the functional state of the lymphatic system despite this surgical resection (13). Besides surgery, dedicated physiotherapy with compression stockings is often prescribed which was similar to our patient. SPECT/CT can also guide physical therapists to apply higher pressures in areas with collaterals during their manual maneuvers and/or use of compression system devices (5).

Though the use of SPECT/CT has been described, due to technical limitations, the previous studies only reported 1 or 2 fields of view SPECT/CT (4, 5). The new 3D-ring CZT SPECT camera allows full SPECT acquisitions, using CZT technology. Our case report shows a full pelvic and limbs SPECT/CT for lymphoscintigraphy, acquired in the same duration as the whole-body planar on the conventional dual-head camera. Considering the whole traditional protocol on a dual-head camera, this all-in-one full SPECT acquisition resulted in a time-reduction of more than 50%, including whole body, statics, and mandatory SPECT/CT. The StarGuide SPECT system can acquire native SPECT images, without performing CT. In this observation, we chose to perform a whole CT to have anatomical details of pelvic, popliteal, and ankle regions. Another option could have been to acquire partial CT volume, for example on the popliteal region, to reduce CT exposure, especially in younger patients. Up to now, two major devices rely on 3D-ring CZT design: Veriton SPECT (Spectrum Dynamics Medical) and StarGuide SPECT (GE Healthcare). A recent study using Veriton SPECT found that these new cameras are reliable and that there is no change in the subjective patient experience (14). Regarding the physical performances, a recent study demonstrated that the Veriton CZT camera has superior sensitivity, higher energy resolution, and better image contrast than the conventional SPECT camera, whereas spatial resolution remains similar (15). To our knowledge, this case is the first to report the use of this new generation of SPECT/CT systems for lymphoscintigraphic explorations. New developments in these systems also allow dynamic acquisitions; thus, the next step could be the early-stage dynamic acquisition of lymphoscintigraphy on these 3D-ring CZT SPECT/CT systems, allowing a 4D lymphoscintigraphic exploration, with the anatomical data of CT.

CONCLUSION

Our results confirmed that the use of SPECT/CT in lymphoscintigraphic investigations of lymphedema could

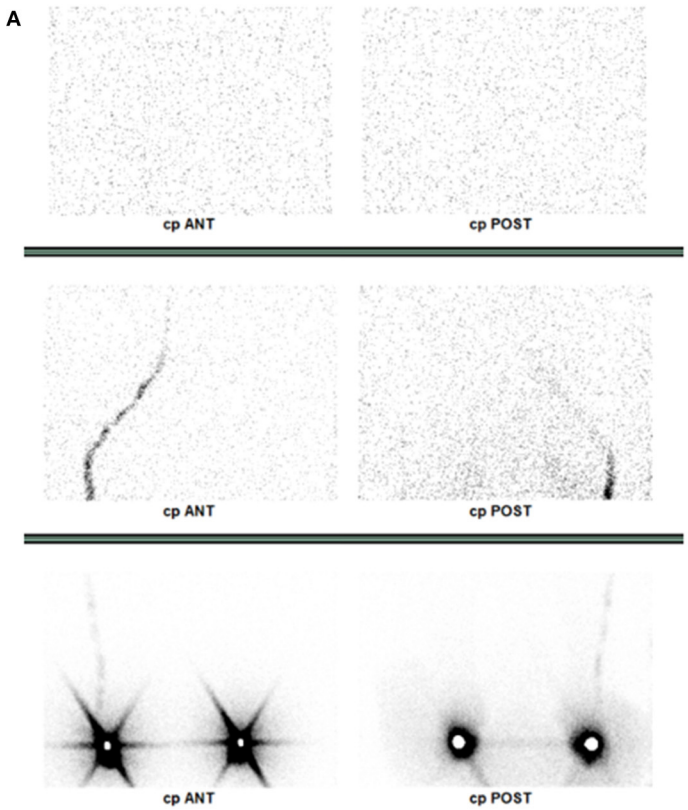

FIGURE 1 | Dual-head conventional camera results. Early anterior and posterior static planar images **(A)**, late anterior and posterior whole-body planar images **(B)**.

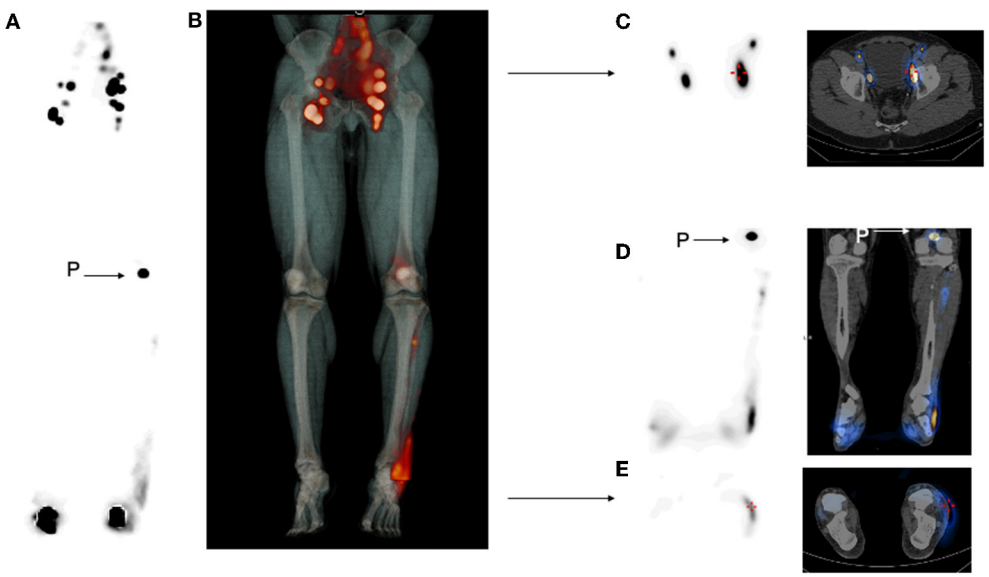

FIGURE 2 | 3D-ring cadmium -zinc-telluride single-photon emission CT (CZT SPECT) images. Maximum intensity projection (MIP) anterior view (SPECT only **A**, fused SPECT/CT **B**). **(C)** Axial SPECT and SPECT/CT on the pelvic region. **(D)** Coronal SPECT and SPECT/CT on the leg. **(E)** Axial SPECT and SPECT/CT on the ankles. P with arrow shows the popliteal node. All SPECT images displayed are native non-corrected images.

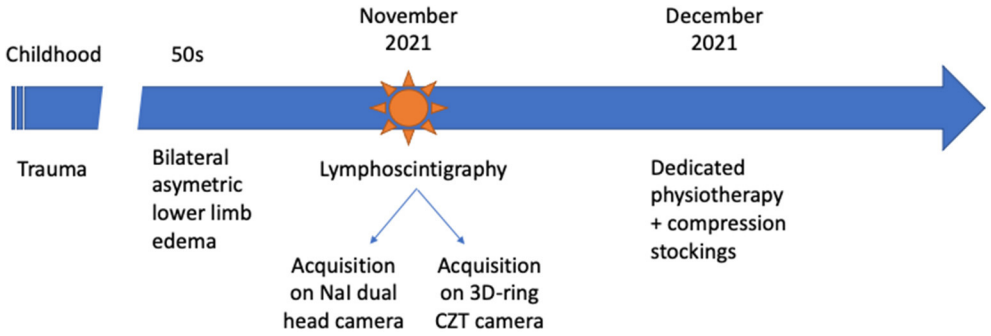

FIGURE 3 | Timeline of diagnosis and intervention for the patient.

be helpful and could be quickly available thanks to 3D-ring CZT cameras for the full exploration of both the pelvic region and limbs. The next step could be the acquisition of early 4D-dynamic SPECT with anatomical CT.

DATA AVAILABILITY STATEMENT

The raw data supporting the conclusions of this article will be made available by the authors, without undue reservation.

ETHICS STATEMENT

The studies involving human participants were reviewed and approved by CPP Nord Ouest IV; ClinicalTrials.gov Identifier: NCT04704349. The patients/participants provided their written informed consent to participate in this study.

AUTHOR CONTRIBUTIONS

HB collected the data and interpreted the diagnosis. MB analyzed the literature and wrote the manuscript. All authors contributed to manuscript revision, and read and approved the submitted version.

ACKNOWLEDGMENTS

The authors would like to thank all the medical and paramedical staff of CHR d'Orléans, and the GE Healthcare engineering team based in Haïfa. This study is part of the French Network of University Hospitals HUGO (Hôpitaux Universitaires du Grand Ouest).

REFERENCES

1. Barbieux R, Roman MM, Riviere F, Leduc O, Leduc A, Bourgeois P, et al. Scintigraphic investigations of the deep and superficial lymphatic systems in the evaluation of lower limb oedema. *Sci Rep.* (2019) 9:13691. doi: 10.1038/s41598-019-49554-7
2. Pecking AP, Alberini JL, Wartski M, Edeline V, Cluzan RV. Relationship between lymphoscintigraphy and clinical findings in lower limb lymphedema (LO): toward a comprehensive staging. *Lymphology.* (2008) 41:1–10.
3. Weiss M, Baumeister RG, Hahn K. Dynamic lymph flow imaging in patients with oedema of the lower limb for evaluation of the functional outcome after autologous lymph vessel transplantation: an 8-year follow-up study. *Eur J Nucl Med Mol Imaging.* (2003) 30:202–6. doi: 10.1007/s00259-002-1020-1
4. Weiss M, Baumeister RG, Frick A, Wallmichrath J, Bartenstein P, Rominger A. Primary lymphedema of the lower limb: the clinical utility of single photon emission computed tomography/CT. *Korean J Radiol.* (2015) 16:188–95. doi: 10.3348/kjr.2015.16.1.188
5. Baulieu F, Bourgeois P, Maruani A, Belgrado JP, Tauveron V, Lorette G, et al. Contributions of SPECT/CT imaging to the lymphoscintigraphic investigations of the lower limb lymphedema. *Lymphology.* (2013) 46:106–19.
6. Maccauro M, Villa G, Manzara A, Follacchio GA, Manca G, Tartaglione G, et al. Lymphoscintigraphy for the evaluation of limb lymphatic flow disorders: Report of technical procedural standards from an Italian Nuclear Medicine expert panel. *Rev Esp Med Nucl Imagen Mol.* (2019) 38:335–40. doi: 10.1016/j.remnie.2019.03.003
7. Bahloul A, Verger A, Blum A, Chawki MB, Perrin M, Melki S, et al. Bone scintigraphy of vertebral fractures with a whole-body CZT camera in a PET-like utilization. *Front Nucl Med.* (2021) 1. doi: 10.3389/fnume.2021.740275
8. Tiwari A, Cheng KS, Button M, Myint F, Hamilton G. Differential diagnosis, investigation, and current treatment of lower limb lymphedema. *Arch Surg.* (2003) 138:152–61. doi: 10.1001/archsurg.138.2.152
9. Szuba A, Shin WS, Strauss HW, Rockson S. The third circulation: radionuclide lymphoscintigraphy in the evaluation of lymphedema. *J Nucl Med.* (2003) 44:43–57.
10. Ter SE, Alavi A, Kim CK, Merli G. Lymphoscintigraphy. A reliable test for the diagnosis of lymphedema. *Clin Nucl Med.* (1993) 18:646–54. doi: 10.1097/00003072-199308000-00003
11. Sundaram PS, Subramanyam P. Lymphoscintigraphy in the evaluation of limb edema. *Clin Nucl Med.* (2013) 38:891–903. doi: 10.1097/RLU.0b013e3182a758f9
12. Lee BB, Laredo J, Neville R. Current status of lymphatic reconstructive surgery for chronic lymphedema: it is still an uphill battle! *Int J Angiol.* (2011) 20:73–80. doi: 10.1055/s-0031-1279685
13. Brorson H, Hoijer P. Standardised measurements used to order compression garments can be used to calculate arm volumes to evaluate lymphoedema treatment. *J Plast Surg Hand Surg.* (2012) 46:410–5. doi: 10.3109/2000656X.2012.714785
14. Komber H, Little D, Cade S, Graham R, Redman S. Comparing the patient experience between a novel 360 degrees gamma camera (VERITON-CT) and a conventional dual head gamma camera. *J Nucl Med Technol.* (2021). doi: 10.2967/jnmt.121.262627. [Epub ahead of print].

15. Desmonts C, Bouthiba MA, Enilorac B, Nganoa C, Agostini D, Aide N. Evaluation of a new multipurpose whole-body CzT-based camera: comparison with a dual-head Anger camera and first clinical images. *EJNMMI Phys.* (2020) 7:18. doi: 10.1186/s40658-020-0284-5

Conflict of Interest: MB received honoraria for StarGuide lectures.

The remaining author declares that this study received funding from GE Healthcare (technical and financial support paid to the institution). The funder was not involved in the study design, collection, analysis, interpretation of data, the writing of this article or the decision to submit it for publication.

Publisher's Note: All claims expressed in this article are solely those of the authors and do not necessarily represent those of their affiliated organizations, or those of the publisher, the editors and the reviewers. Any product that may be evaluated in this article, or claim that may be made by its manufacturer, is not guaranteed or endorsed by the publisher.

frontiers | Frontiers in Medicine

TYPE Original Research
PUBLISHED 02 February 2023
DOI 10.3389/fmed.2023.1119214

OPEN ACCESS

EDITED BY
Greta Mok,
University of Macau, China

REVIEWED BY
Carmelo Caldarella,
Fondazione Policlinico Universitario A. Gemelli IRCCS, Italy
Fei Kang,
Fourth Military Medical University, China

*CORRESPONDENCE
Rong Zheng
✉ zrong99@163.com
Xuejuan Wang
✉ xuejuan_wang@hotmail.com

SPECIALTY SECTION
This article was submitted to Nuclear Medicine, a section of the journal Frontiers in Medicine

RECEIVED 08 December 2022
ACCEPTED 16 January 2023
PUBLISHED 02 February 2023

CITATION
Lin L, Zheng R, Geng J, Wang X, Li M, Fan R, Zheng Y and Yang K (2023) Skeletal standardized uptake values obtained using quantitative SPECT/CT for the detection of bone metastases in patients with lung adenocarcinoma. *Front. Med.* 10:1119214. doi: 10.3389/fmed.2023.1119214

Skeletal standardized uptake values obtained using quantitative SPECT/CT for the detection of bone metastases in patients with lung adenocarcinoma

Lin Lin[1], Rong Zheng[1]*, Jianhua Geng[1], Xuejuan Wang[1]*, Meng Li[2], Rong Fan[1], Yiqing Zheng[1] and Ke Yang[1]

[1]Department of Nuclear Medicine, National Cancer Center/National Clinical Research Center for Cancer/Cancer Hospital, Chinese Academy of Medical Sciences and Peking Union Medical College, Beijing, China, [2]Department of Radiology, National Cancer Center/National Clinical Research Center for Cancer/Cancer Hospital, Chinese Academy of Medical Sciences and Peking Union Medical College, Beijing, China

Purpose: To assess the utility of skeletal standardized uptake values (SUVs) obtained using quantitative single-photon emission computed tomography/computed tomography (SPECT/CT) in differentiating bone metastases from benign lesions, particularly in patients with lung adenocarcinoma.

Methods: Patients with lung adenocarcinoma who had undergone whole-body Tc-99m methyl-diphosphonate (^{99m}Tc-MDP) bone scans and received late phase SPECT/CT were retrospectively analyzed in this study. The maximum SUV (SUVmax); Hounsfield units (HUs); and volumes of osteoblastic, osteolytic, mixed, CT-negative metastatic and benign bone lesions, and normal vertebrae were compared. Receiver operating characteristic curves were used to determine the optimal cutoff SUVmax between metastatic and benign lesions as well as the cutoff SUVmax between CT-negative metastatic lesions and normal vertebrae. The linear correlation between SUVmax and HUs of metastatic lesions as well as that between SUVmax and the volume of all bone lesions were investigated.

Results: A total of 252 bone metastatic lesions, 140 benign bone lesions, and 199 normal vertebrae from 115 patients with lung adenocarcinoma were studied (48 males, 67 females, median age: 59 years). Metastatic lesions had a significantly higher SUVmax (23.85 ± 14.34) than benign lesions (9.67 ± 7.47) and normal vertebrae (6.19 ± 1.46; $P < 0.0001$). The SPECT/CT hotspot of patients with bone metastases could be distinguished from benign lesions using a cutoff SUVmax of 11.10, with a sensitivity of 87.70% and a specificity of 80.71%. The SUVmax of osteoblastic (29.16 ± 16.63) and mixed (26.62 ± 14.97) lesions was significantly greater than that of osteolytic (15.79 ± 5.57) and CT-negative (16.51 ± 6.93) lesions ($P < 0.0001$, $P = 0.0003$, and 0.002). SUVmax at the cutoff value of 8.135 could distinguish CT-negative bone metastases from normal vertebrae, with a sensitivity of 100.00% and a specificity of 91.96%. SUVmax showed a weak positive linear correlation with HUs in all bone metastases and the volume of all bone lesions.

Conclusion: SUVmax of quantitative SPECT/CT is a useful index for distinguishing benign bone lesions from bone metastases in patients with lung adenocarcinoma, particularly in the diagnosis of CT-negative bone metastases, but other factors that may affect SUVmax should be considered.

KEYWORDS

Tc-99m methylene-diphosphonate, quantitative single-photon emission computed tomography/computed tomography, standardized uptake value, lung adenocarcinoma, bone metastases

1. Introduction

According to the International Agency for Research on Cancer (IARC) 2020 global burden of cancer statistics, lung cancer ranks second in global incidence and first in mortality (1). Lung cancer remains the most common cancer type in China and the leading cause of cancer-related deaths (2). Adenocarcinoma has become the most common subtype of lung cancer, with increasing prevalence (3). The skeleton is one of the most common metastatic sites in patients with advanced lung cancer, with an incidence of bone metastasis of 30%−40% (4). Unlike the mostly osteoblastic bone metastases of prostate cancer, the bone metastases of lung cancer may include osteolytic, osteoblastic, mixed, and CT-negative metastases and may exhibit complex CT features. Therefore, it is more challenging to diagnose bone metastases in patients with lung cancer. We here in focused on patients with lung adenocarcinoma, who account for the vast majority of lung cancer cases in China (2, 3).

Bone scintigraphy (BS) is one of the most commonly used methods for early screening and detection of bone metastases in the whole skeleton (5, 6). However, with low regional blood flow and osteogenic activity as well as low spatial resolution, it is relatively insensitive for detecting changes in bone metastatic tumors. Furthermore, some benign lesions can produce a false positive signal during BS evaluation, thereby limiting the specificity of this imaging technique (7). Single-photon emission computed tomography/computed tomography (SPECT/CT) enables characterization of morphological changes and determination of anatomical correlations and attenuation corrections of radiotracer uptake on CT, resulting in a significant improvement in diagnostic accuracy, particularly when assessing indeterminate lesions on planar BS (8). Studies have shown that adding SPECT/CT to BS improves the specificity, positive predictive value, and diagnostic confidence of the reader, thereby reducing the number of equivocal study reports (9, 10). SPECT has conventionally been used as a nonquantitative method; however, wide acceptance of integrated SPECT/CT scanners and development of iterative reconstruction algorithms have made it possible to use quantitative SPECT in clinical settings (11–13).

Quantitative SPECT and positron emission tomography (PET) enable the calculation of standardized uptake values (SUVs), which can be used for disease assessment and interpatient comparisons (14–17). In a previous study, a strong correlation between the SUVs of ^{99m}Tc-hydroxyethylene diphosphonate (HDP) SPECT/CT and those of ^{18}F-NaF PET/CT demonstrated that SPECT is an applicable tool for clinical quantification of bone metabolism in osseous metastases in patients with breast and prostate cancer (18). Furthermore, SUVs can be used to broaden the visual analysis of skeletal structures (18). Previous studies on patients with prostate cancer showed that the SPECT SUVmax of bone metastases was significantly higher than that of benign bone lesions, degenerative joint disease of bone, and benign spinal and pelvic osteoarthritic changes (14, 16, 17, 19). Because the CT manifestations of bone metastases in patients with lung cancer are more complex, the SUVmax results of quantitative SPECT/CT are highly variable among different types of bone lesions in these patients (15, 20). As the feature of SUVmax in patients with lung cancer is quite different from that in patients with prostate cancer, a thorough investigation is necessary. However, few studies have performed quantitative SPECT/CT bone imaging analysis of the SUVmax of bone metastases in patients with lung adenocarcinoma.

This study aimed to analyze the SUVmax levels of bone metastases of four different CT features obtained using quantitative SPECT/CT in patients with lung adenocarcinoma as well as the SUVmax cutoff values to distinguish bone metastases from benign lesions and the SUVmax cutoff values for distinguishing CT-negative bone metastases from normal vertebrae. We also investigated the effect of the volume of lesions and Hounsfield units (HUs) on SUVmax.

2. Materials and methods

2.1. Patients

A total of 115 patients with lung adenocarcinoma who had undergone bone scans and SPECT/CT at the Cancer Hospital, Chinese Academy of Medical Sciences, and Peking Union Medical College from September 2021 to May 2022 were analyzed. The following criteria were used to determine inclusion: (i) bone scans and SPECT/CT performed on the same day; (ii) no receipt of treatment for skeletal metastatic lesions prior to imaging analyses; and (iii) no history of other primary malignancies. The exclusion criteria were as follows: (i) no available bone scan or SPECT/CT results; (ii) patients who were lost to follow-up; and (iii) no definite histopathological diagnosis of the primary lesion.

All patients were followed up for at least 6 months (10.7 ± 2.3, 6.0–14.7 months). For ethical and practical reasons, biopsy-based confirmation of patient bone metastases was not performed; instead, the final diagnosis of these metastases was based on a combination of imaging examination results (BS, CT, MRI, or PET/CT) and clinical follow-up (physical signs and follow-up imaging examinations).

The Ethics Committee of the Cancer Hospital, Chinese Academy of Medical Sciences, and Peking Union Medical College approved this study, which followed the 1964 Helsinki Declaration ethical standards and its subsequent amendments. All patients provided written informed consent.

2.2. Image acquisition

All patients underwent whole-body planar imaging (scanned 2.5–4.5 h after injection)with a low-energy high-resolution collimator and quantitative SPECT/CT (Siemens Symbia Intevo 6, USA) on planar scintigraphy high-uptake regions. SPECT was acquired at a mean patient dose of 831 ± 44 MBq (22.45 ± 1.19 mCi, range: 20.00–25.20 mCi) ^{99m}Tc-MDP intravenous injection (from HTA Co., Ltd., and Beijing Senke Pharmaceutical Co., Ltd) and 0–3.5 h after the whole-body planar bone scan. Images were captured using a 256 × 256 matrix size and 6 degrees rotation/step, 15 seconds/projection. CT scans were performed using adaptive dose modulation at 130 kV and 60 mAs (Siemens Care Dose). The CT data were reconstructed using B60s medium sharp with a slice thickness of 2.5 mm. SPECT images were reconstructed using the Flash 3D algorithm (xSPECT Skeletal mode) with eight iterations, four subsets, and a Gaussian filter. The SPECT reconstructed values were decay-corrected to the time of injection and final values of quantitative radioactivity concentrations were obtained to allow SUV body weight quantification (SUVbw) on post-processed images and measurement of SUVmax (g/ml) using the xSPECT reconstruction algorithm. SUVmax was defined as the

pixel value with the highest activity concentration within a volume of interest (VOI).

2.3. Image interpretation

The ^{99m}Tc-MDP planar and SPECT/CT bone scans were interpreted independently by two nuclear medicine physicians who were blinded to the clinical history and findings of each other. The reviewers had 10 and 8 years of experience in nuclear medicine, respectively. The combination of SPECT and CT images was analyzed first, followed by a planar whole-body bone scan. Disagreements in lesion interpretation were resolved through consensus and joint reading.

For SPECT/CT fusion imaging analysis, bone metastases were diagnosed if the CT revealed osteolytic changes (bone erosion, edge irregularity, no osteosclerosis, or a soft-tissue mass), osteoblastic changes (high bone density without a soft-tissue mass) in areas of abnormal radioactivity concentrations. If an abnormal radioactivity concentration was observed involving the centrum or pedicle of the vertebral arch or another part of the skeleton but the CT did not show eroded bone damage or a soft-tissue mass, an early-stage CT-negative metastatic bone diagnosis was made. A benign lesion was diagnosed if the CT revealed degenerative changes, such as hyperosteogeny, osteosclerosis, osteophytes, Schmorl's nodes, a bone island, or a fracture in the lesion area with an abnormal radioactivity concentration (14).

Using "Siemens 3D Isocontour," hotspot lesions were drawn on transversal, sagittal, and coronal SPECT/CT fusion sections by placing the VOI with the margin threshold set at 40% of the SUVmax (Figure 1: Method 1). The Siemens "Multi-frame Polygon" tool was used to manually draw osteolytic bone lesions on transversal SPECT/CT fusion sections (Figure 1: Method 2). The VOIs of no more than three of the largest bone metastatic lesions visible on SPECT were drawn for patients with multiple metastases. On transversal, sagittal, and coronal SPECT/CT fusion sections, hyperosteopathic lesions or other benign lesions with relatively low uptake were delineated using the Siemens "Ellipsoid" tool (Figure 1: Method 3). On transversal, sagittal, and coronal SPECT/CT fusion sections with volumes ranging from 1 to 5 cm^3, visually normal spinal vertebral body was delineated using the "Ellipsoid" tool, excluding the bone cortex (Figure 1: Method 4). Normal vertebrae were chosen from cervical, thoracic, and lumbar vertebrae, with one for each in the scan field. Bone density values were measured in HUs on the CT images of SPECT/CT.

2.4. Statistical analysis

SPSS software V.22.0 (IBM SPSS) and GraphPad Prism 8.0 were used for statistical analyses. All statistical data are presented as mean ± standard deviation (SD). Mann–Whitney nonparametric test was used to compare median values between two unpaired groups. Kruskal–Wallis test for independent samples was used to compare median values among three or more unpaired groups. Receiver operating characteristic (ROC) curve analysis was used to determine the best SUVmax cutoff value. A P-value of <0.05 was considered statistically significant for all tests. Linear correlations between SUVmax and HUs and between SUVmax and volume were analyzed.

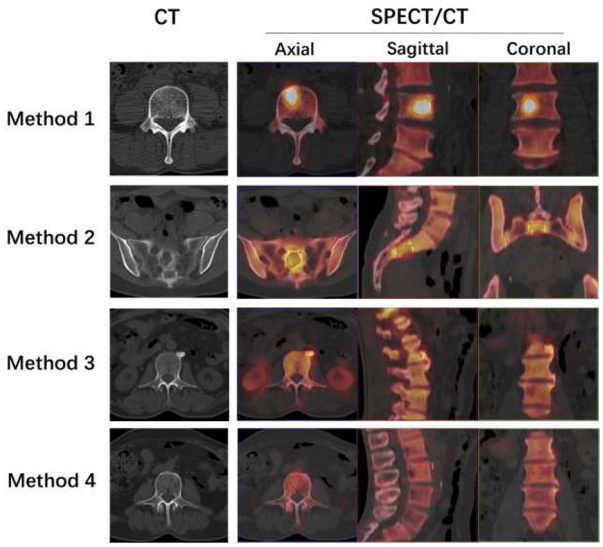

FIGURE 1
Four methods to delineate different VOIs. **Method 1**: The L4 bone metastatic lesion was delineated by putting the tumor VOI at 40% of the SUVmax on the SPECT/CT fusion images of axial, sagittal, and coronal sections. The axial section of CT showed no abnormal density changes. **Method 2**: The Siemens "Multi-frame Polygon" tool was used to manually draw an osteolytic bone metastatic lesion of the sacrum on axial SPECT/CT fusion sections from the top to the bottom of the lesion. Then, the sagittal and coronal images were automatically delineated. The axial section of CT showed osteolytic bone destruction of sacrum. **Method 3**: On axial, sagittal, and coronal SPECT/CT fusion sections, the hyperosteogeny lesion of L2 was delineated using the "Ellipsoid" tool. The axial section of CT showed osteophytes of L2. **Method 4**: The visually normal L3 vertebral body was delineated on axial, sagittal, and coronal SPECT/CT fusion sections with volumes not more than 5 cm^3 using the "Ellipsoid" tool, excluding the bone cortex. The axial section of CT showed normal vertebrae of L3.

3. Results

3.1. Distribution of all lesions and types of benign bone lesions

A total of 252 bone metastatic lesions were analyzed from 115 patients with lung adenocarcinoma (Table 1 shows the characteristics of the patients). Of the 252 metastatic lesions, 123 were located in the spine (cervical, thoracic, and lumbar), 38 in the thorax (including the ribs, clavicle, sternum, and scapula), 75 in the pelvis (including the hip, sacrum, and sacroiliac region), 15 at the limbs, and one in the skull. Among the 140 benign bone lesions, 89 were present in the spine, 12 in the thorax, 25 in the pelvis, and 14 in the limbs. Among the 199 normal vertebrae, 20 were cervical vertebrae, 90 thoracic vertebrae, and 89 lumbar vertebrae.

Among the 140 benign bone lesions, 107 lesions (76.4%) were hyperosteogeny (including 82 osteophytes, 13 hyperplastic sclerosis of the sacroiliac joint, and 12 hyperplasia of the sternoclavicular or costal vertebra joint); 12 lesions (8.6%) were single focal lesions that occurred in the iliac bone or in the proximal femur or humerus, showing a clear boundary of sclerosis (may be bone infarct, bone cyst,

TABLE 1 Participant characteristics.

Characteristic	Value
Mean age (years)*	58.38 ± 9.92 (34–78)
Gender	
Men (*n*, %)	48 (41.7%)
Women (*n*, %)	67 (58.3%)
Metastatic lesions (*n*)†	
0	10
1–5	58
6–10	19
11–20	18
>20	10

*Data are the mean ± standard deviation; data in parentheses are the range.
†The data are patient numbers in the various metastatic number ranges listed below.

TABLE 2 Number of metastatic bone lesions, benign bone lesions, and normal vertebrae as well as their SUVmax, HUs, and volume.

	Metastatic lesions	Benign lesions	Normal vertebrae
Number	252	140	199
SUVmax (mean ± SD)	23.85 ± 14.34	9.67 ± 7.47	6.19 ± 1.46
Median of SUVmax	19.86	8.21	6.03
Min. of SUVmax	4.74	3.49	2.4
Max. of SUVmax	75.33	66.27	11.62
Median HUs	244.1	393.5	159.19
Median volume (cm^3)	8.37	2.61	3.76

SUVmax was measured in g/ml of body weight (BW). The results are presented as the mean ± SD. SUVmax, the maximum standardized uptake value; SD, the standard deviation; Minimum (Min.), the smallest value; Maximum (Max.), the highest possible value.
The volume unit is cm^3. Bone density values were measured in Hounsfield units (HUs).

fibrous dysplasia of bone, or other benign bone lesions); four lesions (2.9%) were osteitis; four lesions (2.9%) were vertebral hemangiomas; three lesions (2.1%) were compacta bone islands; three lesions (2.1%) were bone fractures; three lesions (2.1%) were the Schmorl's nodes; two lesions (1.4%) may have been enchondromas; one lesion (0.7%) may have been fibrous dysplasia of bone; and one lesion (0.7%) may have been a vasculogenic lesion of fibula.

3.2. SUVmax, HUs, and volume differences between metastatic and benign bone lesions and normal vertebrae

The SUVmax of metastatic lesions (23.85 ± 14.34) was higher than that of benign lesions (9.67 ± 7.47) and normal vertebrae (6.19 ± 1.46). The difference among the SUVmax of the three groups was statistically significant ($P < 0.0001$).

The HUs of benign lesions were higher than those of metastatic lesions and normal vertebrae; the HUs of metastatic lesions were higher than those of normal vertebrae; and the difference in HUs among the three groups was statistically significant ($P < 0.0001$). Metastatic lesions had larger volumes than benign lesions and normal vertebrae ($P < 0.0001$), but there was no statistically significant difference between the volumes of benign lesions and normal vertebrae ($P = 0.1309$) (Table 2, Figure 2).

3.3. SUVmax discrimination for bone metastases

Figure 3 depicts the results of SUVmax ROC curve analyses. The SUVmax area under the curve value was 0.9097 (95% CI: 0.8786–0.9407, $P < 0.0001$). The optimal cutoff value for distinguishing hotspots of patients with bone metastases from those of patients with benign lesions in SPECT/CT was 11.10, with a sensitivity of 87.70% and a specificity of 80.71%.

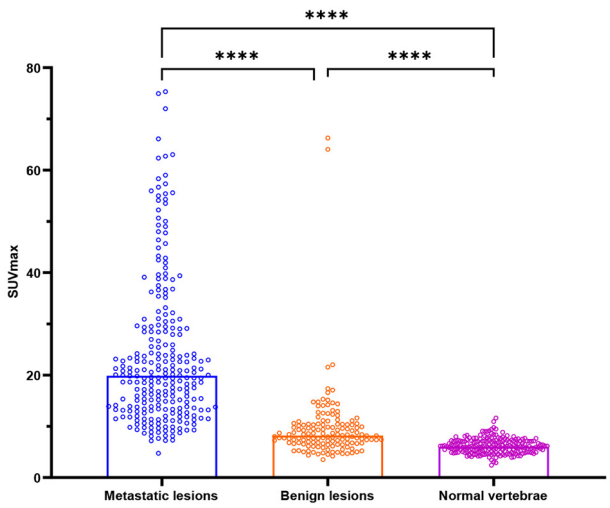

FIGURE 2
Box plots of all lesions in relation to the SUVmax (g/ml) for bone metastases, benign lesions, and normal vertebrae. ****$P < 0.0001$.

3.4. SUVmax, HUs, and volume differences between metastatic lesions and four different CT features

Table 3 shows the number and percentage of total bone metastases for osteoblastic, osteolytic, mixed, and CT-negative metastatic lesions. The most common CT type of bone metastases in patients with lung adenocarcinoma was mixed lesions.

SUVmax was higher in osteoblastic (29.16 ± 16.63) and mixed (26.62 ± 14.97) metastatic lesions than in osteolytic (15.79 ± 5.57) lesions, and it was statistically significant ($P < 0.0001$). The SUVmax of osteoblastic and mixed lesions was significantly higher than that of CT-negative (16.51 ± 6.93) lesions (P-values = 0.0003 and 0.002, respectively). There was no statistically significant difference between the SUVmax of osteoblastic and mixed lesions ($P > 0.9999$) and between the SUVmax of osteolytic and CT-negative lesions ($P > 0.9999$; Table 3, Figure 4).

The average HUs of osteoblastic lesions was significantly greater than that of osteolytic, mixed, and CT-negative lesions ($P < 0.0001$). The average HUs of osteolytic lesions was significantly lower than that of mixed and CT-negative lesions ($P < 0.0001$). However, there was no statistically significant difference in HUs between mixed and CT-negative lesions ($P > 0.9999$). The volumes of the four different CT types of metastases did not differ statistically ($P > 0.05$).

3.5. SUVmax discrimination accuracy for CT-negative bone metastatic lesions

The area under the ROC for distinguishing between CT-negative metastatic lesions and normal vertebrae was 0.9923 (95% CI: 0.9839–1.000; *P*-value < 0.0001; *P*-value < 0.0001). The SUVmax at the cutoff value of 8.135, with a sensitivity of 100.00% and a specificity of 91.96%, can be used to differentiate CT-negative bone metastatic lesions (Figures 5, 6).

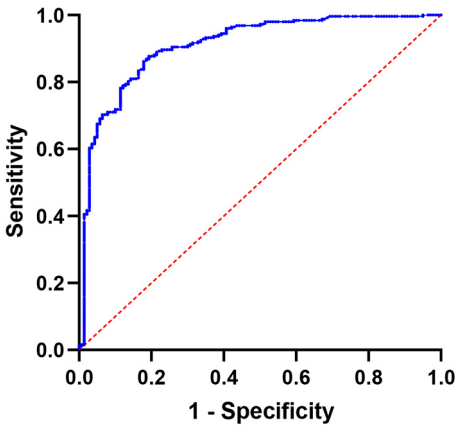

FIGURE 3
Using SUVmax, a receiver operating characteristic (ROC) curve was created to differentiate benign bone lesions from bone metastases; the area under the curve is 0.9097 (95% CI 0.8786–0.9407).

3.6. Linear correlation between SUVmax and HUs and between SUVmax and volume

SUVmax has a weak positive linear correlation with HUs for all bone metastatic lesions [r value = 0.2326 (95% CI: 0.1123–0.3463); *P*-value = 0.0002; Figure 7A]. SUVmax had a weak positive linear correlation with lesion volume for all bone lesions, including benign and metastatic lesions [r value = 0.2772 (95% CI 0.1832–0.3662); *P*-value < 0.0001; Figure 7B].

4. Discussion

Although body size, renal function, skeletal disease extent, and post injection acquisition time may affect SPECT/CT values, the skeletal quantification bone SPECT/CT has the potential to

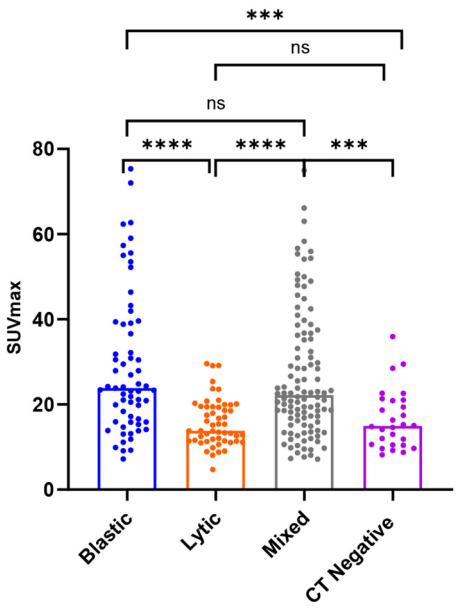

FIGURE 4
Box plots of all lesions in relation to the SUVmax (g/ml) for osteoblastic, osteolytic, mixed, and CT-negative metastatic lesions. ****$P < 0.0001$. ***$P = 0.0003$ and 0.002. $P > 0.9999$ is denoted by ns.

TABLE 3 The number, SUVmax values, HUs, and volume of bone metastatic lesions that were osteoblastic, osteolytic, mixed, or CT-negative.

	Osteoblastic lesions	Osteolytic lesions	Mixed lesions	CT-negative lesions
Number (%)	63 (25%)	53 (21.03%)	108 (42.86%)	28 (11.11%)
SUVmax	29.16 ± 16.63	15.79 ± 5.57	26.62 ± 14.97	16.51 ± 6.93
Median SUVmax	23.87	13.84	22.21	14.95
Min. SUVmax	7.23	4.74	7.18	8.18
Max. SUVmax	75.33	29.60	74.95	35.94
Median HUs	419.44	87.00	260.07	205.66
Median volume (cm^3)	6.70	8.77	8.48	7.47

The number preceding % represents the percentage of all bone metastases. SUVmax was measured in g/ml of body weight (BW). The results are presented as the mean ± SD.
SUVmax, the maximum standardized uptake value; SD, the standard deviation; Minimum (Min.), the smallest value; Maximum (Max.), the highest possible value; Hus, Hounsfield units.
The volume unit is cm^3.

serve as a good biomarker of osteoblastic metabolism (14, 21). Previous studies (14, 16, 19) investigated the SUVs cutoff value to distinguish bone metastases from benign bone lesions. Yiqiu Zhang's and Flavian Tabotta's studies showed that SUVmax had greater accuracy than the average SUV (SUVave or SUVmean) in distinguishing bone metastasis from benign lesions (14, 19). Therefore, in the present study, we chose SUVmax as the only index to distinguish different lesions. To the best of our knowledge, few studies have analyzed SUVmax in bone lesions derived from patients with lung adenocarcinoma. Although the diagnoses of bone metastases in patients with lung adenocarcinoma mainly depend on the characteristics of CT images, the SUVmax of lesions obtained from quantitative SPECT/CT can be important when the CT findings of the bone lesions are atypical or there are high-uptake bone lesions without obvious CT abnormalities. We therefore aimed to explore the probable SUVmax cutoff value of bone metastases in patients with lung adenocarcinoma, especially the SUVmax cutoff value of CT-negative lesions, and analyze the SUVmax level of different CT characteristic bone metastases in patients with lung adenocarcinoma and factors that may affect SUVmax.

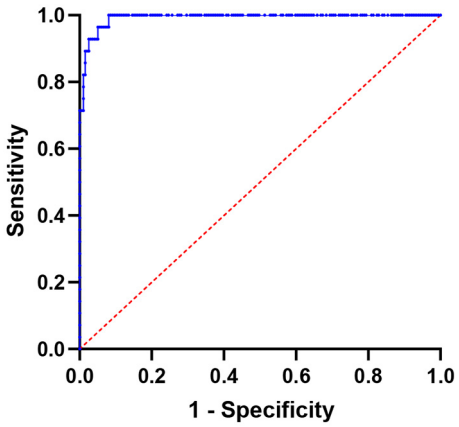

FIGURE 5
Using SUVmax, a receiver operating characteristic (ROC) curve was created to differentiate lesions between normal vertebrae and CT-negative bone metastases; the area under the curve is 0.9923 (95% CI 0.9839–1.000).

The SUVmax cutoff value for distinguishing bone metastases from benign bone lesions in this study was 11.10. This cutoff value was lower than that reported in previous studies, which included either all or some patients with prostate cancer (14, 16, 19). The reason for the lower SUVmax cutoff value in this study may be the lower SUVmax of bone metastases in patients with lung adenocarcinoma than in patients with prostate cancer. A study by Flavian Tabotta, which included 264 prostate cancer bone metastases (mean SUVmax 34.6 ± 24.6) and 24 spinal and pelvic osteoarthritic lesions (mean SUVmax 14.2 ± 3.8), showed an SUVmax cutoff of 19.5 g/ml for distinguishing bone metastases from osteoarthritic lesions (19). A study by Mohd Fazrin showed that the cutoff SUVmax value of ≥20 had a sensitivity of 73.8% and a specificity of 85.4% in differentiating bone metastases (mean SUVmax 36.64 ± 24.84) from degenerative joint disease (mean SUVmax 12.59 ± 9.01) in patients with prostate cancer. Bone metastases of prostate cancer trigger an important osteoblastic reaction and substantially accumulate ^{99m}Tc-2,3-dicarboxy propane1,1-diphosphonate (^{99m}Tc-DPD) or ^{99m}Tc-MDP (19, 22), so the osteoblastic metastases have a higher SUVmax than that reported in our study that included

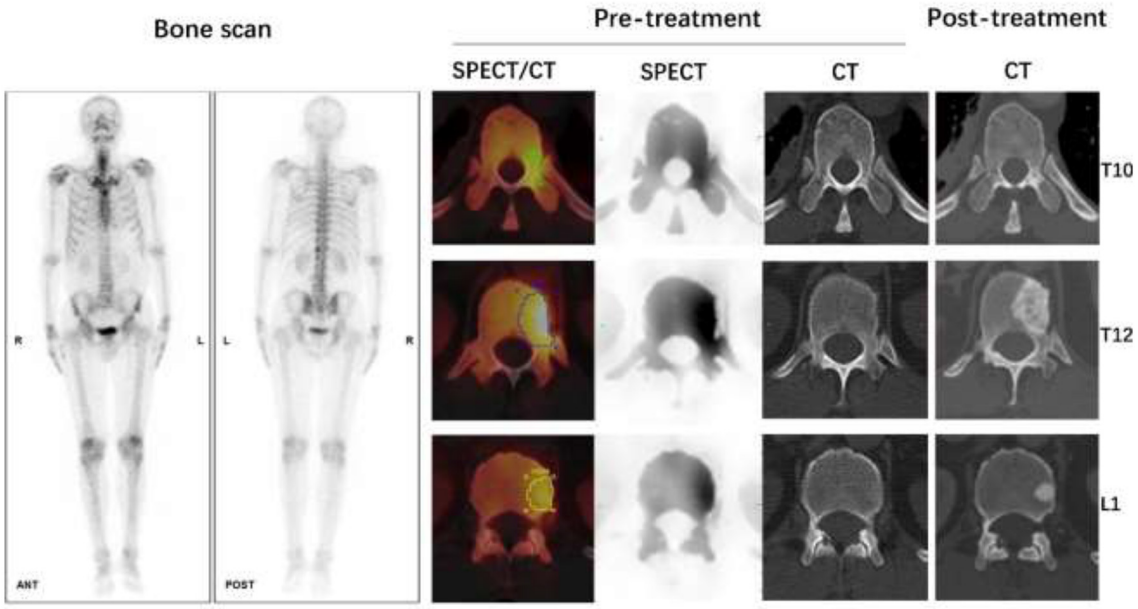

FIGURE 6
Male, 62 years old, CT guided biopsy of a tumor in the lower lobe of the right lung revealed a moderately differentiated adenocarcinoma, with an EGFR 19 mutation. Before treatment, a full-body bone scan revealed suspicious metastasis of the T10, T12, and L1 vertebrae. The SUVmax of lesions on T10, T12, and L1 vertebrae were 9.71, 14.80, and 10.52 g/ml, respectively, according to quantitative SPECT/CT. But the CT scan of these vertebrae on pre-treatment images showed no abnormal bone density changes. After 4 months of Almonertinib therapy, a post-treatment CT scan revealed increased bone mineral density in the high uptake area of SPECT images, confirmed bone metastasis of these vertebrae.

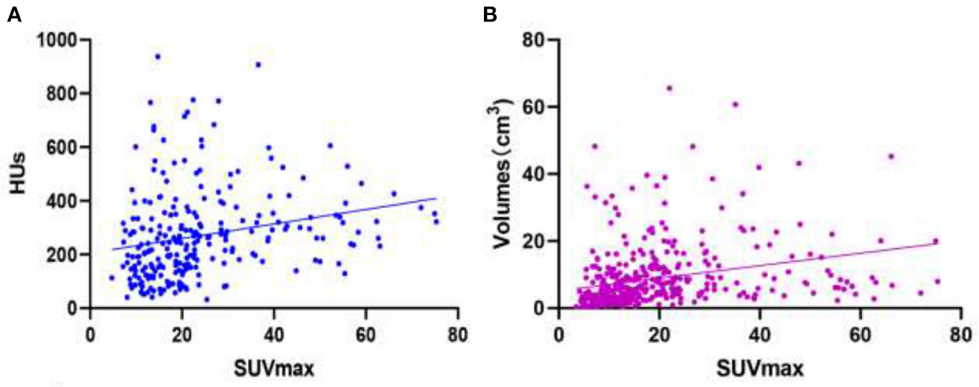

FIGURE 7
Images of linear correlation scatter plots. **(A)** Correlation between SUVmax and HUs from SPECT data for all bone metastatic lesions [*r* value = 0.2326 (95% CI 0.1123–0.3463), *P*-value = 0.0002]. **(B)** Correlation between SUVmax and volumes (cm^3) from SPECT data for all bone lesions [*r* value = 0.2772 (95% CI 0.1832–0.3662), *P*-value < 0.0001].

patients with lung adenocarcinoma (mean SUVmax 23.85 ± 14.34). Even the osteoblastic metastases of lung adenocarcinoma in our study had a lower SUVmax (mean SUVmax 29.16 ± 16.63) than that of osteoblastic metastases in patients with prostate cancer in other studies. Moreover, this study also included 21.03% osteolytic (mean SUVmax 15.79 ± 5.57), 42.86% mixed (mean SUVmax 26.62 ± 14.97), and 11.11% CT-negative (mean SUVmax 16.51 ± 6.93) bone metastatic lesions, which had a lower SUVmax.

Another reason for the lower SUVmax cutoff value in this study may be the lower SUVmax of benign lesions (mean SUVmax 9.67 ± 7.47). The mean age (58.38 ± 9.92) of patients in this study was relatively lower than that in other studies on patients with prostate cancer (mean age 74 ± 10 years and 70.4 ± 7.4 years) (17, 19). During the aging process, changes occur in the extracellular matrix in the intervertebral disks, which result in narrowing of the joint space, nerve impingement, and instability of the joint. Consequent inflammation and remodeling of the bone tissue lead to calcification of the disc and formation of bony spurs or osteophytes (23). Therefore, degenerative lesions will be more obvious and may have higher SUVmax in older patients than in younger patients in the present study. Also, for all bone lesions, SUVmax had a weak linear correlation with volumes of the lesions in this study. This result was inconsistent with that of Fatin Halim's phantom research that showed at a sphere-to-background ratio of 1:4 with a high activity concentration, the SUVmax increased with an increase in sphere diameter (24). Therefore, with a relatively small volume of benign lesions in this study, SUVmax may be underestimated because of the partial volume effect.

In patients with lung adenocarcinoma, high-uptake lesions may be detected on SPECT, without obvious abnormal changes on CT. The diagnosis of such lesions is extraordinarily difficult. In the present study, we attempted to determine the likely SUVmax cutoff value of CT-negative metastatic lesions in patients with lung adenocarcinoma. A previous study on bone metastases from breast cancer revealed that the sensitivity of bone scans for detecting different CT types of bone metastasis was 100% (21/21) for mixed lesions, 94% (15/16) for osteoblastic lesions, 90% (28/31) for osteolytic lesions, and 70% (14/20) for CT-negative lesions (25). SPECT/CT may improve the diagnostic sensitivity of CT-negative lesions. We chose normal vertebrae as the comparative sample of normal bone because normal vertebrae have relatively stable uptake, as shown in previous studies. A study by Mohd Farina (16) showed that the mean SUVmax of 234 normal vertebrae was 7.08 ± 1.97 in patients with prostate cancer. In another study, the mean SUVmax of 120 vertebrae in the no-treatment breast cancer group was 5.37 ± 2.81 (26). The mean SUVmax of 199 normal vertebrae was 6.19 ± 1.46 in our group of patients with lung adenocarcinoma. Moreover, in the present study, most of the CT-negative bone metastatic lesions were located in vertebrae (78.6%, 22/28). The mean SUVmax of CT-negative bone metastatic lesions was 16.51 ± 6.93, when using a cutoff value of 8.135, CT-negative bone metastatic lesions may be discriminated with a sensitivity of 100.00% and a specificity of 91.96%. With quantitative SPECT/CT, when focal high-uptake lesions with an SUVmax of >8.135 are detected, bone metastasis should be highly suspected and further examination with MRI or PET/CT is recommended.

Despite having a lower SUVmax than studies involving patients with prostate cancer, the SUVmax of bone metastases in this study (SUVmax 23.85 ± 14.34, 4.74–75.33) was nearly the same as that in a study by Zhang et al. (14), which included 30 patients with lung cancer and 21 patients with other cancers. In their study, the SUVmax of metastases was 24.77 ± 16.32 (3.90–92.61). When referring to the uptake of ^{99m}Tc-MDP in different kinds of CT features, Guray Gurkan's study, which included different cancer patients and used BS, showed that the mean ROImax (maximum lesion to normal bone count ratio on BS) of osteoblastic bone lesions (6.42 ± 4.22) and mixed metastases (6.32 ± 4.03) was higher than that of osteolytic lesions (5.33 ± 3.60), but there was no significant difference in the mean ROImax in osteolytic, osteoblastic, and mixed lesions ($P > 0.05$) (27). However, in this study using quantitative SPECT/CT, the SUVmax of osteoblastic (29.16 ± 16.63) and mixed (26.62 ± 14.97) lesions was significantly higher than that of osteolytic (15.79 ± 5.57) and CT-negative (16.51 ± 6.93) lesions ($P < 0.05$). A previous study revealed that osteoblastic lesions had significantly higher HUs than osteolytic and mixed lesions ($P < 0.01$) (27). In our study, we discovered that SUVmax had a weak positive linear correlation with HUs for all bone metastatic lesions. As a result, for osteoblastic and mixed lesions that had higher HUs, the SUVmax of osteoblastic

and mixed metastatic lesions was significantly higher than that of osteolytic and CT-negative lesions with lower HUs.

The present study had some limitations. It was conducted retrospectively, and the results may have been influenced by the criteria used to patient selection, for example, some of the patients in this study received the SPECT/CT acquisition delayed by some uncontrollable reasons. The acquisition time may influence the uptake of the normal vertebrae and bone metastatic lesions (21). We will set fixed acquisition time and explore the time influence for the SUVmax in bone metastatic lesions in our future prospective research. Furthermore, majority of the patients in this study lacked histological confirmation of bone metastases; however, all lesions were followed up for more than 0.5 year, and the initial imaging results were confirmed by re-examination of whole-body bone scans and SPECT/CT, CT, MR, or PET/CT scans. Cases that lacked follow-up data were excluded from the study. Some of the patients (47, 40.9%) in the present study had more than six metastatic lesions. There is a possibility that the diagnostic value of SUVmax might be more valuable for patients with less bone metastasis. However, this was a preliminary exploratory study of SUVmax uptake in bone metastases in patients with lung adenocarcinoma. The SUVmax changes of bone metastatic lesions after treatment may have more guidance value for clinical practice of lung adenocarcinoma patients; this is what we will study in the future. Because of the relatively small number of patients in this study, we did not perform a sub analysis on gender-related cutoff values for distinguishing CT-negative bone metastases from normal vertebrae. We will explore the influence of gender with more cases in a future study.

5. Conclusion

SUVmax of quantitative SPECT/CT is a useful index for distinguishing benign bone lesions from bone metastases in patients with lung adenocarcinoma, particularly in the diagnosis of CT-negative bone metastases. However, other factors, such as HUs and volume, which may affect the SUVmax, should still be considered.

Data availability statement

The raw data supporting the conclusions of this article will be made available by the authors, without undue reservation.

Ethics statement

Written informed consent was obtained from the individual(s) for the publication of any potentially identifiable images or data included in this article.

Author contributions

LL, XW, and RZ contributed to the conception and design of the study. LL, RF, YZ, KY, and JG organized the database. ML and JG carried out data statistics and analysis. LL wrote the manuscript. RZ, JG, XW, and ML revised the manuscript. All authors have read and approved the final manuscript.

Funding

This study was supported by Beijing Hope Run Special Fund of Cancer Foundation of China (Subject No. LC2019A16).

Conflict of interest

The authors declare that the research was conducted in the absence of any commercial or financial relationships that could be construed as a potential conflict of interest.

Publisher's note

All claims expressed in this article are solely those of the authors and do not necessarily represent those of their affiliated organizations, or those of the publisher, the editors and the reviewers. Any product that may be evaluated in this article, or claim that may be made by its manufacturer, is not guaranteed or endorsed by the publisher.

Supplementary material

The Supplementary Material for this article can be found online at: https://www.frontiersin.org/articles/10.3389/fmed.2023.1119214/full#supplementary-material

References

1. Sung H, Ferlay J, Siegel RL, Laversanne M, Soerjomataram I, Jemal A, et al. Global cancer statistics 2020: globocan estimates of incidence and mortality worldwide for 36 cancers in 185 countries. *CA Cancer J Clin.* (2021) 71:209–49. doi: 10.3322/caac.21660

2. Cao W, Chen HD Yu YW, Li N, Chen WQ. Changing profiles of cancer burden worldwide and in China: a secondary analysis of the global cancer statistics 2020. *Chin Med J.* (2021) 134:783–91. doi: 10.1097/CM9.0000000000001474

3. Succony L, Rassl DM, Barker AP, McCaughan FM, Rintoul RC. Adenocarcinoma spectrum lesions of the lung: detection, pathology and treatment strategies. *Cancer Treat Rev.* (2021) 99:102237. doi: 10.1016/j.ctrv.2021.102237

4. Kuchuk M, Kuchuk I, Sabri E, Hutton B, Clemons M, Wheatley-Price P. The incidence and clinical impact of bone metastases in non-small cell lung cancer. *Lung Cancer.* (2015) 89:197–202. doi: 10.1016/j.lungcan.2015.04.007

5. Montilla-Soler JL, Makanji R. Skeletal scintigraphy. *Cancer Control.* (2017) 24:137–46. doi: 10.1177/107327481702400206

6. Chang CY, Gill CM, Joseph Simeone F, Taneja AK, Huang AJ, Torriani M, et al. Comparison of the diagnostic accuracy of ^{99m}-Tc-MDP bone scintigraphy and ^{18} F-FDG PET/CT for the detection of skeletal metastases. *Acta Radiol.* (2016) 57:58–65. doi: 10.1177/0284185114564438

7. Liu NB, Zhu L, Li MH, Sun XR, Hu M, Huo ZW, et al. Diagnostic value of 18F-FDG PET/CT in comparison to bone scintigraphy, CT and 18f-Fdg pet for the detection of bone metastasis. *Asian Pac J Cancer Prev.* (2013) 14:3647–52. doi: 10.7314/APJCP.2013.14.6.3647

8. McLoughlin LC, O'Kelly F, O'Brien C, Sheikh M, Feeney J, Torreggiani W, et al. The improved accuracy of planar bone scintigraphy by adding single photon emission computed tomography (SPECT-CT) to detect skeletal metastases from prostate cancer. *Ir J Med Sci.* (2016) 185:101–5. doi: 10.1007/s11845-014-1228-7

9. Zhang Y, Li B, Wu B, Yu H, Song J, Xiu Y, et al. Diagnostic performance of whole-body bone scintigraphy in combination with SPECT/CT for detection of bone metastases. *Ann Nucl Med.* (2020) 34:549–58. doi: 10.1007/s12149-020-01488-1

10. Lofgren J, Mortensen J, Rasmussen SH, Madsen C, Loft A, Hansen AE, et al. A prospective study comparing ^{99m}Tc-hydroxyethylene-diphosphonate planar bone scintigraphy and whole-body SPECT/CT with ^{18}F-fluoride PET/CT and ^{18}F-fluoride PET/MRI for diagnosing bone metastases. *J Nucl Med.* (2017) 58:1778–85. doi: 10.2967/jnumed.116.189183

11. Beck M, Sanders JC, Ritt P, Reinfelder J, Kuwert T. Longitudinal analysis of bone metabolism using SPECT/CT and ^{99m}Tc-diphosphono-propanedicarboxylic acid: comparison of visual and quantitative analysis. *EJNMMI Res.* (2016) 6:60. doi: 10.1186/s13550-016-0217-4

12. Bailey DL, Willowson KP. Quantitative SPECT/CT: spect joins pet as a quantitative imaging modality. *Eur J Nucl Med Mol Imaging.* (2014) 41(Suppl 1):S17–25. doi: 10.1007/s00259-013-2542-4

13. Ritt P, Vija H, Hornegger J, Kuwert T. Absolute quantification in spect. *Eur J Nucl Med Mol Imaging.* (2011) 38(Suppl 1):S69–77. doi: 10.1007/s00259-011-1770-8

14. Zhang Y, Li B, Yu H, Song J, Zhou Y, Shi H. The value of skeletal standardized uptake values obtained by quantitative single-photon emission computed tomography-computed tomography in differential diagnosis of bone metastases. *Nucl Med Commun.* (2021) 42:63–7. doi: 10.1097/MNM.0000000000001311

15. Kitajima K, Tsuchitani T, Takahashi Y, Minami T, Yokoi T, Nakamura A, et al. Usefulness of quantitative bone single-photon emission computed tomography/computed tomography for evaluating the treatment response of bone metastasis in a lung cancer patient. *Case Rep Oncol.* (2021) 14:391–6. doi: 10.1159/000513907

16. Mohd Rohani MF, Mat Nawi N, Shamim SE, Wan Sohaimi WF, Wan Zainon WMN, Musarudin M, et al. Maximum standardized uptake value from quantitative bone single-photon emission computed tomography/computed tomography in differentiating metastatic and degenerative joint disease of the spine in prostate cancer patients. *Ann Nucl Med.* (2019) 34:39–48. doi: 10.1007/s12149-019-01410-4

17. Kuji I, Yamane T, Seto A, Yasumizu Y, Shirotake S, Oyama M. Skeletal standardized uptake values obtained by quantitative SPECT/CT as an osteoblastic biomarker for the discrimination of active bone metastasis in prostate cancer. *Eur J Hybrid Imaging.* (2017) 1:2. doi: 10.1186/s41824-017-0006-y

18. Arvola S, Jambor I, Kuisma A, Kemppainen J, Kajander S, Seppänen M, et al. Comparison of standardized uptake values between ^{99m}Tc-HDP SPECT/CT and ^{18}F-NAF PET/CT in bone metastases of breast and prostate cancer. *EJNMMI Res.* (2019) 9:6. doi: 10.1186/s13550-019-0475-z

19. Tabotta F, Jreige M, Schaefer N, Becce F, Prior JO, Nicod Lalonde M. Quantitative bone SPECT/CT: high specificity for identification of prostate cancer bone metastases. *BMC Musculoskelet Disord.* (2019) 20:619. doi: 10.1186/s12891-019-3001-6

20. Dadgar H, Norouzbeigi N, Jokar N, Zareizadeh J, Gholamrezanezhad A, Ahmadzadehfar H, et al. Comparison of ^{18}F-NAF imaging, ^{99m}Tc-MDP scintigraphy, and ^{18}F-FDG for detecting bone metastases. *World J Nucl Med.* (2022) 21:001–8. doi: 10.1055/s-0042-1748154

21. Nautiyal A, Jha AK, Mithun S, Sawant V, Jadhav R, Khairnar K, et al. Normal skeletal standardized uptake values obtained from quantitative single-photon emission computed tomography/computed tomography: time-dependent study on breast cancer patients. *Indian J Nucl Med.* (2021) 36:398–411. doi: 10.4103/ijnm.ijnm_47_21

22. He F, Matsumoto Y. Basic and clinical associations between bone and cancer. *Immunol Med.* (2020) 43:103–6. doi: 10.1080/25785826.2020.1754084

23. Hayes AJ, Reynolds S, Nowell MA, Meakin LB, Habicher J, Ledin J, et al. Spinal deformity in aged zebrafish is accompanied by degenerative changes to their vertebrae that resemble osteoarthritis. *PLoS ONE.* (2013) 8:e75787. doi: 10.1371/journal.pone.0075787

24. Halim F, Yahya H, Jaafar KN, Mansor S. Accuracy assessment of SUV measurements in SPECT/CT: a phantom study. *J Nucl Med Technol.* (2021) 49:250–5. doi: 10.2967/jnmt.120.259168

25. Sugihara T, Koizumi M, Koyama M, Terauchi T, Gomi N, Ito Y, et al. Bone metastases from breast cancer: associations between morphologic CT patterns and glycolytic activity on pet and bone scintigraphy as well as explorative search for influential factors. *Ann Nucl Med.* (2017) 31:719–25. doi: 10.1007/s12149-017-1202-3

26. Rohani MFM, Yonan SNM, Tagiling N, Zainon W, Udin Y, Nawi NM. Standardized uptake value from semiquantitative bone single-photon emission computed tomography/computed tomography in normal thoracic and lumbar vertebrae of breast cancer patients. *Asian Spine J.* (2020) 14:629–38. doi: 10.31616/asj.2019.0308

27. Gurkan G, Sarikaya I, Sarikaya A. Semiquantitative assessment of osteoblastic, osteolytic, and mixed lytic-sclerotic bone lesions on fluorodeoxyglucose positron emission tomography/computed tomography and bone scintigraphy. *World J Nucl Med.* (2019) 18:132–6. doi: 10.4103/wjnm.wjnm_31_18

frontiers | Frontiers in Medicine

TYPE Original Research
PUBLISHED 03 February 2023
DOI 10.3389/fmed.2023.1083413

OPEN ACCESS

EDITED BY
Giorgio Treglia,
Ente Ospedaliero Cantonale (EOC), Switzerland

REVIEWED BY
Federico Caobelli,
Bern University Hospital, Switzerland
Sangwon Han,
University of Ulsan, Republic of Korea

*CORRESPONDENCE
Greta S. P. Mok
✉ gretamok@um.edu.mo
Tung-Hsin Wu
✉ tunghsinwu@nycu.edu.tw

†These authors have contributed equally to this work

SPECIALTY SECTION
This article was submitted to Nuclear Medicine, a section of the journal Frontiers in Medicine

RECEIVED 29 October 2022
ACCEPTED 16 January 2023
PUBLISHED 03 February 2023

CITATION
Sun J, Yang B-H, Li C-Y, Du Y, Liu Y-H, Wu T-H and Mok GSP (2023) Fast myocardial perfusion SPECT denoising using an attention-guided generative adversarial network. *Front. Med.* 10:1083413. doi: 10.3389/fmed.2023.1083413

Fast myocardial perfusion SPECT denoising using an attention-guided generative adversarial network

Jingzhang Sun[1†], Bang-Hung Yang[2,3†], Chien-Ying Li[2,3], Yu Du[1], Yi-Hwa Liu[4], Tung-Hsin Wu[2*] and Greta S. P. Mok[1,5,6*]

[1]Biomedical Imaging Laboratory (BIG), Department of Electrical and Computer Engineering, Faculty of Science and Technology, University of Macau, Taipa, Macao SAR, China, [2]Department of Biomedical Imaging and Radiological Sciences, National Yang Ming Chiao Tung University, Hsinchu, Taiwan, [3]Department of Nuclear Medicine, Taipei Veterans General Hospital, Taipei City, Taiwan, [4]Department of Internal Medicine, Yale University School of Medicine, New Haven, CT, United States, [5]Center for Cognitive and Brain Sciences, Institute of Collaborative Innovation, University of Macau, Taipa, Macao SAR, China, [6]Ministry of Education Frontiers Science Center for Precision Oncology, Faculty of Health Science, University of Macau, Taipa, Macao SAR, China

Purpose: Deep learning-based denoising is promising for myocardial perfusion (MP) SPECT. However, conventional convolutional neural network (CNN)-based methods use fixed-sized convolutional kernels to convolute one region within the receptive field at a time, which would be ineffective for learning the feature dependencies across large regions. The attention mechanism (Att) is able to learn the relationships between the local receptive field and other voxels in the image. In this study, we propose a 3D attention-guided generative adversarial network (AttGAN) for denoising fast MP-SPECT images.

Methods: Fifty patients who underwent 1184 MBq ^{99m}Tc-sestamibi stress SPECT/CT scan were retrospectively recruited. Sixty projections were acquired over 180° and the acquisition time was 10 s/view for the full time (FT) mode. Fast MP-SPECT projection images (1 s to 7 s) were generated from the FT list mode data. We further incorporated binary patient defect information (0 = without defect, 1 = with defect) into AttGAN (AttGAN-def). AttGAN, AttGAN-def, cGAN, and Unet were implemented using Tensorflow with the Adam optimizer running up to 400 epochs. FT and fast MP-SPECT projection pairs of 35 patients were used for training the networks for each acquisition time, while 5 and 10 patients were applied for validation and testing. Five-fold cross-validation was performed and data for all 50 patients were tested. Voxel-based error indices, joint histogram, linear regression, and perfusion defect size (PDS) were analyzed.

Results: All quantitative indices of AttGAN-based networks are superior to cGAN and Unet on all acquisition time images. AttGAN-def further improves AttGAN performance. The mean absolute error of PDS by AttcGAN-def was 1.60 on acquisition time of 1 s/prj, as compared to 2.36, 2.76, and 3.02 by AttGAN, cGAN, and Unet.

Conclusion: Denoising based on AttGAN is superior to conventional CNN-based networks for MP-SPECT.

KEYWORDS

denoising, attention-guided, deep learning, myocardial perfusion, fast SPECT

1. Introduction

Myocardial perfusion single photon emission computed tomography (MP-SPECT) is a standard method for the quantitative diagnosis of coronary artery disease (CAD) (1). However, the acquisition time for the conventional NaI-based MP-SPECT is relatively long (15-20 min) (2), leading to potential motion artifacts, e.g., upward creep (3), patient's discomfort, lower patient throughput (4), and mismatch artifacts between the sequential MP-SPECT and CT (5, 6). New scanner geometries with parallel-hole (7) or multi-pinhole collimations (8, 9) for MP-SPECT are proposed for better photons detection efficiency and reduced scan time (2-8 min) (10, 11). Advanced reconstruction algorithms (12) also facilitate the possibility of reducing acquisition time without degrading image quality. However, the acquisition time for MP-SPECT is still much longer than CT in general (4). Therefore, it is necessary to pursue fast MP-SPECT, without compromising the image quality and diagnostic accuracy.

Image noise is a substantial problem for fast MP-SPECT due to the limited detected counts and the fact that it degrades the image quality, hampering clinical diagnosis and quantification results (9). Recently, deep learning (DL) methods are promising to reduce the noise for MP-SPECT images. Ramon et al. (13) proposed 3D convolutional neural networks (CNN) to denoise the reconstructed MP-SPECT images with reduced injected dose. Liu et al. used a 3D Unet trained on a noise-to-noise strategy for denoising full dose MP-SPECT reconstructed images and showed improved results as compared to the use of traditional filter (14). They further evaluated the performance of DL-based denoising according to the area under the curve (AUC) of the total perfusion deficit (TPD) scores results (15). Aghakhan et al. (16) used a 2D conditional generative adversarial network (cGAN) for denoising the reduced dose MP-SPECT images from 1/8 to 1/2 dose levels in the projection domain. Shiri et al. (17) proposed a 2D residual CNN (ResNet) to estimate full time (FT) MP-SPECT projection images. Previously, our group implemented a 3D cGAN to denoise fast and low dose MP-SPECT reconstruction (18) and projection (19) images. Our results showed that denoising on the projection domain is superior to the reconstruction domain (19).

However, conventional CNN-based methods use fixed-sized convolutional kernels to convolute one local region within the receptive field at a time, which would be ineffective for learning the feature dependencies across large regions (20). The feature dependencies across large regions can only be learned when the feature maps are down-sampled into a relatively small matrix size after passing through several convolutional layers (21). The attention mechanism has shown to be effective in capturing the long-range dependencies of structural information across large regions (20). It has been implemented for CT segmentation (22) and low dose CT denoising (23). In this study, we propose an attention-based cGAN (AttGAN) in denoising fast MP-SPECT projection images and compare its performance with Unet-based and cGAN-based denoising. We further incorporate the patient defect information into the network to improve the AttGAN performance.

2. Materials and methods

2.1. Patient dataset

Fifty anonymized patients who underwent routine stress SPECT/CT scan ~30 minutes post ^{99m}Tc-sestamibi injection on a clinical SPECT/CT system (NM/CT 870 CZT, GE Healthcare, USA) were retrospectively enrolled in this study under local ethics approval (IRB number 2022-11-002CC, **Table 1**). Among them, 18 were read as having at least a cardiac defect, which had perfusion abnormalities, according to their medical records from SPECT images and clinical histories. Before the SPECT acquisition, a helical CT scan (120 kVp, smart mA (10-150 mA), 0.375 cm slice thickness) was acquired in the heart region for attenuation correction in SPECT reconstruction. The CT reconstruction matrix size was 512 × 512 × variable axial coverage, with a voxel size of 0.9765 mm. Patients were injected with 1,184 MBq ^{99m}Tc-sestamibi, and 60 projections were acquired through 180° from the right anterior oblique to the left posterior oblique positions with a matrix size of 64 × 64. The primary photopeak energy window was centered at 140.5 keV with a 20% width and the scatter window was centered at 120 keV with a 10% width.

The original acquisition time was 10 s/view. We also obtained various fast MP-SPECT projection images by reducing the projection acquisition time to be 7, 5, 3, 2, and 1 s based on the list mode data of the FT images, respectively. All clinical data were reconstructed by the 3D ordered subset expectation maximization (OS-EM) algorithm with 5 iterations and 4 subsets, with CT-based attenuation and dual energy window scatter corrections. The reconstruction matrix size was 64 × 64 × 19 with a voxel size of 0.6096 cm. A 3D post-reconstruction Gaussian filter with a standard deviation of 0.6 voxel was applied on the FT images for data analysis.

TABLE 1 Demographic information for the patient study.

	Female	Male	Total
Gender	13 (26%)	37 (74%)	50 (100%)
Age (years)	69.2 ± 9.73 (56-90)	64.9 ± 11.24 (42-83)	66.0 ± 10.94 (42-90)
BMI (kg/m^2)	24.5 ± 3.13 (21.09-30.47)	25.0 ± 2.65 (17.91-30.11)	25.0 ± 2.92 (17.92-31.60)
Perfusion defect size (PDS, %)	3.23 ± 2.20 (0-7)	4.46 ± 5.57 (0-29)	4.14 ± 4.92 (0-29)
Cardiac defect	2 (4%)	16 (32%)	18 (36%)
CAD risk factors			
Hypertension	6 (12%)	20 (40%)	26 (52%)
Dyslipidaemia	8 (16%)	21 (42%)	29 (58%)
Diabetes	2 (4%)	14 (28%)	16 (32%)
Smoker	0 (0%)	8 (16%)	8 (16%)
Family history of CAD	4 (8%)	9 (18%)	13 (26%)

Mean ± SD and range are presented for age, BMI, and PDS.

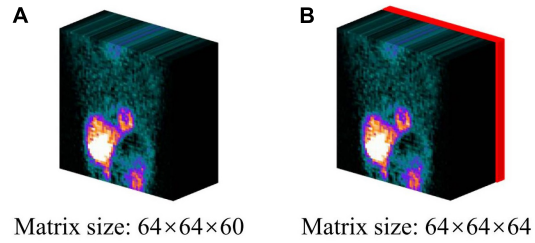

FIGURE 2
The projection datasets used in this study: **(A)** original projection, **(B)** projection incorporating the patient defect information. The defect information block (red) was encoded by binary values (0 = without defect/1 = with defect).

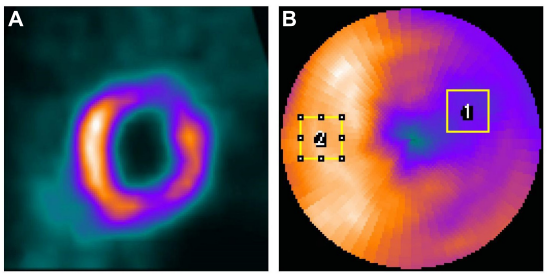

FIGURE 3
(A) The 3D VOI used for voxel-based error calculation. **(B)** Sample ROIs drawn from a polar plot for IR calculation on a selected patient. (ROI_1 was for defect while ROI_2 was for a uniform normal region).

2.2. Attention-guided generative adversarial network (AttGAN)

The architecture of the AttGAN used in this study is shown in Figure 1 (20). Similar to cGAN, AttGAN is comprised of two subnetworks: a generator (Figure 1A) and a discriminator (Figure 1B). The generator, which was conditioned with fast MP-SPECT projection images, transformed the fast MP-SPECT images into estimated FT MP-SPECT projection images. The estimated images were later paired with the original fast MP-SPECT projection images as an estimated sample pair. The fast MP-SPECT projection images were also paired with the corresponding FT MP-SPECT projection images as a real sample pair. The discriminator learned to differentiate between the estimated sample pairs and the real sample pairs.

The Unet-based generator (24) had subunits of encoding, bottleneck, and decoding layers. Each encoding layer was comprised of convolution (3 × 3 × 3), batch normalization (BN) (25), rectified linear unit (ReLU) activation, and dropout with a rate of 50%, followed by max-pooling to down-sample feature maps between layers. The decoding layers mirrored the encoding layers, except the up-sample layers replaced the down-sample layers, and skip connection between the encoding and decoding layers was added. The discriminator was a CNN-based network used in our previous study (19).

The attention modules, which were used for calculating the relationships of each voxel to all other pixels within a feature map, were incorporated together with the skip-connection between the encoding layers and decoding layers in the generator (Figure 1C) (20). The feature maps x from the previous encoding layer g and current decoding layer f were transformed by a convolution (1 × 1 × 1) respectively, where $g(x) = W_g x$ and $f(x) = W_f x$.

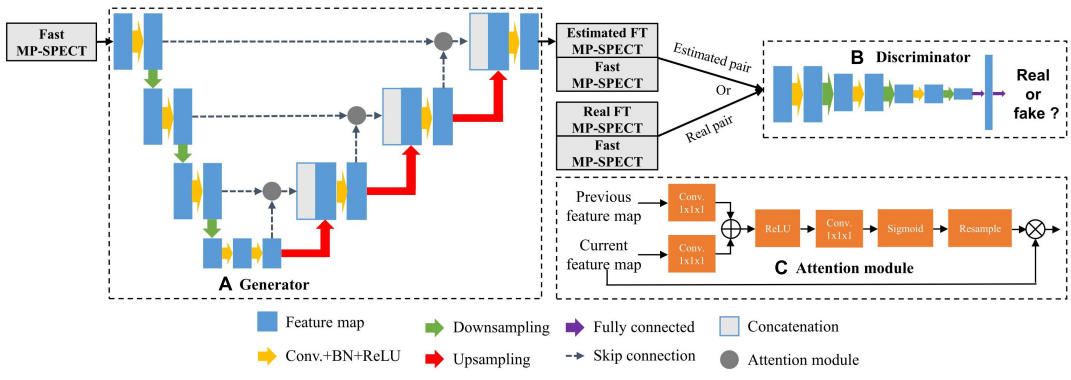

FIGURE 1
The AttGAN architecture used in this study. **(A)** Generator; **(B)** discriminator; **(C)** attention module.

W_g and W_f were trainable parameters. The feature maps of decoding layer $f(x)$ were then down-sampled to be consistent with the size of $g(x)$. We performed an inner product of the two vectors $g(x)$ and $f(x)$ to obtain the feature dependencies between every two voxels:

$$\alpha_{i,j} = f(x_i)^T \cdot g(x_j)$$

The $\alpha_{i,j}$ further went through ReLU activation, convolution ($1 \times 1 \times 1$), and softmax function to normalize and reshape the feature maps to become $r_{i,j}$. Finally, we multiplied $r_{i,j}$ with the feature maps x from the previous encoding layer g to obtain the attention coefficients *Att*:

$$Att = \sum_{i=1}^{N} x_i \cdot r_{i,j}$$

The L_1 loss (26) and the adversarial loss L_{ADV} were used for training the generator g. The discriminator was trained by a cross-entropy loss L_D (19). The final objective function of AttGAN was:

$$L_{AttGAN} = \text{argmin}_G \text{max}_D (L_{ADV}(G, D) + \lambda L_1(G))$$

where λ is set to be 100 to adjust the weight of $V_{L_1}(G)$ (26). The AttGAN was trained by minimizing the loss. The Unet and cGAN structures were the same according to our previous studies (18, 19).

2.3. Data preprocessing

All the intensity values of MP-SPECT projection images were normalized to a range of 0–1 for training. In addition, we further incorporated the binary patient defect information, i.e., with (1) or without defect (0) from patients' own medical records, by embedding four 64 × 64 slices with the same binary values into the projection images (Figure 2).

2.4. Network implementation

The AttGAN incorporating patient defect information (AttGAN-def), AttGAN, cGAN, and Unet were implemented using Tensorflow which ran on a NVIDIA GeForce RTX 2080Ti GPU. The Adam optimizer was applied to optimize this proposed model based on an initial learning rate of 0.0001 and trained to 400 epochs.

We performed a 5-fold cross-validation on the clinical datasets to evaluate four DL approaches for various fast SPECT acquisitions. Specifically, for each fold of evaluation, FT and fast SPECT projection images of 35, 5, and 10 patients were selected for training, validation, and testing, respectively. This process was repeated 5 times and all

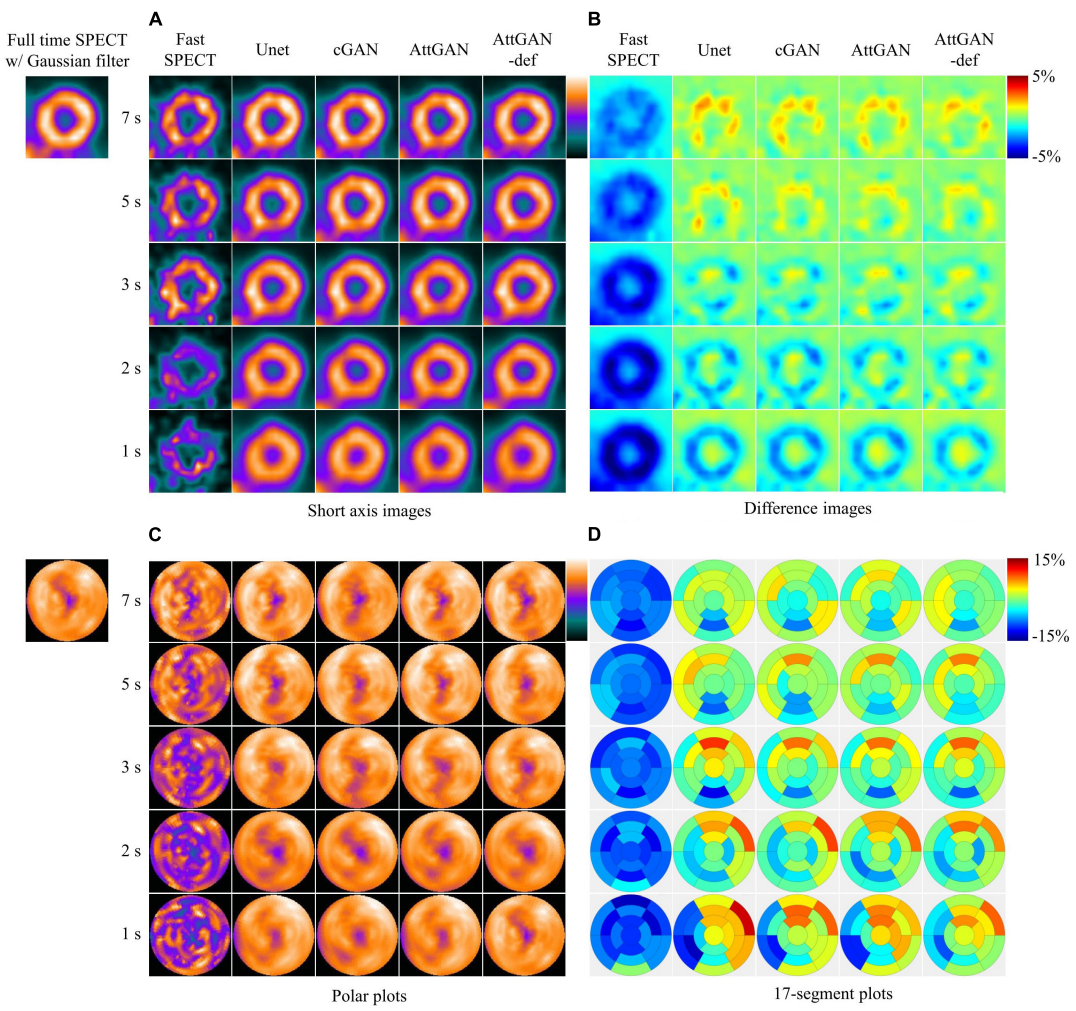

FIGURE 4
Sample images of a normal male patient (age = 67, BMI = 25.4) before and after DL-based denoising for five shorter acquisition times. The images are shown in **(A)** short axis images, **(B)** difference images as compared to FT SPECT, **(C)** polar plots, and **(D)** 17-segment plots.

fifty patient datasets were tested and averaged for the final results. The denoised projections were further reconstructed using the same OS-EM algorithm with 5 iterations and 4 subsets with attenuation and scatter correction. No post-reconstruction filter was applied on the reconstructed images generated from the denoised projections for further analysis.

The hyper-parameters, e.g., number of layers and filters within each layer, were determined based on a training-validation procedure for AttGAN. Specifically, the number of layers varied as 2, 3, 4 and 5, while the number of filters within each layer varied as 8, 16, 24, 32 and 40. The hyper-parameters for cGAN and Unet were determined in our previous study (18, 19). The training time for AttGAN-def, AttGAN, cGAN, and Unet was 2.2, 2.2, 2.0, and 1.9 hr, respectively.

2.5. Data analysis

The voxel-based error of the denoised images was assessed by the normalized mean square error (NMSE), structural similarity index (SSIM), peak signal-to-noise ratio (PSNR), joint histogram, and linear regression measured on a 3D volume-of-interest (VOI, 18 × 18 × 18, Figure 3A) which covered the whole heart. The filtered FT reconstructed MP-SPECT images were used as the reference.

$$\mathrm{NMSE} = \frac{\sum_{k=1}^{N}(I_D - I_{FT})^2}{\sum_{k=1}^{N} I_{FT}{}^2}$$

$$\mathrm{SSIM} = \frac{(2\mu_D\mu_{FT}+C_1)(2\sigma_{D,FT}+C_2)}{(\mu_D^2+\mu_{FT}^2+C_1)(\sigma_D^2+\sigma_{FT}^2+C_2)}$$

$$\mathrm{PSNR} = 10 \cdot \log_{10}\left(\frac{\mathrm{MAX}_{FT}}{\sqrt{\mathrm{MSE}}}\right)$$

where I_D represents the voxel values in denoised reconstructed images, I_{FT} is the voxel values on the filtered FT reconstructed images, N (5832) is the number of voxels in the VOI, μ_D and μ_{FT} are the mean values of the denoised and reference images, σ_D and σ_{FT} are the standard deviations of the denoised and reference images respectively, and $\sigma_{D,FT}$ is the cross-covariance between the

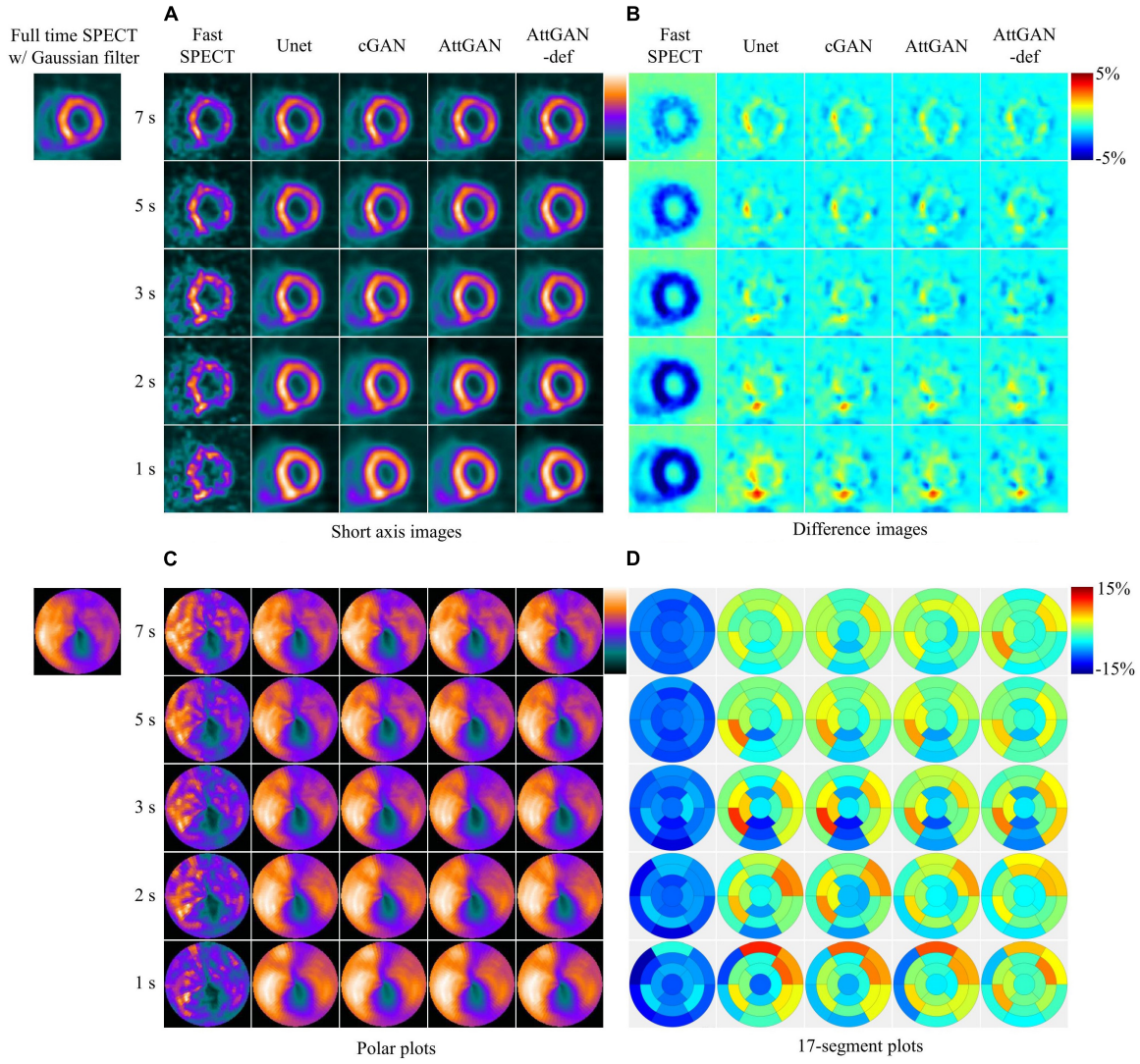

FIGURE 5
Sample images of another male patient (age = 77, BMI = 24.2) with an abnormal perfusion in the LAD and LCX territory before and after DL-based denoising for five shorter acquisition times. The images are shown in **(A)** short axis images, **(B)** difference images, **(C)** polar plots, and **(D)** 17-segment plots.

two images. The constants C_1 and C_2 are set to be 0.01 and 0.02, respectively (17). MAX_{FT} indicates the maximum possible pixel value of the reference images while *MSE* indicates the mean squared error between the denoised and reference images.

Two regions-of-interest (ROI_1 and ROI_2) were drawn on the defect region and a uniform normal region on the polar plots based on visual assessment (Figure 3B) and were adjusted for each patient, respectively. The same ROIs were applied for all denoised images for the same patient. The intensity ratio (IR) was calculated from the mean value of the defect ROI (ROI_1) divided by the mean value of the uniform ROI (ROI_2). The absolute error of IR between FT images and different denoised images was computed.

A clinical relevant index, the perfusion defect size (PDS, %LV), i.e., an index similar to the total perfusion deficit, was measured by the Wackers-Liu CQ^{TM} (WLCQ) software (Voxelon Inc, Watertown, CT) (27). The absolute error of PDS between FT and different denoised images was computed. The Bland–Altman plots were also computed to quantify the agreement of PDS. For the statistical analysis, a two-tailed paired t-test with Bonferroni correction (SPSS, IBM Corporation, Armonk, NY, USA) was performed between AttGAN-def and other denoising methods at different acquisition time/view for NMSE, PSNR, SSIM, PDS, and IR. A p-value of less than 0.05 was considered as statistically significant.

3. Results

3.1. Reconstructed images, polar plots, and 17-segment analysis

Figure 4 shows the short axis fast MP-SPECT images, their corresponding difference images as compared with filtered FT SPECT

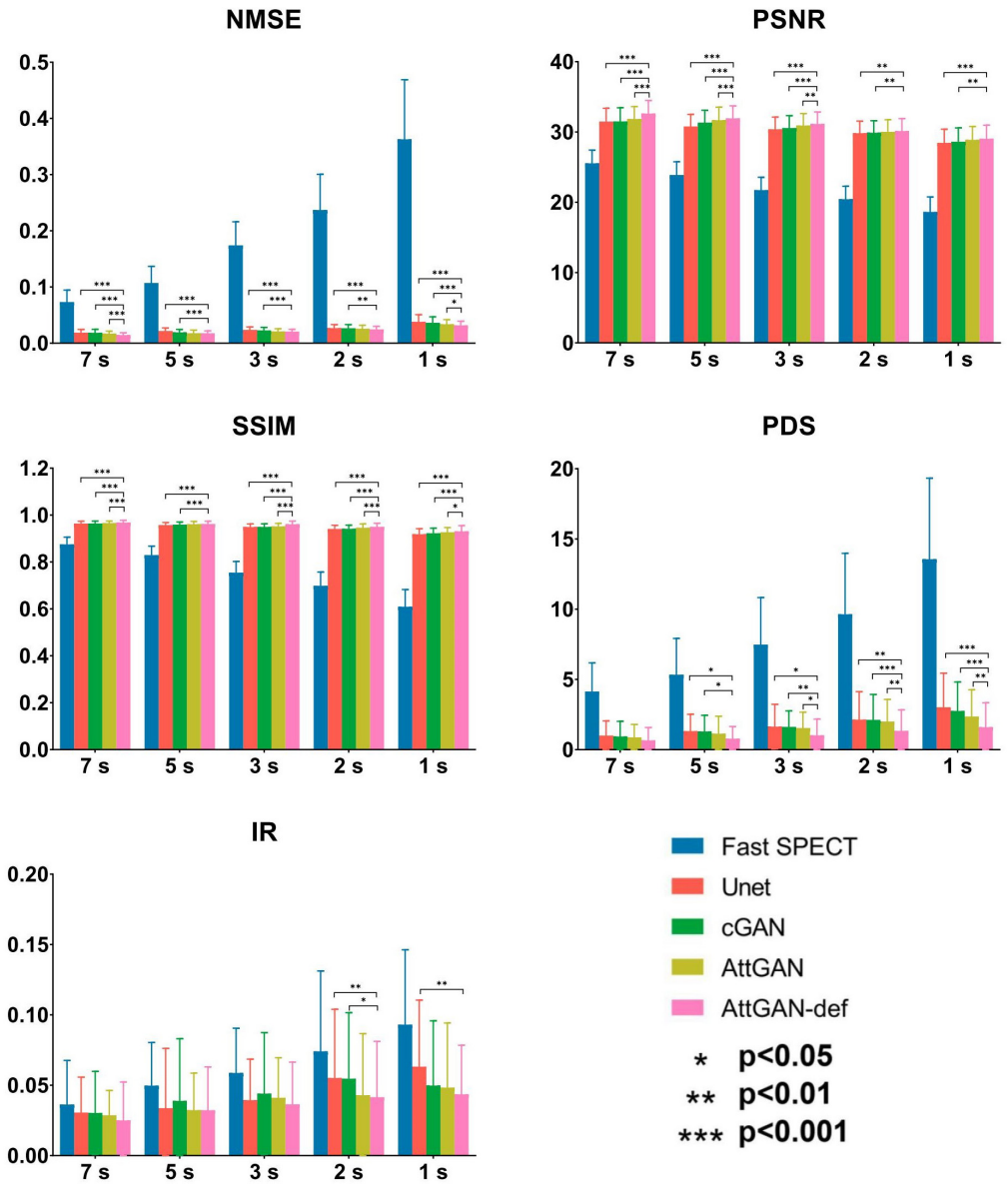

FIGURE 6
Quantitative comparison of NMSE, PSNR, SSIM, PDS, and IR on 50 testing datasets for fast SPECT and different denoised images for five shorter acquisition times. Error bars indicate the standard deviation. The filtered FT SPECT images were used as reference. *p<0.05, **p<0.01, ***p<0.001.

images, polar plots as well as 17-segment plots processed using different DL denoising methods for a normal male patient. Figure 5 shows the same results for a male patient with a defect in the left anterior descending (LAD) and left circumflex artery (LCX) region. It can be observed that all the DL-denoised fast SPECT images are similar to the filtered FT SPECT images based on a visual assessment, with the noise level notably suppressed. Furthermore, it is noted that the proposed AttGAN methods have less bias than Unet and cGAN methods according to their corresponding images. Less bias is also observed from the 17-segment images for the AttGAN and AttGAN-def methods. The denoised images consistently exhibit worse resolution, i.e., more blurring, in shorter acquisition times.

3.2. Quantitative analysis

3.2.1. Physical and clinical indices

Figure 6 summarizes the average quantitative indices on all 50 testing datasets for original fast SPECT and DL-based denoised images. For all indices, DL-based denoising methods improve the image quality as compared to the original fast SPECT images. AttGAN-def obtains the best performance, followed by the AttGAN, cGAN, and Unet. At 1 s/prj fast SPECT images, the NMSE values are 0.0317 ± 0.007, 0.0337 ± 0.008, 0.0363 ± 0.011 and 0.0380 ± 0.013 for AttGAN-def, AttGAN, cGAN, and Unet, respectively, where AttGAN-def has significant difference with the other three DL methods. Similar results are obtained for the PSNR and SSIM values. The absolute errors of IR are 0.0435 ± 0.035, 0.0483 ± 0.046, 0.0498 ± 0.046 and 0.0632 ± 0.047 for AttGAN-def, AttGAN, cGAN and Unet on 1 s/prj fast SPECT images. For the absolute error of PDS, the AttGAN-def yields the lowest difference value among all denoising methods on all noise levels. The denoised images achieve better PDS performance, i.e., 1.60 ± 1.738, 2.36 ± 1.903, 2.76 ± 2.056 and 3.02 ± 2.428 for AttGAN-def, AttGAN, cGAN, and Unet on 1 s/prj fast SPECT images, as compared to the original fast SPECT images. The AttGAN-def has significant difference with the cGAN and Unet while not significant difference with AttGAN on 1 s/prj fast SPECT images. GAN methods outperform Unet in general.

3.2.2. Bland–Altman plots

The Bland–Altman plots of PDS for different denoised methods and fast SPECT images are shown in Figure 7. The dashed lines denote the 95% confidence interval (CI) of the PDS. For 1 s/prj fast SPECT, the AttGAN-def method shows the smallest variance (95% CI: −4.835, +4.435) compared to the reference filtered FT SPECT images, followed by the AttGAN (95% CI: −6.383, +5.423), cGAN (95% CI: −7.402, +5.802), and Unet (95% CI: −8.535, +5.615) methods.

3.2.3. Joint histogram and linear regression analysis

The voxel-based joint histogram and linear regression analysis results are shown in Figure 8. Similar to other quantitative analysis, AttGAN-def obtains the best performance ($R^2 = 0.8633$), followed by the AttGAN ($R^2 = 0.8433$), cGAN ($R^2 = 0.8341$), and Unet ($R^2 = 0.8123$) on 1 s/prj fast SPECT denoised images.

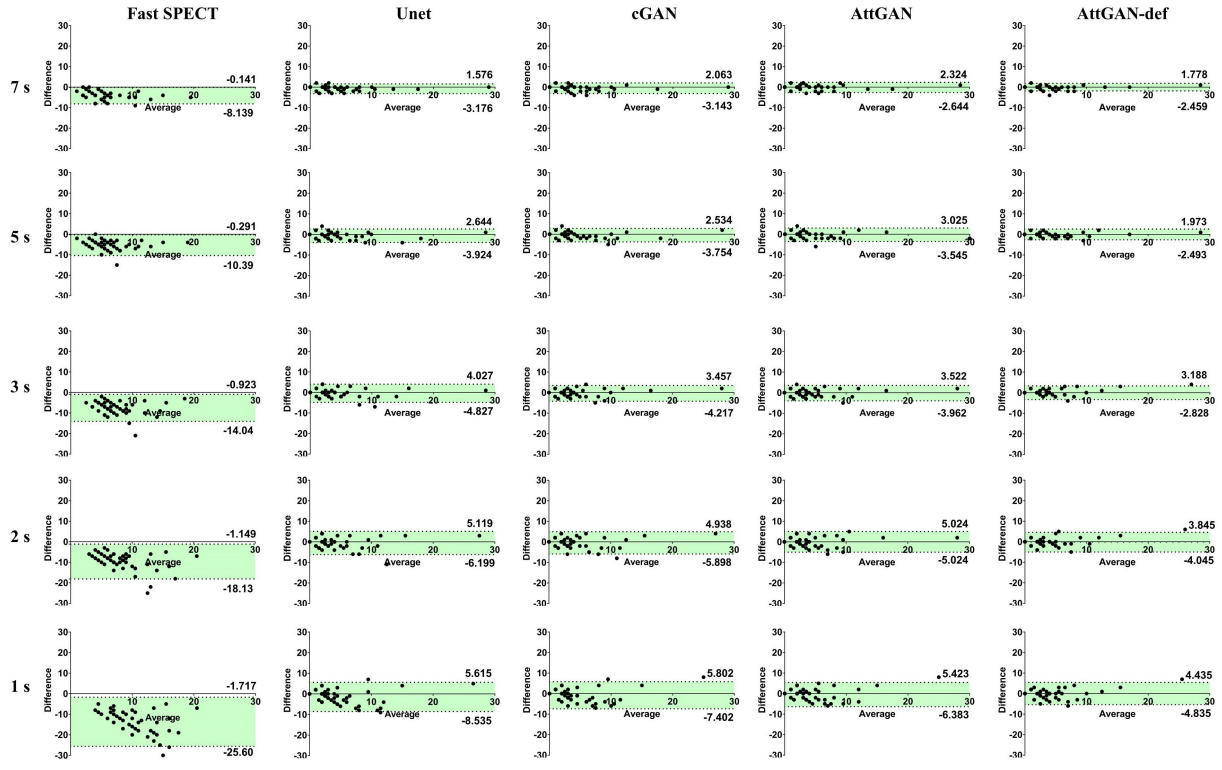

FIGURE 7
The Bland-Altman plots of PDS for fast SPECT different denoised images and acquisition times. The filtered FT SPECT images are used as reference.

4. Discussion

This study aims to assess the potential of attention-based DL network on fast MP-SPECT using clinical datasets. The attention module, inspired by non-local means, was proposed to enable the remote voxels to contribute to the local receptive filter during convolutional filtering (28). To the best of our knowledge, we are the first group to propose using an attention-based DL network for denoising the MP-SPECT images. For the quantitative performance comparison, we used filtered FT MP-SPECT images as the reference since there was no ground truth. Results consistently showed that the AttGAN denoised images had better quantitative accuracy from the difference images, polar plots, 17-segment plots, various physical indices, joint correlation histogram, linear regression and the clinical PDS analysis, as compared to conventional cGAN and Unet (**Figures 4-8**).

Our proposed networks were trained and tested for each dose-specific dataset, respectively, which were acquired on a CZT scanner. The denoising process is similar to an image-to-image translation task, and should be applicable to data acquired from other scanners or other denoised tasks, e.g., low dose SPECT imaging. The difference between low dose and fast SPECT is that the former will be more subject to patient motion with less radiation dose delivered to the patients. This is particularly important for the increasingly young patient population which has higher radiation risk than seniors (29). In our fast SPECT study, the reduction of acquisition time would be beneficial for patients with a sedation demand and patients with less compliance. The reduced acquisition time would further increase the patient throughput. Both low dose and fast SPECT are of clinical interest and can be potentially achieved using DL techniques (17).

Shiri et al. (17) suggested that denoising from half acquisition time per projection outperformed that from half number of

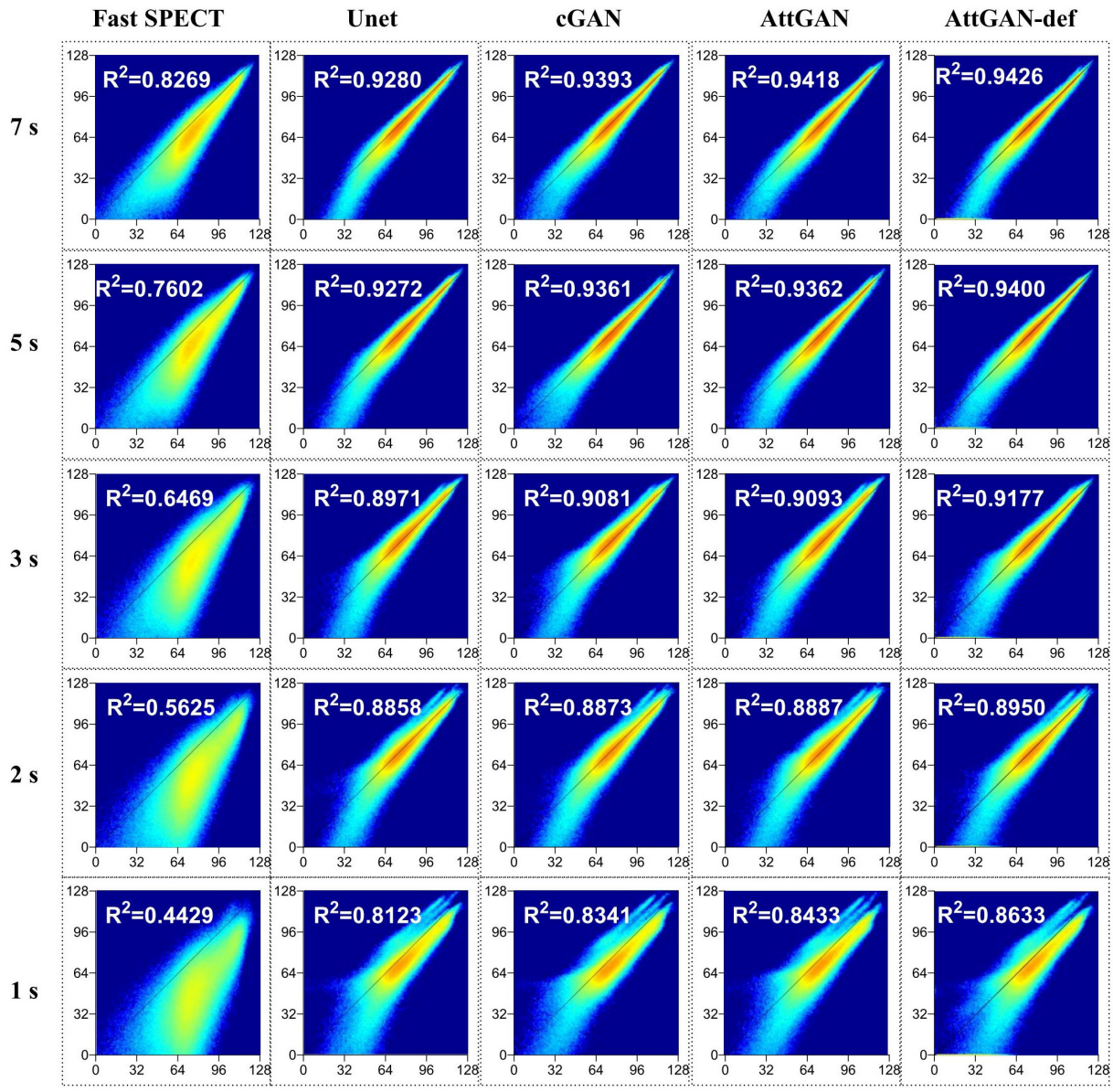

FIGURE 8
Joint histogram and linear regression analysis of fast SPECT and different denoised images in the 50 testing datasets for five shorter acquisition times. The filtered FT images are used as the reference.

projections for fast MP-SPECT by 2D ResNet. According to this reference, our fast MP-SPECT datasets were obtained by reducing the acquisition time per view. Compared with the existing literature, Ramon et al. (13) reported that CNN-based denoising on 1/2 dose level images could achieve image quality comparable to standard full dose images based on the TPD values. Aghakhan et al. (16) claimed that all denoised images on 1/2 dose level would be clinically acceptable by using 2D cGAN in the projection domain. Similarly, in our work, the mean value of the absolute difference for PDS, a similar index to TPD between FT and AttGAN-def denoised images on 1/2 acquisition time of FT is 0.66%. Although our 3D AttGAN results could not be directly compared with the previous studies due to the use of different networks, datasets, imaging protocols, and evaluation methods, the results are consistent.

In addition, some studies have shown that concatenating the gender, BMI, state (stress or rest), and scatter window images to the training dataset can improve the DL performance in the attenuation correction task (30). We first proposed to add patient defect information into the projections for training the AttGAN and showed promising results. Incorporating the defect information into the network structure or loss function could be further investigated but it is beyond the scope of this study. One should note that the defect information was extracted from the patients' medical reports and SPECT images in this study, which may be subjected to potential image artifacts. Moreover, the actual defect information may not be able to be verified as other examination results of the patients, e.g., CT angiography, are not available in this study.

Ramon et al. (13) compared the performance between training on a specific low dose level and training on a collection of various low dose levels at the same time. Their preliminary results showed that a dose-specific network can be more accurate than a "one-size-fits-all" network. Liu et al. (31) proposed a denoising method using an image noise index calculated from the normalized standard deviation in the liver ROI for low dose PET images. The image noise index was embedded as a tunable parameter for training. Their results demonstrated that their denoising method achieved better denoising performance than the "one-size-fits-all" network, while it still could not outperform the dose-specific network. Thus, we trained our DL model using a dose-specific approach, i.e., separately for different image acquisition times, for the best denoising performance. More investigations are warranted for a more generalizable and efficient training strategy, i.e., transfer learning, data preprocessing and adjustment on the loss function for training based on all available data.

Limitations of this study include that the clinical-related evaluation is only conducted by PDS. A more comprehensive clinical analysis and a ROC study of defect detectability are needed to validate the proposed methodology. Another limitation is that our DL networks were trained based on a relatively small patient cohort, i.e., thirty-five patients. Training on a large number of patients would benefit the model performance with less susceptibility of overfitting, though our network's loss function was validated to be converged. Gong et al. proposed to pre-train the DL network with simulation datasets and then fine-tuned it with a limited clinical dataset (32). Their results suggested that using simulation datasets with more realistic imaging conditions or with the use of a more accurate Monte Carlo simulation would generate a more robust pre-trained model.

5. Conclusion

In this work, we investigated the performance of AttGAN in denoising fast MP-SPECT images using clinical datasets. The proposed AttGAN provided superior denoising performance as compared to the conventional cGAN and Unet. Patient defect information could be useful parameter for further improving the AttGAN-based denoising performance.

Data availability statement

The original contributions presented in this study are included in this article/supplementary material, further inquiries can be directed to the corresponding authors.

Ethics statement

The studies involving human participants were reviewed and approved by Institutional Review Board of Taipei Veterans General Hospital (IRB number 2022-11-002CC). The written informed consent was waived due to the retrospective nature of this study.

Author contributions

JS, T-HW, B-HY, and GM were the primary authors of the manuscript. JS was mainly responsible for data processing and analysis. YD was mainly responsible for data analysis and manuscript revision. C-YL was mainly responsible for data collection. T-HW, B-HY, and Y-HL were responsible for clinical interpretation. GM and T-HW were responsible for data interpretation and study integration. All authors contributed to the article and approved the submitted version.

Funding

This work was supported by the Excellent Young Scientists Fund (Hong Kong and Macau, 81922080), Natural Science Foundation of China and Ministry of Science and Technology, Taiwan (MOST 109-2314-B-010-023-MY3).

Conflict of interest

The authors declare that the research was conducted in the absence of any commercial or financial relationships that could be construed as a potential conflict of interest.

Publisher's note

References

1. Underwood S, Anagnostopoulos C, Cerqueira M, Ell P, Flint E, Harbinson M, et al. Myocardial perfusion scintigraphy: the evidence. *Eur J Nuclear Med Mol Imag.* (2004) 31:261–91. doi: 10.1007/s00259-003-1344-5

2. Slomka P, Patton J, Berman D, Germano G. Advances in technical aspects of myocardial perfusion SPECT imaging. *J Nuclear Cardiol.* (2009) 16:255–76. doi: 10.1007/s12350-009-9052-6

3. Zhang D, Pretorius P, Ghaly M, Zhang Q, King M, Mok G. Evaluation of different respiratory gating schemes for cardiac SPECT. *J Nuclear Cardiol.* (2020) 27:634–47. doi: 10.1007/s12350-018-1392-7

4. Wu J, Liu C. Recent advances in cardiac SPECT instrumentation and imaging methods. *Phys Med Biol.* (2019) 64:06TR1. doi: 10.1088/1361-6560/ab04de

5. Zhang D, Yang B, Wu N, Mok G. Respiratory average CT for attenuation correction in myocardial perfusion SPECT/CT. *Ann Nuclear Med.* (2017) 31:172–80. doi: 10.1007/s12149-016-1144-1

6. Zhang Q, Zhang D, Mok G. Comparison of different attenuation correction methods for dual gating myocardial perfusion SPECT/CT. *IEEE Trans Radiat Plasma Med Sci.* (2019) 3:565–71. doi: 10.1109/TRPMS.2019.2899066

7. Kao Y, Better N. D-SPECT: new technology, old tricks. *J Nuclear Cardiol.* (2016) 23:311–2. doi: 10.1007/s12350-015-0290-5

8. Ozsahin I, Chen L, Könik A, King M, Beekman F, Mok G. The clinical utilities of multi-pinhole single photon emission computed tomography. *Quant Imag Med Surg.* (2020) 10:2006–29. doi: 10.21037/qims-19-1036

9. Bocher M, Blevis I, Tsukerman L, Shrem Y, Kovalski G, Volokh L. A fast cardiac gamma camera with dynamic SPECT capabilities: design, system validation and future potential. *Eur J Nuclear Med Mol Imag.* (2010) 37:1887–902. doi: 10.1007/s00259-010-1488-z

10. Brambilla M, Lecchi M, Matheoud R, Leva L, Lucignani G, Marcassa C, et al. Comparative analysis of iterative reconstruction algorithms with resolution recovery and new solid state cameras dedicated to myocardial perfusion imaging. *Phys Med.* (2017) 41:109–16. doi: 10.1016/j.ejmp.2017.03.008

11. Johnson R, Bath N, Rinker J, Fong S, James S, Pampaloni M, et al. Introduction to the D-SPECT for technologists: workflow using a dedicated digital cardiac camera. *J Nuclear Med Technol.* (2020) 48:297–303. doi: 10.2967/jnmt.120.254870

12. Valenta I, Treyer V, Husmann L, Gaemperli O, Schindler M, Herzog B, et al. New reconstruction algorithm allows shortened acquisition time for myocardial perfusion SPECT. *Eur J Nucl Med Mol Imag.* (2010) 37:750–7. doi: 10.1007/s00259-009-1300-0

13. Ramon A, Yang Y, Pretorius P, Johnson K, King M, Wernick M. Improving diagnostic accuracy in low-dose SPECT myocardial perfusion imaging with convolutional denoising networks. *IEEE Trans Med Imag.* (2020) 39:2893–903. doi: 10.1109/TMI.2020.2979940

14. Liu J, Yang Y, Wernick M, Pretorius P, King M. Deep learning with noise-to-noise training for denoising in SPECT myocardial perfusion imaging. *Med Phys.* (2021) 48:156–68. doi: 10.1002/mp.14577

15. Liu J, Yang Y, Wernick M, Pretorius P, Slomka P, King M. Improving detection accuracy of perfusion defect in standard dose SPECT-myocardial perfusion imaging by deep-learning denoising. *J Nucl Cardiol.* (2021) 2021:1–10. doi: 10.1007/s12350-021-02676-w

16. Aghakhan Olia N, Kamali-Asl A, Hariri Tabrizi S, Geramifar P, Sheikhzadeh P, Farzanefar S, et al. Deep learning–based denoising of low-dose SPECT myocardial perfusion images: quantitative assessment and clinical performance. *Eur J Nucl Med Mol Imag.* (2022) 49:1508–22. doi: 10.1007/s00259-021-05614-7

17. Shiri I, Sabet K, Arabi H, Pourkeshavarz M, Teimourian B, Ay M, et al. Standard SPECT myocardial perfusion estimation from half-time acquisitions using deep convolutional residual neural networks. *J Nucl Cardiol.* (2021) 28:2761–79. doi: 10.1007/s12350-020-02119-y

18. Sun J, Du Y, Li C, Wu T, Yang B, Mok G. Pix2Pix generative adversarial network for low dose myocardial perfusion SPECT denoising. *Quant Imag Med Surg.* (2022) 12:3539–55. doi: 10.21037/qims-21-1042

19. Sun J, Jiang H, Du Y, Li C, Wu T, Yang B, et al. Deep learning-based denoising in projection-domain and reconstruction-domain for low dose myocardial perfusion SPECT. *J Nucl Cardiol.* (2022) 2022:1–16. doi: 10.1007/s12350-022-03045-x

20. Zhang H, Goodfellow I, Metaxas D, Odena A. Self-attention generative adversarial networks. *Proceeding of the international conference on machine learning (ICML)*. PMLR (2019). doi: 10.1016/j.compbiomed.2022.105828

21. Schlemper J, Oktay O, Schaap M, Heinrich M, Kainz B, Glocker B, et al. Attention gated networks: learning to leverage salient regions in medical images. *Med Image Analy.* (2019) 53:197–207. doi: 10.1016/j.media.2019.01.012

22. Liu Y, Lei Y, Fu Y, Wang T, Tang X, Jiang X, et al. CT-based multi-organ segmentation using a 3D self-attention U-net network for pancreatic radiotherapy. *Med Phys.* (2020) 47:4316–24. doi: 10.1002/mp.14386

23. Li M, Hsu W, Xie X, Cong J, Gao W. SACNN: self-attention convolutional neural network for low-dose CT denoising with self-supervised perceptual loss network. *IEEE Trans Med Imag.* (2020) 39:2289–301. doi: 10.1109/TMI.2020.2968472

24. Wang Y, Yu B, Wang L, Zu C, Lalush D, Lin W, et al. 3D conditional generative adversarial networks for high-quality PET image estimation at low dose. *Neuroimage.* (2018) 174:550–62. doi: 10.1016/j.neuroimage.2018.03.045

25. Ioffe S, Szegedy C. Batch normalization: accelerating deep network training by reducing internal covariate shift. *Proceeding of the international conference on machine learning (ICML)*. PMLR (2015). doi: 10.1007/s11390-020-0679-8

26. Isola P, Zhu J, Zhou T, Efros A. Image-to-image translation with conditional adversarial networks. *Proceeding of the IEEE conference on computer vision and pattern recognition*. (2017). doi: 10.1109/CVPR.2017.632

27. Liu Y. Quantification of nuclear cardiac images: the yale approach. *J Nucl Cardiol.* (2007) 14:483–91. doi: 10.1016/j.nuclcard.2007.06.005

28. Buades A, Coll B, Morel J. A non-local algorithm for image denoising. *Proceeding of the IEEE computer society conference on computer vision and pattern recognition (CVPR)*. IEEE (2005).

29. Gelfand M, Lemen L. *PET/CT and SPECT/CT dosimetry in children: the challenge to the pediatric imager seminars in nuclear medicine*. Amsterdam: Elsevier (2007).

30. Chen X, Zhou B, Shi L, Liu H, Pang Y, Wang R, et al. CT-free attenuation correction for dedicated cardiac SPECT using a 3D dual squeeze-and-excitation residual dense network. *J Nucl Cardiol.* (2021) 2021:1–16. doi: 10.1007/s12350-021-02672-0

31. Liu Q, Liu H, Mirian N, Ren S, Viswanath V, Karp J, et al. A personalized deep learning denoising strategy for low-count PET images. *Phys Med Biol.* (2022) 67:145014. doi: 10.1088/1361-6560/ac783d

32. Gong K, Guan J, Liu C, Qi J. PET image denoising using a deep neural network through fine tuning. *IEEE Trans Radiat Plasma Med Sci.* (2018) 3:153–61.

frontiers | Frontiers in Medicine

TYPE Original Research
PUBLISHED 22 March 2023
DOI 10.3389/fmed.2023.1118531

OPEN ACCESS

EDITED BY
Jincheng Wang,
Nanjing Drum Tower Hospital,
China

REVIEWED BY
Pardeep Kumar,
National Institute of Mental Health and Neurosciences, India
Xiao Li,
Shanghai Pudong Hospital,
China

*CORESPONDENCE
Nipun Verma
✉ nipun29j@gmail.com
Baljinder Singh
✉ drbsingh5144@yahoo.com

SPECIALTY SECTION
This article was submitted to Gastroenterology, a section of the journal Frontiers in Medicine

RECEIVED 07 December 2022
ACCEPTED 03 March 2023
PUBLISHED 22 March 2023

CITATION
Kaur A, Verma N, Singh B, Kumar A, Kumari S, De A, Sharma RR and Singh V (2023) Quantitative liver SPECT/CT is a novel tool to assess liver function, prognosis, and response to treatment in cirrhosis.
Front. Med. 10:1118531.
doi: 10.3389/fmed.2023.1118531

Quantitative liver SPECT/CT is a novel tool to assess liver function, prognosis, and response to treatment in cirrhosis

Amritjyot Kaur[1], Nipun Verma[2]*, Baljinder Singh[1]*, Ajay Kumar[1], Sunita Kumari[2], Arka De[2], Ratti Ram Sharma[3] and Virendra Singh[2]

[1]Department of Nuclear Medicine, Post Graduate Institute of Medical Education and Research, Chandigarh, India, [2]Department of Hepatology, Post Graduate Institute of Medical Education and Research, Chandigarh, India, [3]Department of Transfusion Medicine, Post Graduate Institute of Medical Education and Research, Chandigarh, India

Background: Functional liver reserve is an important determinant of survival in cirrhosis. The traditional indocyanine green test (ICG) is cumbersome. Hence, we developed and validated a novel liver imaging, a hybrid of SPECT and CT (Q-SPECT/CT), for evaluating disease severity, outcomes, and response to treatment in decompensated cirrhosis (DC).

Methods: We recruited a cohort of DC patients at a tertiary institute between 2016–2019. First, we standardized the Q-SPECT/CT across a predefined range of volumes through phantom experiments. Then we performed clinical and laboratory evaluations, ICG test (retention at 15min), and Q-SPECT/CT at baseline and 12months of granulocyte colony-stimulating factor (G-CSF) and standard medical treatment (SMT).

Results: In 109 DC patients, 87.1% males, aged 51±10years, MELD: 14 (7–21), the percent quantitative liver uptake (%QLU) on Q-SPECT/CT exhibited a strong correlation with CTP (r =−0.728, p <0.001), MELD (r =−0.743; p<0.001) and ICG-R-15 (r =−0.720, p<0.001) at baseline. %QLU had the maximum discrimination (AUC: 0.890–0.920), sensitivity (88.9–90.3%), specificity (81.2–90.7%), and accuracy (85.8–89.4%) than liver volumes on Q-SPECT/CT or ICG test for classifying patients in CTP/MELD based prognostic categories. A significant increase in %QLU (26.09±10.06 to 31.2±12.19, p =0.001) and improvement in CTP/MELD correlated with better survival of G-CSF treated DC patients (p <0.05). SMT did not show any improvement in Q-SPECT/CT or clinical severity scores (p >0.05). %QLU>25 (adj.H.R.: 0.234, p =0.003) and G-CSF treatment (adj.H.R.: 0.414, p =0.009) were independent predictors of better 12-months survival in DC.

Conclusion: Q-SPECT/CT (%QLU) is a novel non-invasive, diagnostic, prognostic, and theragnostic marker of liver reserve and its functions in cirrhosis patients.

Clinical trial registration: Clinicaltrials.gov, NCT02451033 and NCT03415698.

KEYWORDS

decompensated cirrhosis, imaging, SPECT, mortality, G-CSF

1. Introduction

Decompensated cirrhosis (DC) and associated complications such as ascites, gastrointestinal bleeding, infections, hepatic encephalopathy, and hepatocellular carcinoma portend high morbidity and mortality (1, 2). Child-Turcotte-Pugh (CTP) and Model for end-stage-liver disease (MELD) score traditionally assess liver functions and prognosticate cirrhosis patients. However, these scores have inherent limitations for the precise evaluation of liver functions and assessment of response to therapies (3, 4). Problems with CTP score include subjective assessment of ascites and encephalopathy, overestimation of severity due to increased bilirubin in cases of renal insufficiency, hemolysis, and decreased prothrombin complex due to activation of coagulation in case of sepsis (5, 6). All such factors contribute to over or underestimation of the severity of the liver disease. MELD is commonly used for prognosticating and prioritizing patients waiting for liver transplantation (7). It is a validated marker for predicting survival; however, its utility is often impeded due to lab-to-lab variations and different methods used for estimating the creatinine and INR values (8).

Although the indocyanine green (ICG) clearance test is a reference standard for the quantitative assessment of liver functions, it is cumbersome, requires multiple blood samplings, and has a high blood flow dependency. Thus, it is not used in routine clinical practice (9–15). A high functional heterogeneity among the hepatic segments is observed in liver cirrhosis and portal vein thrombus, which may lead to erroneous measurements. We hypothesize that non-invasive and quantitative imaging that can depict the spatial and segmental distribution of the radiotracer in the liver may become a potential substitute for ICG (16, 17). Sulfur-colloid (SC), which is extracted by Kupffer cells with no further clearance, is a surrogate molecule to estimate hepatocyte functions which can be assessed semi-quantitatively by single photon emission computed tomography (SPECT) (16, 18). Further, with the recent advances in image processing, the accurate quantification of the radioactivity distribution is possible. A hybrid SPECT/CT imaging can improve the diagnostic performance for the *in vivo* characterization of liver functions in cirrhosis (19–21).

Granulocyte colony-stimulating factor (G-CSF) is an emerging regenerative treatment in DC G-CSF mobilizes bone marrow stem cells (CD34+ cells) in peripheral blood, which can populate the liver tissue and differentiate into hepatic cells (22–24). Although a complete understanding of G-CSF action is unclear in cirrhosis, the safety and efficacy of G-CSF in hepatitis and chronic liver diseases have been reported (22, 24–26).

In this study, we examined the utility of novel non-invasive quantitative ^{99m}Tc-SC liver SPECT/CT for assessing disease severity, patient outcomes, and therapeutic response to G-CSF treatment in DC patients.

2. Materials and methods

2.1. Patients

We recruited 109 DC patients (95Males:14Females; mean age-51 ± 10 years) randomly assigned to either G-CSF + SMT or SMT (standard medical therapy) in the ongoing studies (25, 26) at a tertiary care center between January 2016 to March 2019. Patient selection criteria and study protocols (NCT02451033, NCT03415698) have been published previously (Supplementary Figures S1, S2).

Briefly, we included DC patients aged 18–80 years with a history of ascites and/or variceal bleeding and/or encephalopathy and/or jaundice. The cirrhosis was diagnosed through the clinical presentation, biochemical tests, radiology, endoscopy, and/or histopathology. We excluded patients with acute-on-chronic liver failure, sepsis, recent variceal bleed, grade III-IV hepatic encephalopathy, acute kidney injury, hepatocellular carcinoma or active malignancy, spleen>18 cm, portal vein thrombosis, cardiac dysfunction, recent alcohol abuse in 3 months, or alcoholic hepatitis, seropositivity for H.I.V., pregnancy, and hypersensitivity to G-CSF. We obtained written informed consent from all participants, followed GCP guidelines, and the protocol was approved by the Institute Ethics Committee (N.K./2,722/Ph.D./1,224).

The eligible patients were randomized using a computer-generated random number table with allocation concealment in the two groups (Supplementary Figure S2). The patients (n = 68) of group-A received standard medical therapy (SMT) plus G-CSF treatment at a dose rate of 5.0 μg/kg subcutaneously every 12.0 h for five consecutive days. This group received four similar cycles of G-CSF treatments at 3.0 months intervals over 1.0 years. The patients (n = 41) of group B received only standard medical therapy (SMT), which included: nutritional support, rifaximin, lactulose, bowel wash, albumin, diuretics, multivitamins, and antibiotics as per guidelines. Fresh frozen plasma and packed red-cell transfusions were administered as and when indicated. Stem cell mobilization was tested with CD34 cell estimation in peripheral blood at baseline and 6 days after therapy in both groups. The patients were followed up till 12 months, death or transplant (whichever was earlier) with physical examination, biochemical parameters, and CTP/MELD scoring. The patients were classified on CTP and MELD-based prognostic categories as CTP-A (n = 10), CTP-B (n = 56), and CTP-C (n = 43) and MELD of ≤15.0 (n = 77) and > 15.0 (n = 32). Study subjects underwent ^{99m}Tc-SC liver and spleen SPECT and ICG tests at baseline and follow-up. The Q-SPECT parameters were evaluated and correlated with the CTP/MELD score and ICG-R15 in both groups of patients.

2.2. Phantom standardization of Q-SPECT/CT

A series of phantom (Jaszczak SPECT phantom, Biodex Medical Systems, Inc., NY, United States) studies were performed using varying volumes (6.0 mL to 3,200 mL) and different radioactivity

Abbreviations: ^{99m}Tc, Technetium-99m; 99mTc-SC, 99mTc-Sulfur colloid; AUC, Area Under the Curve; CTP, Child-Turcotte-Pugh; DC, Decompensated Cirrhosis; FACS, Fluorescence-activated cell sorting; G-CSF, Granulocyte-colony stimulating factor; HBV, Hepatitis B virus; HCV, Hepatitis C virus; ICG, Indocyanine Green; INR, International normalized ratio; LV, Liver volume; MELD, Model for end-stage liver disease; NASH, Non-alcoholic steatohepatitis; Q.L.U., Quantitative Liver Uptake; Q.S.U., Quantitative Spleen Uptake; R.C.P., Radiochemical Purity; R.O.C., Receiver Operator Characteristics; R.O.I., Region of interest; SC, Sulfur-Colloid; SMT, Standard medical therapy; SPECT, Single Photon Emission Computed Tomography; S.V., Spleen volume.

concentrations (28.5 kBq/mL to 151.33 kBq/mL) of pertechnetate ($^{99m}TcO_4^-$) to develop and standardize the optimal processing protocol for accurate quantification (Supplementary Figures S3–S6; Supplementary Table S1). Data were acquired on a dual-headed gamma camera (Symbia- T16, SIEMENS, Erlangen, Germany) in 120 projections (20s/projection) in a 128 × 128 matrix with a zoom factor of 1.0. The data acquired was reconstructed by iterative reconstruction using a butter worth filter (cut off 0.5 cycles/cm) on a dual-head gamma camera. The threshold values varied from 19.0 to 52.0 to obtain the best volume estimation. Counts/voxel were converted into concentration units (μCi/mL) using the regression line, which was used to calculate liver/spleen volume, quantitative liver /spleen uptake, the percentage of injected dose per milliliter of liver/spleen tissue (%ID/mL) respectively.

2.3. Patients' imaging with ^{99m}Tc-S-colloid liver SPECT

Briefly, 4.0–5.0 mCi (148- to 185-MBq) radioactivity of ^{99m}Tc-SC was injected intravenously in each patient (Supplementary Figure S7). Planar liver imaging was done at 20-min post-injection, followed by SPECT/CT acquisition at 30-min using the same gamma camera described above for the phantom standardization. The camera peaked at 140.0 keV with a window of ±20.0%. SPECT data were acquired over 360-degree rotation in 120 projections (20 s/projection) in a 128 × 128 matrix (zoom, 1.5). After SPECT acquisition, low-dose CT (60 mAs and 140 kVP) was performed for the liver region. The images were reconstructed using an iterative reconstruction algorithm and Butterworth smoothing filter. The reconstructed images were analyzed using 3D volumetric analysis software 8.5.10.1 (Symbia.net, Munich, Germany). R.O.I.s were drawn coronal slices using a fixed threshold iso-contouring method to obtain volume and radioactive concentration.

2.4. Indocyanine green retention test

ICG (0.3 mg/kg of body weight) was administered intravenously *via* a peripheral vein. Blood samples were collected at 0, 5-, 10-, 15-, and 20-min post-injection from the contralateral vein. A standard dilution curve was obtained by using varying ICG concentrations. The same was used to estimate the unknown blood ICG levels to measure the dye retention in the liver. The ICG concentrations in standard solution and blood were recorded at 805 nm using a spectrophotometer (Systronics, UV/VIS spectrophotometer118, Gujarat, India). Retention value and plasma disappearance rate were calculated for all the patients. The standard reference ICG retention value was taken as less than 10.0% at 15-min and plasma disappearance rate of more than 18.0 mL/min.

2.5. Fluorescence-activated cell sorting analysis

Fluorescence-activated cell sorting (FACS) technique was used to estimate the circulating hematopoietic progenitor cells (CD34+) in peripheral venous blood on day 0 and at day 6 of initiation of G-CSF therapy using a flow cytometer (BD FACS Canto II, San Jose, California, U.S.A.) (Supplementary Figures S8, S9). Precisely, 2.0 mL of blood was collected in EDTA vacutainer for total nucleated cell count and CD34+ cells estimation.

2.6. Statistical analysis

Numerical values were expressed as mean ± SD or median (range) as appropriate. The unpaired t-test or chi-square was used to compare numerical and categorical variables between groups. A paired t-test or u-test was used to compare the pre-and post-treatment numerical parameters. ANOVA was used to compare numerical data between the three groups. The correlation between numerical variables was expressed through the Pearson correlation coefficient (r) at 95% confidence intervals. Receiver operating characteristics (R.O.C.) curves were used to calculate the area under the curve (AUC), sensitivity, specificity, positive and negative predictive values, and accuracy for differentiating severity grades in liver cirrhosis. The optimal cut-offs of ICG and Q-SPECT/CT for defining severity and mortality were obtained from maximum Youden's index. Kaplan Meier survival and cox-regression were conducted to evaluate survival estimates and hazards of mortality between groups, and the groups were compared with the Log-Rank test. Transplanted and lost to follow-up patients were considered an event for a 12-month transplant-free survival analysis. All statistical tests were two-sided and performed using IBM SPSS v.22 and RStudio v.1.4.1103 at a significance level of $p < 0.05$.

3. Results

We recruited patients aged 51.1 ± 9.3 years, 86% males, predominantly alcohol-related cirrhosis (54.5%), with a CTP of 9 (6–13) and MELD of 14 (7–21) (Supplementary Table S2).

3.1. Standardization protocol

The best threshold value of Q-SPECT was calculated from the phantom imaging data using 3D volumetric analysis (Supplementary Figures S5, S6; Supplementary Table S1). These values were found to be 41.0, 38.0, and 33.0 for activity volume ranges of 6.0–30.0 mL, 500.0–1500.0 mL, and 2,400–3,200 mL, respectively. The estimated threshold values provided significant ($p = 0.001$) correlation of 0.90, 0.98 & 0.97 for the three reference ranges. Further, by using the threshold of 38.0%, the SPECT reconstructed data was used to calculate the different range (28.5 kBq/mL to 151.33 kBq/mL) of radioactivity concentrations and compared with the actual concentrations used for this standardization procedure. For calculating the tracer radioactivity, the regression line equation on attenuation corrected images used was: counts/cc = 6807.3 × μci/cc + 39.0. We used the best-fitted regression line to calculate the volume and radioactivity concentration at baseline and post-G-CSF treatment SPECT data in all the patients (Supplementary data).

TABLE 1 Q-SPECT/CT and ICG parameters among prognostic categories in decompensated cirrhosis.

Parameters	CTP category				MELD category		
	CTP-A (n =10)	CTP-B (n =56)	CTP-C (n=43)	p-Value	MELD<15 (n=77)	MELD>15 (n=32)	p-Value
Q-SPECT/CT: Liver parameters							
LV (mL)	1,200 ± 356	994 ± 253	860 ± 250	0.028	1,021 ± 288	819 ± 205	0.003
%QLU	41.20 ± 3.77	29.79 ± 6.93	15.9 ± 7.83	0.001	30.1 ± 9.0	15.25 ± 5.80	<0.001
%ID/mL (Liver)	0.038 ± 0.016	0.031 ± 0.009	0.019 ± 0.009	0.835	0.031 ± 0.012	0.019 ± 0.007	<0.001
Q-SPECT/CT: Spleen parameters							
SV (mL)	717 ± 457	644 ± 380	735 ± 303	0.997	661 ± 378	734 ± 319	0.264
%QSU	28.10 ± 13.73	29.79 ± 13.41	34.57 ± 12.83	0.940	29.14 ± 12.64	35.36 ± 14.47	0.085
%ID/mL (Spleen)	0.045 ± 0.022	0.051 ± 0.018	0.052 ± 0.021	0.321	0.050 ± 0.019	0.053 ± 0.019	0.988
ICG-test							
R-15 (%)	35.22 ± 8.33	44.4 ± 10.50	54.10 ± 12.03	<0.001	44.62 ± 12.08	53.97 ± 10.71	<0.001

Q-SPECT/CT, Quantitative single photon emission computed tomography; ICG, Indocyanine green; CTP, Child-Turcotte-Pugh; MELD: Model for end stage liver disease; LV, Liver Volume; %QLU, Percentage Quantitative Liver Uptake; %ID/mL, Injected Dose per milliliter; SV, Spleen Volume; %QSU, percentage Quantitative Spleen Uptake; ICG-15, Indocyanine green test (retention value at 15 min).

TABLE 2 Correlation# between quantitative Q-SPECT/CT and CTP, MELD scores, ICG parameters.

99mTc-SC SPECT parameters	CTP	MELD	ICG R-15	PDR
LV	r = − 0.409	r = −0.370	r = −0.427	r = 0.450
	p < 0.001	p < 0.001	p < 0.001	p < 0.001
%QLU	r = −0.728	r = −0.743	r = −0.720	r = 0.754
	p < 0.001	p < 0.001	p < 0.001	p < 0.001
% ID/mL liver	r = −0.471	r = −0.538	r = −0.453	r = 0.461
	p < 0.001	p < 0.001	p < 0.001	p < 0.001
SV	r = 0.089	r = 0.124	r = 0.157	r = −0.176
	(n.s.)	(n.s.)	(n.s.)	(n.s.)
%QSU	r = 0.241	r = 0.218	r = 0.352	r = −0.353
	(n.s.)	(n.s.)	(n.s.)	p < 0.001
% ID/mL spleen	r = 0.128	r = 0.020	r = 0.113	r = −0.094
	(n.s.)	(n.s.)	(n.s.)	(n.s.)
ICG R-15	r = −0.688	r = −0.521	–	–
	p < 0.001	p < 0.001		
PDR	r = −0.670	r = −0.547	–	–
	p < 0.001	p < 0.001		

Q-SPECT/CT, Quantitative single photon emission computed tomography; ICG, Indocyanine green; CTP, Child-Turcotte-Pugh; MELD, Model for end stage liver disease; LV, Liver Volume; %QLU, Percentage Quantitative Liver Uptake; %ID/mL, Injected Dose per milliliter; SV, Spleen Volume; %QSU, Percentage Quantitative Spleen Uptake; ICG R-15, Indocyanine Green retention rate at 15 min; PDR, Plasma Disappearance rate; #Pearson correlation (2-tailed) analysis.

3.2. Descriptive Q-SPECT and ICG-test in cirrhosis

The Q-SPECT and ICG parameters differed in CTP and MELD-based prognostic categories, as illustrated in Table 1. The liver volumes (LV) observed in CTP-C patients were significantly lower than that in CTP-B and A patients (p = 0.028) (Supplementary Figure S8A). The fractional liver uptake (%QLU) was substantially lower in CTP-C patients than in CTP-B and A (p = 0.001) (Supplementary Figure S8B). Likewise, liver volumes and %QLU were lower in the MELD>15 groups than MELD≤15 group, with p = 0.003 and p < 0.001 (Supplementary Figures S9A,B). Quantitative spleen parameters were not different between various Child and MELD classes (p > 0.05) (Table 1). ICG-R15 was significantly lower in CTP-A and B than in C and MELD≤15 than >15 groups (p < 0.001) (Supplementary Figure S10).

3.3. Correlation of Q-SPECT with cirrhosis severity and ICG-test

Table 2: The %QLU exhibited a strong inverse correlation with CTP (r = −0.728, p < 0.001), MELD (r = −0.743; p < 0.001) and reference standard ICG-R15 (r = −0.720, p < 0.001) values, respectively. The percentage of injected dose/mL also showed a significant but moderate correlation with CTP, MELD, and ICG-R15, followed by LV. However, no significant correlation was observed for CTP and MELD scoring with any quantitative spleen parameters. Analysis between CTP, MELD, and ICG parameters (ICG R-15 and P.D.R.) also demonstrated a negative correlation between CTP *and* ICG R-15 (r = −0.670; p = <0.001); CTP *and* P.D.R. (r = −0.670; p = <0.001); MELD and ICG R-15 (r = −0.521; p = <0.001), MELD *and* P.D.R. (r = −0.550; p = <0.001), respectively.

3.4. Performance of Q-SPECT and ICG for disease severity and survival in DC

On R.O.C. analysis (Figure 1), compared to ICG and Liver volume assessment, %QLU showed the highest area under the R.O.C. curve (AUC) for discriminating CTP-A from B (0.920), CTP-B from C (0.891), and MELD≤15 from MELD>15 groups (0.906). The %QLU above 37.2% could differentiate CTP-A from B cirrhosis with

A

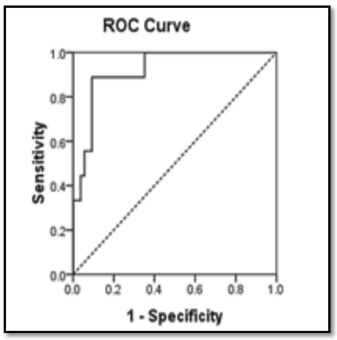

B

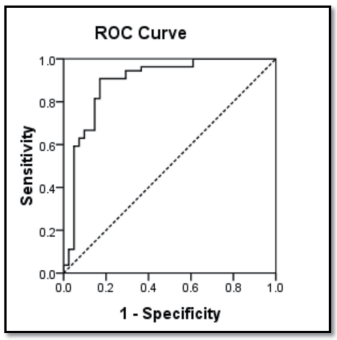

C

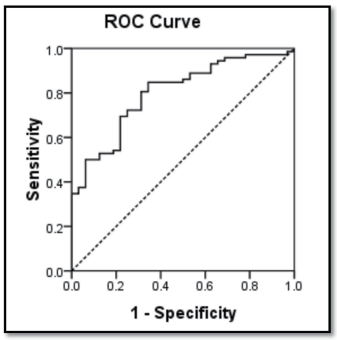

D

	CTP-A vs. CTP-B			CTP B vs. CTP C			MELD ≤15 vs. MELD>15		
	%QLU	LV	ICG R-15	%QLU	LV	ICG-R15	%QLU	LV	ICG R-15
AUC	**0.920***	0.780	0.817	**0.891***	0.643	0.823	**0.906***	0.695	0.800
Sensitivity	**88.9**	88.9	77.8	**88.9**	70.4	74.1	**90.3**	69.4	79.2
Specificity	**90.7**	51.9	77.8	**82.9**	41.5	73.2	**81.2**	56.2	68.8
Diagnostic Accuracy	**89.4**	54.5	77.8	**85.85**	57.0	72.6	**88.1**	66.05	70.20

FIGURE 1
Diagnostic performance of Q-SPECT/CT and ICG-R15 for disease severity in cirrhosis Receiver operating characteristics for percentage quantitative liver uptake (%QLU) to discriminate **(A)** CTP-A vs. B, **(B)** CTP-B vs. C, and **(C)** MELD ≤15 vs. MELD>15 groups, **(D)** performance of %QLU, liver volume (LV), and indocyanine green retention (ICG-15) for CTP and MELD based prognostic categories.

sensitivity and specificity of 88.9 and 90.7%. A value above 22.2% could discriminate CTP-B from C cirrhosis with sensitivity and specificity of 88.9 and 82.9%. A value above 18.7% could classify low MELD from high MELD patients with sensitivity and specificity of 90.3 and 81.2%. Patients with %QLU > 25 at baseline were associated with significantly better 12-month survival than those with %QLU ≤25 (83% vs. 49%, $p < 0.001$) (Figure 2A).

3.5. Impact of G-CSF on stem cells, severity, survival, and Q-SEPCT in cirrhosis

Following the first cycle of G-CSF treatment, there was a significant ($p < 0.001$) increase in %CD34+ cell count (0.8 to 16.4, $p < 0.001$) following G-CSF treatment on day 6 as compared to the "day 0" counts (Supplementary Table S3; Supplementary Figure S11). However, no significant rise was seen in the %CD 34+ cell count (0.85 to 0.90, $p > 0.05$) in the SMT group (Supplementary Table S3; Supplementary Figure S12). The 12-month survival was significantly better in the G-CSF group (75%) than in the SMT group (51%), $p = 0.008$ (Figure 2B). Better survival in G-CSF-treated patients was associated with a significant increase in % QLU at 12 months compared with the baseline (26.1 ± 10.6 to 31.2 ± 12.2, $p = 0.001$) (Table 3). While in group B, the %QLU at 12 months did not change from the baseline value. The observed liver SPECT findings corroborated a significant improvement in CTP and MELD scores only in the G-CSF group. No significant change was noted in any other parameter, including the ICG-R-15 value ($p = 0.07$) at 12 months versus the baseline value (Table 3).

On adjusting for disease severity (MELD), baseline %QLU [H.R.: 0.234, 76.6% lower] and G-CSF treatment [H.R.: 0.414, 58.6% lower] were independently associated with a lower hazard of mortality in DC (Figure 2C). A representative ^{99m}Tc-SC SPECT scan demonstrating an increase in %QLU and LV in a DC patient following G-CSF treatment at 12 months is shown in Figure 3A, while no change in the parameters was noted in a patient who received SMT (Figure 3B).

4. Discussion

We reported a novel non-invasive tool, i.e., Q-SPECT/CT, with parameters such as fractional liver uptake and liver volumes that exhibited a significant correlation with reference standard ICG test and clinical scores (CTP and MELD) in DC patients. %QLU showed the best discriminative ability for severity and survival in DC patients. Moreover, improvement in survival of patients with G-CSF correlated with improvement in %QLU values. Thus, advocating its use and further validation to assess the liver functions in DC patients semi-quantitatively. Our results are in agreement with Zuckerman et al. (3), who reported an inverse correlation ($r = -0.64$, $p < 0.001$) between %QLU and CTP scores. They also reported a negative correlation ($r = -0.84$, $p < 0.001$) between %QLU and ICG in patients with compensated cirrhosis. In another study, a significant correlation ($p = 0.001$) was reported between CTP class and ^{99m}Tc-SC scan findings and was shown relevant for predicting prognosis in H.C.C. patients (16).

In liver cirrhosis, there is a high functional heterogeneity among the hepatic segments, which requires dynamic imaging that can

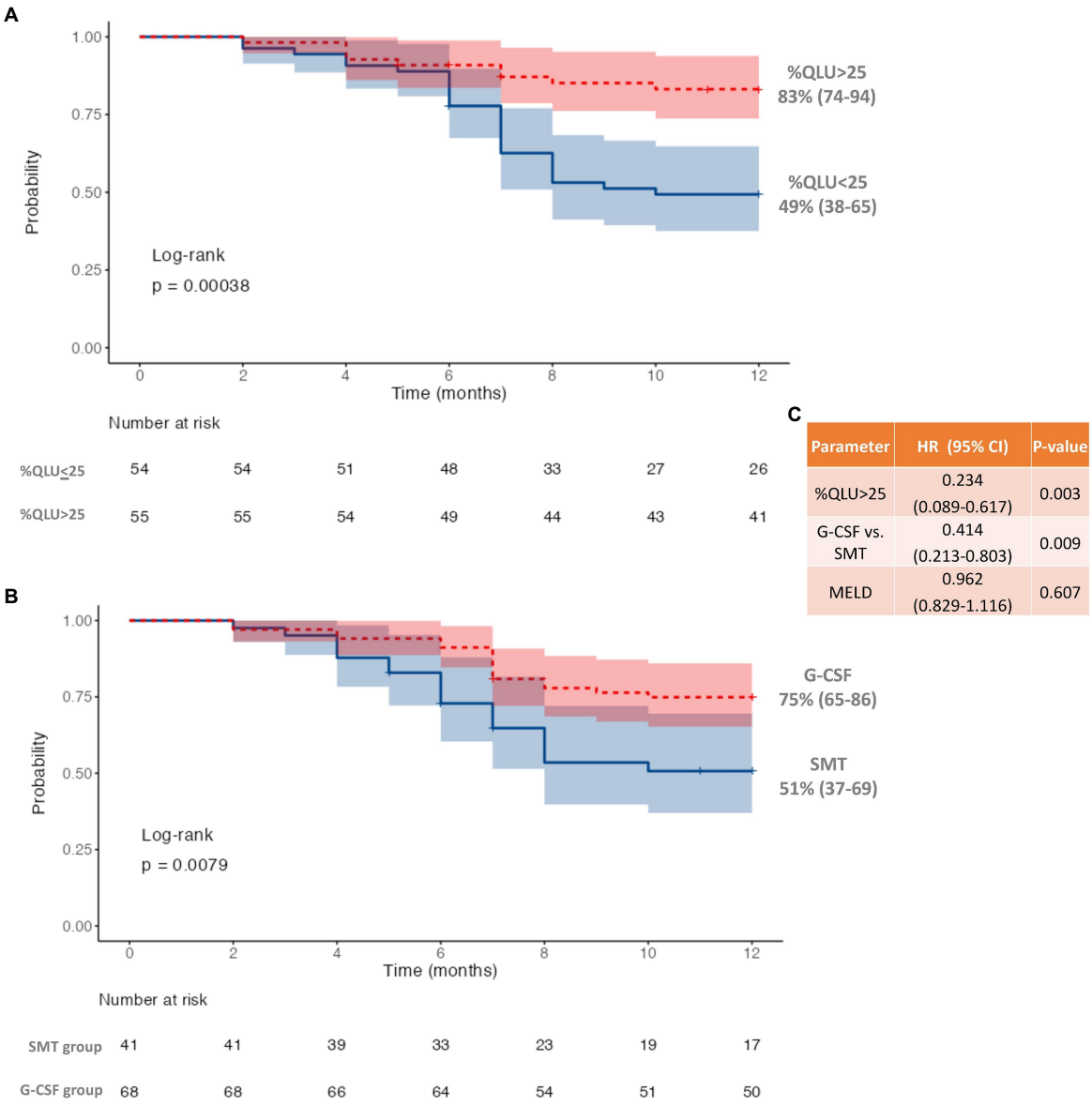

FIGURE 2
Twelve-month survival in decompensated cirrhosis **(A)** based on quantitative liver uptake (%QLU), **(B)** based on granulocyte colony-stimulating factor (G-CSF) treatment, and **(C)** Cox-regression for independent predictors of mortality.

estimate spatial functional distribution in the liver (16, 27–29). The "gold standard" ICG test lack such evaluation. Therefore, in the present study, we compared the diagnostic accuracy of ^{99m}Tc-SC SPECT with the ICG test for estimating liver severity. On R.O.C. analysis, we demonstrated that %QLU on Q-SPECT/CT was a more accurate parameter than LV and ICG tests for stratifying DC patients according to their CTP and MELD scores.

In a recent study, the total liver function, which is a product of functional liver volume and liver/spleen counts, showed a sensitivity and specificity of 88.0 and 86.0% for differentiation of CTP A from B cirrhosis (16). In our study, the %QLU parameter offered a better sensitivity and specificity of 88.9 and 90.7% for classifying CTP-A from B cirrhosis. However, the ICG-R15 showed lower sensitivity and specificity (77.8% each) for such differentiation. The sub-optimal diagnostic performance of ICG in end-stage liver disease patients can be attributed to hyperbilirubinemia, intrahepatic shunt, or capillarization due to the same transport system of bile in hepatocytes, which could underestimate the ICG R-15 values in patients with DC (10–15). Therefore, the quantitative liver SPECT may add valuable information to DC patients.

G-CSF is a hematopoietic growth factor that stimulates the bone marrow to produce and release granulocytes and stem cells to the injured region (30–32). Further, the mobilization of CD34+ cells, triggered by G-CSF, may be helpful in hepatic tissue repair and regeneration (22, 24, 25). In the present study, we evaluated the diagnostic utility of quantitative liver SPECT for functional liver assessment and response evaluation to GCSF treatment in DC patients.

In two clinical studies, an improvement in one-year survival and disease severity score with multiple cycles of GCSF has been reported (25, 26). In another study, Garg et al. showed that 12 doses of G-CSF

TABLE 3 Change in disease severity scores, Q-SPECT/CT and ICG parameters in G-CSF treated (Group A) and Standard medical therapy groups (Group B).

Parameter	Group A			Group B		
	Baseline	Follow up	*p*-Value#	Baseline	Follow up	*p*-Value#
	Mean±SD	Mean±SD		Mean±SD	Mean±SD	
	Range	Range		Range	Range	
	Median	Median		Median	Median	
CTP	9.16 ± 1.65	7.40 ± 1.15	<0.001	8.14 ± 1.09	8.78 ± 1.88	0.264
	(6–13)	(5–10)		(6–10)	(7–12)	
	9	7		8	8	
MELD	13.61 ± 2.89	11.48 ± 2.63	<0.001	13.07 ± 2.73	14.85 ± 3.27	0.391
	(8–19)	(7–17)		(8–18)	(11–22)	
	14	12		13	14.5	
Q-SPECT-liver parameters						
%QLU	26.09 ± 10.6	31.21 ± 12.19	0.001	27.49 ± 9.3	26.4 ± 11.6	0.667
LV	976 ± 275	1,025 ± 251	0.215	955 ± 206	988 ± 260	0.691
% ID/mL (Liver)	0.028 ± 0.014	0.031 ± 0.010	0.165	0.029 ± 0.011	0.027 ± 0.007	0.484
Q-SPECT-spleen parameters						
%QSU	31.5 ± 12.67	29.10 ± 10.95	0.335	32.3 ± 12.4	30.7 ± 13.0	0.120
SV	674 ± 364	638 ± 340	0.552	486 ± 191	558 ± 222	0.213
% ID/mL (Spleen)	0.052 ± 0.020	0.050 ± 0.017	0.469	0.056 ± 0.019	0.049 ± 0.025	0.189
ICG R-15	46.7 ± 12.0	42.7 ± 12.6	0.066	43.09 ± 8.29	43.34 ± 10.36	0.814
PDR	5.93 ± 4.93	6.49 ± 4.18	0.148	5.73 ± 1.36	5.88 ± 1.54	0.937

Q-SPECT/CT, Quantitative single photon emission computed tomography; ICG, Indocyanine green; CTP, Child-Turcotte-Pugh; MELD, Model for end stage liver disease; LV, Liver Volume; %QLU, Percentage Quantitative Liver Uptake; %ID/mL, Injected Dose per milliliter; SV, Spleen Volume; %QSU, Percentage Quantitative Spleen Uptake; ICG R-15, Indocyanine Green retention rate at 15 min; PDR, Plasma Disappearance rate.

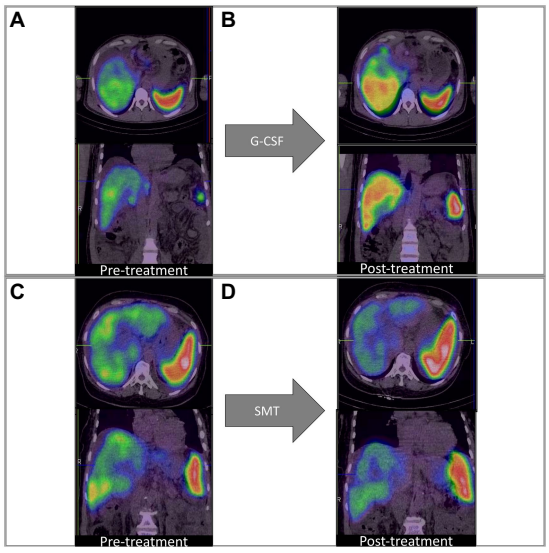

FIGURE 3
Q-SPECT/CT liver images with granulocyte colony-stimulating factor; G-CSF treatment [Panels **(A,B)**] and standard medical treatment (SMT) [Panels **(C,D)**] in representative DC patients. **(A,B)** Rise in %QLU (30 to 45%) and LV (964 to 1,016cc) after G-CSF treatment **(C,D)** Fall in %QLU (41 to 36%) and LV (1,264 to 965cc) after SMT treatment.

(5 μg/kg/dose) nearly doubled the survival in a group of ACLF patients predominantly of alcoholic etiology (22). It was observed that the %QLU at 12-mo post-G-CSF treatment was significantly higher ($p = 0.002$) than noted at the baseline level. These image findings thus suggest an improvement in liver function following G-CSF treatment.

Furthermore, we observed that the %QLU in G-CSF treated group of patients corroborated with the corresponding improvement in CTP and MELD score in group-A. However, both groups observed no significant change in ICG R-15 values. This finding may be attributed to intrahepatic shunts and capillarization found in cirrhosis which may falsely reflect the retention/clearance of the dye from the hepatocytes (33, 34). It is thus highlighted that the %QLU parameter of ^{99m}Tc-SC-SPECT may be used non-invasively for accurate response evaluation to therapies in liver cirrhosis of different etiologies.

Limitations of the study include single-center design and limited generalization to outpatient DC patients; however, we could demonstrate the utility of Q-SPECT in a relatively large number of DC patients. We could not demonstrate the correlation of splenic SPECT parameters with CTP, MELD, or ICG R-15 indices, suggesting the limited utility of splenic parameters for evaluating liver functions. We hypothesize that splenic SPECT would reflect portal hypertension and its severity, which is poorly represented by ICG, CTP, or MELD scores and hence not reflected in our study.

In conclusion, we showed that Q-SPECT/CT of the liver is a reliable marker of quantitative liver functions in DC patients. %QLU

correlates well with disease severity and reference standard (ICG test) in cirrhosis. %QLU can be used to non-invasively assess the severity, outcomes, and response to disease-modifying therapies such as G-CSF in cirrhosis.

Lay summary

Quantitative liver function assessment is often challenging in liver cirrhosis patients. We developed and validated a novel single photon emission computed tomography-based fractional liver uptake parameter for non-invasive semi-quantitative evaluation of liver functions in cirrhosis. The fractional liver uptake correlated well with the gold standard; indocyanine green test, disease severity scores, and patient survival in cirrhosis. G-CSF treatment improved disease severity scores, survival, and fractional liver uptake, while no change was observed with standard medical therapy in decompensated cirrhosis.

Data availability statement

The datasets presented in this article are not readily available because the data are not publicly available due to privacy or ethical restrictions. Requests to access the datasets should be directed to drbsingh5144@yahoo.com.

Ethics statement

The studies involving human participants were reviewed and approved by PGIMER Institute Ethics Committee. The patients/participants provided their written informed consent to participate in this study.

Author contributions

AKa, BS, and VS: conceptualization. AKa, NV, VS, and AD: data curation. AKa and NV: formal analysis, visualization, and writing – original draft. AKa, BS, VS, AKu, NV, AD, and SK: investigation. AKa, BS, VS, NV, AD, and RS: methodology. BS and VS: project administration and resources. AKa, NV, and AKu: software. BS and VS: supervision. BS and NV: validation. AKa, NV, and BS: writing – review and editing.

Conflict of interest

The authors declare that the research was conducted in the absence of any commercial or financial relationships that could be construed as a potential conflict of interest.

Publisher's note

All claims expressed in this article are solely those of the authors and do not necessarily represent those of their affiliated organizations, or those of the publisher, the editors and the reviewers. Any product that may be evaluated in this article, or claim that may be made by its manufacturer, is not guaranteed or endorsed by the publisher.

Supplementary material

The Supplementary material for this article can be found online at: https://www.frontiersin.org/articles/10.3389/fmed.2023.1118531/full#supplementary-material

References

1. Zhou W-C. Pathogenesis of liver cirrhosis. *World J Gastroenterol*. (2014) 20:7312–24. doi: 10.3748/wjg.v20.i23.7312

2. Mansour D, McPherson S. Management of decompensated cirrhosis. *Clin Med*. (2018) 18:s60–5. doi: 10.7861/clinmedicine.18-2-s60

3. Zuckerman E, Slobodin G, Sabo E, Yeshurun D, Naschitz JE, Groshar D. Quantitative liver-spleen scan using single photon emission computerized tomography (SPECT) for assessment of hepatic function in cirrhotic patients. *J Hepatol*. (2003) 39:326–2. doi: 10.1016/S0168-8278(03)00296-4

4. Durand F, Valla D. Assessment of prognosis of cirrhosis. *Semin Liver Dis*. (2008) 28:110–2. doi: 10.1055/s-2008-1040325

5. Moseley RH. Sepsis and cholestasis. *Clin Liver Dis*. (2004) 8:83–94. doi: 10.1016/S1089-3261(03)00134-X

6. Plessier A, Denninger M-H, Consigny Y, Pessione F, Francoz C, Durand F, et al. Coagulation disorders in patients with cirrhosis and severe sepsis. *Liver Int*. (2003) 23:440–8. doi: 10.1111/j.1478-3231.2003.00870.x

7. Malinchoc M, Kamath PS, Gordon FD, Peine CJ, Rank J, Borg Ter PCJ. A model to predict poor survival in patients undergoing transjugular intrahepatic portosystemic shunts. *Hepatology*. (2000) 31:864–71. doi: 10.1053/he.2000.5852

8. Cholongitas E, Marelli L, Kerry A, Senzolo M, Goodier DW, Nair D, et al. Different methods of creatinine measurement significantly affect MELD scores. *Liver Transpl*. (2007) 13:523–9. doi: 10.1002/lt.20994

9. Ma JD, Nafziger AN, Mylott W, Haughey DB, Rocci ML, Bertino JS. Quantitative assessment of hepatic blood flow using intravenous indocyanine green. *Eur J Clin Pharmacol*. (2008) 64:1133–4. doi: 10.1007/s00228-008-0519-1

10. Gasperi AD, Mazza E, Prosperi M. Indocyanine green kinetics to assess liver function: ready for a clinical dynamic assessment in major liver surgery? *World J Hepatol*. (2016) 8:355–7. doi: 10.4254/wjh.v8.i7.355

11. Vos JJ, Wietasch JKG, Absalom AR, Hendriks HGD, Scheeren TWL. Green light for liver function monitoring using indocyanine green? An overview of current clinical applications. *Anaesthesia*. (2014) 69:1364–76. doi: 10.1111/anae.12755

12. Halle BM, Poulsen TD, Pedersen HP. Indocyanine green plasma disappearance rate as dynamic liver function test in critically ill patients. *Acta Anaesthesiol Scand*. (2014) 58:1214–9. doi: 10.1111/aas.12406

13. Cui Y, König J, Leier I, Buchholz U, Keppler D. Hepatic uptake of bilirubin and its conjugates by the human organic anion-transporting polypeptide SLC21A6. *J Biol Chem*. (2001) 276:9626–30.

14. Shinohara H, Tanaka A, Kitai T, Yanabu N, Inomoto T, Satoh S, et al. Direct measurement of hepatic indocyanine green clearance with near-infrared spectroscopy: separate evaluation of uptake and removal. *Hepatol Baltim Md*. (1996) 23:137–4. doi: 10.1002/hep.510230119

15. Mizuguchi T, Kawamoto M, Meguro M, Hui TT, Hirata K. Preoperative liver function assessments to estimate the prognosis and safety of liver resections. *Surg Today*. (2014) 44:1–10. doi: 10.1007/s00595-013-0534-4

16. Bowen SR, Chapman TR, Borgman J, Miyaoka RS, Kinahan PE, Liou IW, et al. Measuring total liver function on sulfur colloid SPECT/CT for improved risk stratification and outcome prediction of hepatocellular carcinoma patients. *EJNMMI Res*. (2016) 6:57. doi: 10.1186/s13550-016-0212-9

17. Bennink RJ, Tulchinsky M, de Graaf W, Kadry Z, van Gulik TM. Liver function testing with nuclear medicine techniques is coming of age. *Semin Nucl Med*. (2012) 42:124–7. doi: 10.1053/j.semnuclmed.2011.10.003

18. Hoefs JC, Wang F, Kanel G, Braunstein P. The liver-spleen scan as a quantitative liver function test: correlation with liver severity at peritoneoscopy. *Hepatology*. (1995) 22:1113–21. doi: 10.1002/hep.1840220415

19. Mariani G, Bruselli L, Kuwert T, Kim EE, Flotats A, Israel O, et al. A review on the clinical uses of SPECT/CT. *Eur J Nucl Med Mol Imaging*. (2010) 37:1959–85. doi: 10.1007/s00259-010-1390-8

20. Buck AK, Nekolla S, Ziegler S, Beer A, Krause BJ, Herrmann K, et al. Spect/Ct. *J Nucl Med*. (2008) 49:1305–19. doi: 10.2967/jnumed.107.050195

21. Bybel B, Brunken RC, DiFilippo FP, Neumann DR, Wu G, Cerqueira MD. SPECT/CT imaging: clinical utility of an emerging technology. *Radiographics*. (2008) 28:1097–13. doi: 10.1148/rg.284075203

22. Garg V, Garg H, Khan A, Trehanpati N, Kumar A, Sharma BC, et al. Granulocyte Colony–stimulating factor mobilizes CD34+ cells and improves survival of patients with acute-on-chronic liver failure. *Gastroenterology*. (2012) 142:505–512.e1. doi: 10.1053/j.gastro.2011.11.027

23. Assy N, Minuk GY. Liver regeneration: methods for monitoring and their applications. *J Hepatol*. (1997) 26:945–2. doi: 10.1016/S0168-8278(97)80266-8

24. Singh V, Sharma A, Narasimhan L, Bhalla A, Sharma N, Sharma R. Granulocyte Colony-stimulating factor in severe alcoholic hepatitis: a randomized pilot study. *Am J Gastroenterol*. (2014) 109:1417–23. doi: 10.1038/ajg.2014.154

25. Verma N, Kaur A, Sharma R, Bhalla A, Sharma N, de A, et al. Outcomes after multiple courses of granulocyte colony-stimulating factor and growth hormone in decompensated cirrhosis: a randomized trial. *Hepatology*. (2018) 68:1559–73. doi: 10.1002/hep.29763

26. De A, Kumari S, Singh A, et al. Multiple cycles of granulocyte Colony-stimulating factor increase survival times of patients with decompensated cirrhosis in a randomized trial. *Clin Gastroenterol Hepatol Off Clin Pract J Am Gastroenterol Assoc*. (2020) 19:375–383.e5. doi: 10.1016/j.cgh.2020.02.022

27. Matesan MM, Bowen SR, Chapman TR, Miyaoka RS, Velez JW, Wanner MF, et al. Assessment of functional liver reserve: old and new in 99mTc-sulfur colloid scintigraphy. *Nucl Med Commun*. (2017) 38:577–6. doi: 10.1097/MNM.0000000000000695

28. Garcea G, Ong SL, Maddern GJ. Predicting liver failure following major hepatectomy. *Dig Liver Dis*. (2009) 41:798–6. doi: 10.1016/j.dld.2009.01.015

29. Bowen SR, Saini J, Chapman TR, Miyaoka RS, Kinahan PE, Sandison GA, et al. Differential hepatic avoidance radiation therapy: proof of concept in hepatocellular carcinoma patients. *Radiother Oncol J Eur Soc Ther Radiol Oncol*. (2015) 115:203–0. doi: 10.1016/j.radonc.2015.04.011

30. Deotare U, Al-Dawsari G, Couban S, Lipton JH. G-CSF-primed bone marrow as a source of stem cells for allografting: revisiting the concept. *Bone Marrow Transplant*. (2015) 50:1150–6. doi: 10.1038/bmt.2015.80

31. Tay J, Levesque J-P, Winkler IG. Cellular players of hematopoietic stem cell mobilization in the bone marrow niche. *Int J Hematol*. (2017) 105:129–0. doi: 10.1007/s12185-016-2162-4

32. Takano H, Ueda K, Hasegawa H, Komuro I. G-CSF therapy for acute myocardial infarction. *Trends Pharmacol Sci*. (2007) 28:512–7. doi: 10.1016/j.tips.2007.09.002

33. Kawasaki S, Sugiyama Y, Iga T, Hanano M, Sanjo K, Beppu T, et al. Pharmacokinetic study on the hepatic uptake of indocyanine green in cirrhotic patients. *Am J Gastroenterol*. (1985) 80:801–6.

34. Skak C, Keiding S. Methodological problems in the use of indocyanine green to estimate hepatic blood flow and ICG clearance in man. *Liver*. (1987) 7:155–2. doi: 10.1111/j.1600-0676.1987.tb00336.x

frontiers | Frontiers in Medicine

TYPE Original Research
PUBLISHED 28 June 2023
DOI 10.3389/fmed.2023.1145351

OPEN ACCESS

EDITED BY
Greta Mok,
University of Macau, China

REVIEWED BY
Hamid Sabet,
Massachusetts General Hospital and Harvard Medical School, United States
Glenn Wells,
University of Ottawa Heart Institute, Canada

*CORRESPONDENCE
Tianyu Ma
✉ maty@tsinghua.edu.cn

†These authors have contributed equally to this work

RECEIVED 16 January 2023
ACCEPTED 02 June 2023
PUBLISHED 28 June 2023

CITATION
Wang R, Zhang D, Hu Y, Lyu Z and Ma T (2023) High-sensitivity cardiac SPECT system design with collimator-less interspaced mosaic-patterned scintillators.
Front. Med. 10:1145351.
doi: 10.3389/fmed.2023.1145351

High-sensitivity cardiac SPECT system design with collimator-less interspaced mosaic-patterned scintillators

Rui Wang[1,2,3†], Debin Zhang[1,2,3†], Yifan Hu[1,2,3†], Zhenlei Lyu[1,2,3] and Tianyu Ma[1,2,3*]

[1]Department of Engineering Physics, Tsinghua University, Beijing, China, [2]Key Laboratory of Particle and Radiation Imaging, Ministry of Education (Tsinghua University), Beijing, China, [3]Institute for Precision Medicine, Tsinghua University, Beijing, China

Purpose: Single-photon emission computed tomography (SPECT) is an important tool for myocardial perfusion imaging (MPI). Mechanical collimators cause the resolution-sensitivity trade-off in the existing cardiac SPECT systems, which hinders fast cardiac scan capability. In this work, we propose a novel collimator-less cardiac SPECT system with interspaced mosaic-patterned scintillators, aiming to significantly improve sensitivity and reduce scan time without trading-off image resolution.

Methods: We propose to assemble a collimator-less cardiac SPECT with 7 mosaic-patterned detector modules forming a half-ring geometry. The detector module consists of 10 blocks, each of which is assembled with 768 sparsely distributed scintillators with a size of 1.68 mm × 1.68 mm × 20 mm, forming a mosaic pattern in the trans-axial direction. Each scintillator bar contains 5 GAGG(Ce) scintillators and 5 optical-guide elements, forming a mosaic pattern in the axial direction. In the Monte Carlo simulations, the in-plane resolution and axial resolution are evaluated using a hot-rod phantom and 5 disk phantoms, respectively. We simulate a cardiac phantom that is placed in a water-filled cylinder and evaluate the image performance with different data acquisition time. We perform image reconstruction with the expectation–maximization algorithm using system matrices derived from the simulation of a uniform cylindrical source filling the field-of-view (FOV). Besides, a 2-D prototype system is designed to demonstrate the feasibility of the collimator-less imaging concept.

Results: In the simulation system, the sensitivity is 16.31%±8.85% in a 180 mm (Φ)×100 mm (L) FOV. The 6-mm rods in the hot rod phantom and the 5-mm disks in the disk phantom are clearly separable. Satisfactory MPI image quality is achieved in the cardiac phantom study with an acquisition time of 30 s. In prototype experiments, the point sources with an 8 mm center-to-center distance are clearly separable at different positions across the FOV.

Conclusion: The study reveals a promising approach to high-sensitivity SPECT imaging without a heavy-metal collimator. In cardiac imaging, this approach opens the way to a very fast cardiac scan with good resolution. Further works are ongoing to build a practical 3-D imaging system based on the existing design.

KEYWORDS

myocardial perfusion imaging (MPI), single-photon emission computed tomography (SPECT), collimator, system design, mosaic pattern

1. Introduction

Coronary artery disease (CAD) is the third leading cause of mortality worldwide associated with 17.8 million deaths annually (1). Myocardial perfusion imaging (MPI) is one of the most frequently used non-invasive diagnostic methods for assessing coronary blood flow. MPI identifies regional abnormalities in coronary artery blood flow and determines the physiological relevance to myocardial function and viability. Single-photon emission computerized tomography (SPECT) is the most commonly used imaging technique for MPI diagnosis (2). The typical imaging protocol involves intravenous injection of a radioactive blood flow marker (i.e., ^{99m}Tc-sestamibi, ^{201}Tl-chloride, or ^{99m}Tc-tetrofosmin), tomographic data acquisition under stress and rest conditions, and volumetric/regional myocardial uptake analysis (3, 4).

Cardiac SPECT imaging performance has been rapidly improving over the last 10 years. With a conventional dual-head SPECT scanner, the detection efficiency is around ~130 cps/Mbq and the image resolution is ~15.3 mm (FWHM) without the resolution recovery techniques according to the National Electrical Manufactures Association NU-12001 protocol, where the standard orbit radius for dual-head SPECT is 15 cm (5, 6). The typical injected dose is 15–30 mCi for ^{99m}Tc-sestamibi, a most widely used tracer in MPI imaging (7). The acquisition time is around 15 min with dual-head cameras for nearly all the imaging protocols. With the introduction of new detector technology, optimized collimator, and system design dedicated for imaging the heart region, improved performance has been successfully achieved in terms of reduced scan time, lower radiation dose, and higher imaging resolution. Representative systems include the NM 530c® SPECT(General Electric) and D-SPECT® (Spectrum Dynamics). Both systems utilize the new cadmium zinc telluride (CZT) detectors to achieve better energy resolution (~6%@140 keV) and intrinsic spatial resolution (2.5 mm) (8–11). A new diverging–converging (SMARTZOOM) collimator in IQ·SPECT® (Siemens) is developed that increases the photon sensitivity (6, 12, 13). Other dedicated system configurations optimized for cardiac imaging are also proposed, such as Cardius® 3XPO system (Digirad) and CardiArc® scanner. Cardius® system employs a cardio-centric orbit instead of a body-centered orbit with a compact triple-headed geometry moving around a sitting patient. In this case, the scanners are placed close enough to the chest for image quality enhancement (14). CardiArc® scanner applies a stationary curved scanner head and a unique curved lead sheet with a series of slits rotating back and forth during data acquisition (14, 15). Other dedicated cardiac SPECT systems developed in research labs are also reported (16–23), and some are commercially available (24, 25). Besides, the coded-aperture collimator has been developed for small animal imaging, which can be regarded as a highly multiplexed pinhole collimator achieving higher sensitivity while maintaining good image resolution (26). However, the performance of coded-aperture SPECT is still limited by the resolution-sensitivity trade-off. In Table 1, we summarize the performance of representative dedicated cardiac SPECT systems in comparison with conventional general-purpose systems. In general, dedicated cardiac SPECT systems achieve ~0.03–0.1% of sensitivity and ~6–10 mm of image resolution with an acquisition time of 4.5 to 10 min (5, 6, 15, 27, 28).

Fast scanning is critical for cardiac imaging. However, existing cardiac SPECT scanners require a certain mechanical collimator to form projection, which causes substantial photon loss and tempers sensitivity. Compared to the conventional parallel-hole collimator, although focusing collimators such as multi-pinhole, slit-slat, or cardiac fan-beam collimators effectively improves the resolution-sensitivity trade-off in the heart FOV, the inevitably dramatic photon loss on the mechanical collimators still lead to an overall low sensitivity for the imaging system and strongly limit the fast imaging capability.

Compton camera is one collimator-less imaging method that can improve system sensitivity significantly. Compton-camera has been used in small animal imaging studies with millimeter-level resolution (29–31). However, it has not been applied for cardiac imaging in the human body due to the limited position resolution for far-field imaging. Also, the Compton camera is not suitable for low-energy (<200 keV) gamma source imaging (32).

Recently, our lab has proposed a novel collimator-less gamma camera design using a metal-free 3-D position-sensitive scintillator detector. With the interspaced mosaic-patterned scintillators, one scintillator is naturally collimated by other scintillators, and the detector response is sensitive to the directional position of the incoming gamma ray, providing sufficient information for radiation source imaging in a 4π field-of-view (FOV). We have achieved fast directional gamma-ray imaging with a high-sensitivity portable collimator-less gamma-camera design for nuclear security applications (33). Besides, we have also developed a new mosaic-patterned gamma camera embedding scintillators and heavy metal elements, achieving better imaging performance for middle- and high-energy sources (34).

In this work, we aim to improve the sensitivity of cardiac SPECT imaging to a new level by extending the collimator-less gamma imaging technique from 2-D directional imaging to 3-D tomographic SPECT imaging. We propose to assemble a ring-shaped system with multiple mosaic patterned, uncollimated scintillator blocks that allow a flexible system design. We perform Monte Carlo simulations to evaluate the resolution and sensitivity performance and investigate the cardiac imaging feasibility with an anthropomorphic phantom. We test the imaging feasibility with a 2-D experimental prototype.

TABLE 1 System performance of the dedicated cardiac SPECT systems as compared with the conventional dual-head system.

Name	Conventional	D-SPECT	NM 530c	IQ-SPECT	Cardius
Detector	NaI/PMT	CZT	CZT	Dual NaI/PMT	pixelated CsI(Tl) with photodiodes
Collimator	Parallel-hole	Parallel-hole	Multi-pinhole	SMARTZOOM	Cardiac fan-beam
Acquisition time (min)	16	6	10	4.5	7.5
Sensitivity (Cps/MBq)	130	850	460	390	324
Resolution (mm)	15.3	8.6	6.7	15	9.2

2. Materials and methods

2.1. Collimator-less imaging concept and simulated cardiac SPECT system

2.1.1. Collimator-less imaging concept

The collimator-less imaging concept is shown in Figure 1A. Detectors 2 and 3 are separately placed between the source and detector 1. In this way, the photon absorption on detectors 2 and 3 naturally forms photon collimation for detector 1. Besides, the absorbed photons on detectors 2 and 3 are also contributable to the image formation process, leading to significant sensitivity improvement compared to conventional mechanical collimation.

Figure 1B shows the cross-section of a complete collimator-less detector block. We propose to place multiple individual GAGG(Ce) scintillators inside the block to form a mosaic pattern in the trans-axial plane. Compared to our previously used mosaic-patterned detector for a planar gamma imager (33), in this work, we use a sparser mosaic pattern to spread the incoming gamma photons over more detector elements. We also choose a circular-shaped detector block instead of a square-shaped block in the SPECT imaging system to reduce gaps between detectors. As shown in Figure 1C, when a gamma source is placed at different positions, the accumulated photon count distribution (i.e., the projection) is dependent on the source position.

2.1.2. System design

Figure 2A illustrates a designed collimator-less cardiac SPECT system. We place 7 detector modules surrounding the patient's body to form a half-ring geometry. As shown in Figure 2B, the intended FOV to cover the heart region is 180 mm (Φ) × 100 mm (L), which is suitable for the majority of patients under a survey of cardiac and thoracic anatomy of cardiac patients (20). The system is designed to accommodate the body contour, which is mimicked by an elliptical region with the size of 400 mm (long axis) × 300 mm(short axis) in the cross-sectional plane. The 7 detector modules are evenly spaced from the 60° right anterior angular position to the 30° left posterior position. Their geometrical centers are on a 600-mm-diameter circle.

2.1.3. Detector module design

Figure 3 shows the geometrical setup of a detector module. Each module contains 10 detector blocks that are stacked axially. The size of each detector block is 149.52 mm (Φ) × 20 mm (L). Each cylindrical detector block consists of 768 GAGG(Ce) scintillator bars with a size of 1.68 mm × 1.68 mm × 20 mm. In each block, the scintillator bars form a mosaic pattern as shown in the trans-axial view of Figure 3.

We propose to assemble a mosaic-patterned scintillator bar by interlacing five 1.68 mm × 1.68 mm × 2 mm GAGG(Ce) scintillator and five optical-guide segments (k-9 glass, Epic Crystal, China) as shown in Figure 4, where each scintillator is glued to the adjacent k-9 glass segment. The linear attenuation coefficient of the k-9 glass for 140 keV

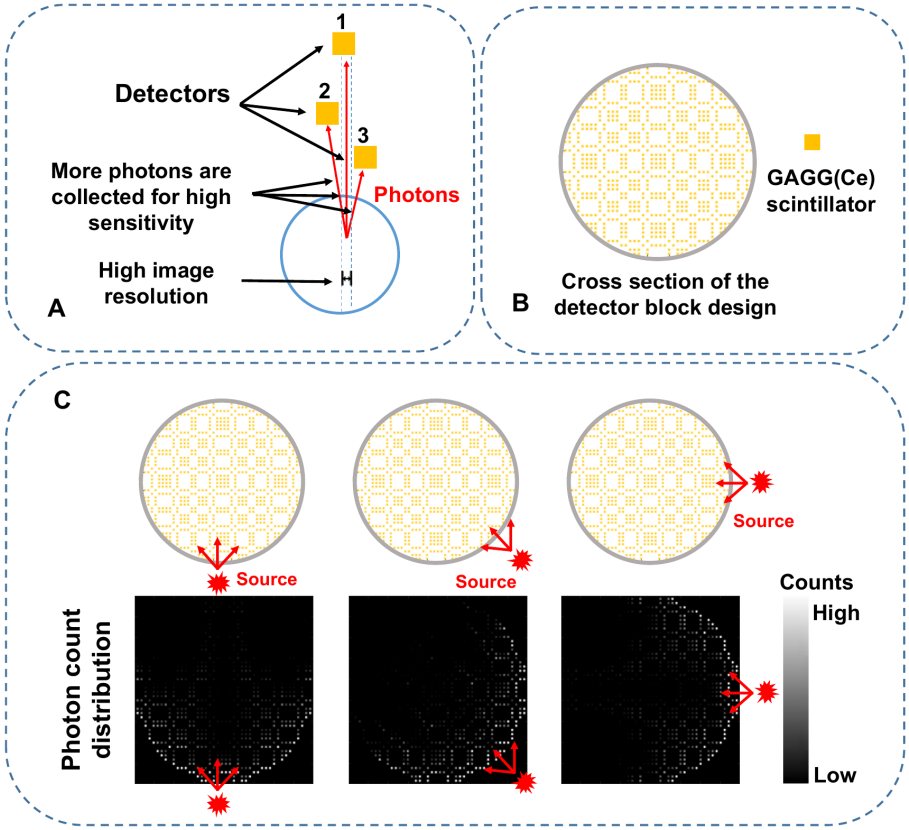

FIGURE 1
(A) Schematic diagram of the proposed self-collimation concept with three individual detectors. The red lines indicate gamma photons detected by the specific detector in the blue dashed region. **(B)** 2-D mosaic scintillation design in the trans-axial plane. **(C)** Schematic diagram of the photon counts distribution. The red-arrow lines represent the paths of the incoming photons from three different directions.

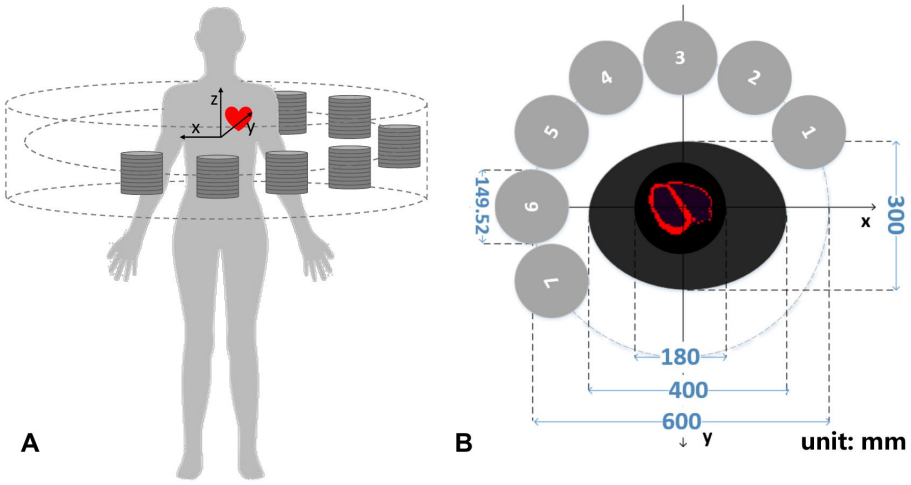

FIGURE 2
(A) 3-D schematic diagram and **(B)** transverse cross-section of the cardiac imager system (unit: mm).

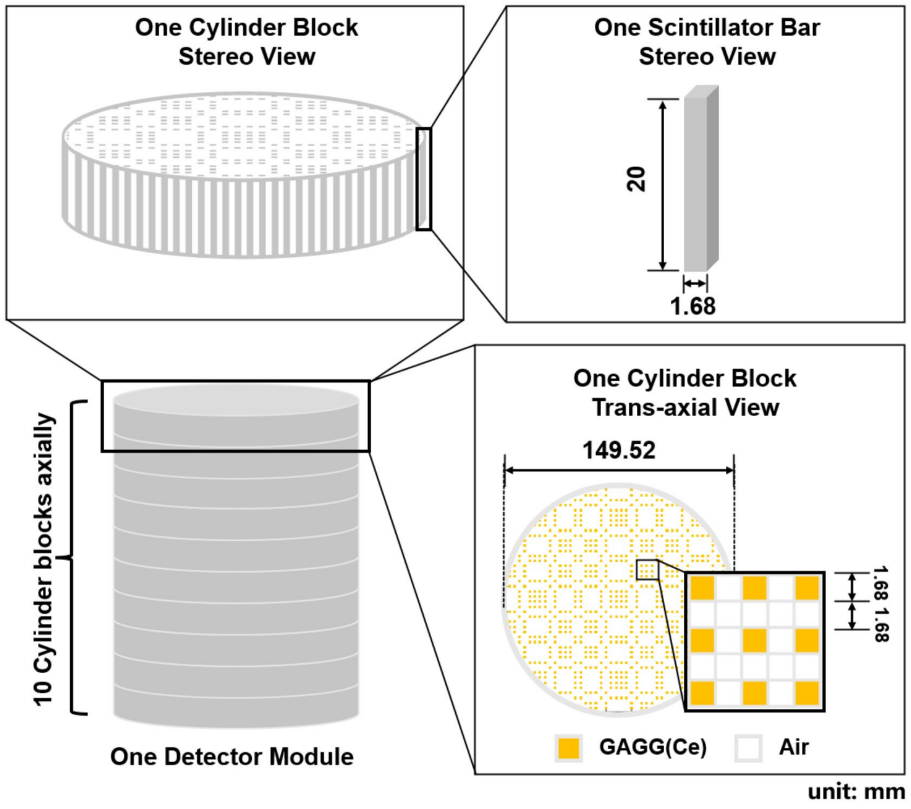

FIGURE 3
Stereo view and trans-axial view of one detector module (unit: mm).

photons is 0.399 cm^{-1}, which is significantly lower than that of the GAGG(Ce) scintillator (4.746 cm^{-1}). The refraction indexes for the k-9 glass and the GAGG(Ce) scintillator are 1.5 and 1.9 respectively, which are close to each other. Such a design both allows an interspaced, mosaic-patterned spatial structure of the GAGG(Ce) scintillators and enables efficient optical-photon transportation for each scintillator to the two silicon photo-multipliers (SiPM). The entire detector block contains 38,400 spatially separated scintillator segments. In the cross-sectional plane, each scintillator bar is wrapped with total-reflective materials. The space between each scintillator bar is simply filled with air. Therefore, the electric signal readout is independently operated for each scintillator bar with two SiPMs on both ends.

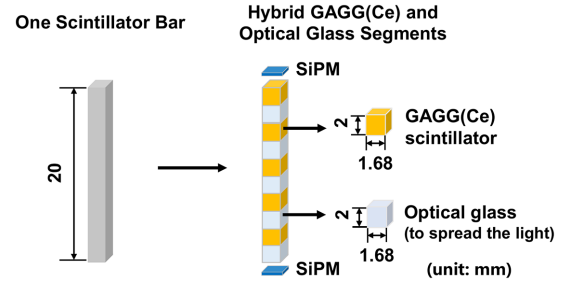

FIGURE 4
Schematic diagram of hybrid GAGG(Ce) and optical glass segments forming the mosaic pattern in the axial direction (unit: mm).

2.1.4. Monte Carlo simulations

We evaluate the system performance through Monte-Carlo simulations with the GATE v8.0 package (35). We model the half-ring cardiac imaging system in Sections 2.1.2 and 2.1.3 and simulate the transportation and detection process for 140 keV gamma photons to mimic ^{99m}Tc labeled tracers. We set an intrinsic energy resolution of 20% at 140 keV for the GAGG(Ce) scintillators based on our previous experimental measurement (33) and acquire the data in a 112–168 keV energy window. In the simulations, the position of each event is determined by the scintillator element within which the maximum deposited energy is recorded.

We evaluate the imaging performance using three types of phantoms, including a hot-rod phantom to test the in-plane resolution performance, 5 disk phantoms to test the axial resolution performance, and a 3-D cardiac phantom to mimic the MPI imaging scenario. In cardiac imaging simulations, we place a water-filled cylindrical attenuator ($\Phi = 200$ mm, H = 100 mm) in the FOV to account for the photon scattering and attenuation effects during projection data acquisition. No water-filled attenuator is applied in the hot-rod and disk phantom studies. We perform multiple rounds of simulations for both hot-rod and cardiac phantoms with different activity and acquisition time combinations during the image formation process.

The projection data are defined by concatenating the record counts in the detector elements of all the seven cylinder-shaped scintillator blocks into a single vector.

$$Y_{simu} = \left[y_{1,1}, y_{1,2}, \ldots, y_{1,n}, y_{2,1}, y_{2,2}, \ldots, y_{2,n}, \ldots, y_{m,1}, y_{m,2} \ldots, y_{m,n} \right]^T, \quad (1)$$

Where $y_{k,l}$ is the number of events acquired by detector element l on detector module k. $n = 768$ (in trans-axial plane) $\times$ 50 (in axial direction) denotes the total number of scintillator bars in one detector module. $m = 7$ denotes the total number of detector modules.

We perform long-time Monte Carlo simulations to derive system matrices for the three phantom studies (36). A uniform ^{99m}Tc cylindrical source (180 mm (Φ) $\times$ 100 mm (L)) filling the FOV is simulated for all three phantom studies. In the cardiac phantom study, we place the water-filled cylindrical attenuator ($\Phi = 200$ mm, H = 100 mm) in the FOV to account for the attenuation and scattering effect. In each study, we acquire around 2×10^{12} events so that the impact of noise is minimal. Each recorded list-mode event contains the emission and detection position information during the simulation process. The system matrix $[A_{ij}]$ representing the probability that a photon emitted from jth voxel detected in the ith detector bin is approximated by the total number of recorded events in the ith detector bin and emitted from jth voxel. Table 2 summarizes the geometry parameters, and the counting statistics of the simulated system matrices for three phantom studies.

A hot-rod phantom (Φ = 180 mm, H = 100 mm) with a hot-rod size of 4, 5, 6, 7, 8, and 9 mm is utilized to evaluate the image resolution in the trans-axial plane. There is no background activity in the phantom, and the distances between the hot rods are twice their diameters. A total of 0.45 mCi activity is in the phantom, which is equivalent to 30 mCi tracer injection in the human body multiplied by 1.5% ^{99m}Tc-sestamibi tracer uptake in the myocardium (37). Four imaging time cases are simulated, which are 20 min, 5 min, 1 min, and 20 s, and correspond to a total of 2.26×10^9, 5.66×10^8, 1.13×10^8, 3.77×10^7 events in the projection, respectively. Besides, considering the statistical noise in the Monte-Carlo simulation, we calculate the forward projection as a noise-free case to evaluate the optimal imaging performance. The forward projection is generated by direct multiplication of the system matrix and the 1-D scalar flattened from the 3-D volumetric hot-rod phantom image.

Five disk-shaped phantoms are applied to measure image resolution in the axial plane. Each phantom contains five cylindrical disks of equal size arranged axially at the same interval. The thickness of the cylindrical disk in each phantom is 4, 5, 6, 7, and 8 mm, respectively. The diameter of the cylindrical disk is 120 mm and the interval between two adjacent disks is twice the thickness of the disk for each phantom. We simulate a total of 0.45 mCi activity and 20 min acquisition time for each phantom.

In the 3-D cardiac phantom study, the tracer activity distribution in the myocardium is extracted from the XCAT phantom (38), where the relative uptake activity is 75 in the myocardium, 2 in the blood pool, and 2 in the coronary arteries and veins. Instead of a non-uniform attenuating medium in the XCAT phantom, the water-filled cylindrical attenuator ($\Phi = 200$ mm, H = 100 mm) described before is applied around the cardiac region to simulate photon scattering and attenuation effects. Five imaging cases include the acquisition time of 20 min, 5 min, 1 min, 30 s, and 20 s each with 0.45 mCi tracer uptake in the heart, producing corresponding to a total of 2.26×10^9, 5.66×10^8, 1.13×10^8, 5.66×10^7, 3.77×10^7 events in the projection, respectively. The voxel size of the reconstructed image is 3×3×3 mm^3 for cardiac study, while the voxel size is 2×2×2 mm^3 for hot-rod phantom and disk phantom study.

2.1.5. Reconstruction settings

We perform the image reconstruction with an ordered subset expectation maximization (OSEM) algorithm (39).

$$f_j^{(k,q)} = \frac{f_j^{(k,q-1)}}{\sum_{i \in S_q} A_{ij}} \sum_{i \in S_q} A_{ij} \frac{y_i}{\sum_l A_{il} f_l^{(k,q-1)}}, \quad (2)$$

where f_j denotes the image value in j^{th}pixel, y_i denotes the number of photon counts detected in i^{th} detector bin, q and k are indices of subsets and iterations, respectively. S_q is the q^{th} subset of the projection data. There are a total of 268,800 projection bins, which are grouped into 35 subsets. The algorithm uses parallel processing with the GPU card based on the MATLAB platform, running on a

TABLE 2 Summary of geometry parameters, counting statistics involved in generating the system matrices.

System configuration	FOV dimension	Voxel size	Number of voxels	Number of detector bins	Average recorded events per voxel
hot-rod phantom w/o water-filled attenuator	180 mm (Φ) × 100 mm(H)	2 mm × 2 mm × 2 mm	90×90×50	268,800	4.01×10^6
disk phantom w/o water-filled attenuator	180 mm (Φ) × 100 mm(H)	2 mm × 2 mm × 2 mm	90×90×50	268,800	4.01×10^6
Cardiac phantom w water-filled attenuator	180 mm (Φ) × 100 mm(H)	3 mm × 3 mm × 3 mm	60×60×34	268,800	1.72×10^7

workstation with Intel Xeon Silver 4,110 CPU, 1 TB memory, and an NVIDIA TITAN Xp GPU card with 12 GB GPU memory. Each iteration takes 10 min, 10 min, and 5 min for hot-rod, disk, and cardiac phantom reconstruction.

In all cases, we empirically determine an iteration number that represents an optimal trade-off between resolution and noise. The iteration numbers for the hot-rod, disk, and cardiac phantom study are 50,10, and 50, respectively. We also apply a post-reconstruction Gaussian filter with empirically chosen parameters. Specifically, the Gaussian filter with a kernel size of 7 and FWHM of 2 mm is applied in hot-rod and disk image processing. The Gaussian filter with a kernel size of 7 and FWHM of 7 mm is applied in cardiac image processing.

2.2. Experimental prototype system

2.2.1. Detector design

We perform proof-of-concept experiments with a mosaic-patterned detector block developed in our lab (33). The detector setup is different from the system design in Section 2.1. The aim of following experiments is to demonstrate the feasibility of performing collimator-less SPECT imaging, rather than validating the predicted performance in simulations.

The detector block is shown in Figure 5. The size of the detector block is 67.5 mm × 67.5 mm × 20 mm. There are 128 spatially separated GAGG(Ce) scintillator (Epic Crystal, China) bars embedded in the plastic framework in one detector block. The size of each GAGG(Ce) scintillator bar is 2.1 mm × 2.1 mm × 20.0 mm, and the distance between two adjacent scintillator bars is 4.2 mm. Each scintillator is wrapped with a 0.15 mm thickness $BaSO_4$ reflector (Epic Crystal, China). The mosaic-patterned scintillator block is optically coupled to two 16 × 16 SiPM boards (Onsemi, FJ30035) at both ends. Each SiPM board is connected to one front-end board with customized ASIC chips (40) that produce analog signals of 2-D position(X/Y) and energy(E) with in-chip anger-logic resistor networks. On the back of a single SiPM board, four self-developed ASIC chips are positioned, each generating one set of X, Y, and E signals for every recorded event. Subsequently, the X, Y, and E signals are digitized using A/D converters (AD9637, 12-bit, and 80 MHz sampling rates) located on the digital processing board(DPB) for data analysis.

2.2.2. System configuration and gantry

As shown in Figure 6, We rotate a planar phantom about the central axis for 13 steps, which is equivalent to placing the detector at the 13 positions surrounding the object. In this way, we virtually define a half-ring imaging system with 13 detector blocks surrounding the 2-D FOV.

2.2.3. Data acquisition and reconstruction settings

In the 2-D experimental case, the projection vector is also expressed as Eq. (1), where the number of detector modules is $m = 13$ and the total number of scintillators in one detector module is $n = 128$. The experimental system response matrix is $A_{\text{exp}} \in \mathbb{R}_{N\times M}$, where $M = 10^4$ is the total number of voxels in the FOV, and $N = 128 \times 13$ is the total number of detector bins in the virtual system.

We use a ~ 9.7 mCi ^{99m}Tc point source with a diameter of 0.69 mm to measure the system matrix of the single detector module. As shown in Figure 7, we place the point source on a holder that is fixed to a translation stage. We measure a single-detector system matrix with a FOV size of 100 mm × 100 mm and a voxel size setting of 3 mm × 3 mm. There are 35 × 35 measurement positions during the experiment. Around 1.4 M events are collected with 10s acquisition in each measurement position. The FOV of the single-detector system matrix is expanded from 35 × 35 grids (x = −51: 3: 51 mm, y = −51: 3: 51 mm) to 103 × 103 grids (x = −51: 1: 51 mm, y = −51: 1: 51 mm) by cubic spline interpolation. Then, we calculate the system matrix for the half-ring-system from the single-detector system matrix according to rotational geometry symmetry.

To evaluate the imaging performance of the experimental prototype, we conduct a point-source-based experiment. The diameter of the point source is 0.69 mm. To mimic the 13-detector system in Figure 6 based on one detector block, we calculate the relative location of the source and each detector block, and place the point source at these locations to acquire projection data, respectively. Then, all 13 projection data vectors are concatenated to form the projection of the half-ring system for one point source in the FOV.

To evaluate the system resolution when imaging multiple point sources at a certain distance, we place a point source at different positions and acquired a list-mode dataset at each position. We precisely know the distance between each position by moving the point source from one position to the other using the translational stage. We generate the projection data by binning the list-mode events at all the individual positions into a single projection. This generated projection is equivalent to the one measured with multiple point sources at different positions. We evaluate two cases, a two-point-source phantom with an 8-mm center-to-center distance and a 2-by-2 point source array with an 8-mm center-to-center distance. In the

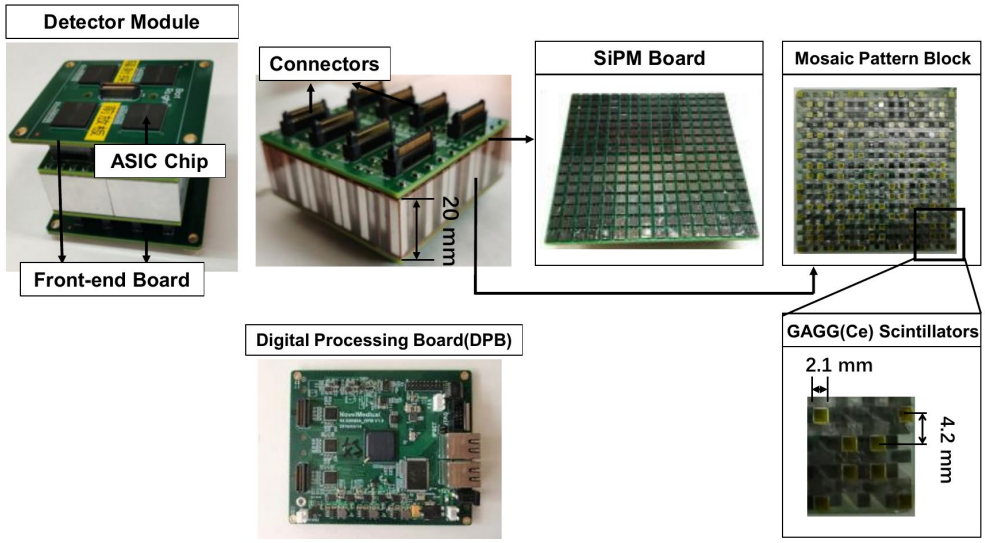

FIGURE 5
Experimental detector modules.

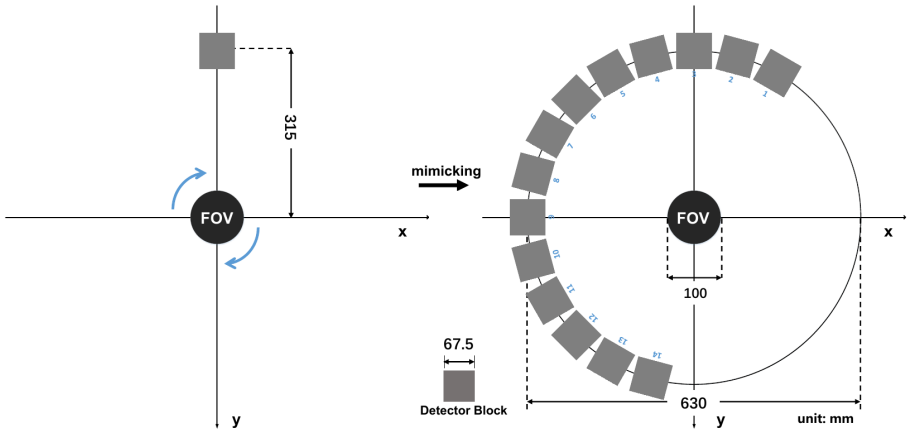

FIGURE 6
Transverse cross-section of the experimental prototype imager system (unit: mm).

two-point source experiment, we evaluate three imaging cases with equivalent acquisition times of 240 s, 24 s, and 2.4 s using 0.45 mCi total activity of point sources. In the 2-by-2 point source experiment, the total acquisition time for all the point sources is around 30 min.

We apply the maximum likelihood expectation maximization (MLEM) algorithm, i.e., using one subset in Eq. (2) for image reconstruction in the experiments. Similar to the simulation studies, early-stop iterations and the post-reconstruction Gaussian filter are empirically chosen as well.

3. Results

3.1. Simulated cardiac SPECT system

The sensitivity was determined as the number of recorded events detected from the detector bins divided by the number of emitted photons in each voxel during the Monte-Carlo simulation. Figure 8 shows the sensitivity map of the simulated cardiac SPECT in three axial slices. The average measured sensitivity in the whole FOV is 16.31 ± 8.85%. There is no big difference between the sensitivity maps at different axial positions.

The energy spectra of ^{99m}Tc from the simulation is shown in Figure 9. From the results, the characteristic photo-peak is identified at the correct position clearly without the water-filled cylindrical attenuator in the FOV, while the photo-peak shifts to the left due to the scatters with the attenuator.

Figure 10 demonstrates the in-plane resolution performance. With an acquisition time from 20 min down to 1 min, the hot-rod image has similar quality compared with the noise-free case, with the hot rod sections from 6 mm to 9 mm all separable. With 20 s acquisition, the reconstructed image shows visible distortion, however, the 6-mm hot rods are still visualized. In Figure 11, The disk phantom with 5-mm disk thickness and 10-mm disk separation is clearly separable.

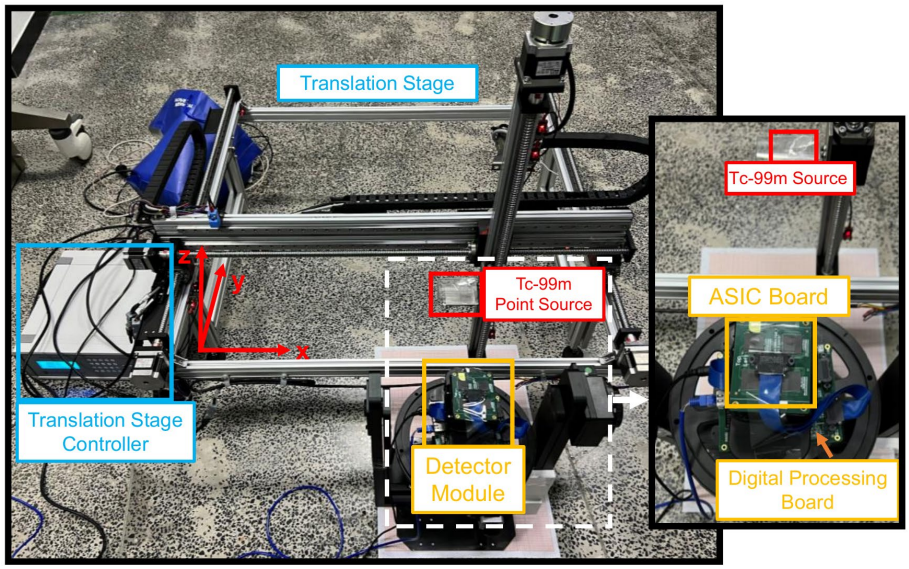

FIGURE 7
The experimental platform.

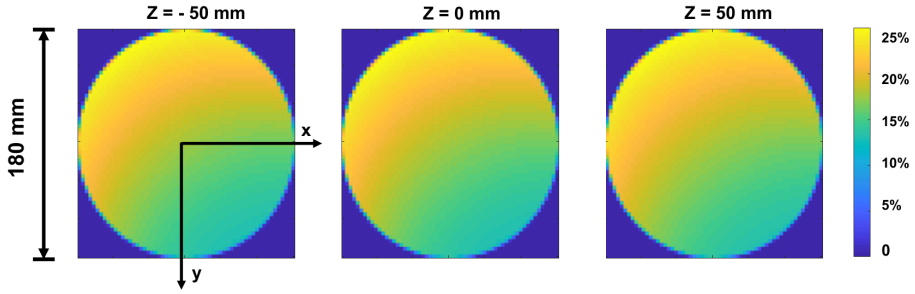

FIGURE 8
Sensitivity map of top-slice, medium-slice, and bottom-slice in the FOV (Φ = 180 mm, H=100 mm).

In the cardiac phantom study (Figure 12), the images with 20 min and 5 min acquisition time show clear contour and evenly distributed activity in the left ventricular myocardial region. When the acquisition time is shortened to 1 min and 30 s, slight image quality degradation is observed, but the radioactivity distribution in the left ventricular myocardial region is still satisfactorily reconstructed. The image with 20 s acquisition shows noticeable activity discontinuity in the myocardium.

3.2. Experimental prototype system

The experimentally measured energy spectra of ^{99m}Tc is shown in Figure 13. The characteristic photo-peak is identified at the correct energy position clearly.

Figure 14 shows the reconstructed images of two point sources aligned in vertical (Figure 14A) and horizontal (Figure 14B) directions and placed at different positions in the FOV. The center-to-center distance of the point sources is 8 mm, and the diameter of each source is 0.68 mm. With an acquisition time of 240 s and 24 s, the point sources are separable at all the positions tested. With 2.4 s acquisition time, the two-point sources are undistinguishable at several positions.

Figure 15 shows the reconstructed images of a 2-by-2 point source array placed at different positions in the FOV. The center-to-center distance is 8 mm. In all the cases, the point sources are clearly separable.

4. Discussion

In this study, we propose a novel cardiac SPECT imaging system design with only scintillators and without heavy metal materials. The key innovation is the mosaic-patterned scintillator assembly that allows one scintillator to be naturally collimated by other scintillators in front of it, enabling the determination of a photon's pathway without sacrificing other photons as a mechanically collimated SPECT usually does. Therefore, it is possible to significantly improve the imaging speed for cardiac SPECT imaging.

Current work and two previous studies (33, 41) from our lab are under the same "self-collimation" concept but with different objectives and system setups. The main contribution of this work

— different from the work in (33) is that we for the first time demonstrate the feasibility of tomographic imaging using a collimator-less mosaic-patterned scintillator block in this work. In contrast, the study in (33) reports imaging performance in a spherical plane in the far field, which is fundamentally different from tomographic imaging where line integrals through image voxels are involved. This work implements the concept of using scintillators as collimators in a fundamentally different way compared with the approach described in (41). Here, a collimator-less imaging system is used, and the 3D photon position information is acquired using dual-end-readout technology for the mosaic-patterned scintillator. In contrast, the detectors in (41) are assembled as multiple separate layers, with photon position information read out using a single SiPM array on the back side and a metal layer placed between the object and the first detector layer. As a result, there are significant differences in imaging system design and performance between the two approaches.

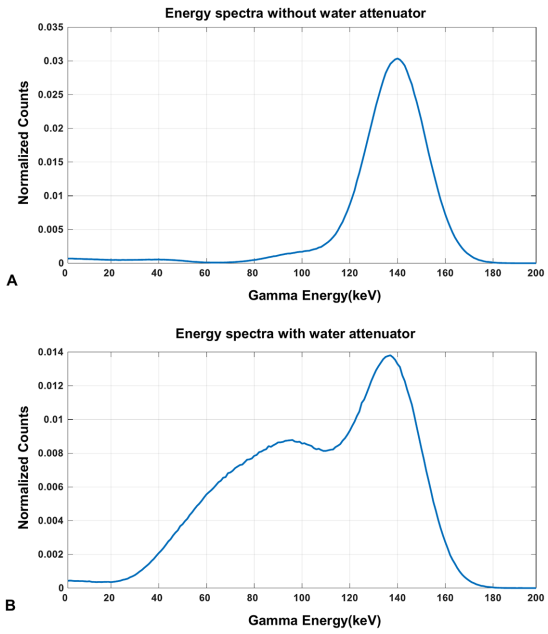

FIGURE 9
The energy spectra of ^{99m}Tc source measured in the simulation **(A)** without the water-filled cylindrical attenuator and **(B)** with the water-filled cylindrical attenuator in the FOV.

We have investigated the feasibility of simulation and proof-of-concept experiments. In simulations, we designed a half-ring cardiac SPECT with 7 mosaic-patterned detector modules and demonstrated that the system offers satisfactory image quality at routine tracer injection dose levels clinically. The image resolution is comparable to state-of-the-art dedicated cardiac SPECT systems. The reported sensitivity in the designed system (16.31% ± 8.85% in a 180 mm (Φ) × 100 mm (L)) is extremely high. However, since the collimation geometry and detection efficiency vary from one scintillator to another in a complicated way, one cannot simply compare the absolute sensitivity to a conventional SPECT with parallel-hole or pinhole collimation. Further research is required to explicitly analyze the image signal-to-noise property of the collimator-less SPECT system. However, the cardiac phantom study in Figure 12 shows reasonably good MPI images acquired in 30 s, which suggests a significant imaging speed improvement with the proposed system. In the experiments, we have successfully acquired artifact-free images of multiple point sources across the FOV. To the best of our knowledge, this may be the first cardiac SPECT image that is generated without a heavy-metal collimator. The experimentally achieved in-plane image resolution performance is comparable with existing dedicated cardiac SPECT scanners.

Our imaging system relies on photons interacting with the scintillator material, potentially producing scattered events across multiple scintillators via Compton scattering. However, our Monte Carlo simulations indicate that the detected Compton-scattering events in our proposed scintillator block are approximately 9.4% in an energy window between 112 keV and 168 keV. Of these events, around 3% result in inter-crystal scatter events, making the impact of scattering events insignificant in our system.

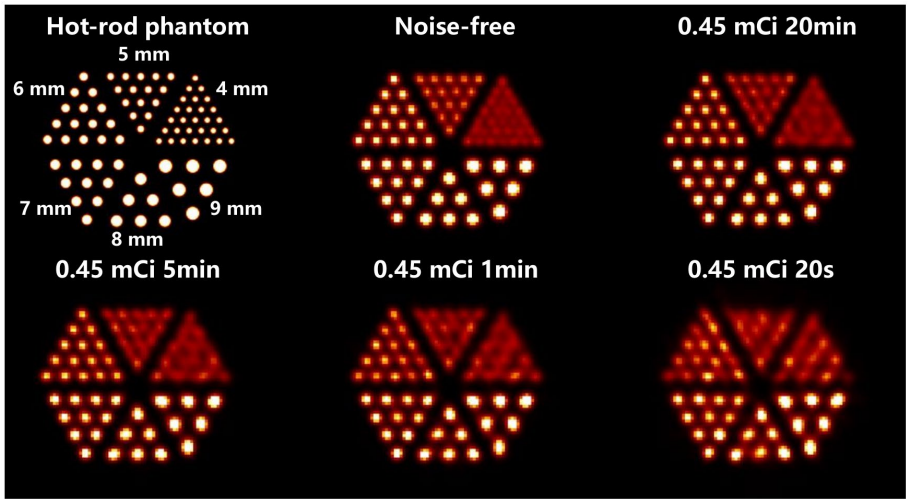

FIGURE 10
Reconstructed images of the hot-rod phantom using OS-EM reconstruction algorithm in different imaging cases.

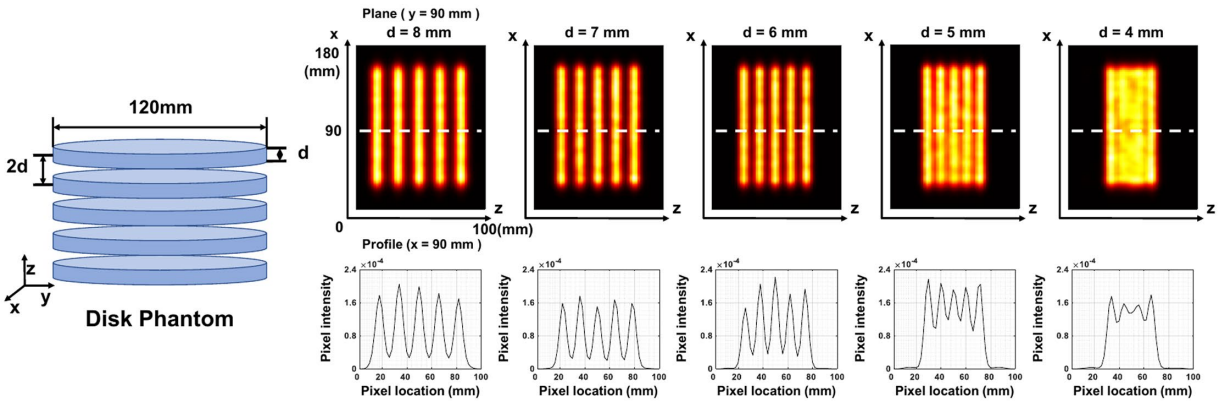

FIGURE 11
Reconstructed images of five disk phantoms with different disk thicknesses. The center of the image is at (90,90,50) mm. The plane image is at y=90 mm, and the corresponding z-profile is at x=90 mm.

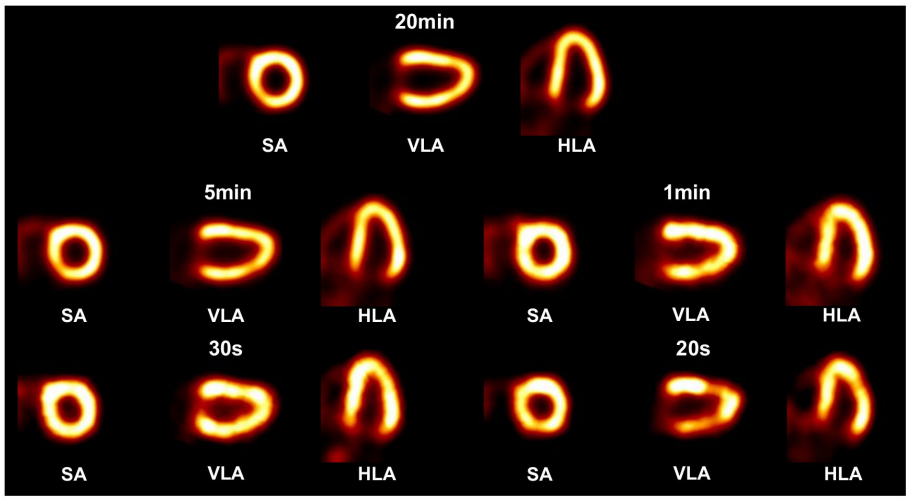

FIGURE 12
Reconstructed images of a 3-D cardiac phantom in short-axis (SA), vertical long-axis (VLA), and horizontal long-axis (HLA) using OS-EM algorithm in different scan time cases.

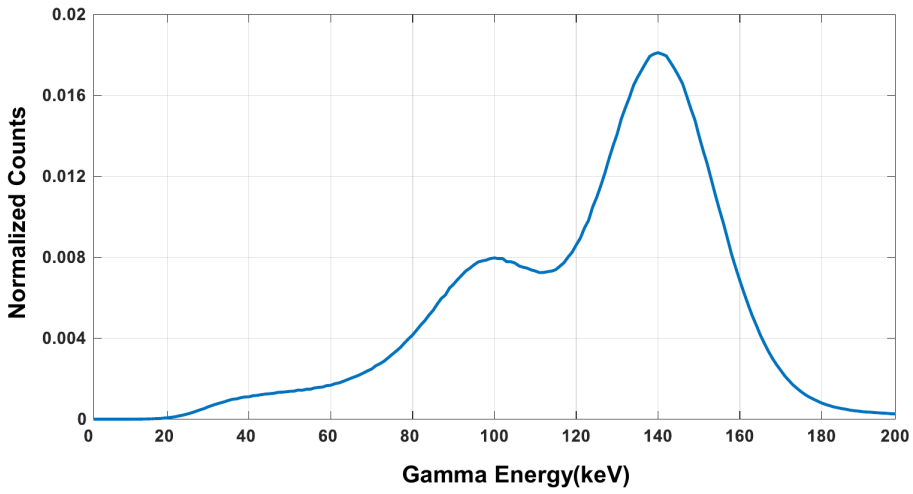

FIGURE 13
Energy spectra of ^{99m}Tc measured in the experiment.

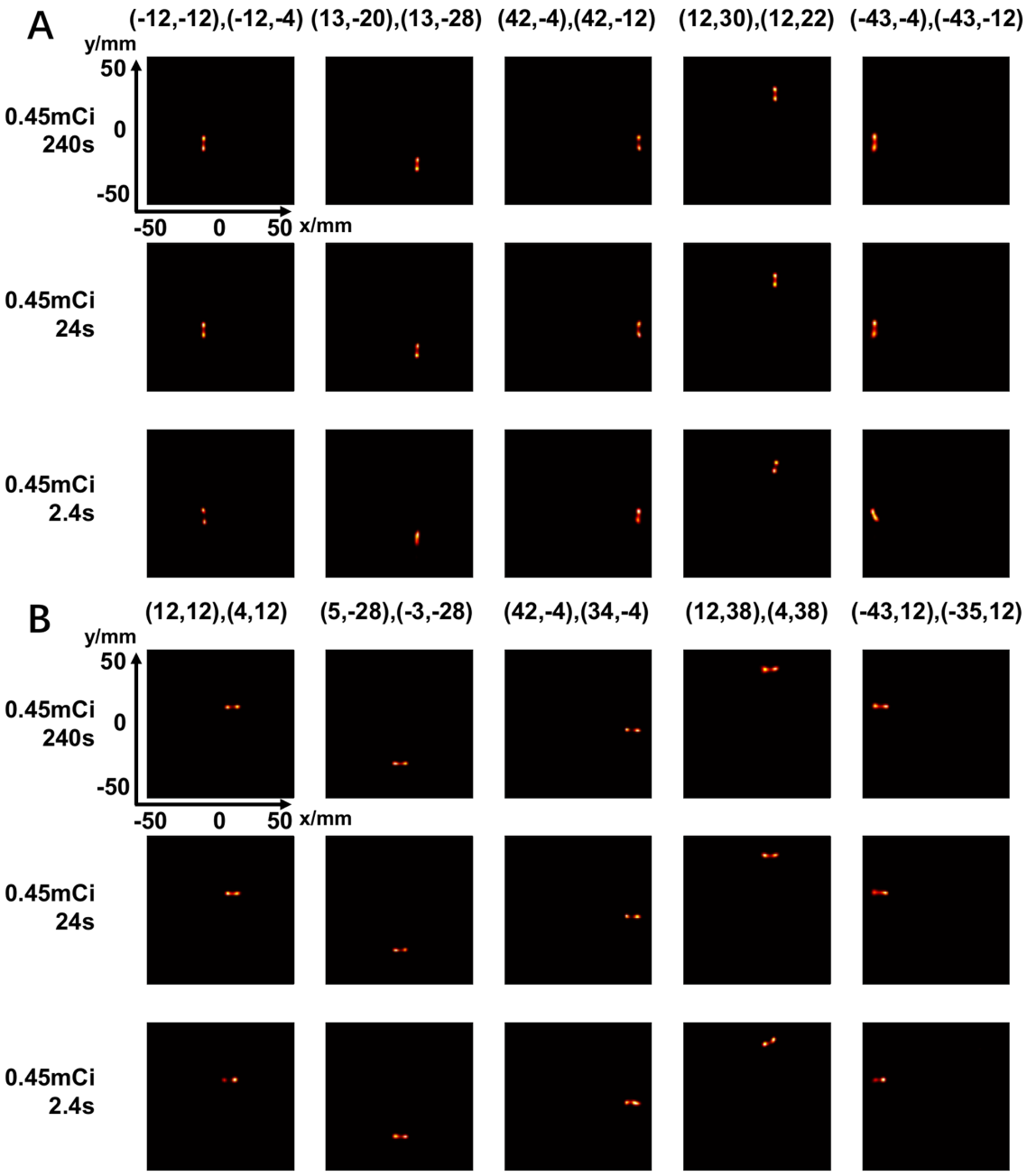

FIGURE 14
Reconstructed images of two-point-source placed at different positions in vertical directions **(A)** and horizontal directions **(B)** under different scan time (240 s, 24 s, 2.4 s) (unit: mm).

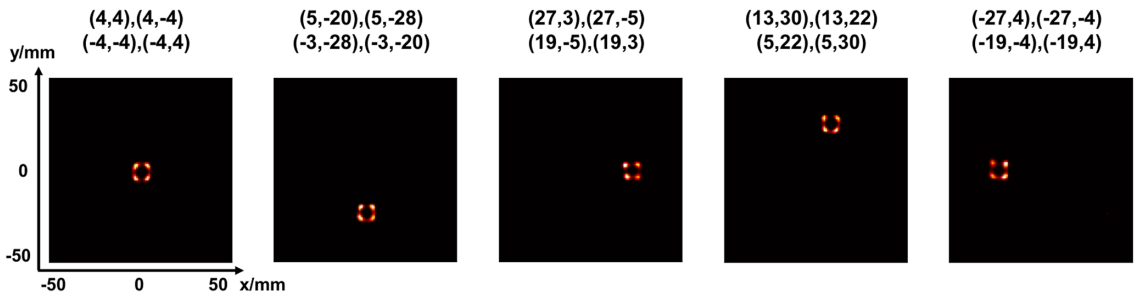

FIGURE 15
Reconstructed images of four-point-source at five positions in the FOV (unit: mm).

This study has several limitations. Firstly, the cardiac phantom study shows that scattering events do not significantly degrade image quality in a uniform water phantom of fixed size. However, we did not consider the impact of non-uniform body attenuation and scattering in our simulations. Scattering can have a more pronounced effect on patients with a large BMI. Secondly, the residual tracer activity out of the FOV (such as liver) is not included as well, which may cause further image quality degradation. Thirdly, our currently available detector only implements a mosaic-patterned design in the trans-axial direction, which differs from the proposed imaging system design. Furthermore, the experiments we conducted were in a planar field of view. Further work is ongoing to assemble a 3-D imaging system that matches the simulation design and investigate the impact of non-uniform body attenuation and scattering in different patient sizes.

5. Conclusion

We propose a novel collimator-less cardiac SPECT system by using a mosaic-patterned scintillator block design that allows detector collimation through other detectors in the front. We propose a half-ring cardiac SPECT design with 7 mosaic-patterned detector modules. The simulation study demonstrates that 6-mm hot rod separation and super high detection efficiency ($16.31 \pm 8.85\%$) are achievable. The prototype experiment demonstrates the feasibility of multi-point-source imaging with an 8-mm point-source separation capability. The proposed cardiac SPECT allows myocardial SPECT scan in less than a minute with a highly flexible and scalable system structure. We conclude that it is possible to achieve high-performance SPECT imaging without a heavy-metal collimator, and our work opens the way to a very fast SPECT MPI scan with reasonable resolution.

Data availability statement

The raw data supporting the conclusions of this article will be made available by the authors, without undue reservation.

Author contributions

RW: methodology, validation, formal analysis, investigation, and writing – original draft. DZ: methodology and formal analysis. YH: methodology and investigation. ZL: project administration. TM: conceptualization, supervision, writing – review and editing, and funding acquisition. All authors contributed to the article and approved the submitted version.

Funding

This work is supported by Beijing Natural Science Foundation (No. Z220010), Tsinghua Precision Medicine Foundation, Tsinghua University Initiative Scientific Research Program, and National Natural Science Foundation of China (No. 81727807). This work uses the computational resources supported by Tsinghua National Laboratory for Information Science and Technology and Tsinghua High-performance Computing Center (THPCC).

Conflict of interest

The authors declare that the research was conducted in the absence of any commercial or financial relationships that could be construed as a potential conflict of interest.

References

1. Brown JC, Gerhardt TE, Kwon E. Risk factors for coronary artery disease In: . *Statpearls*. Treasure Island (FL): StatPearls Publishing Copyright © (2022) StatPearls Publishing LLC

2. Dewey M, Siebes M, Kachelrieß M, Kofoed KF, Maurovich-Horvat P, Nikolaou K, et al. Clinical quantitative cardiac imaging for the assessment of myocardial Ischaemia. *Nat Rev Cardiol* (2020) 17:427–50. doi: 10.1038/s41569-020-0341-8

3. Gibbons RJ. Myocardial perfusion imaging. *Heart* (2000) 83:355–60. doi: 10.1136/heart.83.3.355

4. Henzlova MJ, Cerqueira MD, Mahmarian JJ, Yao S-S. Stress protocols and tracers. *J Nucl Cardiol* (2006) 13:e80–90. doi: 10.1016/j.nuclcard.2006.08.011

5. Imbert L, Poussier S, Franken PR, Songy B, Verger A, Morel O, et al. Compared performance of high-sensitivity cameras dedicated to myocardial perfusion Spect: a comprehensive analysis of phantom and human images. *J Nucl Med* (2012) 53:1897–903. doi: 10.2967/jnumed.112.107417

6. Slomka PJ, Berman DS, Germano G. New cardiac cameras: single-photon emission Ct and pet. *Semin Nucl Med* (2014) 44:232–51. doi: 10.1053/j.semnuclmed.2014.04.003

7. Henzlova MJ, Duvall WL, Einstein AJ, Travin MI, Verberne HJ. Asnc imaging guidelines for Spect nuclear cardiology procedures: stress, protocols, and tracers. *J Nucl Cardiol* (2016) 23:606–39. doi: 10.1007/s12350-015-0387-x

8. Dorbala S, Ananthasubramaniam K, Armstrong IS, Chareonthaitawee P, DePuey EG, Einstein AJ, et al. Single photon emission computed tomography (Spect) myocardial perfusion imaging guidelines: instrumentation, acquisition, processing, and interpretation. *J Nucl Cardiol* (2018) 25:1784–846. doi: 10.1007/s12350-018-1283-y

9. Erlandsson K, Kacperski K, van Gramberg D, Hutton BF. Performance evaluation of D-Spect: a novel Spect system for nuclear cardiology. *Phys Med Biol* (2009) 54:2635–49. doi: 10.1088/0031-9155/54/9/003

10. Hutton BF, Erlandsson K, Thielemans K. Advances in clinical molecular imaging instrumentation. *Clin Transl Imaging* (2018) 6:31–45. doi: 10.1007/s40336-018-0264-0

11. Bocher M, Blevis IM, Tsukerman L, Shrem Y, Kovalski G, Volokh L. A fast cardiac gamma camera with dynamic Spect capabilities: design, system validation and future potential. *Eur J Nucl Med Mol Imaging* (2010) 37:1887–902. doi: 10.1007/s00259-010-1488-z

12. Nakajima K, Okuda K, Momose M, Matsuo S, Kondo C, Sarai M, et al. Iq·Spect technology and its clinical applications using multicenter Normal databases. *Ann Nucl Med* (2017) 31:649–59. doi: 10.1007/s12149-017-1210-3

13. Vija AH, Malmin R, Yahil A, Zeintl J, Bhattacharya M, Rempel TD, et al. A method for improving the efficiency of myocardial perfusion imaging using conventional Spect and Spect/Ct imaging systems. IEEE Nuclear Science Symposuim & Medical Imaging Conference. 30 Oct.-6 Nov. 2010. (2010).

14. DePuey EG. Advances in Spect camera software and hardware: currently available and new on the horizon. *J Nucl Cardiol* (2012) 19:551–81. doi: 10.1007/s12350-012-9544-7

15. Patton JA, Slomka PJ, Germano G, Berman DS. Recent technologic advances in nuclear cardiology. *J Nucl Cardiol* (2007) 14:501–13. doi: 10.1016/j.nuclcard.2007.06.003

16. Mao Y, Yu Z, Zeng GL. Segmented slant hole collimator for stationary cardiac Spect: Monte Carlo simulations. *Med Phys* (2015) 42:5426–34. doi: 10.1118/1.4928484

17. Hui L., Jing W., Si C., Shi W., Ma T. Development of stationary dedicated cardiac Spect with multi-pinhole collimators on a clinical scanner. 2015 IEEE nuclear science symposium and medical imaging conference (NSS/MIC). (2015).

18. Ogawa K, Ichimura Y. Simulation study on a stationary data acquisition Spect system with multi-pinhole collimators attached to a triple-head gamma camera system. *Ann Nucl Med* (2014) 28:716–24. doi: 10.1007/s12149-014-0865-2

19. Bowen JD, Huang Q, Ellin JR, Lee TC, Shrestha U, Gullberg GT, et al. Design and performance evaluation of a 20-aperture multipinhole collimator for myocardial perfusion imaging applications. *Phys Med Biol* (2013) 58:7209–26. doi: 10.1088/0031-9155/58/20/7209

20. Chang W, Ordonez CE, Liang H, Li Y, Liu J. C-Spect—a clinical cardiac Spect/Tct platform: design concepts and performance potential. *IEEE Trans Nucl Sci* (2009) 56:2659–71. doi: 10.1109/TNS.2009.2028138

21. Kalluri K, Bhusal N, Shumilov D, Konik A, Mukherjee J, Pretorius P. et al. Multi-pinhole cardiac Spect performance with hemi-ellipsoid detectors for two geometries. 2015 IEEE nuclear science symposium and medical imaging conference (NSS/MIC). IEEE. (2015).

22. Uzun-Özşahin D, Bläckberg L, Moghadam N, Fakhri GE, Sabet H. Gate simulation of a high-performance stationary Spect system for cardiac imaging. 2016 IEEE nuclear science symposium, medical imaging conference and room-temperature semiconductor detector workshop (NSS/MIC/RTSD). 2016 29 Oct.-6 Nov. 2016. (2016).

23. Bläckberg L, Sajedi S, Anderson OA, Feng Y, Fakhri GE, Furenlid L. et al. Dynamic cardiac Spect for diagnostic and Theranostics applications: Latest results. 2020 IEEE nuclear science symposium and medical imaging conference (NSS/MIC). 2020 31 Oct.-7 Nov. 2020. (2023).

24. Wacholz C, Hruska C, OConnor M. Veriton multi-CZT detector SPECT/CT system acceptance testing. *J Nucl Med* (2020) 61:3003.

25. Le Rouzic G, Zananiri R. First performance measurements of a new multi-detector CZT-based SPECT/CT system: Ge Starguide. *J Nucl Med* (2021) 62:1125.

26. Van Audenhaege K, Van Holen R, Vandenberghe S, Vanhove C, Metzler SD, Moore SC. Review of Spect collimator selection, optimization, and fabrication for clinical and preclinical imaging. *Med Phys* (2015) 42:4796–813. doi: 10.1118/1.4927061

27. Chaudhari AJ, Badawi RD. Application-specific nuclear medical in vivo imaging devices. *Phys Med Biol* (2021) 66:10TR01. doi: 10.1088/1361-6560/abf275

28. Wu J, Liu C. Recent advances in cardiac Spect instrumentation and imaging methods. *Phys Med Biol* (2019) 64:06TR01. doi: 10.1088/1361-6560/ab04de

29. Omata A, Kataoka J, Fujieda K, Sato S, Kuriyama E, Kato H, et al. Performance demonstration of a hybrid Compton camera with an active pinhole for wide-band X-ray and Gamma-ray imaging. *Sci Rep* (2020) 10:14064. doi: 10.1038/s41598-020-71019-5

30. Kishimoto A, Kataoka J, Koide A, Sueoka K, Iwamoto Y, Taya T, et al. Development of a compact scintillator-based high-resolution Compton camera for molecular imaging. *Nucl Instrum Methods Phys Res, Sect A* (2017) 845:656–9. doi: 10.1016/j.nima.2016.06.056

31. Takeda S, Odaka H, Sn I, Watanabe S, Aono H, Takahashi T, et al. Demonstration of in-vivo multi-probe tracker based on a Si/Cdte semiconductor Compton camera. *IEEE Trans Nucl Sci* (2012) 59:70–6. doi: 10.1109/TNS.2011.2178432

32. Lee T, Lee W. Compact hybrid gamma camera with a coded aperture for investigation of nuclear materials. *Nucl Instrum Methods Phys Res, Sect A* (2014) 767:5–13. doi: 10.1016/j.nima.2014.07.031

33. Hu Y, Fan P, Lyu Z, Huang J, Wang S, Xia Y, et al. Design and performance evaluation of a 4π-view gamma camera with mosaic-patterned 3d position-sensitive scintillators. *Nucl Instrum Methods Phys Res, Sect A* (2022) 1023:165971. doi: 10.1016/j.nima.2021.165971

34. Hu Y, Lyu Z, Fan P, Xu T, Wang S, Liu Y, et al. A wide energy range and 4π-view gamma camera with interspaced position-sensitive scintillator Array and embedded heavy metal bars. *Sensors* (2023) 23:953. doi: 10.3390/s23020953

35. Jan S, Santin G, Strul D, Staelens S, Assié K, Autret D, et al. Gate: a simulation toolkit for pet and Spect. *Phys Med Biol* (2004) 49:4543–61. doi: 10.1088/0031-9155/49/19/007

36. Yao R, Ma T, Shao Y. Derivation of system matrix from simulation data for an animal Spect with slit-slat collimator. *IEEE Trans Nucl Sci* (2009) 56:2651–8. doi: 10.1109/TNS.2009.2022940

37. Husain SS. Myocardial perfusion imaging protocols: is there an ideal protocol? *J Nucl Med Technol* (2007) 35:3–9.

38. Segars WP, Sturgeon G, Mendonca S, Grimes J, Tsui BM. 4d Xcat phantom for multimodality imaging research. *Med Phys* (2010) 37:4902–15. doi: 10.1118/1.3480985

39. Hudson HM, Larkin RS. Accelerated image reconstruction using ordered subsets of projection data. *IEEE Trans Med Imaging* (1994) 13:601–9. doi: 10.1109/42.363108

40. Zhu X, Deng Z, Chen Y, Liu Y, Liu Y. Development of a 64-channel readout Asic for an 8x8 Sspm Array for pet and Tof-pet applications. *IEEE Trans Nucl Sci* (2016) 63:1–8. doi: 10.1109/TNS.2016.2518808

41. Ma T, Wei Q, Lyu Z, Zhang D, Zhang H, Wang R, et al. Self-collimating Spect with multi-layer interspaced mosaic detectors. *IEEE Trans Med Imaging* (2021) 40:2152–69. doi: 10.1109/TMI.2021.3073288

frontiers | Frontiers in Cardiovascular Medicine

TYPE Original Research
PUBLISHED 04 July 2023
DOI 10.3389/fcvm.2023.1115135

OPEN ACCESS

EDITED BY
Roberto Massari,
National Research Council (CNR), Italy

REVIEWED BY
Peter Michael Van Dam,
University Medical Center Utrecht, Netherlands
Xiaoli Zhang,
Capital Medical University, China

*CORRESPONDENCE
Zheng-Jie Wang
bkzg1234@163.com
Xing-Guo Jing
1225298848@qq.com

RECEIVED 03 December 2022
ACCEPTED 19 June 2023
PUBLISHED 04 July 2023

CITATION
Wang X-H, Li M-D, Xie F-X, Liang H, Yang L, Wei X-F, Pang H, Wang Z-J and Jing X-G (2023) Prognostic utility of ^{99m}Tc-MIBI single photon emission computerized tomography myocardial perfusion imaging in patients with ischemia and non-obstructive coronary artery disease.
Front. Cardiovasc. Med. 10:1115135.
doi: 10.3389/fcvm.2023.1115135

Prognostic utility of ^{99m}Tc-MIBI single photon emission computerized tomography myocardial perfusion imaging in patients with ischemia and non-obstructive coronary artery disease

Xiao-Hui Wang, Meng-Dan Li, Fu-Xiang Xie, Huan Liang, Lu Yang, Xiao-Fei Wei, Hua Pang, Zheng-Jie Wang* and Xing-Guo Jing*

Department of Nuclear Medicine, The First Affiliated Hospital of Chongqing Medical University, Chongqing Medical University, Chongqing, China

Objective: The aim of our study was to evaluate the prognostic value of gated SPECT MPI in non-obstructed coronary arteries (INOCA) patients, sought to stratify patients more accurately and thus derive more reliable prognostic information.
Materials and methods: In total, 167 patients with INOCA were enrolled. The patients were divided into two groups according to their SSS. Patients were followed-up regularly in terms of major adverse cardiovascular event (MACE), including cardiac death, nonfatal myocardial infarction, stroke, re-hospitalization with angina pectoris, and recurrent angina pectoris. Kaplan-Meier curves and Cox's proportional hazards models were used to analyze survival and identify predictive factors.
Results: Adverse cardiac events occurred in 33 cases (19.8%). The rate of MACE was higher in the summed stress score (SSS) ≥4 group than in the SSS 0–3 group (30.1% vs. 9.5%, respectively, $P = 0.001$) and MACE-free survival was lower (annual MACE-free rates of 87.5% vs. 96.2%, respectively, $P = 0.003$). Event-free survival was consistently higher in patients with normal arteries than in those with non-obstructive coronary artery disease (annual MACE-free rates of 96.1% and 88.4%, $P = 0.035$). When the SSS and the CAG results were combined, patients with normal coronary arteries (SSS 0–3) had the best prognosis and those with non-obstructive coronary artery stenosis (SSS ≥ 4) had the worst. However, the early prognosis of patients with non-obstructive coronary artery disease and SSS of 0–3 was comparable to that of patients with normal coronary arteries and SSS ≥ 4 (annual MACE-free rates of 100%, 94.6%, 93.1%, and 78.2%, respectively). Multivariate Cox's regression indicated that the SSS [hazard ratio (HR) = 1.126, 95% confidence interval (CI) 1.042–1.217, $P = 0.003$] and non-obstructive coronary artery disease (HR = 2.559, 95% CI 1.249–5.246, $P = 0.01$) were predictors of adverse cardiac events.
Conclusion: SPECT MPI data were prognostic for INOCA patients, thus identifying groups at high risk. The long-term predictive efficacy of such data exceeded that of CAG data. A combination of the two measures more accurately stratified INOCA patients in terms of risk.

KEYWORDS

SPECT, myocardial perfusion imaging, INOCA, MACE, prognosis

1. Introduction

About 112 million people worldwide suffer from angina pectoris (1), which is the most common symptom of ischemic heart disease. In up to 70% of patients who undergo invasive coronary angiography (CAG) to treat angina pectoris, there is no evidence of obstructive coronary artery stenosis (stenosis < 50%) (2); their symptoms are often mistakenly considered non-cardiac in nature, resulting in inadequate follow-up treatment (3). CAG as the gold standard, aimed at the detection of obstructive CAD, whereas the other reasons for angina pectoris complaints are not investigated. Clinically, a disease with symptoms or signs of myocardial ischemia but without obstructive coronary artery stenosis evident in CAG is defined as ischemia of non-obstructive coronary arteries (INOCA). The clinical manifestations of INOCA are extensive and varied, and the symptom burden may change over time (4). Few studies have evaluated INOCA therapy and there is no evidence-based normative therapy (5). The symptoms are not specific and CAG does not reveal obstructive disease. If the doctor does not consider non-obstructive myocardial ischemia, the absence of obstructive coronary artery stenosis in CAG may trigger a misdiagnosis. Because they have not been appropriately diagnosed, such patients often complain of persistent chest pain and are likely to undergo repeated coronary angiography and other medical assessments, triggering physical limitations, a decline in their quality of life, anxiety, and depression (6). Ischemia changes can develop even without obvious severe coronary artery obstruction (7–9). Single photon emission computed tomography (SPECT) myocardial perfusion imaging (MPI) is the most reliable noninvasive method by which to detect myocardial ischemia (10–13); the technique directly examines coronary artery perfusion and determines the specific location, scope, and extent of ischemia (14). MPI accurately evaluates the prognosis of patients with coronary heart disease. Given the poor prognosis of some patients with INOCA, and the fact that symptoms of angina pectoris are associated with adverse events (15), might MPI usefully evaluate the prognosis of patients with INOCA, and accurately classify such patients, allowing selective interventions? Here, we divided angina pectoris patients with normal CAG data into different groups based on the results of SPECT MPI and CAG and explored the prognostic utility of SPECT MPI in patients with INOCA.

2. Materials and methods

2.1. Study population

This study complied with the Declaration of Helsinki and was approved by the ethical review board of the First Affiliated Hospital of Chongqing Medical University, Chongqing, China. Informed written consent was obtained from all patients. We enrolled all consecutive patients with non-obstructive coronary artery disease aged >18 years and hospitalized between June 1, 2017 and December 31, 2021, who met the following inclusion criteria: typical symptoms and signs of myocardial ischemia; <50% stenosis of the main branches of the coronary artery, as confirmed by CAG, including 0% stenosis; finish ^{99m}Tc-MIBI SPECT stress and at rest myocardial perfusions after admission; and complete clinical data. The exclusion criteria were a history of coronary heart disease; any acute myocardial infarction (all ECGs were classified as normal or not myocardial infarction), acute cardiac insufficiency, valvular disease, congenital heart disease, or cardiomyopathy; musculoskeletal disease, chronic obstructive pulmonary disease, digestive system disease, mental disorders; a malignant tumor or severe liver or kidney disease; and expected survival for less than 1 year.

2.2. CAG results analysis

At the time of CAG, a cardiologist graded the severity of a coronary artery obstruction visually based on the percentage of stenosis, obtain an estimated value, then measurements are made on the screen to verify the accuracy of visual measurement, and the measured value shall prevail. Patients with major epicardial or branch vessels (diameter ≥2.0 mm) with <50% stenosis (including 0% stenosis) were classified as having either normal coronary arteries (0%) or non-obstructive coronary arteries (1%–49%) (16).

2.3. SPECT image acquisition and analysis

Patients were told to pause use of beta-blockers, calcium antagonists, nitrates, and any products containing caffeine for 24–48 h before SPECT. MPI featured respiratory gated^{99m}Tc-sestamibi (^{99m}Tc-MIBI) stress-rest alternate-day imaging. Stress testing was performed using the Bruce program and a treadmill exercise; the treadmill speed and slope were gradually increased until the heart rate attained 85% of the expected maximum (190 minus age) or when the patient exhibited angina pectoris, dyspnea, arrhythmia, a drop in blood pressure, or an ECG ST segment downshift >1 mm. Then, 740 MBq ^{99m}Tc-MIBI was immediately injected intravenously and exercise continued for 1 min; 30 min later, patients were given a fatty meal. Stress myocardial tomography was performed at 90 min after injection. ECG data and blood pressure were monitored before, during, and after treatment. We used a GE Discovery SPECT/CT670 instrument equipped with a low-energy universal parallel hole collimator. The acquisition matrix was 128 × 128 from the right anterior oblique 45° point to the left posterior oblique 45° point. In total, 30 frames were collected over 40 s and the filtered back-projection method was used to reconstruct each image. A fatty meal was eaten 30 min after injection on the next day, and gated resting MPI was performed 90 min later. The stress and rest perfusion images were evaluated by at least two senior nuclear-medicine physicians using a double-blinded method based on a 17-segment left-ventricular model and a five-point scale (17) (0 = normal perfusion; 1 = mildly decreased, unable to determine

whether abnormal; 2 = moderately reduced, abnormality evident; 3 = significant reduction, 4 = perfusion defect). If the two doctors did not agree, all doctors in the department were consulted and a consensus emerged. Perfusion scores were calculated to indicate myocardial perfusion abnormalities and their severity; the summed stress score (SSS) is the sum of all perfusion defects evident on the stress image, the summed rest score (SRS) is the sum of all defects apparent on the resting image, and the summed difference score (SDS) is the difference between the stress and rest scores. Left-ventricular (LV) functional parameters including the LV end-diastolic volume (EDV), LV end-systolic volume (ESV), and LV ejection fraction (LVEF) were calculated automatically by the QGS software. The patients were divided into an SSS 0–3 group and an SSS ≥ 4 group.

2.4. Follow-up

All patients were followed up every 6 months by our physicians, who contacted the patients or their family members to assess clinical status. We recorded major adverse cardiovascular event (MACE) including cardiac death, nonfatal myocardial infarction, stroke, re-hospitalization for angina pectoris, and recurrent angina pectoris. The survival time was from the time of MPI examination to the occurrence of the first MACE. If no MACE occurred during follow-up, the survival time was from the time of MPI examination to the end of follow-up.

2.5. Statistical analysis

All statistical analysis was performed using SPSS ver. 26.0 for Windows (SPSS Inc., Chicago, IL, USA). Continuous values are expressed as means ± SD or (median, inter quartile ranges) and categorical variables are given as percentages. The independent-samples *t*-test or Mann–Whitney *U*-test was used to compare numerical variables and the chi-square or Fisher exact test to compare categorical variables. The MACE-free survival rate was estimated by drawing Kaplan-Meier curves, and differences between survival curves were evaluated using the log-rank test. Univariate and multivariate Cox's proportional hazards models were employed to identify predictors of adverse events. Factors significant at $P < 0.1$ in univariate analysis were included in the multivariate analysis. We calculated hazard ratios (HRs) with 95% confidence intervals (CIs). Two-sided *P*-values < 0.05 were considered to indicate significance.

3. Results

3.1. Baseline clinical characteristics

In total, 167 patients were included. Table 1 shows the baseline data. There were 84 cases in the SSS 0–3 group (male/female 35/48) and 83 in the SSS ≥ 4 group (male/female 44/39). CAG showed that 102 patients had normal coronary arteries and 65 had non-obstructive coronary arteries. There were no significant differences in sex, age, or risk factors for coronary heart disease between the two groups. The proportion of patients with non-obstructive coronary arteries was higher in the SSS 0–3 group than in the SSS ≥ 4 group ($P = 0.02$), and such patients were less likely to be on an angiotensin-converting enzyme inhibitor/angiotensin II receptor (ACEI/ARB). There were no between-group differences in the use of aspirin, clopidogrel, beta-blockers, or calcium-channel blockers (CCBs).

TABLE 1 Comparison of baseline data between the two groups.

Variables	SSS 0–3 group (*n* = 84)	SSS ≥ 4 group (*n* = 83)	*P*-value
Demographics			
Age (years)	61.2 ± 8.68	59.07 ± 9.82	0.139
Female, *n* (%)	48 (57.1)	39 (47.0)	0.189
Risk factors			
Hypertension, *n* (%)	44 (52.4)	40 (48.2)	0.588
Diabetes, *n* (%)	18 (21.4)	24 (28.9)	0.265
Hyperlipidemia, *n* (%)	29 (34.5)	28 (33.7)	0.914
Smoking history, *n* (%)	26 (32.7)	28 (33.7)	0.824
Family history, *n* (%)	7 (8.6)	4 (4.8)	0.325
Non-obstructive coronary artery, *n* (%)	40 (47.6)	25 (30.1)	0.02
Medication			
Aspirin, *n* (%)	36 (42.9)	40 (48.2)	0.489
Clopidogrel, *n* (%)	23 (27.4)	23 (27.7)	0.962
ACEI/ARB, *n* (%)	21 (25.3)	37 (44.6)	0.009
Beta-blocker, *n* (%)	37 (44.0)	45 (54.2)	0.189
CCB, *n* (%)	19 (22.9)	22 (26.5)	0.589
Statin, *n* (%)	73 (86.9)	77 (92.8)	0.21

ACEI/ARB, angiotensin-converting enzyme inhibitor or angiotensin II receptor blocker; CCB, calcium channel blockers.

3.2. SPECT MPI results

Table 2 summarizes the SPECT MPI results. Compared to the SSS 0–3 group, LV function was significantly impaired in the SSS ≥ 4 group, showed with a lower LVEF and a higher end-diastolic

TABLE 2 Comparison of SPECT data between the two groups (median, IQR).

Variables	SSS 0–3 group (*n* = 84)	SSS ≥ 4 group (*n* = 83)	*P*-value
Quantitative analysis index			
SSS	(0, 0)	(8, 7)	<0.001
SDS	(0, 0)	(3, 8)	<0.001
SRS	(0, 0)	(5, 4)	<0.001
Left ventricular functional parameters			
Stress LVEF (%)	(63, 11)	(59, 13)	0.027
Stress EDV (ml)	(75.5, 39)	(83, 45)	0.048
Stress ESV (ml)	(32, 32)	(33, 34)	0.306
Rest LVEF (%)	(64, 12)	(60, 15)	0.008
Rest EDV (ml)	(72, 41)	(80, 40)	0.054
Rest ESV (ml)	(30, 30)	(33, 30)	0.157

SSS, summed stress score; SRS, summed rest score; SDS, summed difference score; EDV, end-diastolic volume; ESV, end-systolic volume; LVEF, left ventricular ejection fraction.

volume (EDV) under both stress and rest. Patients with high SSS evidenced more severe myocardial perfusion damage and their LV function was affected accordingly.

3.3. Clinical outcomes

The average follow-up time was 24.15 ± 1.02 months. For the entire cohort, 33 MACEs (19.8%) occurred, including 2 cases (1.2%) of stroke, 12 cases (7.2%) of re-hospitalization to treat angina pectoris or heart failure, and 19 cases (11.4%) of angina pectoris recurrence, but no cardiac death or nonfatal myocardial infarction occurred. In the SSS 0–3 group of patients, eight MACEs (9.5%) occurred, including 1 case (1.2%) of stroke, 4 cases (4.8%) of re-hospitalization because of angina pectoris, and 3 cases (3.6%) of angina pectoris recurrence. In the SSS ≥ 4 group of patients, 23 MACEs (30.1%) occurred, including 1 case (1.2%) of stroke, 8 cases (9.6%) of re-hospitalization with angina pectoris, and 16 cases (19.3%) of angina pectoris recurrence. The incidence of MACE differed significantly between the two groups ($P < 0.01$) (Table 3).

As shown in Figure 1A, in the patients with normal coronary arteries, the incidences of MACE in the SSS 0–3 and SSS ≥ 4 groups were 4.5% and 27.6%, respectively ($P = 0.003$); in those with non-obstructive coronary arteries, the incidences in the SSS 0–3 and SSS ≥ 4 groups were 15.0% and 36.0%, respectively ($P = 0.051$). CAG revealed that the incidences of MACE in patients with normal and non-obstructive coronary arteries were 17.6% and 23.1%, respectively ($P = 0.39$). In the SSS 0–3 group, the incidences of MACE were 4.5% in patients with normal coronary arteries and 15% in those with non-obstructive coronary arteries ($P = 0.208$), while in the SSS ≥ 4 group, the incidences were 27.6% and 36%, respectively ($P = 0.443$) (Figure 1B). Thus, the higher the SSS, the higher the MACE incidence. CAG revealed that although the incidence of MACE was higher in the patients with non-obstructive coronary arteries than in those with normal arteries, this difference did not attain statistical significance. SSS were more closely related to the incidence of MACE than was non-obstructive coronary artery status. Figure 1C shows the occurrence of MACE predicted by combining SSS and CAG results ($P = 0.004$).

3.4. Survival analysis

Figure 2A shows the Kaplan-Meier survival curves of the SSS 0–3 and SSS ≥ 4 groups; the respective survival rates for 1, 2, 3, and 4 years were 96.2% and 87.5%, 91.2% and 72.1%, 84.1% and 63.1%, and 74.8% and 52.5%. In survival analysis of the normal coronary artery patients and the non-obstructive coronary artery patients, the survival rates of the SSS ≥ 4 patients were always lower (Figures 2B,C). Survival analysis was performed for all patients, stratified by the severity of myocardial ischemia (group 1: SSS 0–3; group 2: SSS 4–8; group 3: SSS 9–13; and group 4: SSS > 13). The annual MACE-free rates of groups 1, 2, 3, and 4 were 96.2%, 90.9%, 100%, and 78.6%, respectively (Figure 2D). A strong correlation was evident between SSS and the prognosis of INOCA patients: the higher the SSS, the lower the survival rate.

Based on the CAG data, we performed survival analysis of all patients, SSS 0–3, and SSS ≥ 4 patients. The respective survival rates of the normal and non-obstructive coronary artery groups for 1, 2, and 3 years were 96.1% and 88.4%, 87.6% and 70.7%, and 79.3% and 66.0% (Figure 3A). Regardless of grouping, survival rates were always higher in patients with normal coronary arteries, indicating that obstruction significantly affected the survival of patients with INOCA (Figures 3B,C). Based on Kaplan-Meier curves obtained by combining SSS and angiographic results, the annual MACE-free rates of the four groups were 100%, 94.6%, 93.1%, and 78.2%, respectively (Figure 3D). The prognosis of the normal coronary artery patients with SSS of 0–3 was the best, and that of non-obstructive coronary artery patients with SSS ≥ 4 was the worst. Thus, a combination of the SPECT MPI and CAG data predicted the prognosis of patients with INOCA more accurately.

TABLE 3 Comparison of incidence of MACE between the two groups (*n*, %).

Outcomes	SSS 0–3 group ($n = 84$)	SSS ≥ 4 group ($n = 83$)	*P*-value
Stroke	1 (1.2)	1 (1.2)	1
Re-hospitalization for angina pectoris or heart failure	4 (4.8)	8 (9.6)	0.222
Recurrent angina pectoris	3 (3.6)	16 (19.3)	0.001
Total	8 (9.5)	25 (30.1)	0.001

MACE, major adverse cardiac event; SSS, summed stress score.

3.5. Analysis of prognostic factors

To identify factors predictive of MACE, we performed Cox's univariate and multivariate regression analyses. In univariate analysis, a non-obstructive coronary artery ($P = 0.004$), the SSS ($P = 0.039$), SRS ($P = 0.002$), and stress EDV ($P = 0.088$) were risk factors for MACE. Factors with *P*-values < 0.1 were included in the multivariate model. The SSS (HR = 1.126, 95% CI 1.042–1.217) and a non-obstructive coronary artery (HR = 2.559, 95% CI 1.249–5.246) were risk factors for MACE, but the predictive effect of the SSS was higher than that of non-obstructive coronary artery status (Table 4).

4. Discussion

Our study investigated the prognostic value of MPI in patients with INOCA, the data show that MPI was highly and independently predictive of MACE, moreover, INOCA patients with non-obstructive coronary artery have a worse prognosis than those with normal coronary artery, which contributes to our unfolding knowledge regarding the adverse event risk associated with INOCA patients.

Although there have been many studies on INOCA, the pathogenesis, diagnosis, treatment, and prognosis of stable chest pain and INOCA remain very controversial (15). With the CAG either obstructions are detected or in some cases spasms. In case

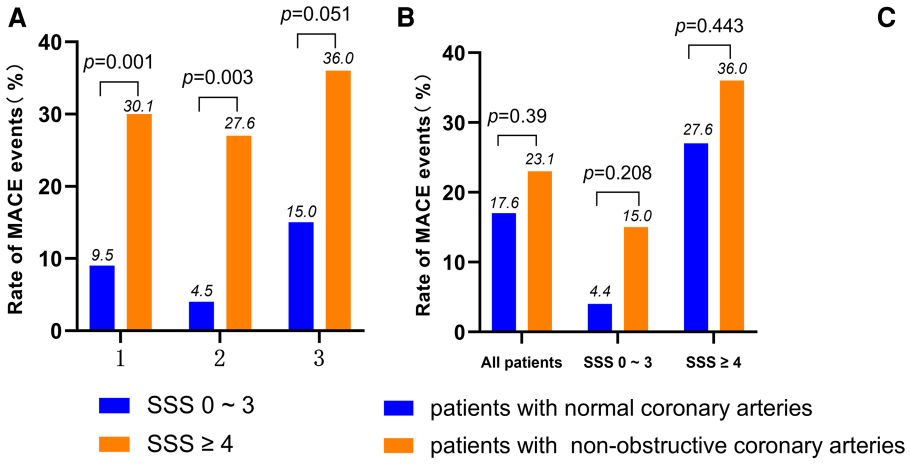

FIGURE 1
(A) Rate of MACE according to the result of SSS in all patients, normal coronary arteries patients and non-obstructive coronary arteries patients (1: *all patients*; 2: *normal coronary arteries patients*; 3: *non-obstructive coronary arteries patients*). (B) Rate of MACE according to the result of CAG in all patients, SSS 0–3 score patients and SSS ≥ 4 score patients. (C) Rate of MACE according to the result of SSS and the result of CAG in all patients (a: *patients of normal coronary arteries with SSS 0–3*; b: *patients of non-obstructive coronary arteries with SSS 0–3*; c: *patients of normal coronary arteries with SSS ≥ 4*; d: *patients of non-obstructive coronary arteries with SSS ≥ 4*). MACE, major adverse cardiac events; MPI, myocardial perfusion imaging; CAG, coronary angiography; SSS, summed stress score.

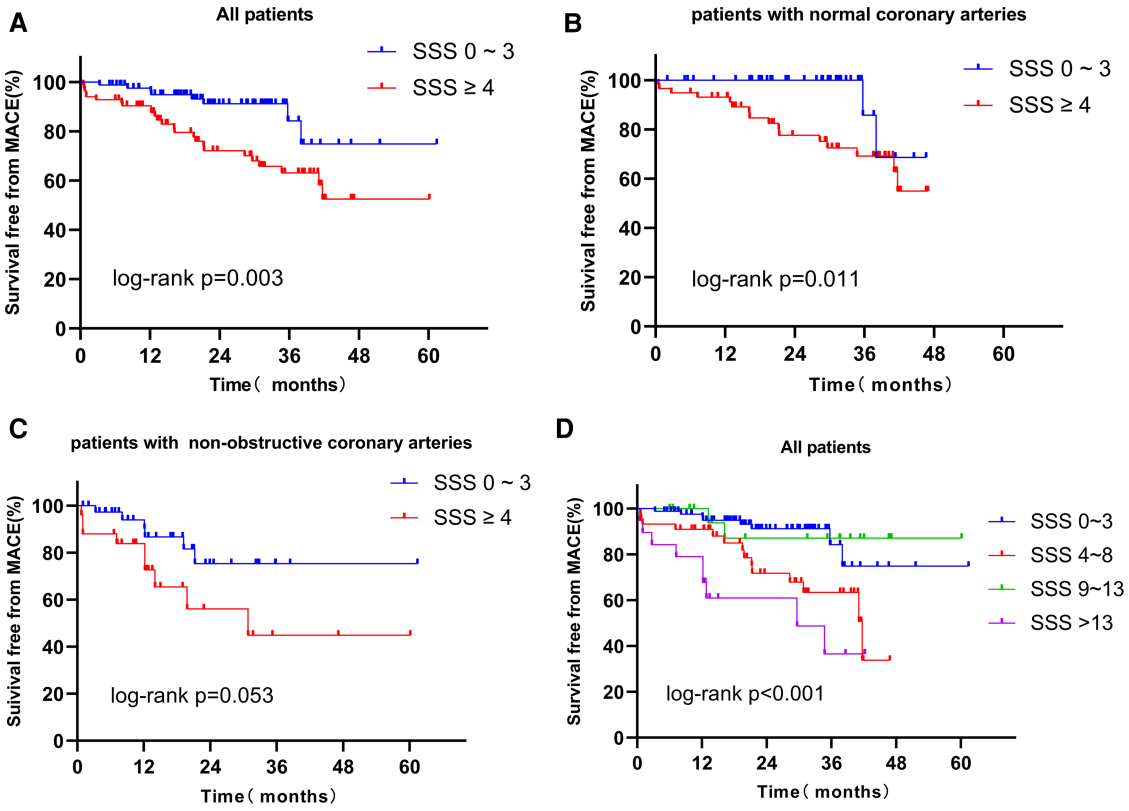

FIGURE 2
(A) Kaplan-Meier curves for freedom from MACE according to the result of SSS in all patients. (B) Kaplan-Meier curves for freedom from MACE according to the result of SSS in patients with normal coronary arteries. (C) Kaplan-Meier curves for freedom from MACE according to the result of SSS in patients with non-obstructive coronary arteries. (D) Kaplan-Meier curves for freedom from MACE according to the result of extent of ischemia myocardial (*Group 1: SSS 0–3: no myocardial ischemia; Group 2: SSS 4–8, mild myocardial ischemia; Group 3: SSS 9–13, moderate myocardial ischemia; Group 4: SSS > 13, severe myocardial ischemia*). MACE, major adverse cardiac event; SSS, summed stress score.

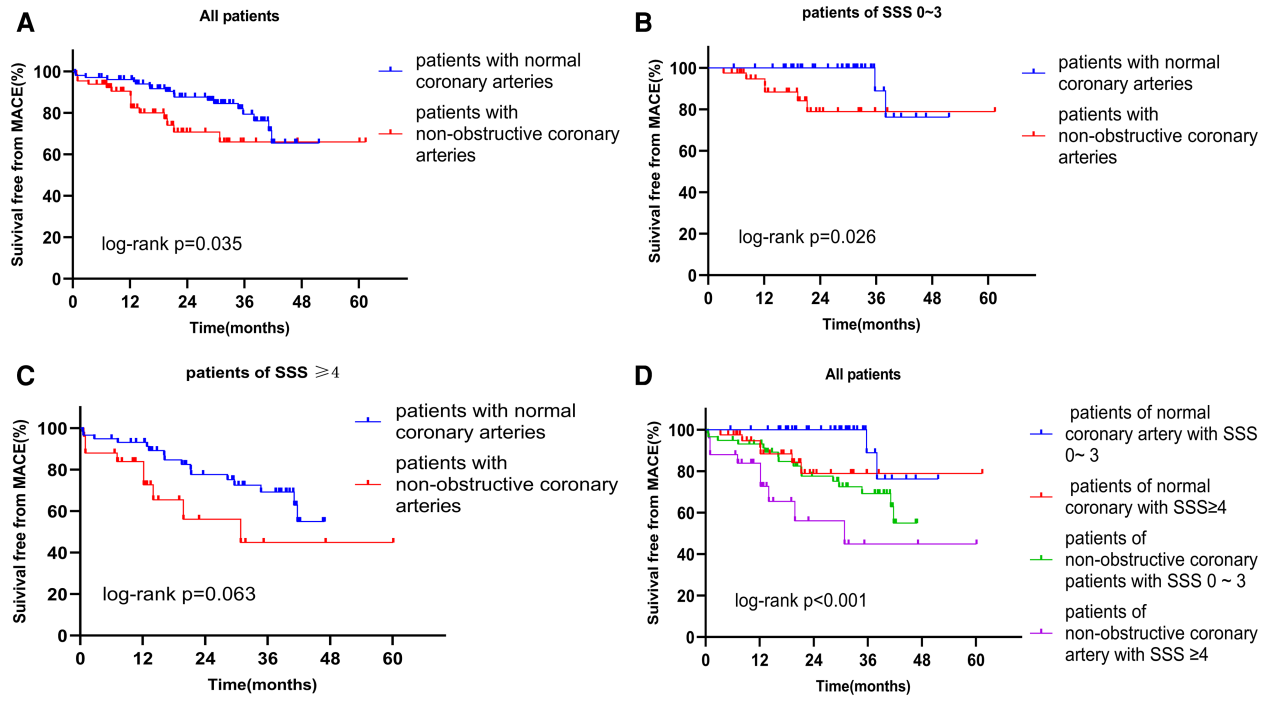

FIGURE 3
(A) Kaplan-Meier curves for freedom from MACE according to the result of CAG in all patients. (B) Kaplan-Meier curves for freedom from MACE according to the result of CAG in patients of SSS 0–3. (C) Kaplan-Meier curves for freedom from MACE according to the result of CAG in patients of SSS ≥ 4. (D) Kaplan-Meier curves for freedom from MACE according to the result of SSS and the result of CAG. MACE, major adverse cardiac event; SSS, summed stress score; CAG, coronary angiography.

TABLE 4 Univariate and multivariate COX regression analysis of MACE.

	Univariate		Multivariate	
	HR (95% CI)	*P*-value	HR (95% CI)	*P*-value
Age	1.019 (0.984–1.056)	0.291		
Sex	1.078 (0.554–2.136)	0.829		
Hypertension	0.777 (0.389–1.552)	0.475		
Diabetes	1.08 (0.501–2.327)	0.844		
Hyperlipidemia	0.555 (0.240–1.280)	0.167		
Smoking history	1.016 (0.483–2.138)	0.966		
Family history	0.879 (0.21–3.684)	0.86		
Non-obstructive coronary artery	2.082 (1.037–4.183)	0.039	2.559 (1.249–5.246)	0.01
Aspirin	0.834 (0.417–1.669)	0.608		
Clopidogrel	1.584 (0.749–3.351)	0.229		
ACEI/ARB	0.858 (0.408–1.804)	0.687		
Beta-blocker	0.902 (0.454–1.791)	0.769		
CCB	0.927 (0.402–2.136)	0.858		
Statin	1.465 (0.446–4.813)	0.529		
SSS	1.075 (1.03–1.122)	0.001	1.126 (1.042–1.217)	0.003
SRS	1.007 (1.012–1.145)	0.018	0.912 (0.791–1.052)	0.207
SDS	1.126 (1.044–1.214)	0.102		
Stress LVEF	0.981 (0.956–1.007)	0.152		
Stress EDV	1.005 (0.999–1.012)	0.088	1.004 (0.996–1.012)	0.288
Stress ESV	1.006 (0.999–1.013)	0.12		
Rest LVEF	1.007 (0.977–1.039)	0.64		
Rest EDV	1.004 (0.998–1.011)	0.185		
Rest ESV	1.004 (0.996–1.012)	0.318		

ACEI/ARB, angiotensin-converting enzyme inhibitor or angiotensin II receptor blocker; CCB, calcium channel blockers; SSS, summed stress score; SRS, summed rest score; SDS, summed difference score; EDV, end-diastolic volume; ESV, end-systolic volume; LVEF, left ventricular ejection fraction; HR, hazard ratio; CI, confidence interval.

the obstructions are not severe enough to limit the blood flow severely, the CAG will be classified as minor obstructive or maybe also normal. SPECT MPI May be a good tool to distinguish local changes in the heart. We used MPI to evaluate INOCA prognoses; after a follow-up of 24.15 ± 1.02 months, about half (83/167) of all patients evidenced abnormal MPI data ($SSS \geq 4$). The incidence of MACE was 3.2-fold higher in the $SSS \geq 4$ group than in the SSS 0–3 group. For patients with normal coronary arteries, the incidence was 6.1-fold higher in the $SSS \geq 4$ group than in the SSS 0–3 group; for those with non-obstructive coronary arteries, the incidence was 2.4-fold higher in the $SSS \geq 4$ group than in the SSS 0–3 group. When the SSS and CAG data were combined, patients with an $SSS \geq 4$ and non-obstructive coronary artery status evidenced the highest incidence of MACE (36%).

All included patients with chest pain were normal in CAG but almost half evidenced abnormal SPECT MPI results (**Figure 4**) and were at increased risk for adverse cardiovascular outcomes. The reason may be that such patients suffer from coronary microvascular disease and/or epicardial coronary artery spasms that mismatch coronary blood supply and demand (8). Many recent studies have confirmed that coronary microvascular dysfunction is associated with an increased risk for adverse cardiac outcomes in patients with INOCA (18, 19). No existing technique directly observes the anatomy of the human coronary artery microcirculation. We found that the incidences of MACE in patients with SSS of 0–3 and $SSS \geq 4$ were 4.5% and 27.6%, respectively, in the whole cohort, without myocardial infarction and death, comparable to those reported by Alqaisi (20) and Liu et al. (21), this indicates that MACE events in INOCA patients are better than obstructive CAD. The multivariate proportional hazard model showed that every unit increase in the SSS increased the MACE risk by 12.6%. Thus, even if there is no obstructive coronary artery disease, the probability of MACE in patients with abnormal SPECT MPI data is still significant, and their prognosis is often worse. All patients were further grouped by their SSS (a measure of ischemia severity). The Kaplan-Meier curve showed that the prognosis of the non-ischemia group was the best, and that of the severe ischemia group was the worst, similar to the results of previous studies (22, 23), indicating that the prognosis of INOCA patients is affected by myocardial ischemia and that survival becomes increasingly poorer as ischemia becomes aggravated. Unexpectedly, the prognosis of patients with moderate ischemia was better than that of those with mild ischemia, possibly for the reason: after patients with $SSS \geq 4$ were re-grouped, the SSS 9–13 group had the lowest number of patients and the least MACE, so it showed the best long-term prognosis on the survival curve. SPECT MPI is demanding in terms of equipment, and on patients and operators; it is less popular

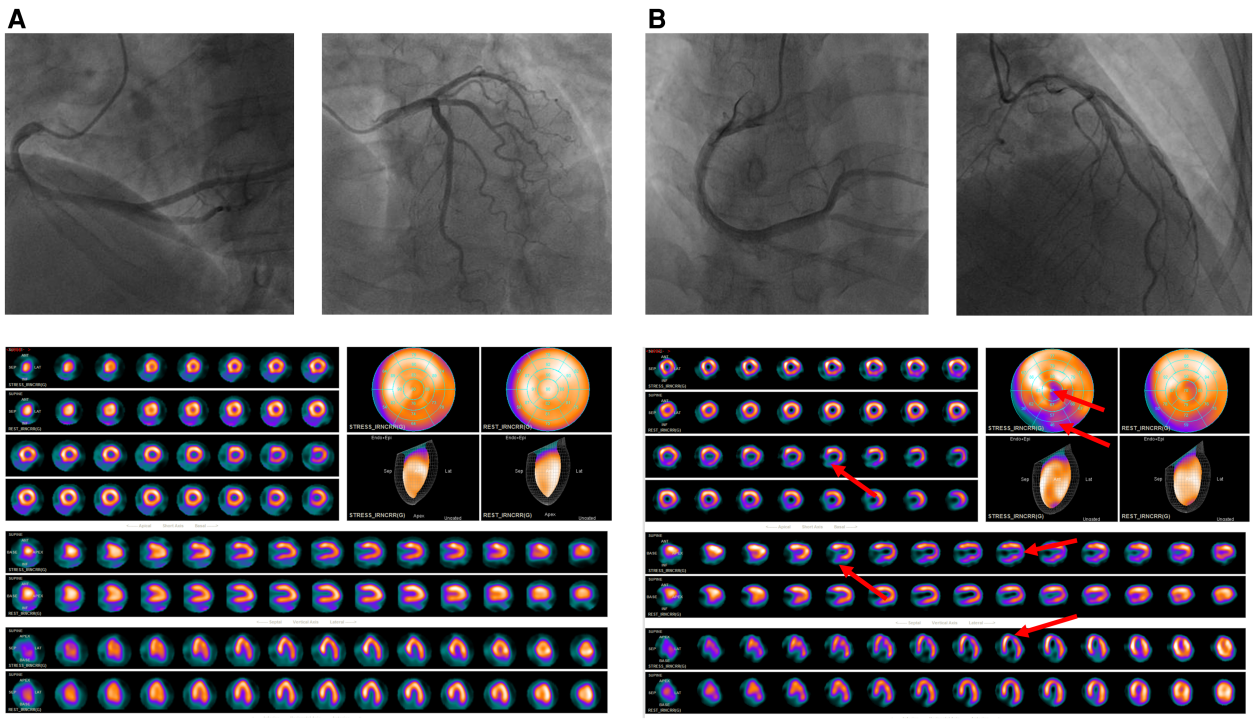

FIGURE 4
(A) A 60-year-old female patient presented to the cardiology department of our hospital for "chest pain for 2 + months", CAG suggested that there was no stenosis in the left and right coronary arteries; SPECT MPI was normal, the SSS = 0, by the follow-up date of 25 months, the patient did not have MACE (B) A 52-year-old female patient presented to the cardiology department of our hospital for "repeated chest pain for 6 days and aggravation for 11 h", CAG suggested that there was no stenosis in the left and right coronary arteries; SPECT MPI indicates sparse radioactive distribution of left ventricular part of the segments in stressing phase (red arrow), and filling in resting phase, considering myocardial infarction, the SSS = 9, the patient was re-hospitalized 8 months later due to angina pectoris.

than CAG in clinics. Many institutions perform only CAG. However, if patients have clinical symptoms of coronary heart disease, particularly angina pectoris, these should not be taken lightly even if CAG reveals no obstructive coronary heart disease. SPECT MPI evaluates myocardial ischemia status and its severity, assisting in treatment decisions. Interestingly, COX regression analysis showed that SDS was not an independent predictor of MACE, this may be a proportion of our included patients had an irreversible myocardial ischemia, which affected its predictive function.

Multivariate regression analysis also showed that the risk for MACE was 2.6-fold higher in patients with non-obstructive coronary arteries than in patients with normal coronary arteries; we thus further examined the prognosis and survival of such patients. Using the CAG data, all patients, and patients with SSS of 0–3 and ≥4, were divided into normal and non-obstructive coronary artery groups. The survival rates of the non-obstructive coronary artery groups were always lower than those of the other groups. Jespersen et al. (15) showed that, compared to a reference population with no ischemic heart disease, patients with normal coronary arteries but symptoms of angina pectoris, and patients with non-obstructive coronary arteries but symptoms of angina pectoris have an increased risk of MACE by 52% and 85% respectively, and as the extent of vascular stenosis rose, the risk for MACE and mortality from various causes gradually increased. Another study (24) showed that the risks for repeat CAG examination in patients with normal and non-obstructive coronary arteries were 2.3% and 5.5%, respectively. For each additional segment of non-obstructive coronary artery disease, the mortality rate increased by 6% (95% CI 1%–12%, $P = 0.021$). Both our findings and those described above indicate that even when coronary artery stenosis is less than 50% in INOCA patients, non-obstructive coronary lesions predict an increased risk for adverse cardiovascular outcomes, perhaps because the endothelial function of non-obstructive coronary arteries is impaired and development of atherosclerotic coronary artery disease is thus more likely (25), and/or a non-obstructive coronary artery features diffuse non-obstructive atherosclerosis with "compensatory" coronary remodeling (26) and the normal structure has thus been damaged. For such patients, the rates of re-hospitalization and repeat angiography caused by increasingly problematic symptoms rise, adding to the economic and psychological burdens on patients and their families, social medical pressure, and economic costs. Clinicians must strive to avoid such negative effects.

We combined SSS and CAG data to analyze the survival of all patients. The survival curves showed that the early prognosis of non-obstructive coronary artery patients with SSS of 0–3 was similar to that of normal coronary artery patients with SSS ≥ 4, but over time the prognosis of the latter patients was poorer than that of the former. In other words, in the long run, the predictive power of SPECT MPI was higher than that of CAG. The best prognosis was that for patients with normal coronary arteries and SSS of 0–3 (annual survival 100%), whereas patients with SSS ≥ 4 had the worst prognosis (annual survival 78.2%); such patients require much more attention than they presently receive. In institutions that prefer CAG, non-obstructive coronary artery lesions should not be ignored; SPECT MPI is essential. A combination of the data of both examinations increased the prognostic accuracy for INOCA patients.

In addition, we found that the proportion of non-obstructive coronary artery patients was higher in the SSS 0–3 group than in the SSS ≥ 4 group. In other words, there was no direct correlation between SSS and the extent of coronary artery stenosis in the INOCA patients. Coronary atherosclerosis was not the principal cause of myocardial ischemia in the INOCA patients.

Some limitations to our study should be mentioned. First, we found that drugs did not improve the INOCA prognosis, whereas previous studies have found that statins significantly reduced the incidence of MACE in INOCA patients (16). This could have been because of drug non-compliance by our patients, which may have affected our findings. Second, our sample size was small; more patients are required to draw more accurate conclusions.

Secondly, the definite diagnosis of the origin of INOCA is based on coronary function tests with for instance acetylcholine or adenosine to elucidate the true origin, but the patients in this study did not have coronary functional testing, in a future study, we do this analysis with patients undergoing such test. In addition, this was a retrospective single-center study and the results are thus not necessarily generally applicable. There may have been some selection bias. Larger multicenter studies are needed to verify our conclusions. Our average follow-up time was short. Some patients did not develop MACE; cardiovascular deaths and nonfatal myocardial infarctions were rare.

Importantly, we not only confirmed the prognostic utility of SPECT MPI in patients with INOCA but also combined SPECT MPI and CAG data to develop a new and accurate risk-stratification method for INOCA patients. We found that SPECT MPI yielded valuable prognostic information on INOCA patients, identifying those at higher risk. By measuring the response to myocardial perfusion, SPECT MPI identifies myocardial ischemia, and its location and severity, and also comprehensively evaluates coronary artery anatomy and function. The long-term predictive efficacy of the data is even higher than that of CAG data. The combination of the two datasets enhanced the accuracy of INOCA patients' risk stratification.

The English in this document has been checked by at least two professional editors, both native speakers of English. For a certificate, please see: http://www.textcheck.com/certificate/5dUdCx.

Data availability statement

The original contributions presented in the study are included in the article/Supplementary Material, further inquiries can be directed to the corresponding authors.

Ethics statement

The studies involving human participants were reviewed and approved by the Ethics Committee of the First Affiliated Hospital of Chongqing Medical University. The patients/participants provided their written informed consent to participate in this study.

Author contributions

X-HW contributed to data collection, writing, revision, and statistical analysis of the manuscript. M-DL, HL, LY, and X-FW contributed to the data collection. HP, Z-JW and X-GJ had the idea of the manuscript. All authors contributed to the article and approved the submitted version.

Funding

This work is supported by Chongqing medical scientific research project (2021MSXM042), General program of Chongqing Natural Science Foundation (cstc2020jcyj-msxmX0713), the Open Project Program of Nuclear Medicine and Molecular Imaging Key Laboratory of Sichuan Province.

Conflict of interest

The authors declare that the research was conducted in the absence of any commercial or financial relationships that could be construed as a potential conflict of interest.

Publisher's note

References

1. Global, regional, and national disability-adjusted life-years (DALYs) for 333 diseases and injuries and healthy life expectancy (HALE) for 195 countries and territories, 1990-2016: a systematic analysis for the Global Burden of Disease Study 2016. *Lancet (London, England)*, (2017) 390(10100): 1260–1344. doi: 10.1016/S0140-6736(17)32130-X

2. Reeh J, Therming CB, Heitmann M, Højberg S, Sørum C, Bech J, et al. Prediction of obstructive coronary artery disease and prognosis in patients with suspected stable angina. *Eur Heart J*. (2019) 40(18):1426–35. doi: 10.1093/eurheartj/ehy806

3. Kunadian V, Chieffo A, Camici PG, Berry C, Escaned J, Maas AHEM, et al. An EAPCI expert consensus document on ischaemia with non-obstructive coronary arteries in collaboration with European society of cardiology working group on coronary pathophysiology & microcirculation endorsed by coronary vasomotor disorders international study group. *Eur Heart J*. (2020) 41(37):3504–20. doi: 10.1093/eurheartj/ehaa503

4. Johnston WF, Jain A, Saad WE, Upchurch GR Chest pain from excluded inferior vena cava filter after stent placement. *J Vasc Surg Venous Lymphat Disord*. (2014) 2 (1):70–3. doi: 10.1016/j.jvsv.2013.06.001

5. Suhrs HE, Michelsen MM, Prescott E. Treatment strategies in coronary microvascular dysfunction: a systematic review of interventional studies. *Microcirculation*. (2019) 26(3):e12430. doi: 10.1111/micc.12430

6. Johnson BD, Shaw LJ, Buchthal SD, Bairey Merz CN, Kim H-W, Scott KN, et al. Prognosis in women with myocardial ischemia in the absence of obstructive coronary disease: results from the national institutes of health-national heart, lung, and blood institute-sponsored women's ischemia syndrome evaluation (WISE). *Circulation*. (2004) 109(24):2993–9. doi: 10.1161/01.CIR.0000130642.79868.B2

7. Taqueti VR, Dorbala S, Wolinsky D, Abbott B, Heller GV, Bateman TM, et al. Myocardial perfusion imaging in women for the evaluation of stable ischemic heart disease-state-of-the-evidence and clinical recommendations. *J Nucl Cardiol*. (2017) 24(4):1402–26. doi: 10.1007/s12350-017-0926-8

8. Crea F, Camici PG, Bairey Merz CN. Coronary microvascular dysfunction: an update. *Eur Heart J*. (2014) 35(17):1101–11. doi: 10.1093/eurheartj/eht513

9. Cavusoglu Y, Entok E, Timuralp B, Vardareli E, Kudaiberdieva G, Birdane A, et al. Regional distribution and extent of perfusion abnormalities, and the lung to heart uptake ratios during exercise thallium-201 SPECT imaging in patients with cardiac syndrome X. *Can J Cardiol*. (2005) 21(1):57–62. PMID: 15685304

10. Caobelli F, Haaf P, Haenny G, Pfisterer M, Zellweger MJ. Prognostic value of myocardial perfusion scintigraphy in asymptomatic patients with diabetes mellitus at high cardiovascular risk: 5-year follow-up of the prospective multicenter BARDOT trial. *Eur J Nucl Med Mol Imaging*. (2021) 48(11):3512–21. doi: 10.1007/s00259-021-05349-5

11. Kassab K, Hussain K, Torres A, Iskander F, Iskander M, Khan R, et al. The diagnostic and prognostic value of near-normal perfusion or borderline ischemia on stress myocardial perfusion imaging. *J Nucl Cardiol*. (2022) 29(2):826–35. doi: 10.1007/s12350-020-02375-y

12. Fearon WF, Nishi T, De Bruyne B, Boothroyd DB, Barbato E, Tonino P, et al. Clinical outcomes and cost-effectiveness of fractional flow reserve-guided percutaneous coronary intervention in patients with stable coronary artery disease: three-year follow-up of the FAME 2 trial (fractional flow reserve versus angiography for multivessel evaluation). *Circulation*. (2018) 137(5):480–7. doi: 10.1161/CIRCULATIONAHA.117.031907

13. Smit JM, Hermans MP, Dimitriu-Leen AC, van Rosendael AR, Dibbets-Schneider P, de Geus-Oei L-F, et al. Long-term prognostic value of single-photon emission computed tomography myocardial perfusion imaging after primary PCI for STEMI. *Eur Heart J Cardiovasc Imaging*. (2018) 19(11):1287–93. doi: 10.1093/ehjci/jex332

14. Dorbala S, Ananthasubramaniam K, Armstrong IS, Chareonthaitawee P, DePuey EG, Einstein AJ, et al. Single photon emission computed tomography (SPECT) myocardial perfusion imaging guidelines: instrumentation, acquisition, processing, and interpretation. *J Nucl Cardiol*. (2018) 25(5):1784–846. doi: 10.1007/s12350-018-1283-y

15. Jespersen L, Hvelplund A, Abildstrøm SZ, Pedersen F, Galatius S, Madsen JK, et al. Stable angina pectoris with no obstructive coronary artery disease is associated with increased risks of major adverse cardiovascular events. *Eur Heart J*. (2012) 33(6):734–44. doi: 10.1093/eurheartj/ehr331

16. Chow BJW, Small G, Yam Y, Chen L, McPherson R, Achenbach S, et al. Prognostic and therapeutic implications of statin and aspirin therapy in individuals with nonobstructive coronary artery disease: results from the CONFIRM (COronary CT angiography EvaluatioN for clinical outcomes: an InteRnational multicenter registry) registry. *Arterioscler Thromb Vasc Biol*. (2015) 35(4):981–9. doi: 10.1161/ATVBAHA.114.304351

17. Henzlova MJ, Duvall WL, Einstein AJ, Travin MI, Verberne HJ. ASNC imaging guidelines for SPECT nuclear cardiology procedures: stress, protocols, and tracers. *J Nucl Cardiol*. (2016) 23(3):606–39. doi: 10.1007/s12350-015-0387-x

18. Boerhout CKM, de Waard GA, Lee JM, Mejia-Renteria H, Lee SH, Jung J-H, et al. Prognostic value of structural and functional coronary microvascular dysfunction in patients with non-obstructive coronary artery disease; from the multicentre international ILIAS registry. *EuroIntervention*. (2022) 18(9):719–28. doi: 10.4244/EIJ-D-22-00043

19. Abdu FA, Liu L, Mohammed A-Q, Yin G, Xu B, Zhang W, et al. Prognostic impact of coronary microvascular dysfunction in patients with myocardial infarction with non-obstructive coronary arteries. *Eur J Intern Med*. (2021) 92:79–85. doi: 10.1016/j.ejim.2021.05.027

20. Alqaisi F, Albadarin F, Jaffery Z, Tzogias L, Dawod M, Jacobsen G, et al. Prognostic predictors and outcomes in patients with abnormal myocardial perfusion imaging and angiographically insignificant coronary artery disease. *J Nucl Cardiol*. (2008) 15(6):754–61. doi: 10.1007/BF03007356

21. Liu L, Abdu FA, Yin G, Xu B, Mohammed A-Q, Xu S, et al. Prognostic value of myocardial perfusion imaging with D-SPECT camera in patients with ischemia and no obstructive coronary artery disease (INOCA). *J Nucl Cardiol*. (2021) 28 (6):3025–37. doi: 10.1007/s12350-020-02252-8

22. Engbers EM, Timmer JR, Mouden M, Knollema S, Jager PL, Ottervanger JP. Prognostic value of myocardial perfusion imaging with a cadmium-zinc-telluride SPECT camera in patients suspected of having coronary artery disease. *J Nucl Med*. (2017) 58(9):1459–63. doi: 10.2967/jnumed.116.188516

23. Huang J-Y, Yen R-F, Huang C-K, Liu C-J, Cheng M-F, Chien K-L, et al. Long-term prognostic value of computed tomography-based attenuation correction on thallium-201 myocardial perfusion imaging: a cohort study. *PloS One*. (2021) 16(10):e0258983. doi: 10.1371/journal.pone.0258983

24. Jespersen L, Abildstrom SZ, Hvelplund A, Madsen JK, Galatius S, Pedersen F, et al. Burden of hospital admission and repeat angiography in angina pectoris patients with and without coronary artery disease: a registry-based cohort study. *PloS One*. (2014) 9(4):e93170. doi: 10.1371/journal.pone.0093170

25. Bugiardini R, Manfrini O, Pizzi C, Fontana F, Morgagni G. Endothelial function predicts future development of coronary artery disease: a study of women with chest pain and normal coronary angiograms. *Circulation*. (2004) 109(21):2518–23. doi: 10.1161/01.CIR.0000128208.22378.E3

26. Lee B-K, Lim H-S, Fearon WF, Yong AS, Yamada R, Tanaka S, et al. Invasive evaluation of patients with angina in the absence of obstructive coronary artery disease. *Circulation*. (2015) 131(12):1054–60. doi: 10.1161/CIRCULATIONAHA.114.012636

frontiers | Frontiers in Medicine

TYPE Original Research
PUBLISHED 15 August 2023
DOI 10.3389/fmed.2023.1171118

OPEN ACCESS

EDITED BY
Giorgio Treglia,
Ente Ospedaliero Cantonale (EOC), Switzerland

REVIEWED BY
Carmelo Caldarella,
Fondazione Policlinico Universitario A. Gemelli IRCCS, Italy
Hamid Sabet,
Massachusetts General Hospital and Harvard Medical School, United States

*CORRESPONDENCE
Pai-Yi Chiu
paiyibox@gmail.com
Guang-Uei Hung
106143@gmail.com
Greta S. P. Mok
gretamok@um.edu.mo

†These authors share senior authorship

RECEIVED 21 February 2023
ACCEPTED 17 July 2023
PUBLISHED 15 August 2023

CITATION
Du Y, Jiang H, Lin C-N, Peng Z, Sun J, Chiu P-Y, Hung G-U and Mok GSP (2023) Generative adversarial network-based attenuation correction for ^{99m}Tc-TRODAT-1 brain SPECT. *Front. Med.* 10:1171118. doi: 10.3389/fmed.2023.1171118

Generative adversarial network-based attenuation correction for ^{99m}Tc-TRODAT-1 brain SPECT

Yu Du[1,2], Han Jiang[1], Ching-Ni Lin[3], Zhengyu Peng[1], Jingzhang Sun[1], Pai-Yi Chiu[4*†], Guang-Uei Hung[5*†] and Greta S. P. Mok[1,2*†]

[1]Biomedical Imaging Laboratory (BIG), Department of Electrical and Computer Engineering, Faculty of Science and Technology, University of Macau, Taipa, Macau SAR, China, [2]Center for Cognitive and Brain Sciences, Institute of Collaborative Innovation, University of Macau, Taipa, Macau SAR, China, [3]Department of Nuclear Medicine, Show Chwan Memorial Hospital, Lukong Town, Changhua County, Taiwan, [4]Department of Neurology, Show Chwan Memorial Hospital, Lukong Town, Changhua County, Taiwan, [5]Department of Nuclear Medicine, Chang Bing Show Chwan Memorial Hospital, Lukong Town, Changhua County, Taiwan

Background: Attenuation correction (AC) is an important correction method to improve the quantification accuracy of dopamine transporter (DAT) single photon emission computed tomography (SPECT). Chang's method was developed for AC (Chang-AC) when CT-based AC was not available, assuming uniform attenuation coefficients inside the body contour. This study aims to evaluate Chang-AC and different deep learning (DL)-based AC approaches on ^{99m}Tc-TRODAT-1 brain SPECT using clinical patient data on two different scanners.

Methods: Two hundred and sixty patients who underwent ^{99m}Tc-TRODAT-1 SPECT/CT scans from two different scanners (scanner A and scanner B) were retrospectively recruited. The ordered-subset expectation-maximization (OS-EM) method reconstructed 120 projections with dual-energy scatter correction, with or without CT-AC. We implemented a 3D conditional generative adversarial network (cGAN) for the indirect deep learning-based attenuation correction (DL-AC$_\mu$) and direct deep learning-based attenuation correction (DL-AC) methods, estimating attenuation maps (μ-maps) and attenuation-corrected SPECT images from non-attenuation-corrected (NAC) SPECT, respectively. We further applied cross-scanner training (cross-scanner indirect deep learning-based attenuation correction [cull-AC$_\mu$] and cross-scanner direct deep learning-based attenuation correction [call-AC]) and merged the datasets from two scanners for ensemble training (ensemble indirect deep learning-based attenuation correction [eDL-AC$_\mu$] and ensemble direct deep learning-based attenuation correction [eDL-AC]). The estimated μ-maps from (c/e)DL-AC$_\mu$ were then used in reconstruction for AC purposes. Chang's method was also implemented for comparison. Normalized mean square error (NMSE), structural similarity index (SSIM), specific uptake ratio (SUR), and asymmetry index (%ASI) of the striatum were calculated for different AC methods.

Results: The NMSE for Chang's method, DL-AC$_\mu$, DL-AC, cDL-AC$_\mu$, cDL-AC, eDL-AC$_\mu$, and eDL-AC is 0.0406 ± 0.0445, 0.0059 ± 0.0035, 0.0099 ± 0.0066, 0.0253 ± 0.0102, 0.0369 ± 0.0124, 0.0098 ± 0.0035, and 0.0162 ± 0.0118 for scanner A and 0.0579 ± 0.0146, 0.0055 ± 0.0034, 0.0063 ± 0.0028, 0.0235 ± 0.0085, 0.0349 ± 0.0086, 0.0115 ± 0.0062, and 0.0117 ± 0.0038 for scanner B, respectively. The SUR and %ASI results for DL-AC$_\mu$ are closer to CT-AC, Followed by DL-AC, eDL-AC$_\mu$, cDL-AC$_\mu$, cDL-AC, eDL-AC, Chang's method, and NAC.

10.3389/fmed.2023.1171118

Conclusion: All DL-based AC methods are superior to Chang-AC. DL-AC$_\mu$ is superior to DL-AC. Scanner-specific training is superior to cross-scanner and ensemble training. DL-based AC methods are feasible and robust for ^{99m}Tc-TRODAT-1 brain SPECT.

KEYWORDS

deep learning, generative adversarial network, attenuation correction, dopamine transporter SPECT, ^{99m}Tc-TRODAT-1

Introduction

Dopamine transporter (DAT) single photon emission computed tomography (SPECT) is well established and widely used for Parkinson's disease (PD) diagnosis. The current PD diagnosis from DAT SPECT is mainly based on the visual assessment of the decreased striatal uptakes and the asymmetry of left and right striatum uptake for indirect measurement of DAT decrement (1). Iodine ^{123}-radiolabeled 2β-carbomethoxy-3β-(4-iodophenyl)-N-(3-fluoropropyl) nortropane (^{123}I-FP-CIT) (2) and ^{99m}Tc-[2[[2-[[[3-(4-chlorophenyl)-8-methyl-8-azabicyclo[3,2,1]-oct-2-yl]-methyl](2-mercaptoethyl) amino]ethyl]amino]ethane-thiolato(3-)-N2,N2′,S2,S2]oxo-[1R-(exo-exo)])) (99mTc-TRODAT-1) (3) are two common tracers for DAT SPECT, with the former more common in Western countries and the latter more common in Asia. ^{123}I-FP-CIT is a European Medicines Agency (EMA) and U.S. Food and Drug Administration (FDA)-approved tracer to differentiate PD from essential tremor. Compared to ^{123}I-FP-CIT, ^{99m}Tc-TRODAT-1 has a lower binding ratio of the striatum, lower thyroid uptake, and can be produced at a lower cost without a cyclotron. Though the clinical utility of CT-based attenuation correction (AC) (4) is controversial in ^{123}I-FP-CIT SPECT (5), CT-based AC has been proven to improve SPECT image quality and quantification accuracy in DAT SPECT (6, 7). In hybrid SPECT/CT systems, CT scans can be used as attenuation maps (μ-maps) for AC in brain SPECT reconstructions. However, many existing SPECT-only systems or recently proposed dedicated brain SPECT images (8) are not integrated with CT scanners. In addition, the extra CT radiation dose in SPECT/CT poses substantial health concerns (9) and is not routinely performed in some centers. Potential mismatches between SPECT and CT images due to the involuntary and voluntary movements of PD patients can also degrade AC performance (10, 11). CT-less AC is thus of significant research and clinical impact for DAT SPECT.

Chang's AC method is a conventional CT-less AC method for brain SPECT that assumes a uniform attenuation coefficient for the volume of interest (VOI) (12). However, the assumption of a uniform μ-map would introduce estimation errors to AC, especially for bones. Deep learning (DL) methods recently emerged as a promising alternative for SPECT AC (13). Shi et al. (14) and Yang et al. (15) first performed DL-based AC on SPECT. Shi et al. (14) generated μ-maps from non-attenuation-corrected (NAC) SPECT images (indirect deep learning-based attenuation correction [DL-AC$_\mu$]) using a 3D conditional generative adversarial network (cGAN) for myocardial perfusion (MP) SPECT. Yang et al. (15) and Chen et al. (16) estimated AC MP SPECT images directly from NAC MP SPECT images (direct deep learning-based attenuation correction [DL-AC]) using different deep convolutional neural networks. Chen et al. (17) and Du et al. (18) compared the AC performance of DL-AC and DL-AC$_\mu$ and demonstrated that indirect estimation of μ-maps is superior to direct estimation of AC SPECT on MP SPECT. Chen et al. (19) further investigated the feasibility of transfer learning-based AC for MP SPECT images from different scanners, tracers, and acquisition protocols. For brain SPECT, Sakaguchi et al. (20) developed a 2D convolutional neural networks (CNN)-based autoencoder for the direct generation of AC from NAC images for brain perfusion SPECT. Murata et al. (21) compared Chang's AC with a 2D autoencoder and U-Net for DL-AC for brain perfusion SPECT. Chen et al. have proposed CNN-based μ-map generation for brain perfusion SPECT (22) and ^{123}I-FP-CIT SPECT (23) using NAC SPECT input in simulations, demonstrating improved absolute quantification accuracy. A diagram explaining DL-AC$_\mu$ and DL-AC is shown in Figure 1. In this study, we implemented a conventional first-order Chang's method and a 3D cGAN for DL-AC and DL-AC$_\mu$, respectively. We then compared their performance for ^{99m}Tc-TRODAT-1 brain SPECT based on clinical data from two scanners in a single center with different acquisition protocols, field-of-view, and voxel sizes.

Abbreviations: SPECT, single photon emission computed tomography; DAT, dopamine transporter; ^{123}I-FP-CIT, Iodine 123-radiolabeled 2β-carbomethoxy-3β-(4-iodophenyl)-N-(3-fluoropropyl) nortropane; 99mTc-TRODAT-1, 99mTc-[2[[2-[[[3-(4-chlorophenyl)-8-methyl-8-azabicyclo[3,2,1]-oct-2-yl]-methyl](2-mercaptoethyl)amino]ethyl]amino]ethane-thiolato(3-)-N2,N2′,S2,S2]oxo-[1R-(exoexo)]); AC, attenuation correction; μ-map, attenuation map; DL, deep learning; cGAN, conditional generative adversarial network; CNN, convolutional neural networks; OS-EM, ordered-subset expectation-maximization; DL-AC$_\mu$, indirect deep learning-based attenuation correction; DL-AC, direct deep learning-based attenuation correction; cDL-AC$_\mu$, cross-scanner indirect deep learning-based attenuation correction; cDL-AC, cross-scanner direct deep learning-based attenuation correction; eDL-AC$_\mu$, ensemble indirect deep learning-based attenuation correction; eDL-AC, ensemble direct deep learning-based attenuation correction; NMSE, normalized mean square error; SSIM, structural similarity index; SUR, specific uptake ratio; %ASI, asymmetry index.

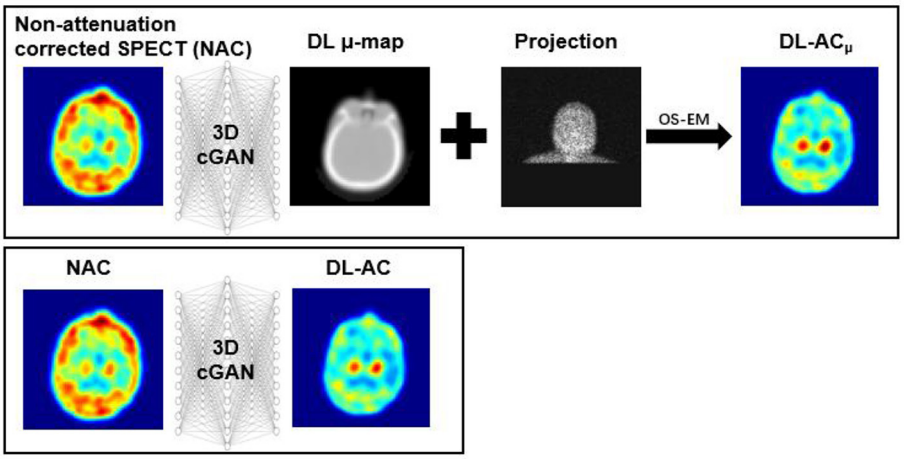

FIGURE 1
Diagram of DL-AC$_\mu$ (indirect) and DL-AC (direct) methods.

TABLE 1 Demographic information for the patient study.

	Scanner A		Scanner B	
Dataset	Training + validation	Testing	Training + validation	Testing
Patient number	100	30	100	30
Age (years)	72.74 ± 13.14 (range: 29 to 98)	71.17 ± 10.28 (range: 49 to 88)	70.88 ± 9.84 (range: 35 to 87)	72.20 ± 7.85 (range: 55 to 85)
p-value	0.56		0.50	
Sex	50 male /50 female	18 male/12 female	55 male/45 female	14 male/16 female
p-value	0.067		0.096	

TABLE 2 Acquisition protocols for the patient study.

	Scanner A	Scanner B
Hospital	Chang Bing Show Chwan Memorial Hospital	Show Chwan Memorial Hospital
Model	GE Infinia Hawkeye	SIEMENS Symbia
Injection activity	1,110 MBq	925 MBq
Acquisition time (s/view)	60	45
Collimator type	LEHR	
Primary/scatter window (keV)	126 to 154/114 to 126	126 to 154/109 to 126
Projection number	120 over 360°	90 over 360° 31, 120 over 360° (99)
Reconstruction	OS-EM; 8 iterations × 4 subsets	
	Dual-energy window scatter correction, with or without attenuation correction	
Post-reconstruction filter	3D Gaussian filter	3D Gaussian filter
	σ = 0.8 voxels	σ = 1.2 voxels
Matrix/voxel size (mm)	64 × 64 × 64/4.4181 (30); 128 × 128 × 128/2.761 (100)	128 × 128 × 128/2.6970
CT scan	4-slice, 2.5 mAs,	2-slice, 10 mAs,
	140 kVp, 1.9 pitch,	130 kVp, 1.5 pitch,
	5 mm thickness	3 mm thickness

Materials and methods

Clinical dataset

Two hundred and sixty anonymized patients (Table 1) who underwent ^{99m}Tc-TRODAT-1 scan in two widely used clinical SPECT/CT systems (Infinia Hawkeye, GE Healthcare, Wauwatosa, WI, USA; Symbia, Siemens Healthineers, Erlangen, Germany) from two affiliated centers were retrospectively recruited under the local ethics approval (SCMH_IRB No: 1110704). Unpaired *t*-test on age and χ^2 test on gender showed no significant difference between the training-validation dataset and the testing dataset (all ps>0.05). The acquisition protocols of the two scanners are shown in Table 2. CT was acquired for SPECT AC after the SPECT scan. The CT was manually registered to SPECT by the scanner software and converted to the μ-map using a bilinear model (4). No mismatches were observed between the CT and SPECT images in this study.

SPECT projections were reconstructed with dual-energy window scatter correction (24), with or without CT-based AC. The SPECT images with a matrix size of 64 × 64 × 64 and a voxel size of 0.4418 cm/voxel from scanner A were resampled to a matrix size of 128 × 128 × 128 and a voxel size of 0.2761 cm/voxel. We implemented the first-order Chang's method for conventional CT-less AC in brain SPECT. The uniform μ-maps were based on the NAC SPECT brain mask. An intensity threshold of 2 was used to separate the brain from the background. The masks were applied with uniform attenuation coefficients

of 0.148 cm^{-1} (25). The 0.148 cm^{-1} attenuation coefficients were then converted to 0.0408 $voxel^{-1}$ for scanner A and 0.0399 $voxel^{-1}$ for scanner B by multiplying with a voxel size of 0.2761 cm/voxel and 0.2697 cm/voxel to get the Chang's method μ-maps, which were used in reconstruction for Chang-AC.

Conditional generative adversarial network

We implemented a 3D cGAN (18, 26) using Tensorflow on an NVIDIA GeForce RTX 3090 GPU with 24 GB RAM. An Adam optimizer was applied using an adaptive learning rate with an initial value of 0.001 and trained for up to 400 epochs. For our cGAN (Figure 2), a U-Net-based generator is trained to generate a realistic μ-map or AC SPECT, while a CNN-based discriminator is trained to differentiate between the true μ-map and the generated μ-map or between the true AC SPECT and the generated AC SPECT. The U-Net-based generator consists of encoder, bottleneck, and decoder layers. Each layer contains a 3 × 3 × 3 convolution, a batch normalization, and a leaky rectified linear unit (LeakyReLU). For encoder layers, a down-sampling layer of 2 × 2 × 2 max pooling was connected to down-sample feature maps. For bottleneck layers, a dropout layer with a 50% dropout rate was used to avoid over-fitting. For decoder layers, the up-sampling layer was used to recover the input image size. Skip connection was applied for DL-AC but not for DL-AC_μ due to the large structural difference between SPECT and CT images (18, 27).

L_1 loss was used to train the generator as it can enforce low-frequency correctness and encourage less blurring as compared to the commonly used L_2 (28). The cross-entropy-based discriminator loss (L_D) was used to train the discriminator. The discriminator loss combined with generator loss (L_1) was used to train the generator.

The objective function of cGAN can be expressed as follows:

$$G^* = \arg\min_G \max_D V_{L_D}(G, D) + \lambda V_{L1}(G) \quad (1)$$

where λ is an adjustable parameter (28) [$\lambda = 20$ in this study (14)] used to control the balance between objective function $V_{L_D}(G, D)$ and $V_{L1}(G)$.

Whole images instead of patches were used as training input to provide more information on the 3D patient contour (18). The patient dataset of each scanner was divided into 90, 10, and 30 for training, validation, and testing, respectively. Data augmentation by horizontal and vertical flips was used to enhance the training dataset, i.e., a total of 270 datasets were used for training. As supervised learning methods, the AC SPECT and NAC SPECT images were paired to train DL-AC, while the μ-maps and NAC SPECT images were paired to train DL-AC_μ. The input NAC SPECT images for DL-AC_μ were normalized to a range of [0, 1], better matching the range of attenuation coefficients from the μ-maps. Network hyperparameters were chosen based on our previous DL-based AC for MP SPECT, i.e., 3 layers and 48 feature maps for DL-AC_μ and 2 layers and 48 feature maps for DL-AC (18).

To confirm the robustness of the DL-based AC methods, we applied cross-scanner training (cross-scanner indirect deep learning-based attenuation correction [cDL-AC_μ] and cross-scanner direct deep learning-based attenuation correction [cDL-AC]), i.e., testing data from scanner A based on a model trained from scanner B and vice versa. We also merged the datasets from two scanners for ensemble training (ensemble indirect deep learning-based attenuation correction [eDL-AC_μ] and ensemble direct deep learning-based attenuation correction [eDL-AC]). The same data augmentation technique used in scanner-specific training was applied in cross-scanner and ensemble training.

Data analysis

Normalized mean square error (NMSE) and structural similarity index (SSIM) for the whole brain were computed on the NAC, Chang's AC, and DL-based AC images as compared to the CT-AC SPECT images. The count profile across the striatum region was also drawn to measure the count distribution of different AC methods.

Specific uptake ratio (SUR) (Equation 2) of the whole striatum to the background regions and asymmetry index (%ASI) (Equation 3) of the left and right striatum were calculated based on the striatal VOIs delineated by an experienced nuclear medicine physician (Figure 3). The 2D striatal regions of interest (ROIs) were delineated slice by slice, stacking to form a 3D VOI. For the background, a 2D ROI (10 pixels × 6 pixels) in the cerebellum region was chosen, excluding ventricular regions. Bland–Altman plots were applied to SUR and %ASI results to evaluate the potential difference between different AC methods as compared to CT-AC. A paired t-test was performed on NMSE, SSIM between different DL-based methods, and on SUR and %ASI each between AC method and CT-AC. Bonferroni correction was applied for tests with multiple comparisons.

$$SUR = \frac{MeanCounts_{striatum} - MeanCounts_{background}}{MeanCounts_{background}} \quad (2)$$

$$\%ASI = \left| \frac{SUR_{left\ striatum} - SUR_{right\ striatum}}{SUR_{left\ striatum} + SUR_{right\ striatum}} \right| \times 100\% \quad (3)$$

Results

Figures 4A, B shows sample Chang's μ-map, DL-AC_μ, cDL-AC_μ, and eDL-AC_μ generated μ-maps of scanner A and corresponding error maps using CT-based μ-map as reference. The brain contours are well recovered, while the bony structures could be better restored for DL-AC_μ. Figures 4C, D shows SPECT images of different AC methods and corresponding error maps using CT-AC SPECT as a reference. Three axial slices containing the highest striatum counts are displayed for comparison. All DL-based AC methods show improved image quality as compared to NAC and Chang-AC, while DL-AC_μ is better than DL-AC from a visual assessment based on the error maps. The errors are increased by cross-scanner and ensemble training, while c/eDL-AC_μ has fewer errors than the corresponding c/eDL-AC. Figures 5A, B shows the sample results of Chang's μ-maps, different DL-AC_μ generated μ-maps, and SPECT images of different AC methods on scanner B.

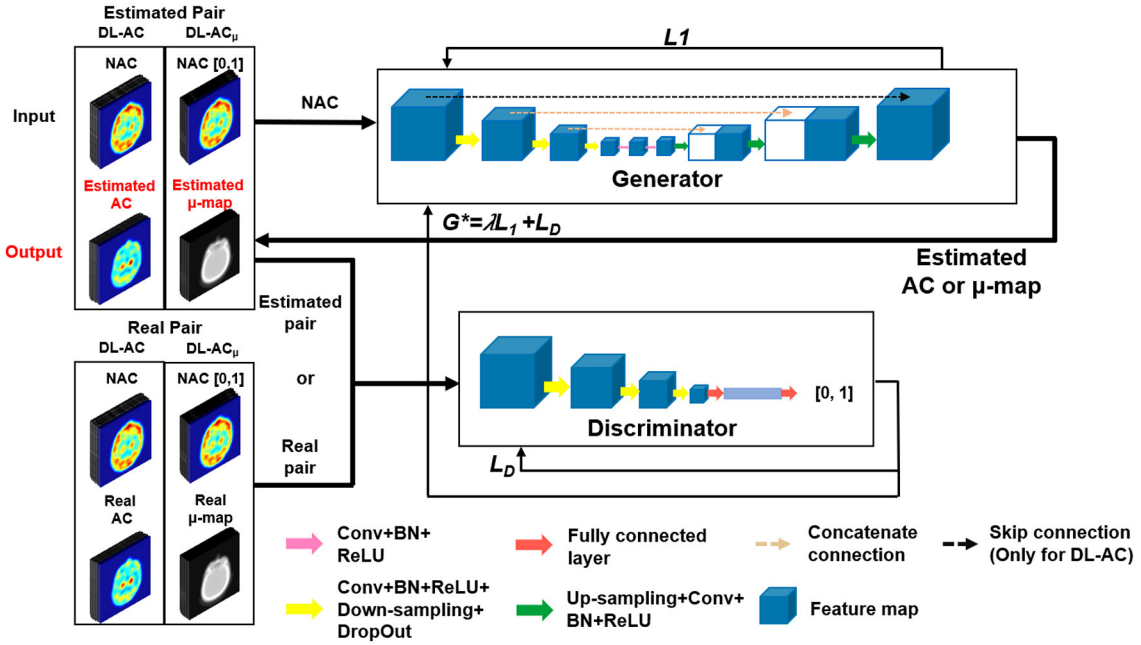

FIGURE 2
Diagram of 3D cGAN used in this study.

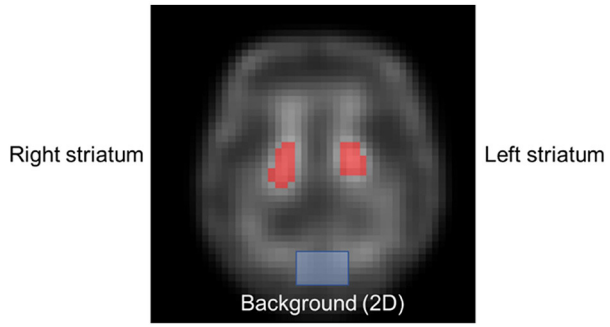

FIGURE 3
Sample delineated striatum ROIs (red mask) and background (blue mask).

The results are similar to scanner A. Both DL-based AC methods are better than Chang-AC and NAC, while DL-AC$_\mu$ is better than DL-AC. Though the cross-scanner and ensemble training DL-based methods show performance degradation compared to scanner-specific training, they still show fewer errors than Chang-AC. The 2D count profiles of 40 pixels across the striatum region by different AC methods for the same patients are shown in Figure 6. The profiles of all DL-based AC methods are much closer to CT-AC compared to Chang-AC and NAC, while the profile of DL-AC$_\mu$ is also less deviated from CT-AC as compared to DL-AC. eDL-AC$_\mu$ has errors between DL-AC$_\mu$ and DL-AC, followed by cDL-AC$_\mu$, cDL-AC, and eDL-AC.

The NMSE and SSIM results of the two scanners are shown in Tables 3, 4. For μ-maps, DL-AC$_\mu$ achieves the lowest NMSE and highest SSIM (all ps < 0.001), followed by eDL-AC$_\mu$ and cDL-AC$_\mu$ for both scanners. All DL-based methods have generated better μ-maps than Chang's μ-maps for both scanners. For SPECT images, the NMSE of all AC methods is lower than NAC. All DL-based AC methods are better than Chang-AC. DL-AC$_\mu$ has a significantly lower NMSE than DL-AC ($p < 0.05$) for both scanners. The NMSE values of eDL-AC$_\mu$ and cDL-AC$_\mu$ are lower than eDL-AC and cDL-AC, respectively. The SSIM follows the same trend as the NMSE. The SUR and %ASI results are shown in Table 5. There is no significant difference between DL-AC$_\mu$/DL-AC and CT-AC ($p > 0.05$) on SUR for both scanners. There is also no significant difference between DL-AC$_\mu$/DL-AC/eDL-AC$_\mu$/cDL-AC$_\mu$ and CT-AC ($p > 0.05$) on %ASI for both scanners. Cross-scanner and ensemble training increase the errors on SUR and %ASI scanner-specific training.

The Bland–Altman plots of SUR processed by NAC, Chang-AC, and DL-based methods using CT-AC as a reference are shown in Figure 7. NAC shows lower SUR values (mean difference of −0.3984 for scanner A and −0.1770 for scanner B) than CT-AC. Chang-AC shows an overestimated attenuation (mean difference of +0.2532 for scanner A and +0.1262 for scanner B). All DL-based AC methods have a narrower distribution than NAC and Chang-AC, except cDL-AC and eDL-AC. Both DL-AC$_\mu$ and DL-AC have similar SUR values to CT-AC. DL-AC$_\mu$ shows a narrower distribution compared to DL-AC with a smaller standard deviation, i.e., 95% confidence interval (CI) of [−0.0733, 0.1948] vs. [−0.1780, 0.1398] for scanner A and [−0.0291, 0.0469] vs. [−0.1424, 0.0469] for scanner B. Figure 8 shows the Bland–Altman plots of the %ASI results, which are similar to those of SUR. The 95% CI with CT-AC for NAC, Chang-AC, DL-AC$_\mu$, and DL-AC are [−53.65, 69.51], [−21.44, 20.38], [−3.798, 5.993], [−6.203, 8.186] for scanner A and [−11.59, 19.25], [−8.300, 7.009], [−3.345, 3.352], [−5.583,

10.3389/fmed.2023.1171118

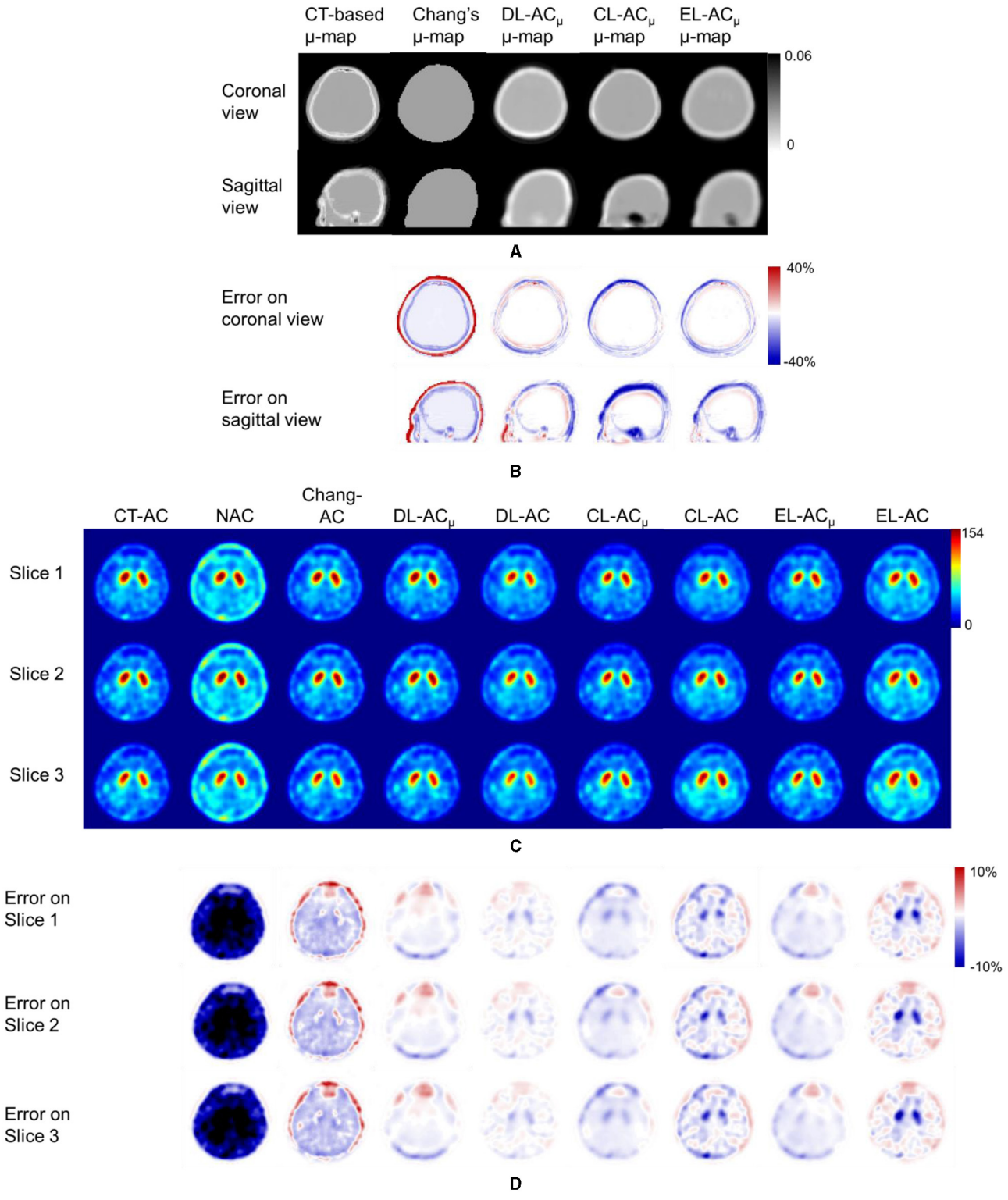

FIGURE 4
Representative image results of a 38-year-old male patient on scanner A. **(A)** Sample μ-maps generated by different methods. **(B)** Corresponding error maps of different μ-maps as compared to CT-based μ-map. **(C)** Sample axial slices with the highest striatum uptake from different AC SPECT images. **(D)** Corresponding error maps of different AC methods as compared to CT-AC.

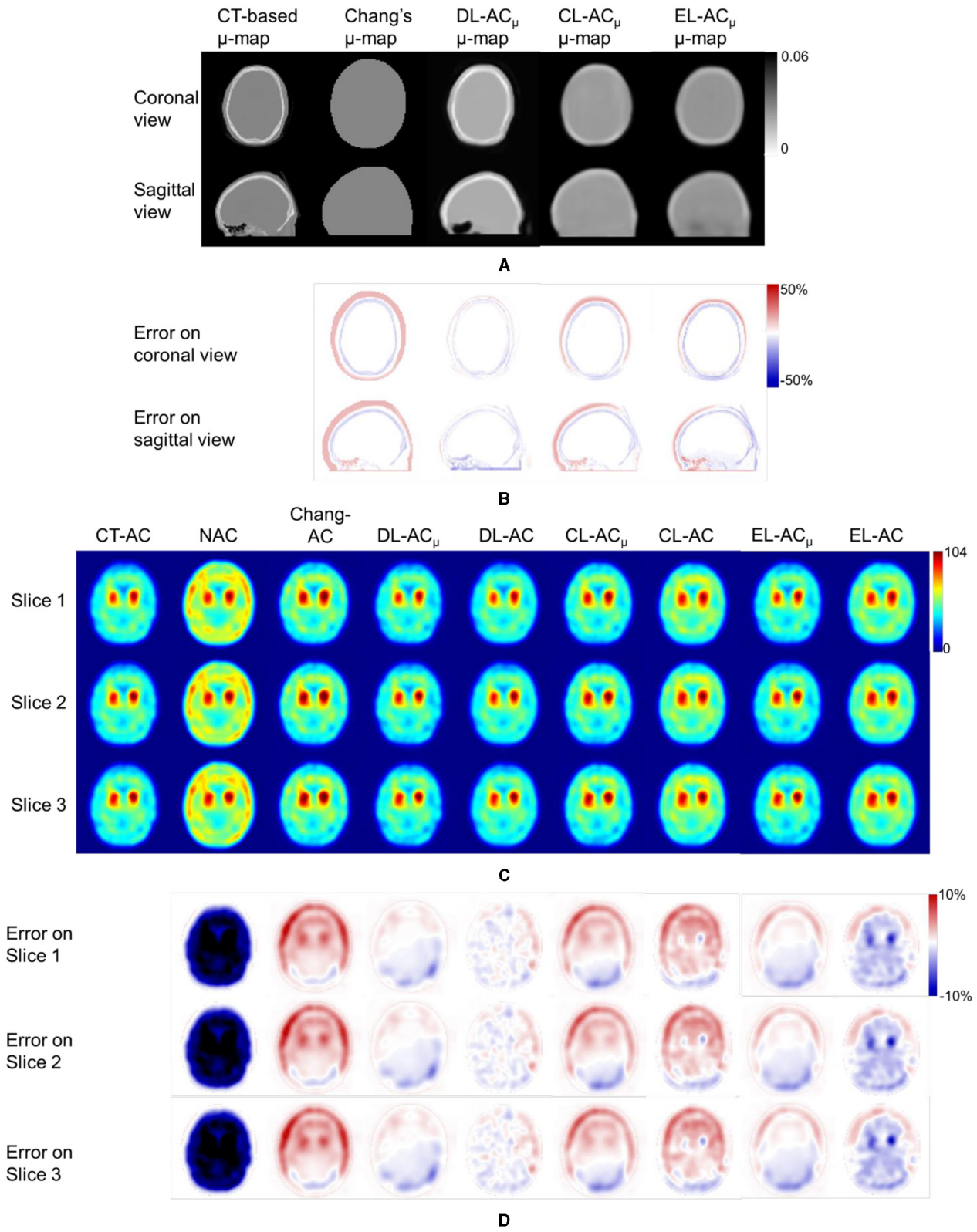

FIGURE 5
Representative results of a 71-year-old female patient on scanner B. **(A)** Sample μ-maps generated by different methods. **(B)** Corresponding error maps of different μ-maps as compared to CT-based μ-map. **(C)** Sample axial slices with the highest striatum uptake from different AC SPECT images. **(D)** Corresponding error maps of different AC methods as compared to CT-AC.

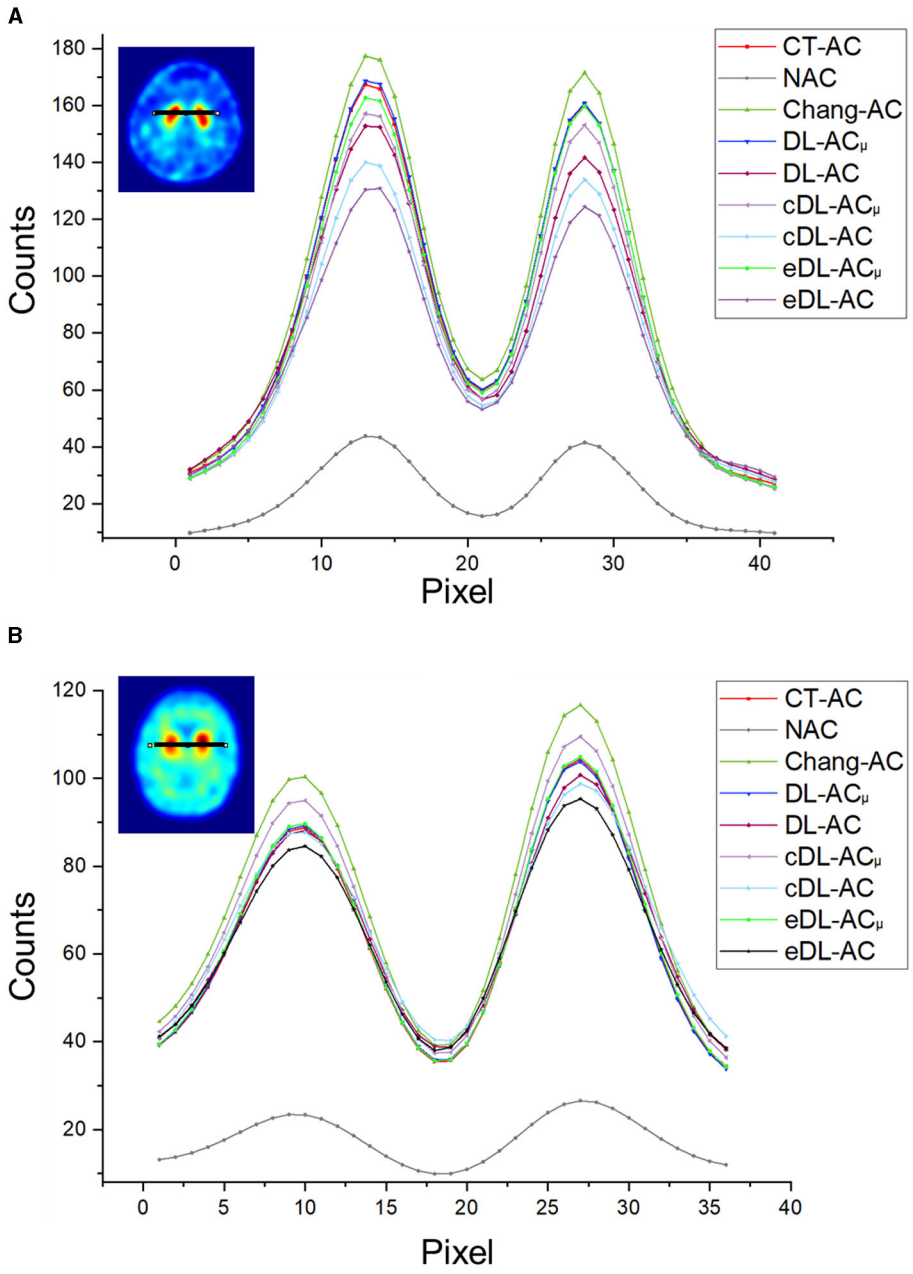

FIGURE 6
Count profiles of different AC methods of **(A)** a 38-year-old male patient on scanner A from Figure 4 and **(B)** a 71-year-old female patient on scanner B from Figure 5.

4.675] for scanner B, respectively. For cross-scanner and ensemble training, the 95% CI with CT-AC for cDL-AC$_\mu$, cDL-AC, eDL-AC$_\mu$, and eDL-AC are [−16.30, 22.87], [−18.57, 24.87], [−6.203, 8.186], [−17.94, 28.38] for scanner A, and [−5.025, 8.762], [−7.441, 8.005], [−5.893, 7.168], [−9.158, 8.832] for scanner B.

Discussion

Our study is the first DL-based AC study using clinical ^{99m}Tc-TRODAT-1 brain SPECT data. In addition, we recruited patient data from two scanners with different acquisition protocols, field-of-view, and voxel sizes to show the robustness of DL-based AC methods on different scanners. Despite slight differences between the two scanners, e.g., brain orientation and field-of-view, spatial resolution, and CT slice thickness, their results showed similar trends for different AC methods. Murata et al. (21) demonstrate that 2D autoencoder and U-Net-based direct DL-AC are better than NAC and Chang's AC for brain perfusion SPECT. Chen et al. (23) suggest that CNN-estimated μ-map could be a promising substitute for CT-based μ-map for ^{123}I-FP-CIT scans. Our results are consistent with theirs in that DL-based AC is better than NAC

TABLE 3 NMSE and SSIM measurements on μ-maps generated by different methods on 30 tested patients of scanner A and 30 tested patients of scanner B.

Scanner	A		B	
Metric	NMSE	SSIM	NMSE	SSIM
Chang-AC	0.2933 ± 0.0383	**0.9766** ± 0.0072	**0.2824** ± 0.0306	**0.9718** ± 0.0064
DL-AC_μ	0.0348 ± 0.0133	0.9935 ± 0.0127	0.0591 ± 0.0185	0.9917 ± 0.0042
cDL-AC_μ	0.1427 ± 0.0305	0.9856 ± 0.0124	0.1345 ± 0.0345	0.9849 ± 0.0051
p-value	2.11×10^{-15}	4.74×10^{-17}	6.91×10^{-24}	4.98×10^{-15}
eDL-AC_μ	0.0532 ± 0.0158	0.9917 ± 0.0137	0.0702 ± 0.0215	0.9916 ± 0.0034
p-value	1.42×10^{-8}	2.97×10^{-23}	8.52×10^{-7}	2.66×10^{-8}

TABLE 4 NMSE and SSIM measurements on SPECT images with different AC methods on 30 tested patients of scanner A and 30 tested patients of scanner B.

Scanner	A		B	
Metric	NMSE	SSIM	NMSE	SSIM
NAC	0.4495 ± 0.0193	0.9187 ± 0.0977	0.3900 ± 0.0338	0.9038 ± 0.0170
Chang-AC	0.0406 ± 0.0445	0.9415 ± 0.0144	0.0579 ± 0.0146	0.9562 ± 0.0081
DL-AC_μ	0.0059 ± 0.0035	0.9982 ± 0.0036	0.0055 ± 0.0034	0.9973 ± 0.0011
DL-AC	0.0099 ± 0.0066	0.9974 ± 0.0016	0.0063 ± 0.0028	0.9938 ± 0.0017
p-value	1.90×10^{-4}	1.84×10^{-3}	3.68×10^{-4}	2.34×10^{-19}
cDL-AC_μ	0.0253 ± 0.0102	0.9913 ± 0.0136	0.0235 ± 0.0085	0.9932 ± 0.0025
cDL-AC	0.0369 ± 0.0124	0.9900 ± 0.0027	0.0349 ± 0.0086	0.9930 ± 0.0019
p-value	3.80×10^{-4}	1.07×10^{-3}	4.46×10^{-7}	0.11
eDL-AC_μ	0.0098 ± 0.0035	0.9935 ± 0.0027	0.0115 ± 0.0062	0.9963 ± 0.0017
eDL-AC	0.0162 ± 0.0118	0.9965 ± 0.0024	0.0117 ± 0.0038	0.9950 ± 0.0017
p-value	6.92×10^{-27}	2.11×10^{-2}	0.67	1.24×10^{-14}

TABLE 5 SUR and %ASI measurements on SPECT images with different AC methods on 30 tested patients of scanner A and 30 tested patients of scanner B.

Scanner	A		B	
Metric	SUR (*p*-value)	%ASI (*p*-value)	SUR (*p*-value)	%ASI (*p*-value)
CT-AC	0.71 ± 0.33	11.75 ± 15.52	0.67 ± 0.21	9.01 ± 7.37
NAC	0.40 ± 0.18 (2.47×10^{-16})	19.88 ± 23.59 (8.92×10^{-4})	0.49 ± 0.22 (2.65×10^{-11})	12.83 ± 12.43 (1.24×10^{-2})
Chang-AC	0.80 ± 0.38 (2.75×10^{-2})	10.17 ± 15.90 (8.13×10^{-3})	0.76 ± 0.26 (5.28×10^{-16})	8.13 ± 6.54 (1.85×10^{-3})
DL-AC_μ	0.68 ± 0.37 (0.13)	12.54 ± 14.93 (0.31)	0.68 ± 0.21 (0.12)	9.01 ± 7.17 (0.99)
DL-AC	0.77 ± 0.35 (4.68×10^{-5})	13.01 ± 20.46 (0.07)	0.62 ± 0.20 (0.08)	8.83 ± 8.01 (0.87)
cDL-AC_μ	0.59 ± 0.40 (1.70×10^{-9})	12.88 ± 15.63 (0.11)	0.74 ± 0.22 (1.82×10^{-9})	8.90 ± 7.43 (0.91)
cDL-AC	0.55 ± 0.38 (3.34×10^{-10})	13.44 ± 21.58 (2.65×10^{-11})	0.70 ± 0.22 (2.11×10^{-2})	8.54 ± 7.64 (5.70×10^{-2})
eDL-AC_μ	0.64 ± 0.35 (0.09)	12.65 ± 15.19 (0.55)	0.68 ± 0.21 (0.13)	9.04 ± 8.02 (0.96)
eDL-AC	0.58 ± 0.41 (9.55×10^{-9})	13.25 ± 21.03 (2.50×10^{-5})	0.53 ± 0.22 (3.87×10^{-9})	10.97 ± 10.31 (3.87×10^{-2})

and Chang's method. We further demonstrate that the generation of μ-map is superior to the direct generation of AC SPECT for ^{99m}Tc-TRODAT-1 SPECT.

Furthermore, to the best of our knowledge, there is also no comparison of Chang's method with direct and indirect DL-based AC methods for DAT SPECT. As expected, the results show that Chang-AC has generally better image quality and quantitative results than NAC. However, the assumption of uniform attenuation coefficients over the whole brain is obviously problematic for brain SPECT, as attenuation coefficients for skull bone (0.21∼0.27

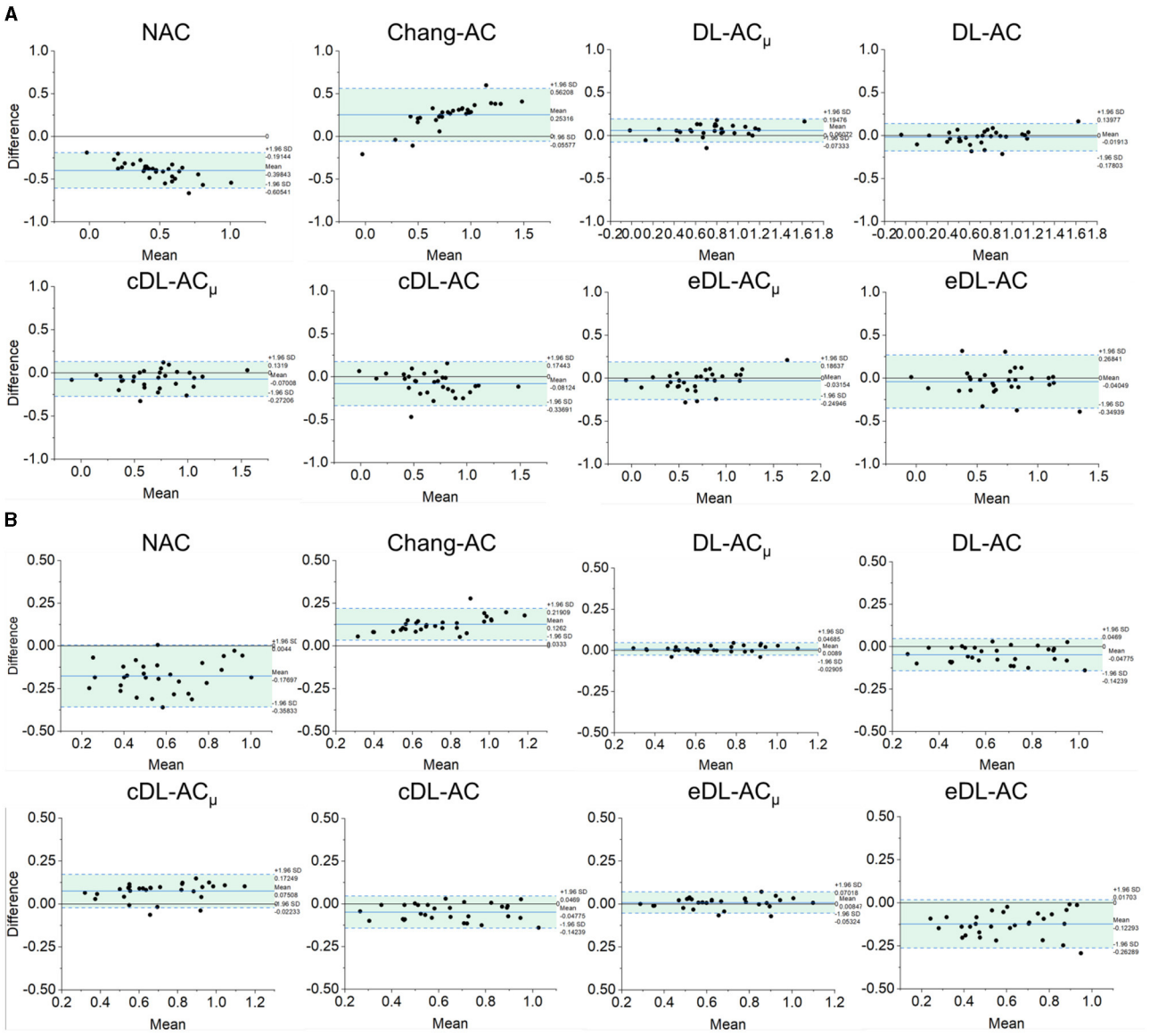

FIGURE 7
Bland–Altman plots of SUR results of different AC methods, using CT-AC as the reference of **(A)** scanner A and **(B)** scanner B (the dotted lines indicate 95% CI, and the blue lines indicate the mean values).

cm^{-1}), soft tissues (0.14∼0.15 cm^{-1}), and nasal cavity or mouth (∼0 cm^{-1}) are quite different based on the measurements on our data, consistent with previous measurements (4). There are also potential errors in the estimation of the brain contour on SPECT-reconstructed images in Chang's method. In this study, Chang's μ-maps are ∼2–4 voxels larger than the original CT-based μ-maps in three dimensions (Figure 4). This is probably attributed to the inherent limitation of the use of thresholding method to generate Chang's μ-maps (25). A larger μ-map would lead to an overestimation of attenuation outside the skull region, i.e., the red rim in Figures 4B, 5B. Thus, DL-based methods could provide a promising alternative.

For DL-AC$_\mu$, the μ-maps can generally be estimated well for both scanners. That could be attributed to NAC SPECT images providing a rough estimate of the brain contour based on the background uptake. For all quantitative indices, all AC methods significantly improve the image quality as compared to NAC, while both DL-based methods are significantly better than Chang-AC (Figures 4–8). The use of a DL-generated μ-map for the AC purpose outperforms a direct DL-AC approach, even with cross-scanner and ensemble training, showing better robustness of indirect DL-AC$_\mu$ than direct DL-AC, which is consistent with our previous MP SPECT study (18).

Although the cross-scanner and ensemble training models have better NMSE and SSIM than Chang-AC, their performance is still inferior to scanner-specific training. This could be caused by the differences between the two scanners' data, e.g., voxel size, injection dose, acquisition time, and patient positioning, leading to slightly different SPECT and CT image characteristics. Transfer learning aims to address this problem by fine-tuning the pre-trained model

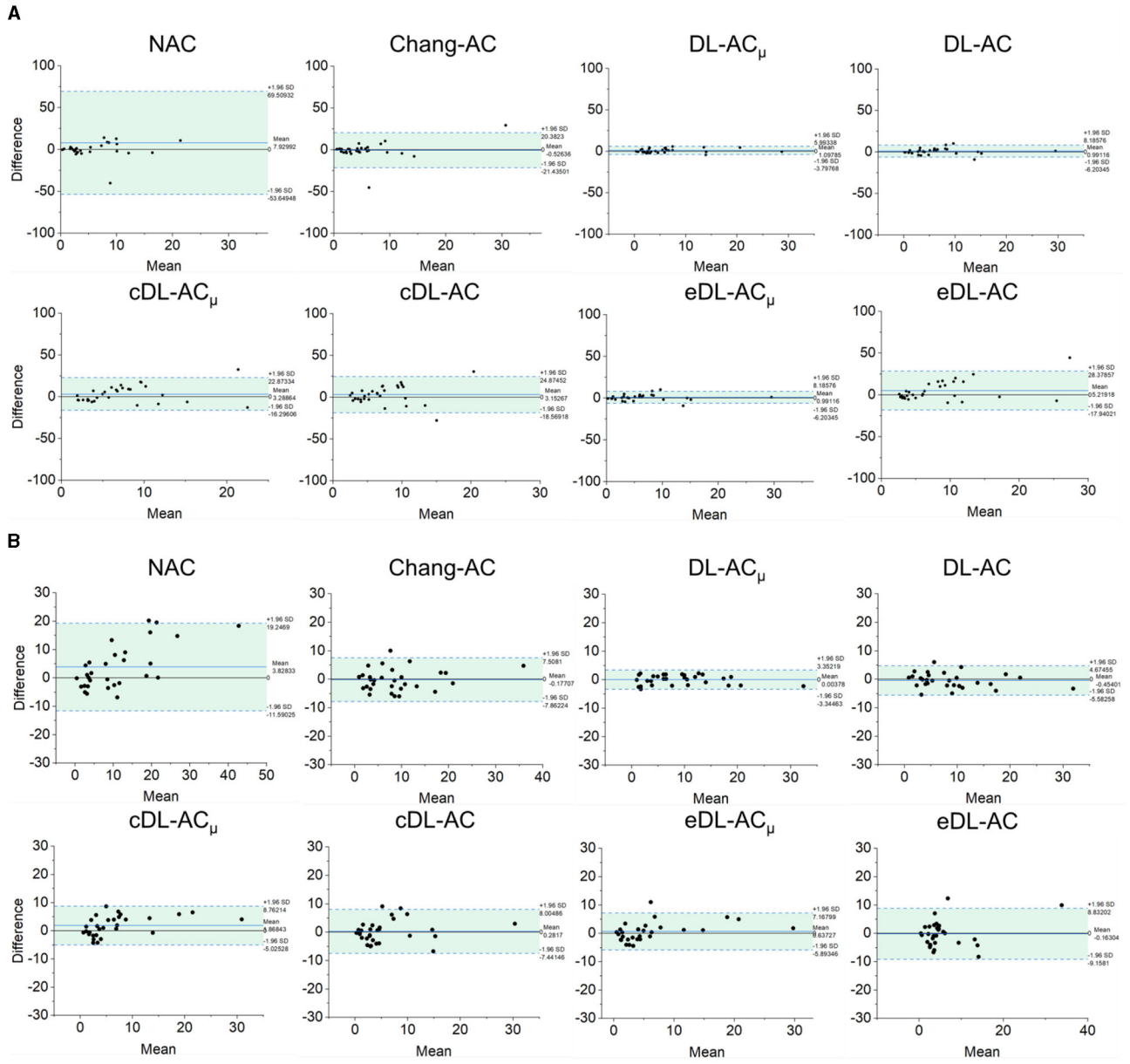

FIGURE 8
Bland–Altman plots of %ASI results of different AC methods, using CT-AC as the reference of **(A)** scanner A and **(B)** scanner B (the dotted lines indicate 95% CI, and the blue lines indicate the mean values).

with a small dataset from the target scanner (19). This study is beyond the scope of this study and is ongoing in our group (29).

The SUR and %ASI are highly related to the clinical diagnosis of PD by the detection of decrement in DAT and asymmetry uptake in the left and right striatum. NAC has a much lower SUR than other AC methods, as counts are substantially attenuated toward the center of the brain, where the striatum is located. Chang-AC shows an overestimated SUR compared to CT-AC, which has been reported by previous studies (25, 30), yet it is still better than NAC. Thus, NAC may lead to a false positive, and Chang-AC may lead to a false negative diagnosis. All AC methods have better SUR and %ASI results than NAC. For DL-based methods, the SUR and %ASI values are much closer to CT-AC compared to Chang-AC except for cross-scanner-tested cDL-AC and ensemble-trained eDL-AC, indicating an improved count recovery in both the striatal region and background. DL-AC$_\mu$ is the best AC method for SUR and %ASI. For (c/e)DL-AC$_\mu$, we have applied normalization to SPECT image intensity, which is not applied on (c/e)DL-AC to keep the counts invariable. Our proposed DL-based AC can improve quantitative accuracy, image quality, and clinical diagnosis accuracy of DAT SPECT, reducing the radiation dose (31, 32), the additional scan time of CT scans, and potential mismatches concern between SPECT and CT images for AC and providing a CT-less AC option for SPECT without integrated CT.

There are certain limitations to this study. Involuntary head motion is commonly observed in patients with neurodegenerative

disease (33). It may lead to a mismatch between SPECT and CT data (34–36), which could be reduced by registration (37) and motion-tracking methods (38). Previously, we showed that this mismatch compromises DL-based AC performance, but it is still better than NAC in MP SPECT (18). We expect a similar result for DL-based AC in DAT SPECT.

Conclusion

This is the first clinical evaluation of DL-based AC methods for DAT SPECT. Both DL-based methods improve image quality and quantitative accuracy as compared to Chang-AC and NAC. DL-AC_{μ} is consistently better than DL-AC on clinical patient data on two scanners with different acquisition protocols and post-processing parameters.

New knowledge gained

Deep learning-based attenuation correction (AC) is feasible for DAT SPECT. Indirect generation of attenuation maps is better and more robust than direct generation of attenuation-corrected SPECT images from non-attenuation-corrected SPECT images and Chang's AC for DAT SPECT.

Data availability statement

Patient data are not allowed to be shared with the public due to patient confidentially. Requests to access the datasets should be directed to P-YC (paiyibox@gmail.com) and G-UH (106143@gmail.com).

Ethics statement

The studies involving human participants were reviewed and approved by Institutional Review Board of Chang Bing Show Chwan Memorial Hospital (IRB number: 1110704). The written consent was waived due to the retrospective nature of this study.

Author contributions

YD and GM were the primary authors of the manuscript. YD was mainly responsible for data processing and analysis. HJ, ZP, and JS were mainly responsible for data analysis and manuscript revision. C-NL was mainly responsible for data collection. HJ, C-NL, P-YC, and G-UH were responsible for clinical interpretation. GM and G-UH were responsible for data interpretation and study integration. All authors contributed to the article and approved the submitted version.

Funding

This study received an External Industrial Research Collaboration Grant (EF062/FST/MSP/2023/ZJFCYLKJ) from Zhejiang Fuchuan Medical Technology Co., Ltd. The funder was not involved in the study design, collection, analysis, interpretation of data, the writing of this article, or the decision to submit it for publication. This study was also supported by a research grant from Show Chwan Memorial Hospital (IRD-110015).

Conflict of interest

The authors declare that the research was conducted in the absence of any commercial or financial relationships that could be construed as a potential conflict of interest.

Publisher's note

All claims expressed in this article are solely those of the authors and do not necessarily represent those of their affiliated organizations, or those of the publisher, the editors and the reviewers. Any product that may be evaluated in this article, or claim that may be made by its manufacturer, is not guaranteed or endorsed by the publisher.

References

1. Suwijn SR, van Boheemen CJM, de Haan RJ, Tissingh G, Booij J, de Bie RMA. The diagnostic accuracy of dopamine transporter SPECT imaging to detect nigrostriatal cell loss in patients with Parkinson's disease or clinically uncertain parkinsonism: a systematic review. *EJNMMI Res.* (2015) 5:12. doi: 10.1186/s13550-015-0087-1

2. Booij J, Tissingh G, Boer GJ, Speelman JD, Stoof JC, Janssen AG, et al. [123I]FP-CIT SPECT shows a pronounced decline of striatal dopamine transporter labelling in early and advanced Parkinson's disease. *J Neurol Neurosurg Psychiatry.* (1997) 62:133–40. doi: 10.1136/jnnp.62.2.133

3. Kung HF, Kim H-J, Kung M-P, Meegalla SK, Plössl K, Lee H-K. Imaging of dopamine transporters in humans with technetium-99m TRODAT 1. *Eur J Nucl Med.* (1996) 23:1527–30. doi: 10.1007/BF01254479

4. Patton JA, Turkington TG. SPECT/CT physical principles and attenuation correction. *J Nucl Med Technol.* (2008) 36:1–10. doi: 10.2967/jnmt.107.046839

5. Lapa C, Spehl TS, Brumberg J, Isaias IU, Schlögl S, Lassmann M, et al. Influence of CT-based attenuation correction on dopamine transporter SPECT with [(123)I]FP-CIT. *Am J Nucl Med Mol Imaging.* (2015) 5:278–86.

6. Bieńkiewicz M, Górska-Chrzastek M, Siennicki J, Gajos A, Bogucki A, Mochecka-Thoelke A, et al. Impact of CT based attenuation correction on quantitative assessment of DaTSCAN (123 I-Ioflupane) imaging in diagnosis of extrapyramidal diseases. *Nuclear Medicine Review.* (2008) 11:53–8.

7. Rajeevan N, Zubal IG, Ramsby SQ, Zoghbi SS, Seibyl J, Innis RB. Significance of nonuniform attenuation correction in quantitative brain SPECT imaging. *Journal of Nuclear Medicine.* (1998) 39:1719–26.

8. Stam MK, Verwer EE, Booij J, Adriaanse SM, de Bruin CM, de Wit TC. Performance evaluation of a novel brain-dedicated SPECT system. *EJNMMI Physics.* (2018) 5:4. doi: 10.1186/s40658-018-0203-1

9. Rausch I, Füchsel FG, Kuderer C, Hentschel M, Beyer T. Radiation exposure levels of routine SPECT/CT imaging protocols. *Eur J Radiol.* (2016) 85:1627–36. doi: 10.1016/j.ejrad.2016.06.022

10. Zhang D, Ghaly M, Mok GS. Interpolated CT for attenuation correction on respiratory gating cardiac SPECT/CT—a simulation study. *Med Phys.* (2019) 46:2621–8. doi: 10.1002/mp.13513

11. Zhang D, Yang B-H, Wu NY, Mok GSP. Respiratory average CT for attenuation correction in myocardial perfusion SPECT/CT. *Ann Nucl Med.* (2017) 31:172–80. doi: 10.1007/s12149-016-1144-1

12. Chang L-T, A. method for attenuation correction in radionuclide computed tomography. *IEEE Trans Nucl Sci.* (1978) 25:638–43. doi: 10.1109/TNS.1978.4329385

13. Chen X, Liu C. Deep-learning-based methods of attenuation correction for SPECT and PET. *J Nucl Cardiol.* (2022). doi: 10.1007/s12350-022-03007-3

14. Shi L, Onofrey JA, Liu H, Liu Y-H, Liu C. Deep learning-based attenuation map generation for myocardial perfusion SPECT. *Eur J Nuclear Med Mol Imag.* (2020) 47:10. doi: 10.1007/s00259-020-04746-6

15. Yang J, Shi L, Wang R, Miller EJ, Sinusas AJ, Liu C, et al. Direct attenuation correction using deep learning for cardiac SPECT: a feasibility study. *J Nucl Med.* (2021) 62:1645–52. doi: 10.2967/jnumed.120.256396

16. Chen X, Zhou B, Shi L, Liu H, Pang Y, Wang R, et al. CT-free attenuation correction for dedicated cardiac SPECT using a 3D dual squeeze-and-excitation residual dense network. *J Nucl Cardiol.* (2021). doi: 10.1007/s12350-021-02672-0

17. Chen X, Zhou B, Xie H, Shi L, Liu H, Holler W, et al. Direct and indirect strategies of deep-learning-based attenuation correction for general purpose and dedicated cardiac SPECT. *Eur J Nucl Med Mol Imaging.* (2022) 49:3046–60. doi: 10.1007/s00259-022-05718-8

18. Du Y, Shang J, Sun J, Wang L, Liu Y-H, Xu H, et al. Deep-learning-based estimation of attenuation map improves attenuation correction performance over direct attenuation estimation for myocardial perfusion SPECT. *J Nucl Cardiol.* (2022) 2022:1–16. doi: 10.1007/s12350-022-03092-4

19. Chen X, Hendrik Pretorius P, Zhou B, Liu H, Johnson K, Liu Y-H, et al. Cross-vender, cross-tracer, and cross-protocol deep transfer learning for attenuation map generation of cardiac SPECT. *J Nucl Cardiol.* (2022) 2022:1–13. doi: 10.1007/s12350-022-02978-7

20. Sakaguchi K, Kaida H, Yoshida S, Ishii K. Attenuation correction using deep learning for brain perfusion SPECT images. *Ann Nucl Med.* (2021) 35:589–99. doi: 10.1007/s12149-021-01600-z

21. Murata T, Yokota H, Yamato R, Horikoshi T, Tsuneda M, Kurosawa R, et al. Development of attenuation correction methods using deep learning in brain-perfusion single-photon emission computed tomography. *Med Phys.* (2021) 48:4177–90. doi: 10.1002/mp.15016

22. Chen Y, Goorden MC, Beekman FJ. Automatic attenuation map estimation from SPECT data only for brain perfusion scans using convolutional neural networks. *Phys Med Biol.* (2021) 66:065006. doi: 10.1088/1361-6560/abe557

23. Chen Y, Goorden MC, Beekman FJ. Convolutional neural network based attenuation correction for 123I-FP-CIT SPECT with focused striatum imaging. *Phys Med Biol.* (2021) 66:195007. doi: 10.1088/1361-6560/ac2470

24. Smith M, Jaszczaki R. Generalized dual-energy-window scatter compensation in spatially varying media for SPECT. *Phys Med Biol.* (1994) 39:531. doi: 10.1088/0031-9155/39/3/016

25. Lange C, Seese A, Schwarzenböck S, Steinhoff K, Umland-Seidler B, Krause BJ, et al. CT-based attenuation correction in I-123-ioflupane SPECT. *PLoS ONE.* (2014) 9:e108328. doi: 10.1371/journal.pone.0108328

26. Mirza M, Osindero S. Conditional generative adversarial nets. *arXiv*. [preprint].

27. Decuyper M, Maebe J, Van Holen R, Vandenberghe S. Artificial intelligence with deep learning in nuclear medicine and radiology. *EJNMMI Physics.* (2021) 8:81. doi: 10.1186/s40658-021-00426-y

28. Isola P, Zhu J-Y, Zhou T, Efros AA. (2017). "Image-to-image translation with conditional adversarial networks," in *Proceeding of the IEEE Conference on Computer Vision and Pattern Recognition* (Hawaii, HI: IEEE). doi: 10.1109/CVPR.2017.632

29. Sun H, Du Y, Lu L, Lin C-N, Hung G-U, Chiu P-Y, et al. (2023). "Cross-tracer and cross-scanner transfer learning based attenuation map generation for brain SPECT," in *Abstract presented at Society of Nuclear Medicine and Molecular Imaging 2023 Annual Meeting* (Chicago, IL).

30. Maltais DD, Jordan LG, Min H-K, Miyagawa T, Przybelski SA, Lesnick TG, et al. Confirmation of ^{123}I-FP-CIT SPECT quantification methods in dementia with lewy bodies and other neurodegenerative disorders. *J Nucl Med.* (2020) 61:1628–35. doi: 10.2967/jnumed.119.239418

31. Law W-Y, Yang C-C, Chen L-K, Huang T-C, Lu K-M, Wu T-H, et al. Retrospective gating vs. prospective triggering for noninvasive coronary angiography: assessment of image quality and radiation dose using a 256-slice CT scanner with 270 ms gantry rotation. *Academic Radiol.* (2011) 18:31–9. doi: 10.1016/j.acra.2010.07.013

32. Lee Y-W, Yang C-C, Mok GS, Wu T-H. Infant cardiac CT angiography with 64-slice and 256-slice CT: comparison of radiation dose and image quality using a pediatric phantom. *PLoS ONE.* (2012) 7:e49609. doi: 10.1371/journal.pone.0049609

33. Tahmasian M, Bettray LM, van Eimeren T, Drzezga A, Timmermann L, Eickhoff CR, et al. A systematic review on the applications of resting-state fMRI in Parkinson's disease: does dopamine replacement therapy play a role? *Cortex.* (2015) 73:80–105. doi: 10.1016/j.cortex.2015.08.005

34. Lu Z, Chen G, Lyu Y, Chen Y, Mok GSP. Technical note: Respiratory impacts on static and respiratory gated (99m) Tc-MAA SPECT/CT for liver radioembolization: a simulation study. *Med Phys.* (2022) 49:5330–9. doi: 10.1002/mp.15682

35. Lyu Y, Chen G, Lu Z, Chen Y, Mok GSP. The effects of mismatch between SPECT and CT images on quantitative activity estimation—a simulation study. *Z Med Phys.* (2023) 33:54–69. doi: 10.1016/j.zemedi.2022.03.004

36. Lu Z, Chen G, Lin KH, Wu TH, Mok GSP. Evaluation of different CT maps for attenuation correction and segmentation in static (99m) Tc-MAA SPECT/CT for (90) Y radioembolization treatment planning: a simulation study. *Med Phys.* (2021) 48:3842–51. doi: 10.1002/mp.14991

37. Lu Z, Chen G, Jiang H, Sun J, Lin KH, Mok GSP, et al. and CT misregistration reduction in [(99m)Tc]Tc-MAA SPECT/CT for precision liver radioembolization treatment planning. *Eur J Nucl Med Mol Imaging.* (2023) 50:1–2. doi: 10.1007/s00259-023-06149-9

38. Chemli Y, Tétrault M-A, Marin T, Normandin MD, Bloch I, El Fakhri G, et al. Super-resolution in brain positron emission tomography using a real-time motion capture system. *Neuroimage.* (2023) 272:120056. doi: 10.1016/j.neuroimage.2023.120056

frontiers | Frontiers in Medicine

TYPE Original Research
PUBLISHED 28 September 2023
DOI 10.3389/fmed.2023.1211726

OPEN ACCESS

EDITED BY
Nicolas A. Karakatsanis,
Cornell University, United States

REVIEWED BY
Kjell Erlandsson,
University College London, United Kingdom
Benjamin Auer,
Brigham and Women's Hospital and Harvard Medical School, United States
Arda Konik,
Dana–Farber Cancer Institute, United States

*CORRESPONDENCE
Greta S. P. Mok
✉ gretamok@um.edu.mo

RECEIVED 25 April 2023
ACCEPTED 31 August 2023
PUBLISHED 28 September 2023

CITATION
Huang W and Mok GSP (2023) Multi-pinhole collimator design in different numbers of projections for brain SPECT.
Front. Med. 10:1211726.
doi: 10.3389/fmed.2023.1211726

Multi-pinhole collimator design in different numbers of projections for brain SPECT

Wenbo Huang[1] and Greta S. P. Mok[1,2]*

[1]Biomedical Imaging Laboratory (BIG), Department of Electrical and Computer Engineering, Faculty of Science and Technology, University of Macau, Taipa, Macau SAR, China, [2]Center for Cognitive and Brain Sciences, Institute of Collaborative Innovation, University of Macau, Taipa, Macau SAR, China

Purpose: High resolution and sensitivity brain SPECT is promising for the accurate diagnosis of Alzheimer's disease (AD) and Parkinson's disease (PD). Multi-pinhole (MPH) collimators with a good performance in imaging small field-of-view (FOV) could be better used for brain SPECT. In this study, we aim to evaluate the impact of varying the number of pinholes and the number of projections on the performance of MPH brain SPECT.

Methods: The system design was based on a commercial clinical dual-head SPECT/CT scanner, with target spatial resolutions of 12 mm and 8 mm for AD and PD SPECT, respectively. In total, 1–25 pinholes were modeled for 64, 32, 16, 8, 4, and 2 projections. The 3D NURBS-based HUman Brain (NHUB) phantom was used in the analytical simulation to model ^{99m}Tc-HMPAO and ^{99m}Tc-TRODAT distributions. The 2D Derenzo hot-rod phantom and star phantom were used in Monte Carlo simulations to evaluate the spatial resolution and angular sampling performance of MPH. The influence of different detector positions was also evaluated for 2, 4, and 6 angular views. The projections were reconstructed using the 3D MPH ML-EM method. Normalized mean square error, coefficient of variation, and image profiles were evaluated.

Results: Along with the decrease in the number of projections, more pinholes are required to achieve the optimum performance. For 32 projections, 9- and 7-pinhole collimators provide the best normalized mean square error (NMSE) to the coefficient of variation (COV) trade-off for ^{99m}Tc-HMPAO and ^{99m}Tc-TRODAT, respectively. Detector positions substantially affect the image quality for MPH SPECT for 2 and 4 angular views. The smallest rod size for the Derenzo hot-rod phantom, which could be resolved, is 7.9 mm for the MPH general purpose collimator (MPGP) with more than 16 projections and 6.4 mm for MPH high-resolution collimator (MPHR) with more than 8 projections.

Conclusion: The number of pinholes affects the performance of the MPH collimator, especially when the projection views become fewer. More pinholes are required for fewer projections to provide better angular sampling in MPH for complex activity distributions. Detector positions affect the image quality of MPH SPECT for 2 and 4 angular views, where L-mode acquisition is slightly superior to H-mode. MPH collimators exhibited improved spatial resolution and angular sampling compared with both LEHR and single pinhole collimators.

KEYWORDS

multi-pinhole collimator, brain SPECT, Alzheimer's disease, Parkinson's disease, angular sampling

1. Introduction

With the increase in the aging population worldwide, neurodegenerative diseases such as Alzheimer's disease (AD) and Parkinson's disease (PD) pose a substantial burden in society. Fifty million people are estimated to suffer from dementia throughout the world in 2018, and this number is expected to triple by 2050 (1). On the other hand, in 2016, ~6.1 million individuals suffered from PD globally, and it caused 3.2 million disability-adjusted life years and 211,296 deaths (2). Currently, the number of drugs available for the treatment of Alzheimer's disease and Parkinson's disease is limited (3, 4), Lecanemab-irmb (5) and aducanumab (6) are currently the only two drugs approved by the US Food and Drug Administration (FDA) for AD treatment, both work by reducing the deposition of amyloid beta plaque. Levodopa (7) is the most effective medication for Parkinson's disease. Deep brain stimulation (8), which involves the surgical implantation of electrodes into a specific area of the brain, is another effective method for controlling symptoms. However, despite these available treatment options, the diseases cannot be cured yet. Early intervention remains the most effective treatment approach for both conditions. Thus, early diagnosis for delayed disease progression is increasingly important for these two diseases.

Along with the development of different tracers that can target beta-amyloid (9), tau protein (10), synaptic vesicle glycoprotein 2A (SV2A) density (11), acetylcholine (12), brain perfusion (13), and dopaminergic system (14), the role of radionuclide imaging, including PET and SPECT, in neurodegenerative diseases is well recognized. Usually, highly demanding production and transportation processes are needed for PET, especially if short-lived isotopes are used, whereas the half-life of SPECT isotopes is longer. Thus, SPECT is generally more accessible and economical than PET for PD and AD diagnosis and treatment monitoring. Current brain SPECT tracers include Tc-99m-labeled hexamethyl propylene amine oxime (HMPAO) for cerebral blood flow, ^{99m}Tc-TRODAT, and ^{123}I-ioflupane for targeting dopamine transporters in the striatum region, which can detect the onset of the disease much earlier than the development of symptoms. ^{99m}Tc-TRODAT is a more common DAT tracer in Asia as compared with ^{123}I-ioflupane. The biodistributions of these two tracers are similar, but ^{99m}Tc-TRODAT has a lower striatal uptake with less photon scattering and penetration (15), while ^{123}I-ioflupane suffers from contamination of high-energy photons.

The sensitivity of SPECT is much lower than PET due to the physical collimation, which is required to determine the incident angle of the gamma photons. Ma et al. have proposed a novel self-collimating SPECT system as a potential solution (16, 17). However, as for now, collimators remain an essential component in clinical SPECT. For brain imaging, as the object is smaller than the detector field-of-view (FOV), better trade-off can be achieved by using converging collimators, e.g., fan beam, cone beam, or pinhole collimators as compared with conventional parallel-hole collimators. Multi-pinhole (MPH) collimators have been proposed to further improve the resolution and sensitivity trade-off and the sampling problem of single-pinhole collimators. When the pinholes are focused on a common volume, MPH collimators can obtain multiple projections at a single detector location to improve both angular and axial sampling (18). Another advantage of MPH collimators is that the collimator penetration is greatly reduced as compared with other collimators, particularly for tracers with down scattering from high-energy photons, e.g., ^{123}I (19), a common radionuclide for PD tracer such as ^{123}I-ioflupane.

The MPH reconstructed image quality, e.g., resolution, detection efficiency, and artifacts depends on the number of pinholes, placement of pinholes, magnification factor, projection overlapping, truncation, aperture size, and acceptance angle (18, 20–22). Recently, different types of MPH collimators for clinical brain SPECT imaging have been proposed, mainly for research applications (23–28). However, there are limited studies to investigate the designs of MPH collimators for brain SPECT (29, 30). Our previous study proposed an optimized MPH design by maximizing the sensitivity for a target spatial resolution for a single angular position of a flat panel detector (31), showing 268% sensitivity improvement as compared with a conventional parallel-hole collimator based on the same spatial resolution. Improved sampling and sensitivity in MPH SPECT imaging can potentially reduce the number of required projection views, and the optimal MPH design may be different for different numbers of projections and brain applications. Moreover, improved sensitivity may not necessarily be translated to better image quality. Our current study evaluated the MPH performance for various numbers of projections based on actual reconstructed image quality. We aimed to investigate the performance of MPH collimators with various pinhole configurations for a number of different projection views in MPH brain perfusion and DAT SPECT.

2. Materials and methods

2.1. System description

Our system design is based on a commercial clinical dual-head SPECT/CT scanner (Infinia Hawkeye 4, GE Healthcare, USA). The active detector area is 540 mm × 400 mm, with 9.525 mm NaI crystal and a 3.2 mm intrinsic resolution. The maximum system radius of the system is 344 mm, which is the distance from the center of the field of view (CFOV) to the surface of the detector. The minimum system radius is 292 mm, which is large enough to accommodate and clear the shoulders of the 95 percentile Chinese population based on the national standard GB/T 10000-1988 (32). Meanwhile, the minimum radius of rotation (ROR) is set to be 135 mm, which is large enough to provide a 200 mm FOV for MPH SPECT to cover heads of 95 percentile

Abbreviations: AD, Alzheimer's disease; COV, coefficient of variation; FOV, field-of-view; GATE, Geant4 Application for Tomographic Emission; LEHR, low energy high resolution; MLEM, maximum likelihood expectation maximization; MPGP, multi-pinhole general purpose; MPH, multi-pinhole; MPHR, multi-pinhole high resolution; NHUB, NURBS-based Human Brain; NMSE, normalized mean square error; PD, Parkinson's disease; ROR, radius-of-rotation; SBR, striatal binding ratio; SPECT, single photon emission computed tomography; VOI, volume-of-interest.

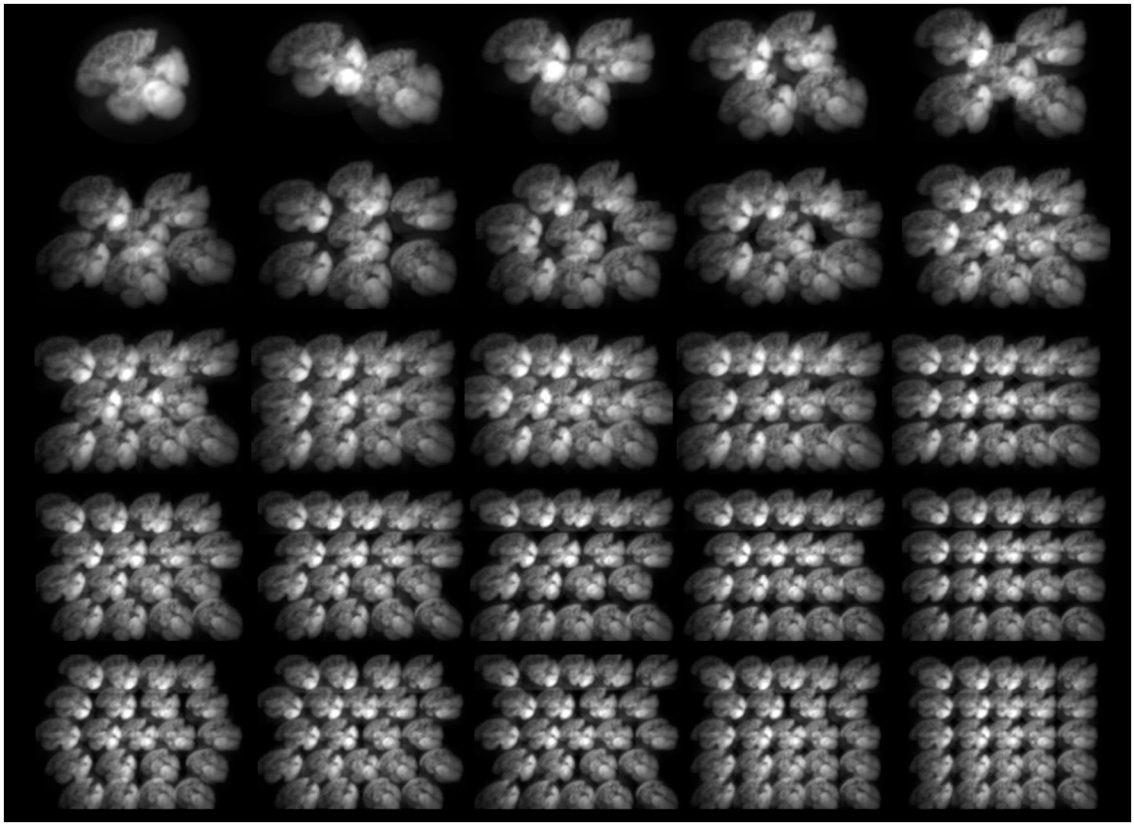

FIGURE 1
Sample noise-free projections of HMPAO generated by MPGP collimators with different numbers of pinholes ($n = 1–25$).

Chinese population based on the national standard GB/T 2428-1998 (33).

Two sets of MPH collimators for different target planar system spatial resolutions (R_t): (1) 12 mm for AD (Multi-Pinhole General Purpose, MPGP); and (2) 8 mm for PD (Multi-Pinhole High Resolution, MPHR) are evaluated. The first one is the same system resolution for a low energy high resolution (LEHR) parallel-hole collimator at 225 mm ROR, a common setting for cerebral blood flow Tc-99m HMPAO SPECT. The second one is used for imaging the striatum region with a higher resolution requirement. The pinholes on the collimator are positioned with projections fully utilizing the coverage of the detector area, providing more number of angular and axial sampling, and keeping the total projection overlapping among all pinhole projections $< 20\%$ (20, 34) (Figure 1). The pinhole arrangement is the same for MPGP and MPHR, while the pinhole aperture size is smaller for the latter. We model different numbers of projections ($n = 2–64$) and pinholes ($n = 1–25$), as well as ROR and corresponding collimator length for the respective target resolution. The specific design parameters for different MPH collimators are listed in Supplementary Table S1. In addition, as a dual-head SPECT scanner, two detectors can be configured as perpendicular (L-mode) or parallel (H-mode) to each other (35), with the latter being a more common setting in conventional brain SPECT using LEHR. In this study, we also evaluate various MPH performances for H- and L-modes with different detector positions for brain SPECT.

2.2. Phantoms

The NURBS-based HUman Brain (NHUB) phantom (36) with ^{99m}Tc-HMPAO and ^{99m}Tc-TRODAT distributions is modeled for AD and PD imaging, respectively. For HMPAO, the uptake ratios of various normal regions are set based on the study mentioned in the reference (37) (Figure 2A), e.g., gray to white matter is ~10:1, while the striatal binding ratio (SBR) is set to 9:1 (38) (Figure 2B) for normal TRODAT distributions. The voxel size and matrix size of the phantom are set to be $3.125 \times 3.125 \times 3.125$ mm^3 and $64 \times 64 \times 64$, respectively.

We also simulate a 2D Derenzo phantom (Figure 2C) and a 2D star phantom (Figure 2D), with the former to demonstrate the system resolution while the latter to demonstrate the angular sampling of the proposed MPH collimators. Hot rods with diameters of 4.8 mm, 6.4 mm, 7.9 mm, 9.5 mm, 11.1 mm, and 12.7 mm are modeled in the Derenzo phantom, with rod center-to-center distance twice the rod diameter. The angular interval of each bar in the star phantom is 11.25°. Both phantoms are situated within a water-filled 2D circle container with a radius of 100 mm.

2.3. Analytical simulation

To evaluate the performance of the proposed MPH collimator designs, we first perform analytical simulations based on a 3D

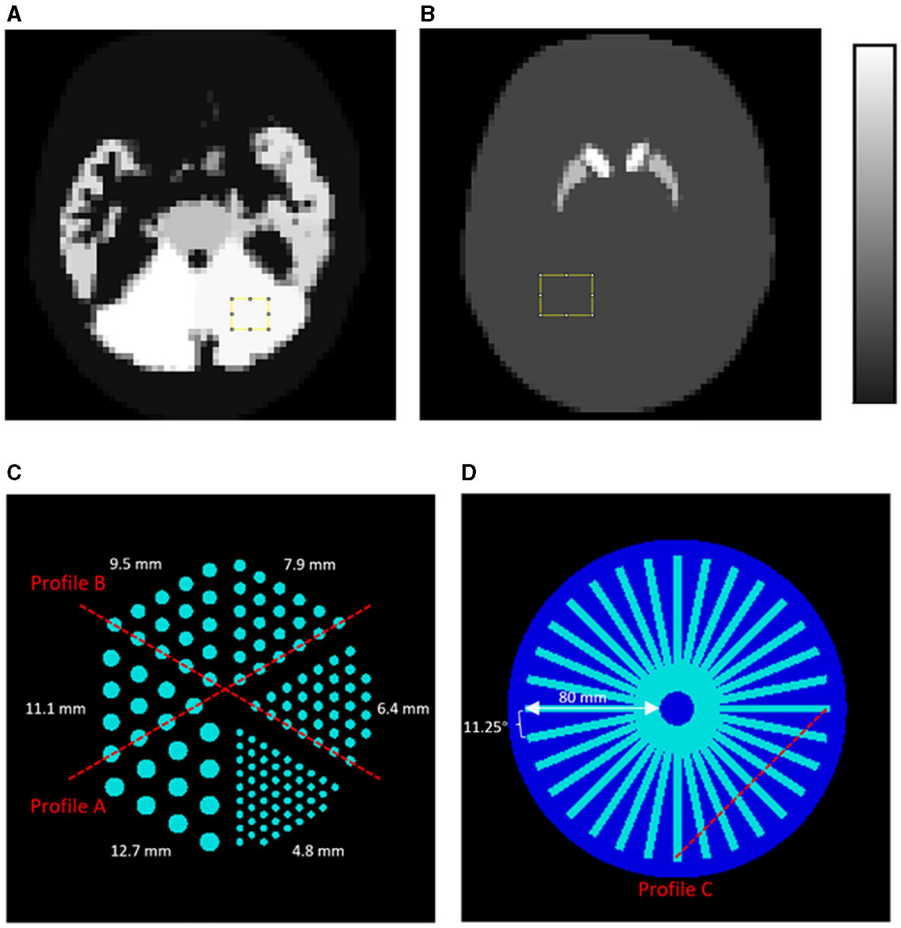

FIGURE 2
NHUB brain phantom with **(A)** ^{99m}Tc-HMPAO distribution and **(B)** ^{99m}Tc-TRODAT distribution. The uniform regions marked by the yellow squares are used for the noise analysis and the background region for calculating the SBR. Moreover, 2D phantoms used in the Monte Carlo simulations: **(C)** a Derenzo hot-rod phantom and **(D)** a cold star phantom made up of 32 columns. Profiles at different locations (red dashed lines) are assessed.

analytical MPH projector (39), without modeling attenuation, scatter, and penetration, assuming perfect corrections.

To determine the optimal number of pinholes for different projection views, we use the NHUB phantom to generate 64, 32, 16, 8, 4, and 2 noise-free projections over 360° based on H-mode acquisition. For each number of projections, we model 1–25 pinholes for HMPAO and 1–20 pinholes for TRODAT. Then, the noise-free projections generated from both MPGP and MPHR collimators are scaled using the count level of clinical LEHR SPECT projection data as reference (C_{ref}) (Eq. 1).

$$C_s = \frac{C_{ref} \times n_p \times S_{MPH}}{n_{ref} \times S_{LEHR}} \quad (1)$$

where C_s is the total count of scaled noise-free projections, n_p is the number of simulated projection views, S_{MPH} is the sensitivity of the MPH collimator with different numbers of pinholes based on previous studies (31), n_{ref} is 120 which represents the number of projection views in the referenced clinical data, and S_{LEHR} is the sensitivity of LEHR collimator which is 0.01%. For ^{99m}Tc-HMPAO, 1,000 MBq injection activity (~5 M projection counts) is set based on The European Association of Nuclear Medicine (EANM) guidelines (40). For ^{99m}Tc-TRODAT, the referenced clinical data were based on a 740 MBq injection activity (~3 million projection counts). Poisson noise is, then, added to the scaled projections, with a mean equal to variance to simulate realistic noise levels.

When projection views are limited, positions of the angular sampling may have a more significant effect on reconstructed image quality. To evaluate this effect, noise-free projections with 2, 4, and 6 views are generated based on H-mode and L-mode with different detector positions. For 2 views, both H- and L-modes are simulated by setting the acquisition position counter-clockwise from 0° to 360°, each with a 20° increment (Figure 3A). For four projections, we simulate H- and L-mode acquisitions with one angular rotation, using the 0°/180° for H-mode and 0°/90° for L-mode as initial positions and set the rotation angle from 0° to 180° to the 2nd position, each with a 20° increment (Figure 3B). The initial positions are chosen based on the two view results. For 6 projections, we set different initial positions ranging from 0° to 50°, with 10° increments. We then model 2 more pairs of detector positions spaced averagely over 360° for both H-mode and L-mode, resulting in each position being spaced 60° apart for H-mode

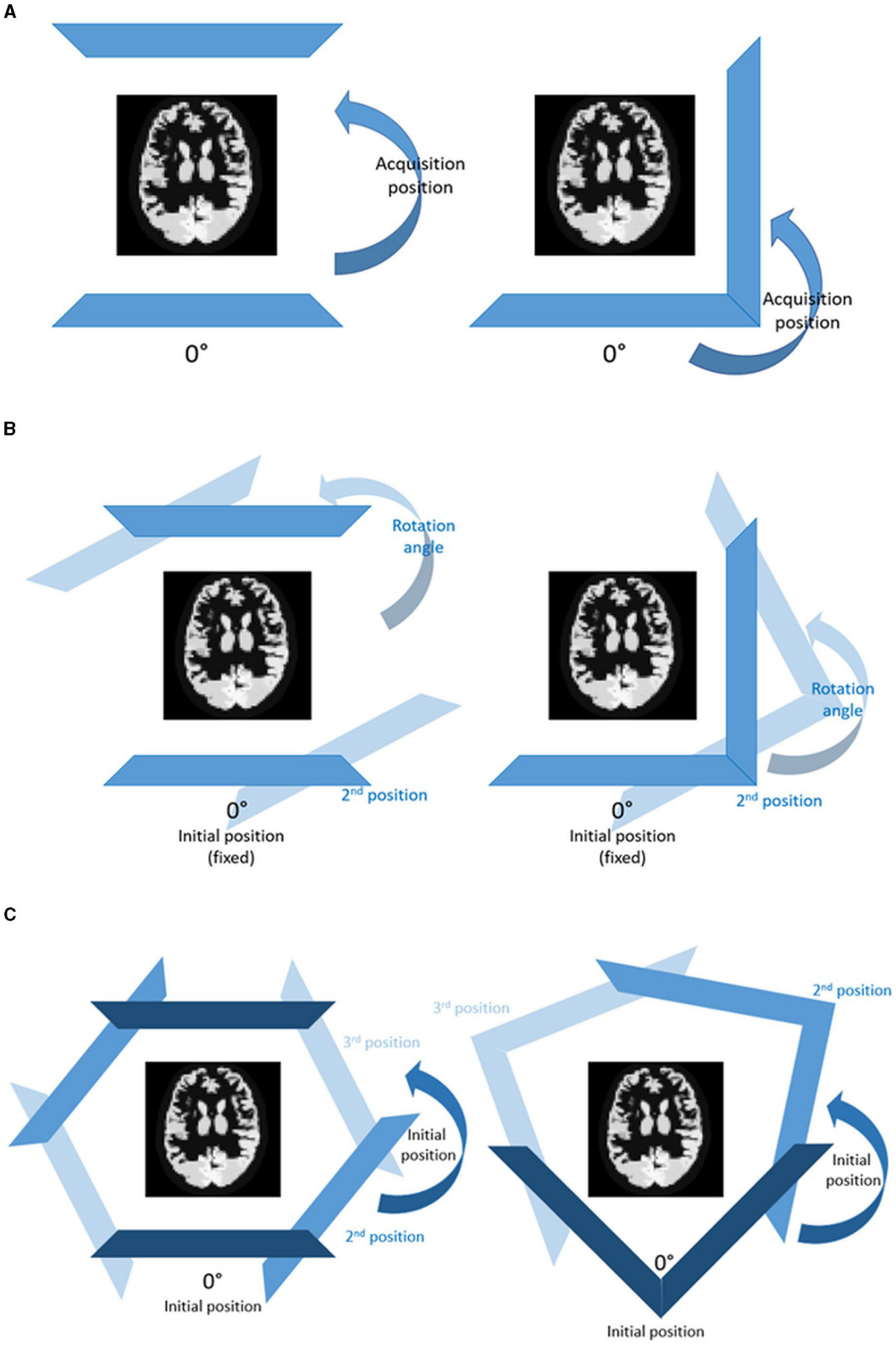

FIGURE 3
H-mode (left) and L-mode (right) configurations for **(A)** 2, **(B)** 4, and **(C)** 6 angular views on both HMPAO and TRODAT distributions using analytical simulations.

and 120° apart for L-mode (Figure 3C). Supplementary Table S2 shows the detector position configurations for 2, 4, and 6 angular views for both HMPAO and TRODAT distributions. We simulate 9-pinhole and 15-pinhole collimators as they have similarly high sensitivity based on our previous studies (31), to investigate if different numbers of pinholes affect the choice of angular positions.

2.4. Monte Carlo simulation

To independently assess collimator performance concerning system resolution and angular sampling, regardless of projection overlapping, truncation, and noise effects, we conducted simulations employing the 2D Derenzo phantom and 2D star phantom through Geant4 Application for Tomographic Emission (GATE) v8.2 (41). GATE provided more realistic evaluations of our proposed MPGP and MPHR collimators, modeling all physical image degradation factors. To compare with the MPH collimator, we also model the LEHR collimator. The MPH collimators are modeled using a tungsten plate measuring 540 mm × 400 mm × 6 mm, while the LEHR collimator is modeled using a lead plate measuring 540 mm × 400 mm × 35 mm (septal length). Pinholes on the collimators are modeled by using two cones with overlapping tips and setting the material to be air. MGHR with smaller pinholes can be modeled by setting two cones further away from each other. In the case of LEHR, regular hexagonal holes were modeled with a side length of 1.5 mm. Other components of the SPECT detector are also modeled, including NaI crystal, lead shielding around the collimator and crystal, and the glass back compartment behind the crystal. All physical image degradation factors, including attenuation, scatter, penetration, and backscatter, are modeled during simulations. To mimic an almost noise-free scenario, we simulated 8 M photons in GATE with no obvious intensity fluctuations observed in the image profiles. We evaluate various configurations of pinholes, including 1, 3, 5, 9, and 14 pinholes, in combination with different numbers of projections: 64, 32, 16, 8, and 4. The acquisition time during the simulation is set to be 1200 s over 360° for all acquisition strategies. As MPGP and MPHR have the same pinhole arrangement, the angular sampling was only evaluated on MPGP using the 2D star phantom.

2.5. Reconstruction

A 3D MPH Maximum-Likelihood Expectation-Maximization (ML-EM) algorithm is used to reconstruct the noise-free projections with up to 1,000 iterations for HMPAO and 100 iterations for TRODAT. The noisy projections are reconstructed with up to 80 iterations for HMPAO and 40 iterations for TRODAT. The 2D Derenzo and star phantom are both reconstructed with up to 40 iterations without scatter and attenuation correction. The voxel size and matrix size of reconstructed images are set to be 3.125 mm and 200 × 200 × 200, respectively, which is large enough to avoid truncation artifacts. Afterward, the reconstructed images are extracted back to the original phantom size, i.e., 64 × 64 × 64 for analytical simulation and 64 × 64 × 1 for Monte Carlo simulation for further analysis.

2.6. Data analysis

Normalized mean square error (NMSE) is evaluated for both noise-free and noisy reconstructed images (Eq. 2). For HMPAO, it is calculated in the whole brain region, while for TRODAT, it is specifically calculated in the striatum region (29 × 23 × 17 voxels for 91 × 72 × 53 mm^3).

$$NMSE = \frac{\sum_{i=1}^{N}(x_i - \lambda_i)^2}{\sum_{i=1}^{N}\lambda_i{}^2} \tag{2}$$

where N is the total number of voxels, λ is the voxel value in the original phantom, x is the voxel value in reconstructed images, and i is the voxel index.

The SBR is calculated for TRODAT based on Eq. 3 as follows:

$$SBR = \frac{\overline{\lambda}_s}{\overline{\lambda}_B} - 1 \tag{3}$$

where $\overline{\lambda}_s$ is the mean value of the striatum region, and $\overline{\lambda}_B$ is the mean value of the background region. The striatum region is obtained by applying the known striatum map. The background region is chosen from a 3D uniform region (10 × 7×9) (Figure 2B). Since the known SBR value for the TRODAT phantom is 9, the SBR error can be calculated as the absolute difference between the estimated SBR value and the ground truth for 40 iterations.

In noisy situations, the coefficient of variation (COV) is measured over a 3D uniform region (10 × 7 × 9) (Figure 2) for both ^{99m}Tc-HMPAO and ^{99m}Tc-TRODAT, to evaluate the noise performance on the noisy reconstructed images (Eq. 4).

$$COV = \frac{\sqrt{\frac{1}{m-1}\sum_{k=1}^{m}(x_k - \overline{x}_k)^2}}{\overline{x}_k} \tag{4}$$

where m is the number of voxels ($m = 630$) in the 3D uniform volume of interest, $\overline{x}_k$ is the mean voxel value of the VOI, x_k is the voxel value in the noisy reconstructed images, and k is the voxel index.

Image profiles are assessed on the reconstructed images of the Derenzo hot-rod phantom (Figure 2C) and star phantom (Figure 2D).

3. Results

3.1. Analytical simulation

Sample NMSE-COV results of noisy reconstructed images are shown in Figures 4, 5 for HMPAO and TRODAT, respectively. For HMPAO, 5, 9, 18, 21, 23, and 21 pinholes provide the best trade-off for 64, 32, 16, 8, 4, and 2 projections, respectively. For TRODAT, 7, 7, 7, 8, 8, and 9 pinholes provide the best trade-off for 64, 32, 16, 8, 4, and 2 projections respectively. A minimum of 32 projections and 16 projections are required for HMPAO and TRODAT, respectively, to provide a similar NMSE-COV trade-off for 64 projections. Figure 6 shows the sample noisy reconstructed

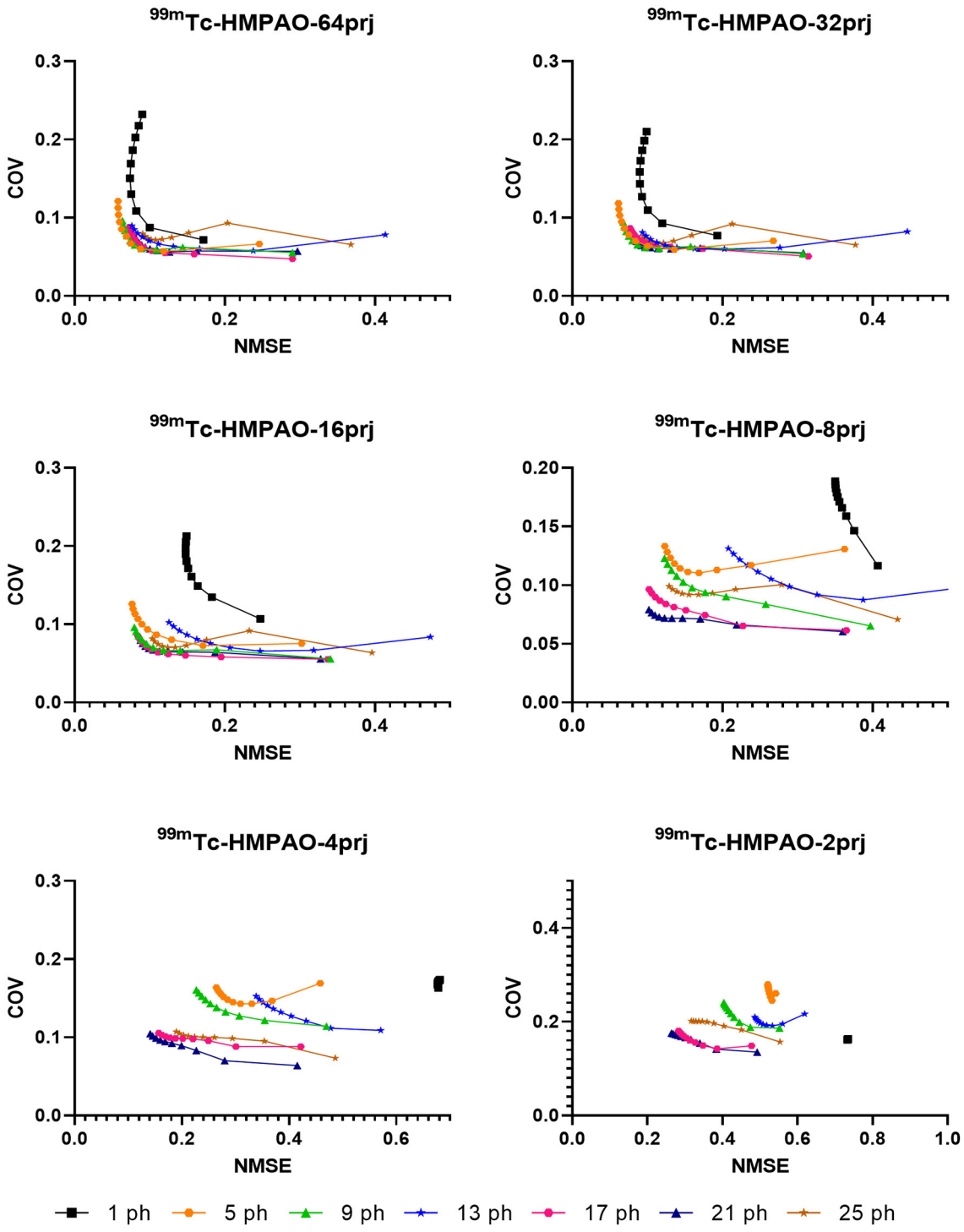

FIGURE 4
NMSE-COV trade-off for a selected number of pinholes and projections for HMPAO.

images for different numbers of projections with an optimum number of pinholes for HMPAO and TRODAT. The noise-free results are presented in Supplementary Figures S1, S2. The SBR error results of the TRODAT with 40 iterations are shown in Figure 7. It shows that 2, 2, 2, 3, 6, and 12 pinholes provide the best results for 64, 32, 16, 8, 4, and 2 projections, respectively.

Our results show that NMSE values fluctuate along with the change in detector positions particularly for 2 and 4 projections. L-mode generally leads to lower NMSE values than H-mode for 2 projections. For 4 projections, L-mode with an 80° rotation angle collimator is a better acquisition strategy for HMPAO, while L-mode with a 20° rotation angle is more

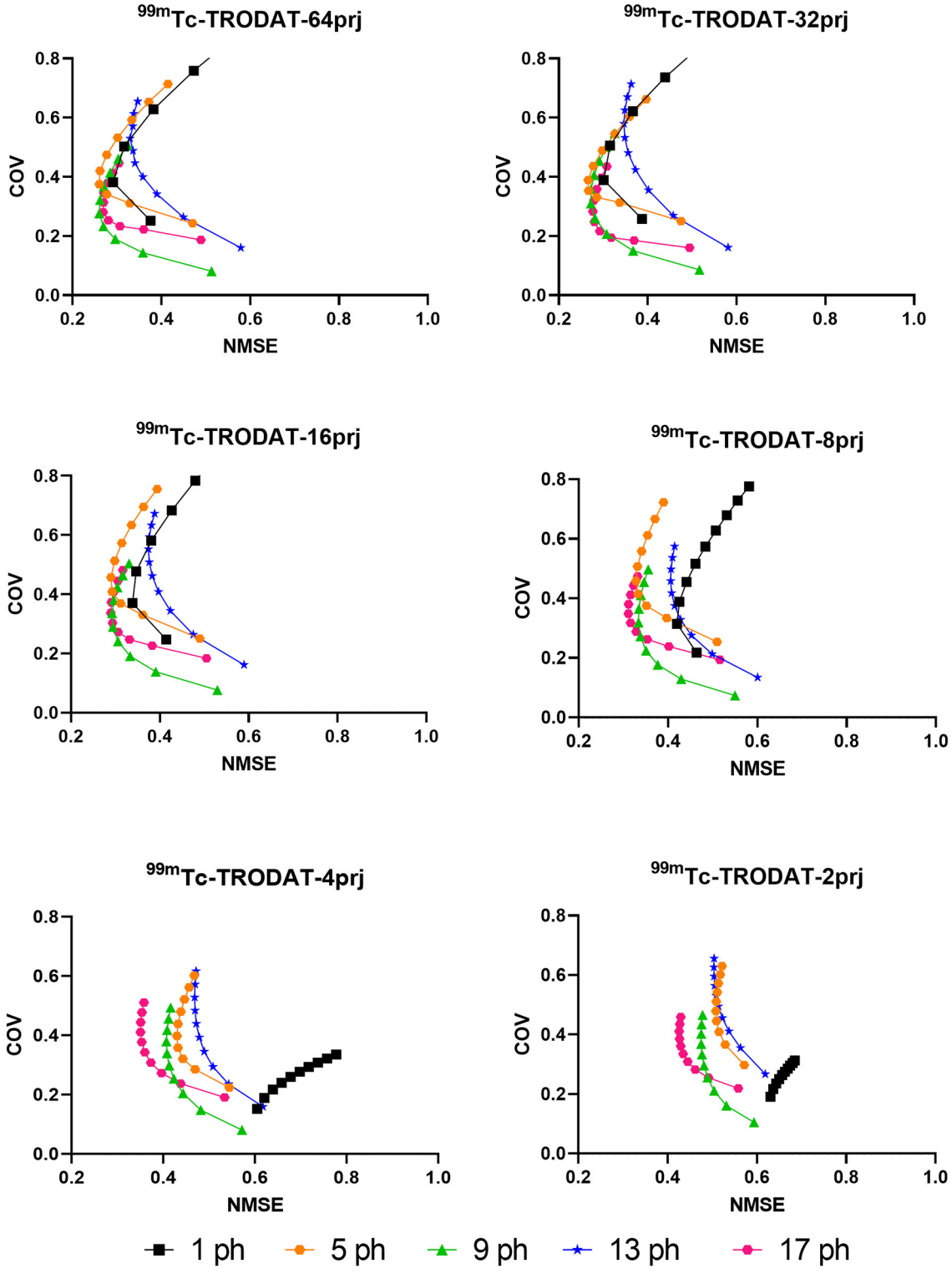

FIGURE 5
NMSE-COV trade-off of striatum region for a selected number of pinholes and projections for TRODAT.

suitable for TRODAT. For the 6 projections, the differences in NMSE values between various acquisition positions are negligible. The detailed NMSE result of noise-free reconstructed images for different detector positions of 2, 4, and 6 projection views are shown in Supplementary Figure S3 for HMPAO and TRODAT, respectively.

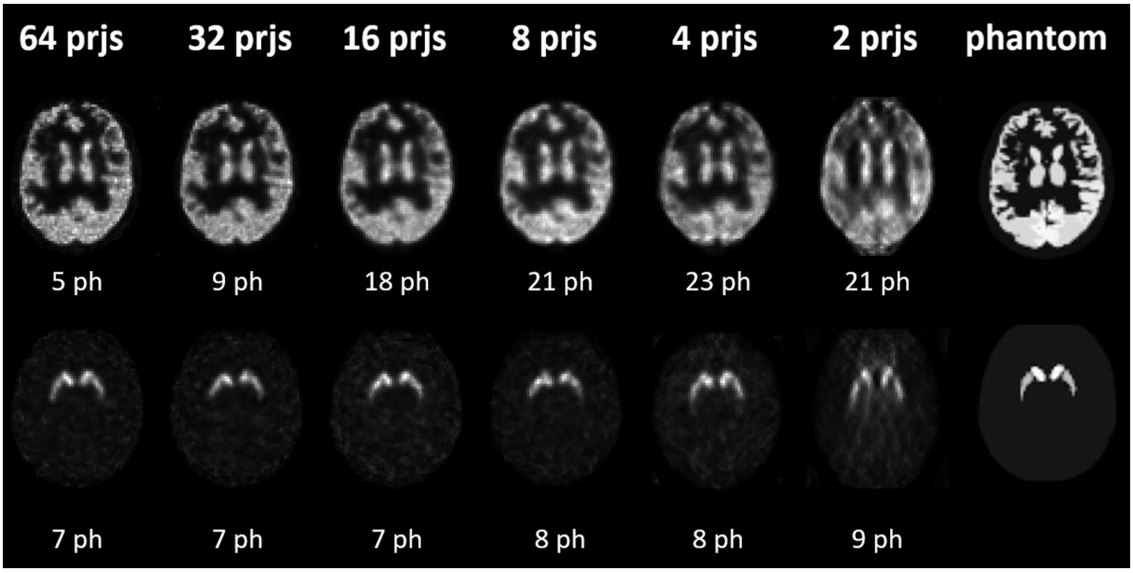

FIGURE 6
Sample noisy reconstructed images for different numbers of projections with an optimum number of pinholes (ph) having the lowest NMSE values for HMPAO **(top row)** and TRODAT **(bottom row)**.

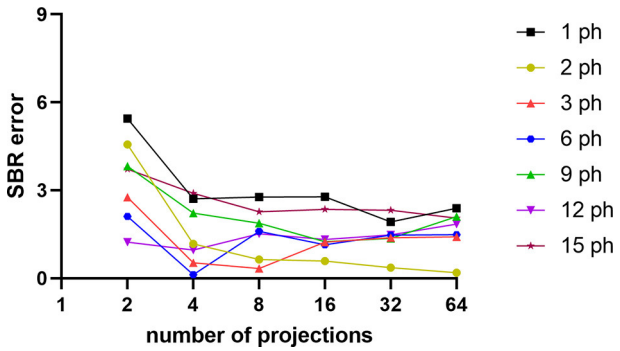

FIGURE 7
SBR errors for different numbers of pinholes and projections for TRODAT with 40 iterations.

3.2. Monte Carlo simulation

Figure 8 displays sample reconstructed images obtained using MPGP and MPHR. The images show different collimator configurations, including LEHR and 1, 5, 9, and 14 pinholes for comparative analysis. The corresponding profiles are shown in Supplementary Figures S4, S5. MPH collimator provides a large improvement in sampling over the single pinhole collimator and LEHR, especially for fewer projections. MPH could resolve similar sizes of rods for 16–64 projections. The minimum rod diameter that could be resolved is 7.9 mm for MPGP with more than 16 projections and 4.8 mm for MPHR with more than 32 projections. In this case, 9-pinhole and 5-pinhole performed better in MPGP and MPHR, respectively, especially for fewer projections.

The results of the cold star phantom simulations are shown in Figure 9. The corresponding profiles are shown in Supplementary Figure S6. The angular sampling performance is substantially worse for single pinhole and LEHR as compared with MPH. The more projections, the better the angular sampling. In general, the performance of 9-pinhole is the best compared with others. All MPH with different numbers of pinholes can provide enough angular sampling with 32 and 64 projections.

4. Discussion

For MPH, multiple magnified or minified projections utilize the whole detector. It improves the system sensitivity and axial and angular samplings (20, 42) as compared with single pinhole or parallel hole collimators which could lead to reduced injection dose or shortened acquisition time for brain SPECT. According to Toossi et al. (43), the smallest hot rods that LEHR could observe are ~9.5–12.7 mm. From Figure 8, one can easily resolve the hot rods with a diameter of 6.4 mm and even 4.8 mm for more projection views when using MPH collimators. Our Monte Carlo results modeling all physics degradations also indicate that MPH collimators are always better than single pinhole and LEHR collimator in terms of sampling, especially for fewer projections. Star phantom simulations (Figure 9) confirm that both numbers of projections and pinholes improve the angular sampling; yet, the differences between 32 and 64 projections for all numbers of pinholes for the MPH collimator are small. These findings align with the results from the study by Zeraatkar et al. (44), who investigated the AdaptiSPECT-C system equipped with 23 detector heads, each comprising a single pinhole aperture. They found that a 2-position increase in angular sampling provided

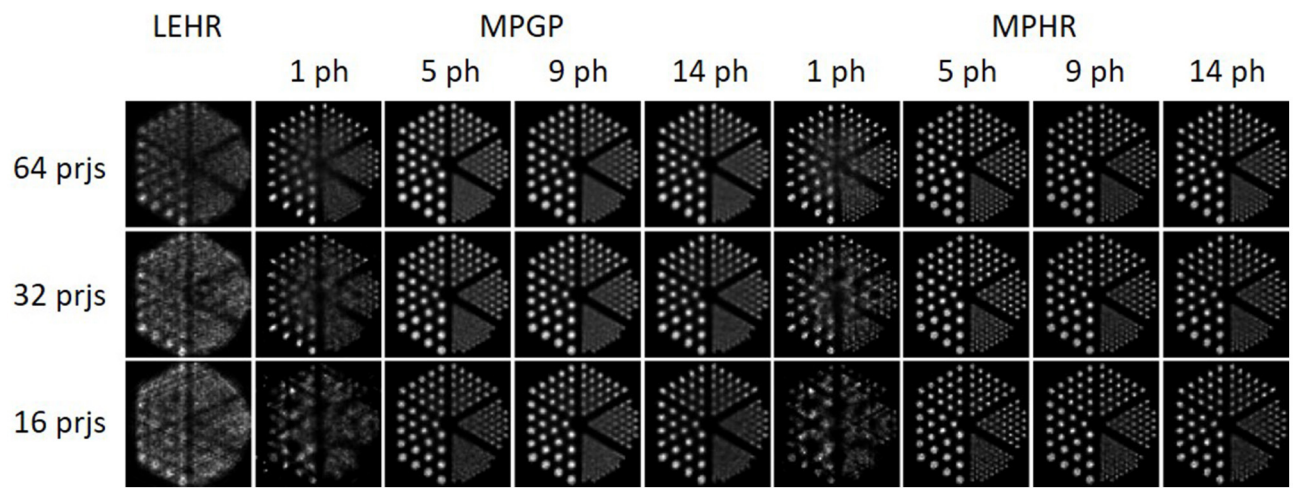

FIGURE 8
The noise-free reconstructed images of LEHR and 1, 5, 9, and 14 pinholes (ph) for MPGP and MPHR with 16, 32, and 64 projections for the Derenzo hot-rod phantom.

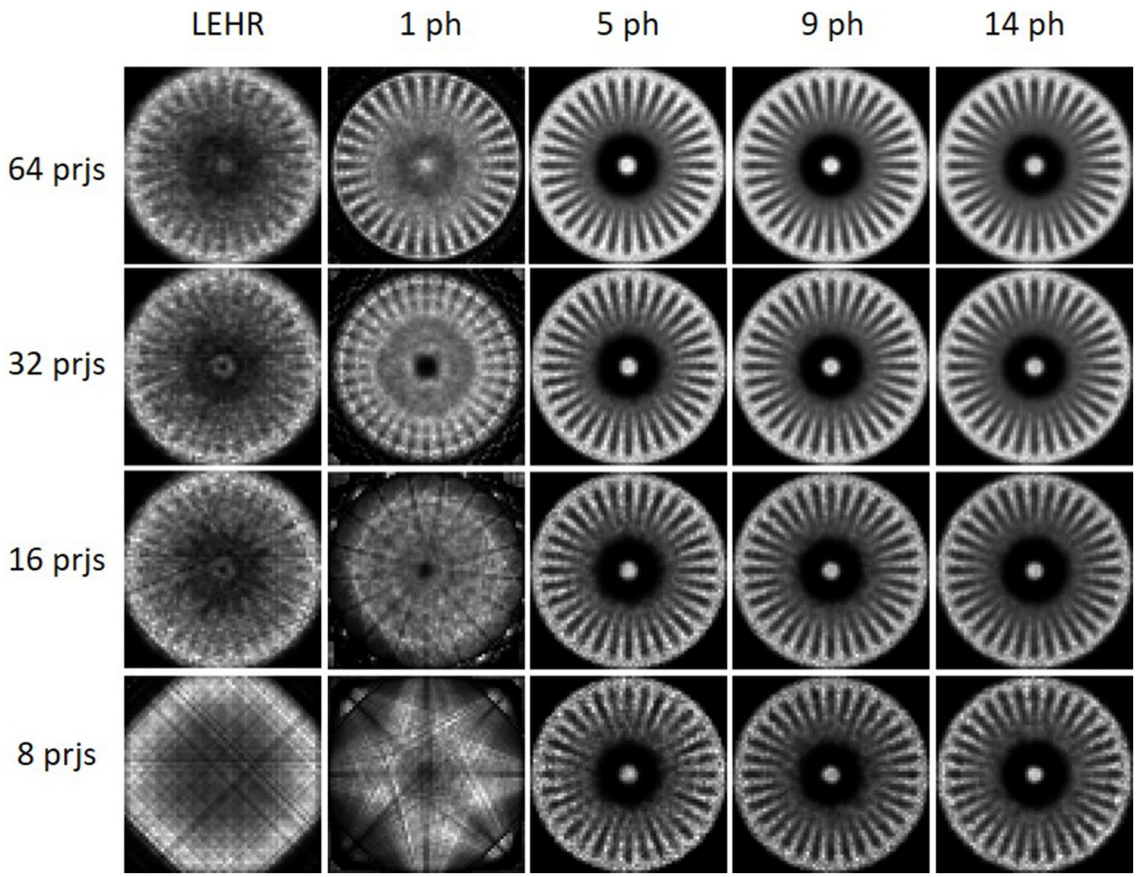

FIGURE 9
The reconstructed images of LEHR and 1, 5, 9, and 14 pinholes (ph, MPGP) with 8, 16, 32, and 64 projections of the cold star phantom.

significant benefits, while a 4-position increase was unnecessary. Similarly, Chen et al. (28) evaluated the sampling in G-SPECT, a full-ring focusing MPH SPECT system equipped with 54 focusing pinholes. Their findings indicated that the system performed similarly when using more bed positions as compared with the lowest number of bed positions, i.e., 4. Both studies found that

once a sufficient number of samplings were achieved, further increases in sampling did not noticeably impact the performance of the system. Both of the studies utilized full-ring SPECT systems, where angular sampling was less of a concern. However, our study was based on a standard dual-head system, and the influence of angular sampling was more prominent. Our results showed that fewer angular positions required more pinholes to achieve the required angular sampling, which was not described in their studies.

In realistic noisy simulations (Figures 4–6), along with the decrease in the projections, both two tracer distributions required more pinholes to achieve better NMSE-COV trade-offs and SBR values as expected. However, increased projection overlapping and further minimizing the number of projections from excessive pinholes may lead to compromised image quality, as demonstrated in this study, that a 9-pinhole provides better performance as compared with a 15-pinhole for 2 to 6 projections. Additionally, in clinical practice, patient positioning would be easier with a reduced number of pinholes to reduce truncation and projection overlapping. Meanwhile, a more complex activity distribution, i.e., HMPAO, will need more pinholes and projection views for sufficient angular sampling as compared with that of TRODAT. Thus, 32 projection views combined with 9 pinholes would be a good acquisition strategy for HMPAO, while 16 projections combined with 7 pinholes would be a good acquisition strategy for TRODAT. Meanwhile, the number of pinholes also has a greater influence on fewer projections. The optimal number of pinholes is less affected by the change in projection numbers for a smaller VOI as expected, i.e., striatum in TRODAT.

There are limited studies investigating detector positions for MPH brain SPECT, particularly within the inherent geometric constraints of a conventional dual-head scanner. Könik et al. (30) preliminarily evaluated the impact of different angular views on MPH SPECT imaging, while this study provided a more thorough investigation for different pinhole and projection numbers and evaluated the effect of detector positions of a conventional dual-head SPECT system for a limited number of projections. Though a full ring system is expected to provide the best dynamic SPECT performance, Huh et al. (45) proposed a 4D spatiotemporal reconstruction method for dynamic sequences of separate respiratory and cardiac phases, utilizing a conventional dual-head SPECT camera with detector rotations. Fewer angular views which lead to fewer detector movements may be advantageous for potential dynamic brain acquisition. We evaluate the influence of different detector positions on MPH brain SPECT with limited angular views (Figure 3, Supplementary Figure S3). In general, two projections provide undiagnostic image quality, regardless of the number of pinholes and detector positions. For four projections, L-mode with an 80° rotation angle is a better acquisition strategy for HMPAO, while L-mode with a 20° rotation angle is better for TRODAT when the starting angle is 0°.

One limitation of this study is that only normal brain phantoms were used for the simulation. For clinical diagnosis of brain diseases, such as AD and PD, a population phantom with asymmetrical striatum or cerebral perfusion with varying levels of defects would be beneficial for a more realistic assessment of the proposed MPH performance (46). The state-of-the-art 360° CZT SPECT system, equipped with parallel-hole collimators, demonstrates excellent spatial resolution and sensitivity in brain imaging. According to the study mentioned in the reference (47), such a system achieves similar spatial resolution (6.4 mm cold rods resolved) and nearly three times sensitivity (0.116%) as compared with our dual-head MPH system (e.g., 9 PH MPGP with 6.4 mm hot rods resolved and a 0.0372% sensitivity). Given the inherent geometric limitations of current systems, we anticipate that the performance of the proposed dual-head MPH SPECT would be inferior to the 360° CZT SPECT, particularly for dynamic studies. Full correction methods, e.g., attenuation, scatter, and geometric-collimator detector response, are yet to be implemented in the MPH reconstruction, to enhance the image quality; smaller hot rods could possibly be retrieved in the Monte Carlo simulations. We also acknowledge that GATE would provide a more realistic simulation setting for the clinical distribution evaluations. However, due to the practical limitations in computational resources and the research purpose of investigating angular sampling effects of MPH in different projection numbers, we utilize a combination of GATE and analytic simulations in this study. The GATE findings offered additional insights into analytical simulations. A performance comparison study based on physical experiments or Monte Carlo simulation is warranted, but it is beyond the scope of this study. Further studies are warranted to evaluate the improvements of the MPH collimator as compared with the fan-beam collimator, which is also common for the clinic brain SPECT practice.

5. Conclusion

In this study, we evaluate the performance of the MPH collimator for various projection views for brain SPECT. Our newly designed MPH collimator offers a spatial resolution of 6.4 mm and 2.2–4.2 times the sensitivity compared with the LEHR collimator for MPGP. For MPHR, it provides a spatial resolution of 4.8 mm and 0.7–1.5 times the sensitivity compared with the LEHR collimator. The number of pinholes affects the performance of the MPH collimator, especially when the projection views become sparse. More pinholes are needed for fewer projections to provide better angular sampling in MPH, especially for complex activity distributions. Our results showed that 32 projection views combined with 9 pinholes would be a good acquisition strategy for HMPAO, while 16 projections combined with 7 pinholes would be a good acquisition strategy for TRODAT. Detector positions substantially affect the image quality for MPH SPECT for 2 and 4 angular views, while L-mode acquisition is slightly superior to H-mode. MPH collimators exhibited improved spatial resolution and angular sampling compared with both LEHR and single pinhole collimators.

Data availability statement

The raw data supporting the conclusions of this article will be made available by the authors, without undue reservation.

Author contributions

WH and GM were the primary authors of the manuscript. WH was mainly responsible for data processing and analysis. GM was responsible for data interpretation and study integration. All authors contributed to the article and approved the submitted version.

Funding

This study was supported by the FDCT Research Grant (0091/2019/A2), the Collaborative Research Grant (MYRG-CRG2022-00011-ICMS), and the Ministry of Educational Frontiers Science Centre for Precision Oncology (SP2023-00001-FSCPO) from University of Macau. The computing was performed in part at SICC which is supported by SKL-IOTSC, University of Macau.

Conflict of interest

The authors declare that the research was conducted in the absence of any commercial or financial relationships that could be construed as a potential conflict of interest.

Publisher's note

All claims expressed in this article are solely those of the authors and do not necessarily represent those of their affiliated organizations, or those of the publisher, the editors and the reviewers. Any product that may be evaluated in this article, or claim that may be made by its manufacturer, is not guaranteed or endorsed by the publisher.

Supplementary material

The Supplementary Material for this article can be found online at: https://www.frontiersin.org/articles/10.3389/fmed.2023.1211726/full#supplementary-material

References

1. Yiannopoulou KG, Papageorgiou SG. Current and future treatments in Alzheimer disease: an update. *J Cent Nerv Syst Dis.* (2020) 12:1179573520907397. doi: 10.1177/1179573520907397

2. Feigin VL, Nichols E, Alam T, Bannick MS, Beghi E, Blake N. Global, regional, and national burden of neurological disorders, 1990-2016: a systematic analysis for the global burden of disease study 2016. *Lancet Neurol.* (2019) 18:459–80. doi: 10.1016/S1474-4422(18)30499-X

3. Cummings J, Lee G, Nahed P, Kambar MEZN, Zhong K, Fonseca J. Alzheimer's disease drug development pipeline: 2022. *Alzheimer's Dementia Trans Res Clin Interv.* (2022) 8:e12295. doi: 10.1002/trc2.12295

4. McFarthing K, Rafaloff G, Baptista M, Mursaleen L, Fuest R, Wyse RK. Parkinson's disease drug therapies in the clinical trial pipeline: 2022 update. *J Parkinson's Dis.* (2022) 2022:1–10. doi: 10.3233/JPD-229002

5. Van Dyck CH, Swanson CJ, Aisen P, Bateman RJ, Chen C, Gee M. Lecanemab in early Alzheimer's disease. *New England J Med.* (2023) 388:9–21. doi: 10.1056/NEJMoa2212948

6. Sevigny J, Chiao P, Bussière T, Weinreb PH, Williams L, Maier M. The antibody aducanumab reduces Aβ plaques in Alzheimer's disease. *Nature.* (2016) 537:50–6. doi: 10.1038/nature19323

7. Parkinson Study Group. Levodopa and the progression of Parkinson's disease. *New England J Med.* (2004) 351:2498–508. doi: 10.1056/NEJMoa033447

8. Limousin P, Foltynie T. Long-term outcomes of deep brain stimulation in Parkinson disease. *Nat Rev Neurol.* (2019) 15:234–42. doi: 10.1038/s41582-019-0145-9

9. Valotassiou V, Archimandritis S, Sifakis N, Papatriantafyllou J, Georgoulias P. Alzheimer's disease: spect and pet tracers for beta-amyloid imaging. *Curr Alzheimer Res.* (2010) 7:477–86. doi: 10.2174/156720510792231757

10. Alster P, Madetko NK, Koziorowski DM, Królicki L, Budrewicz S, Friedman A. Accumulation of tau protein, metabolism and perfusion—application and efficacy of positron emission tomography (PET) and single photon emission computed tomography (SPECT) imaging in the examination of progressive supranuclear palsy (PSP) and corticobasal syndrome (CBS). *Front Neurol.* (2019) 10:101. doi: 10.3389/fneur.2019.00101

11. Cai Z, Li S, Matuskey D, Nabulsi N, Huang Y. PET imaging of synaptic density: a new tool for investigation of neuropsychiatric diseases. *Neurosci Lett.* (2019) 691:44–50. doi: 10.1016/j.neulet.2018.07.038

12. Surguchov A. Biomarkers in Parkinson's disease. *Neurodeg Dis Biomarkers Trans Res Clin Prac.* (2022) 2022:155–80. doi: 10.1007/978-1-0716-1712-0_7

13. Wu H, Lou C, Huang Z, Shi G. SPECT imaging of dopamine transporters with 99mTc-TRODAT-1 in major depression and Parkinson's disease. *J Neuropsychiatry Clin Neurosci.* (2011) 23:63–7. doi: 10.1176/appi.neuropsych.23.1.63

14. Bauckneht M, Arnaldi D, Nobili F, Aarsland D, Morbelli S. New tracers and new perspectives for molecular imaging in Lewy body diseases. *Curr Med Chem.* (2018) 25:3105–30. doi: 10.2174/0929867324666170609080000

15. Hapdey S, Soret M, Buvat I. Quantification in simultaneous 99mTc/123I brain SPECT using generalized spectral factor analysis: a Monte Carlo study. *Phys Med Biol.* (2006) 51:6157. doi: 10.1088/0031-9155/51/23/015

16. Ma T, Wei Q, Lyu Z, Zhang D, Zhang H, Wang R. Self-collimating SPECT with multi-layer interspaced mosaic detectors. *IEEE Trans Med Imaging.* (2021) 40:2152–69. doi: 10.1109/TMI.2021.3073288

17. Zhang D, Lyu Z, Liu Y, He ZX, Yao R, Ma T. Characterization and assessment of projection probability density function and enhanced sampling in self-collimation SPECT. *IEEE Trans Med Imaging.* (2023) 42. doi: 10.1109/TMI.2023.3265874

18. Mok GS, Yu J, Du Y, Wang Y, Tsui BM. Evaluation of a multi-pinhole collimator for imaging small animals with different sizes. *Mol Imag Biol.* (2012) 14:60–9. doi: 10.1007/s11307-011-0472-8

19. Könik A, Auer B, De Beenhouwer J, Kalluri K, Zeraatkar N, Furenlid LR. Primary, scatter, and penetration characterizations of parallel-hole and pinhole collimators for I-123 SPECT. *Phys Med Biol.* (2019) 64:245001. doi: 10.1088/1361-6560/ab58fe

20. Mok GS, Tsui BM, Beekman FJ. The effects of object activity distribution on multiplexing multi-pinhole SPECT. *Phys Med Biol.* (2011) 56:2635. doi: 10.1088/0031-9155/56/8/019

21. Beekman F, van der Have F. The pinhole: gateway to ultra-high-resolution three-dimensional radionuclide imaging. *Eur J Nucl Med Mol Imaging.* (2007) 34:151–61. doi: 10.1007/s00259-006-0248-6

22. Si C, Mok GS, Chen L, Tsui BM. Design and evaluation of an adaptive multipinhole collimator for high-performance clinical and preclinical imaging. *Nucl Med Commun.* (2016) 37:313–21. doi: 10.1097/MNM.0000000000000429

23. Ozsahin I, Chen L, Könik A, King MA, Beekman FJ, Mok GS. The clinical utilities of multi-pinhole single photon emission computed tomography. *Quant Imaging Med Surg.* (2020) 10:2006. doi: 10.21037/qims-19-1036

24. Van Audenhaege K, Vandenberghe S, Deprez K, Vandeghinste B, Van Holen R. Design and simulation of a full-ring multi-lofthole collimator for brain SPECT. *Phys Med Biol.* (2013) 58:6317. doi: 10.1088/0031-9155/58/18/6317

25. Lee TC, Ellin JR, Huang Q, Shrestha U, Gullberg GT, Seo Y. Multipinhole collimator with 20 apertures for a brain SPECT application. *Med Phys.* (2014) 41:112501. doi: 10.1118/1.4897567

26. Tecklenburg K, Forgács A, Apostolova I, Lehnert W, Klutmann S, Csirik J. Performance evaluation of a novel multi-pinhole collimator for dopamine transporter SPECT. *Phys Med Biol.* (2020) 65:165015. doi: 10.1088/1361-6560/ab9067

27. King MA, Mukherjee JM, Könik A, Zubal IG, Dey J, Licho R. Design of a multi-pinhole collimator for I-123 DaTscan imaging on dual-headed SPECT systems in combination with a fan-beam collimator. *IEEE Trans Nucl Sci.* (2016) 63:90–7. doi: 10.1109/TNS.2016.2515519

28. Chen Y, Vastenhouw B, Wu C, Goorden MC, Beekman FJ. Optimized image acquisition for dopamine transporter imaging with ultra-high resolution clinical pinhole SPECT. *Phys Med Biol.* (2018) 63:225002. doi: 10.1088/1361-6560/aae76c

29. Goorden M, Rentmeester M, Beekman F. Theoretical analysis of full-ring multi-pinhole brain SPECT. *Phys Med Biol.* (2009) 54:6593. doi: 10.1088/0031-9155/54/21/010

30. Könik A, Zeraatkar N, Kalluri KS, Auer B, Fromme TJ, He Y. Improved performance of a multipinhole SPECT for DAT imaging by increasing number of pinholes at the expense of increased multiplexing. *IEEE Trans Rad Plasma Med Sci.* (2020) 5:817–25. doi: 10.1109/TRPMS.2020.3035626

31. Chen L, Tsui BM, Mok GS. Design and evaluation of two multi-pinhole collimators for brain SPECT. *Ann Nucl Med.* (2017) 31:636–48. doi: 10.1007/s12149-017-1195-y

32. Standardization Administration of China. *Human Dimensions of Chinese Adults*. National Standard of the People's Republic of China. GB/T 10000 (1988).

33. Standardization Administration of China. *Head-Face Dimensions of Adults*. National Standard of the People's Republic of China. GB/T 2428 (1998).

34. Mok GS, Wang Y, Tsui BM. Quantification of the multiplexing effects in multi-pinhole small animal SPECT: a simulation study. *IEEE Trans Nucl Sci.* (2009) 56:2636–43. doi: 10.1109/TNS.2009.2023444

35. Yan P, Chen L, Tsui BM, Mok GS. Evaluation of stationary and semi-stationary acquisitions from dual-head multi-pinhole collimator for myocardial perfusion SPECT. *J Med Biol Eng.* (2016) 36:675–85. doi: 10.1007/s40846-016-0169-1

36. Rahmim A, Dinelle K, Cheng JC, Shilov MA, Segars WP, Lidstone SC. Accurate event-driven motion compensation in high-resolution PET incorporating scattered and random events. *IEEE Trans Med Imaging.* (2008) 27:1018–33. doi: 10.1109/TMI.2008.917248

37. Imran MB, Kawashima R, Sato K, Kinomura S, Ito H, Koyama M. Mean regional cerebral blood flow images of normal subjects using technetium-99m-HMPAO by automated image registration. *J Nucl Med.* (1998) 39:203–7.

38. Patel A, Simon S, Elangoven IM, Amalchandran J, Jain AS, Thangalakshmi S. Dopamine transporter maging with Tc-99m TRODAT-1 SPECT in Parkinson's isease and its orrelation with linical isease everity. *Asia Oceania J Nucl Med Biol.* (2019) 7:22. doi: 10.22038/AOJNMB.2018.30356.1208

39. Wang Y, Tsui BMW. Pinhole SPECT with different data acquisition geometries: usefulness of unified projection operators in homogeneous coordinates. *IEEE Trans Med Imag.* (2007) 26:298–308. doi: 10.1109/TMI.2006.887372

40. Kapucu ÖL, Nobili F, Varrone A, Booij J, Vander Borght T, Någren K. EANM procedure guideline for brain perfusion SPECT using 99m Tc-labelled radiopharmaceuticals, version 2. *Eur J Nucl Med Mol Imaging.* (2009) 36:2093–102. doi: 10.1007/s00259-009-1266-y

41. Jan S, Santin G, Strul D, Staelens S, Assié K, Autret D. GATE: a simulation toolkit for PET and SPECT. *Phys Med Biol.* (2004) 49:4543. doi: 10.1088/0031-9155/49/19/007

42. Vanhove C, Defrise M, Lahoutte T, Bossuyt A. Three-pinhole collimator to improve axial spatial resolution and sensitivity in pinhole SPECT. *Eur J Nucl Med Mol Imaging.* (2008) 35:407–15. doi: 10.1007/s00259-007-0579-y

43. Toossi MB, Islamian JP, Momennezhad M, Ljungberg M, Naseri SH. SIMIND Monte Carlo simulation of a single photon emission CT. *J Med Phys Assoc Med Phys India.* (2010) 35:42. doi: 10.4103/0971-6203.55967

44. Zeraatkar N, Kalluri KS, Auer B, Könik A, Fromme TJ, Furenlid LR. Investigation of axial and angular sampling in multi-detector pinhole-SPECT brain imaging. *IEEE Trans Med Imaging.* (2020) 39:4209–24. doi: 10.1109/TMI.2020.3015079

45. Huh Y, Shrestha UM, Gullberg GT, Seo Y. Monte carlo simulation and reconstruction: assessment of myocardial perfusion imaging of tracer dynamics with cardiac motion due to deformation and respiration using gamma camera with continuous acquisition. *Front Cardiovas Med.* (2022) 9:871967. doi: 10.3389/fcvm.2022.871967

46. Huang WB, Mok GS. Development of a digital brain phantom population for radionuclide imaging research in Parkinson disease. In: *2022 IEEE Nuclear Science Symposium and Medical Imaging Conference (NSS/MIC).* (2022).

47. Desmonts C, Bouthiba MA, Enilorac B, Nganoa C, Agostini D, Aide N. Evaluation of a new multipurpose whole-body CzT-based camera: comparison with a dual-head Anger camera and first clinical images. *EJNMMI physics.* (2020) 7:1–16. doi: 10.1186/s40658-020-0284-5

frontiers | Frontiers in Medicine

TYPE Original Research
PUBLISHED 13 November 2023
DOI 10.3389/fmed.2023.1246881

OPEN ACCESS

EDITED BY
Harun Ilhan,
LMU Munich University Hospital, Germany

REVIEWED BY
Chentian Shen,
Shanghai Sixth People's Hospital, China
Alfred Ankrah,
Korle Bu Teaching Hospital, Ghana

*CORRESPONDENCE
Kuangyu Shi
✉ kuangyu.shi@dbmr.unibe.ch
Greta S. P. Mok
✉ gretamok@um.edu.mo

RECEIVED 24 June 2023
ACCEPTED 09 October 2023
PUBLISHED 13 November 2023

CITATION
Chen G, Lu Z, Jiang H, Afshar-Oromieh A, Rominger A, Shi K and Mok GSP (2023) Lu-177-PSMA dosimetry for kidneys and tumors based on SPECT images at two imaging time points. *Front. Med.* 10:1246881. doi: 10.3389/fmed.2023.1246881

Lu-177-PSMA dosimetry for kidneys and tumors based on SPECT images at two imaging time points

Gefei Chen[1], Zhonglin Lu[1], Han Jiang[1,2], Ali Afshar-Oromieh[3], Axel Rominger[3], Kuangyu Shi[3]* and Greta S. P. Mok[1,4]*

[1]Biomedical Imaging Laboratory (BIG), Department of Electrical and Computer Engineering, Faculty of Science and Technology, University of Macau, Taipa, Macau SAR, China, [2]PET-CT Center, Fujian Medical University Union Hospital, Fuzhou, Fujian, China, [3]Department of Nuclear Medicine, Bern University Hospital, University of Bern, Bern, Switzerland, [4]Ministry of Education Frontiers Science Center for Precision Oncology, University of Macau, Taipa, Macau SAR, China

Background: Personalized dosimetry for Lu-177-PSMA treatment requires multiple-time-point SPECT/CT scans to calculate time-integrated activity (TIA). This study evaluates two-time-point (TTP) methods for TIA calculation for kidneys and tumors.

Methods: A total of 18 patients treated with 3.7-7.4 GBq Lu-177 PSMA-617 were analyzed retrospectively, including 18 sets of left and right kidneys, as well as 45 tumors. Four quantitative SPECT/CT (4TP) were acquired at 2 h, 20 h, 40 h, 60 h ($n = 11$), or 200 h ($n = 7$) after treatment, and they were fit bi-exponentially as reference. The TTP method was fitted by a mono-exponential washout function using two selected imaging time points for kidneys. For tumors, one uptake and one washout phase were modeled, assuming linear (type I) and same (type II) uptake phase between 0 h to the first time point and mono-exponential washout thereafter. Two single-time-point (STP) methods were also implemented for comparison. TIA calculated by TTP and STP methods were compared with reference to the 4TP TIA.

Results: For the kidneys, the TTP methods using 20 h-60 h and 40 h-200 h had smaller mean absolute errors of 8.05 ± 6.05% and 4.95 ± 3.98%, respectively, as compared to other combinations of time points and STP methods. For tumors, the type I and type II TTP methods using 20h–60 h and 40–200 h had smaller mean absolute errors of 6.14 ± 5.19% and 12.22 ± 4.44%, and 8.31 ± 7.16% and 4.48 ± 7.10%, respectively, as compared to other TTP and STP methods.

Conclusion: The TTP methods based on later imaging time demonstrated fewer errors than the STP methods in kidney and tumor TIA. Imaging at 20 h–60 h and 40 h–200 h could simplify the dosimetry procedures with fewer TIA estimation errors.

KEYWORDS

SPECT, Lu-177 PSMA, curve fitting, single time point, dosimetry

Introduction

Radioligand therapy delivers lethal radiation to targeted cancer cells via radionuclide-labeled cell-targeting compound or ligand. Lu-177-prostate-specific-membrane-antigen (PSMA) targeting metastatic castration-resistant prostate cancer has been proven to prolong progression-free survival and overall survival of patients (1). Sequential post-treatment

SPECT or planar scans are acquired to verify the absorbed dose in dose-limiting critical organs, such as kidneys and bone marrow, to avoid severe side effects before the following treatment cycles (2).

Exponential functions are frequently employed in personalized dosimetry to determine the time activity curves (TAC) by fitting sequential images, usually at 3–5 time points (3) over multiple days after Lu-177-PSMA injection (4–6). However, multiple-time-point imaging imposes burdens on clinics and patients. Simplified imaging protocols are desirable while still preserving the precision of the time-integrated activity (TIA) calculation (7–23). Hänscheid et al. (10) proposed a single-time-point (STP) approach for Y-90-DOTATOC, and Madsen et al. (12) proposed another STP method based on the population-based effective half-life for Lu-177 DOTATATE. However, large errors of TIA (>50%) for Lu-177-PSMA/DOTATATE are observed due to variations in the effective half-life among patients (19), and the optimal imaging time points are also likely to be different for different organs (24), even for the same patient. STP methods have been validated in Lu-177-PSMA data, and the recommended time point was 48 h for kidneys with possible error > 20% (19). Devasial et al. (20) developed a reduced time point method using population-based parameters based on previous Lu-177-DOTATATE cohorts to fit with individual kinetics, which was also evaluated in In-111-DOTATATE patient datasets and was further improved by the use of a model selection method (21). Nonetheless, population-based parameters may not work well for outlier patients and may not be feasible for clinics without an existing large clinical cohort. Fitting a mono-exponential model directly on two-time-point (TTP) Lu-177-DOTATATE/PSMA imaging data has been proposed, with comparable results to those obtained by multiple-time-point images in renal dosimetry (9, 15, 16, 18, 22, 23). However, there is no systematic comparison of the TTP and STP methods for kidneys and tumors, particularly for Lu-177-PSMA-617.

In this study, we aimed to investigate the best imaging time points of the TTP method for kidneys and tumors for Lu-177-PSMA-617. The reference TAC was fitted with four-time-point (4TP) imaging data using a bi-exponential function based on the best goodness of fit. Two STP methods were also implemented for comparison (10, 12).

Materials and methods

Patient population and image acquisition

This retrospective study included 18 anonymized patients with metastatic castration-resistant prostate cancer who were treated at Bern University Hospital between October 2019 and September 2021 under local ethics approval. The patient characteristics are summarized in Table 1.

TABLE 1 Patient demographics.

Characteristics	Median [min, max]
Age at the first therapy	73 [54, 82]
Weight (kg)	80 [56, 99]
Height (m)	1.76 [1.60, 1.87]
BMI (kg/m^2)	25.37 [19.84, 30.47]
Prostate-specific antigen level (ug/L) before treatment	341 [16.9, 6946]

Patients underwent 4 SPECT/CT (Symbia Intevo16, Siemens Healthineers, Germany) at 2, ∼20, ∼40, and ∼60 h ($n = 11$) or ∼200 h ($n = 7$) after injection of 3.7–7.4 GBq Lu-177-PSMA-617, depending on weight, height, and tumor burden of the patient. Projections covering the head to the pelvis in three bed positions were collected with a primary energy window of 187–229 keV and two adjacent scatter windows of 150–187 keV and 229–274 keV. Projections were reconstructed using the ordered subset conjugate gradient algorithm with CT-based attenuation correction, decay correction, and triple-energy window scatter correction up to 60 updates (1 iteration with 12–60 subsets). A post-reconstruction Gaussian filter with sigma from 16.00–20.80 mm was applied. The SPECT reconstruction voxel size was 5.078 × 5.078 × 5.078 mm^3, and the matrix size was 128 × 128 × varying length. The calibration factor for quantitative SPECT was 4.21–4.98 cps/MBq, which was determined from a Lu-177 point source with a known activity of 21.48 MBq placed next to the patient during acquisition. Corresponding low-dose CT (LDCT) data were acquired (100 kV, 27 mA), with a reconstructed voxel size of 1.27 × 1.27 × 2.00 mm^3 and a matrix size of 512 × 512 × varying length.

SPECT images at the first time point (2 h) were registered and resampled to the same voxel size as the corresponding LDCT by rigid and B-spline registration with activity conservation -. Then, other time point SPECT images were registered to the first time point SPECT images using Elastix (25, 26). The left and right kidney contours were delineated slice by slice in the first time point LDCT and SPECT fusion images (Figure 1). A total of 45 tumor contours with diameter >1.5 cm and isolated from other high uptake organs were chosen by a nuclear medicine physician with 10 years of experience and then delineated based on a 40% threshold of maximum counts in the first time point SPECT images (2). The kidney and tumor maps were then applied to all registered SPECT images.

Reference TAC

A bi-exponential function was used to fit the organ-based 4TP data for kidneys and tumors as follows:

$$f(t) = a_1 e^{-k_1 t} + a_2 e^{-k_2 t}, \quad (1)$$

where a_i is the amplitude of the exponential term and k_i is the effective washout or uptake rate.

Abbreviations: 4TP, Four-time-point; LDCT, Low-dose CT; PSMA, Prostate-specific membrane antigen; STP, Single-time-point; TAC, Time activity curve; TIA, Time integrated activity; TTP, Two-time-point; CIs, Confidence intervals.

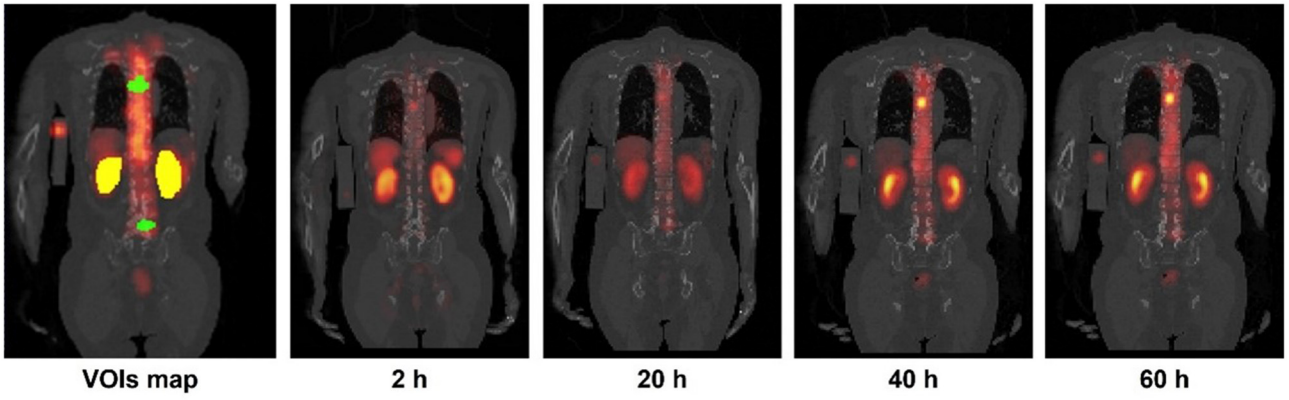

FIGURE 1
Sample kidneys (yellow) and tumor (green) maps delineated on CT and SPECT fusion images. Sample 4TP sequential SPECT/CT images acquired after Lu-177-PSMA administration are also shown.

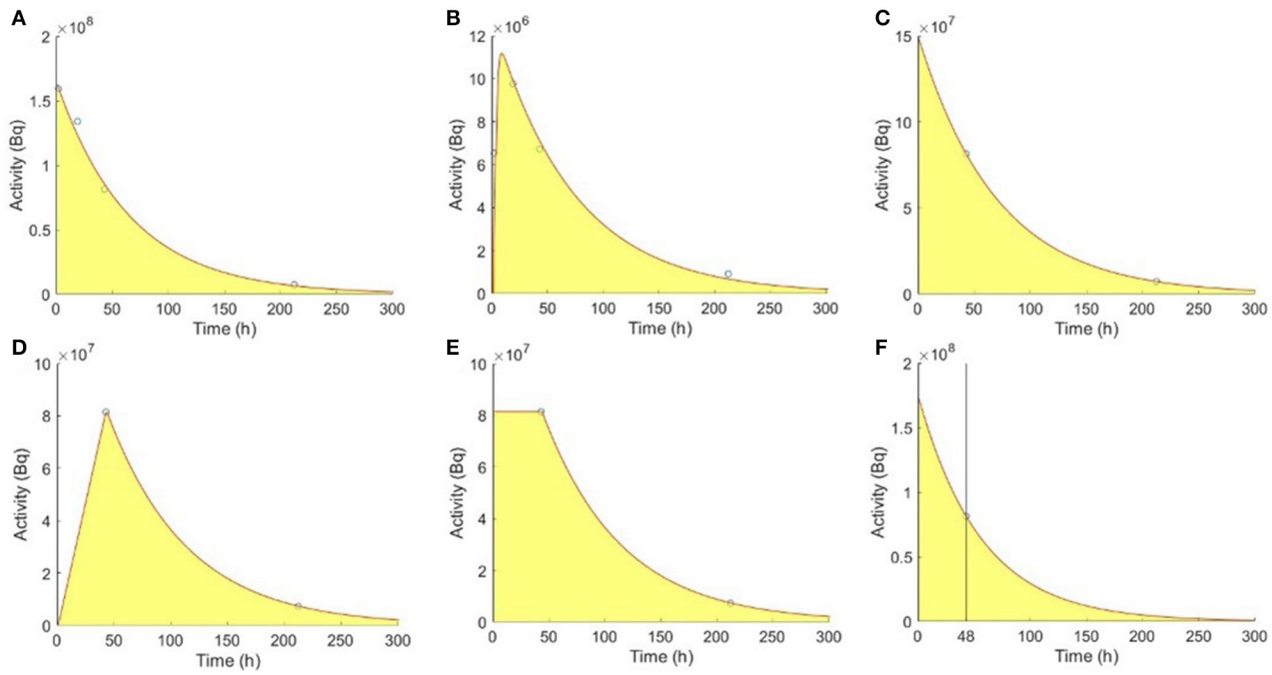

FIGURE 2
Fitting models of the reference 4TP for **(A)** kidneys and **(B)** tumors with one uptake and one washout phase. TTP methods for **(C)** kidneys, **(D)** type I tumors, and **(E)** type II tumors. **(F)** Madsen STP method for kidneys.

The TAC was fitted using a non-linear least-squares algorithm (1). Kidneys were assumed with two washout phases (Figure 2A), while tumors had one uptake and one washout phase using bi-exponential fitting of 4TP data, respectively (Figure 2B).

TTP method

A mono-exponential function was used to fit the organ-based TTP data as follows:

$$f(t) = ae^{-kt} \quad (2)$$

where a is the amplitude of the exponential term and k is the effective washout rate.

For kidneys, a single washout phase was modeled using the mono-exponential function to fit the SPECT data acquired at the first and second selected time points (Figure 2C). Two types of mono-exponential fitting were modeled, considering an extra uptake phase observed for tumors. Assuming no activity at 0 h, type I fitting was modeled by a linear connection between 0 h and the first time point, followed by a mono-exponential function between the first and second time points (Figure 2D). Assuming instantaneous uptake and thus that 0 h and the first time point

TABLE 2 Comparison of TIA calculated by TTP methods with reference TIA for kidneys.

|TIA Error|	2–20 h	2–40 h	2–60 h	2–200 h	20–40 h	20–60 h	20–200 h	40–60 h	40–200 h
Mean ± std (%)	29.34 ± 21.49	11.83 ± 9.71	10.20 ± 8.15	24.84 ± 32.34	17.32 ± 27.61	8.05 ± 6.05	8.71 ± 14.98	8.72 ± 5.37	4.95 ± 3.98
[min, max] (%)	[0.29, 98.77]	[0.08, 40.02]	[0.21, 25.35]	[3.71, 132.21]	[0.04,125.72]	[0.56,18.14]	[0.07,57.77]	[0.73,18.13]	[1.25,14.30]
>10%	28 (77.78%)	17 (47.22%)	9 (40.91%)	11 (78.57%)	17 (47.22%)	7 (31.82%)	3 (21.43%)	8 (36.36%)	2 (14.29%)
>20%	22 (61.11%)	5 (13.89%)	4 (18.18%)	5 (35.71%)	7 (19.44%)	0 (0.00%)	1 (7.14%)	0 (0.00%)	0 (0.00%)

TABLE 3 Comparison of TIA calculated by STP methods with reference TIA for kidneys.

| TIA error |	Madsen at 40 h	Madsen at 60 h	Madsen at 200 h	Hänscheid at 40 h	Hänscheid at 60 h	Hänscheid at 200 h
Mean ± std (%)	9.87 ± 9.23	15.09 ± 8.91	14.81 ± 12.69	10.81 ± 9.70	10.18 ± 8.71	56.30 ± 8.50
[min, max] (%)	[0.45, 35.46]	[3.92, 33.94]	[1.21, 46.76]	[0.15,36.33]	[0.46,30.36]	[38.40,71.30]
>10%	13 (36.11%)	13 (59.09%)	10 (71.43%)	15 (41.67%)	12 (54.55%)	14 (100.00%)
>20%	5 (13.89%)	6 (27.27%)	3 (21.43%)	5 (13.89%)	3 (13.64%)	14 (100.00%)

had the same activity, type II fitting was modeled by a mono-exponential function between the first and second time points (Figure 2E) (23). The TIA for kidneys and tumors were as follows:

$$TIA_{kidneys} = \frac{a}{k} \quad (3)$$

$$TIA_{tumor-I} = \frac{A(t_1)\times t_1}{2} + \frac{ae^{-kt_1}}{k} \quad (4)$$

$$TIA_{tumor-II} = A(t_1) \times t_1 + \frac{ae^{-kt_1}}{k}, \quad (5)$$

where $A(t_1)$ is the activity at the first time point t_1. All combinations of existing time points were evaluated for kidneys, i.e., 2–20 h, 2–40 h, 2–60 h, 2–200 h, 20–40 h, 20–60 h, 20–200 h, 40–60 h, and 40–200 h. For tumors, TTP pairs before 40 h were excluded to avoid the uptake phase extending to infinity, as the tumor activity concentration may peak at approximately 20 h (27).

STP method

The TIA proposed by Madsen et al. (12) was as follows:

$$TIA = \frac{A(t)e^{\hat{k}t}}{\hat{k}}, \quad (6)$$

where $A(t)$ is the organ-based activity measured at imaging time t and $\hat{k}$ is the mean effective washout rate known from previous population-based measurements, i.e., 49.0 h and 82.0 h for kidneys and tumors, respectively (28). Accurate results can be obtained if t was close to or slightly larger than the patient-specific effective half-life (12). One sample using imaging time point at 48 h for kidneys is shown in Figure 2F (19).

The TIA calculated by the Hänscheid STP method (10) was as follows:

$$TIA = A(t) \times \frac{2\times t}{\ln 2} \quad (7)$$

If t fell within 0.75–2.5 times of the organ-specific effective half-life, the TIA error would be <10% (10). Only imaging time points after 30 h were considered for both STP methods in this study, as suggested in the literature (19).

Data analysis

4TP fitting results were evaluated with the goodness-of-fit, i.e., correlation of determination R^2. The effective half-life of the second exponential term was reported.

The percentage of mean TIA absolute error was measured for each method.

$$Errors\,(\%) = \left|\frac{TIA_{\frac{STP}{TTP}}}{TIA_{4TP}} - 1\right| \times 100\% \quad (8)$$

TTP/STP methods with mean absolute error <15% and standard deviation (STD) <10% were selected for further Bland–Altman analysis to evaluate the agreement among different fitting methods with the references for kidneys and tumors. TTP or STP methods with the narrowest 95% confidence intervals (CI) are recommended.

Results

Patient kinetics

The R^2 of kidneys was 0.99 ± 0.02 (range 0.95–1.00) and that of tumors was 0.98 ± 0.02 (range 0.93–1.00). The mean effective half-life of kidneys and tumors was 49.55 ± 18.39 h (range 18.78–101.78 h) and 74.77 ± 41.12 h (range 16.95–191.24 h) for the second washout exponential terms, respectively.

Comparison of kidney TIA

Table 2 shows TIA errors in the TTP methods compared with the reference 4TP TIA in kidneys. Combinations of 2–40 h, 2–60 h, 20–60 h, 40–60 h, and 40–200 h with a mean absolute error <15% and STD <10% were selected for further evaluation. Madsen method at 40 h and Hänscheid method at 40 h and 60 h were selected for further comparison with a mean absolute error <15% and STD <10%, as shown in Table 3.

10.3389/fmed.2023.1246881

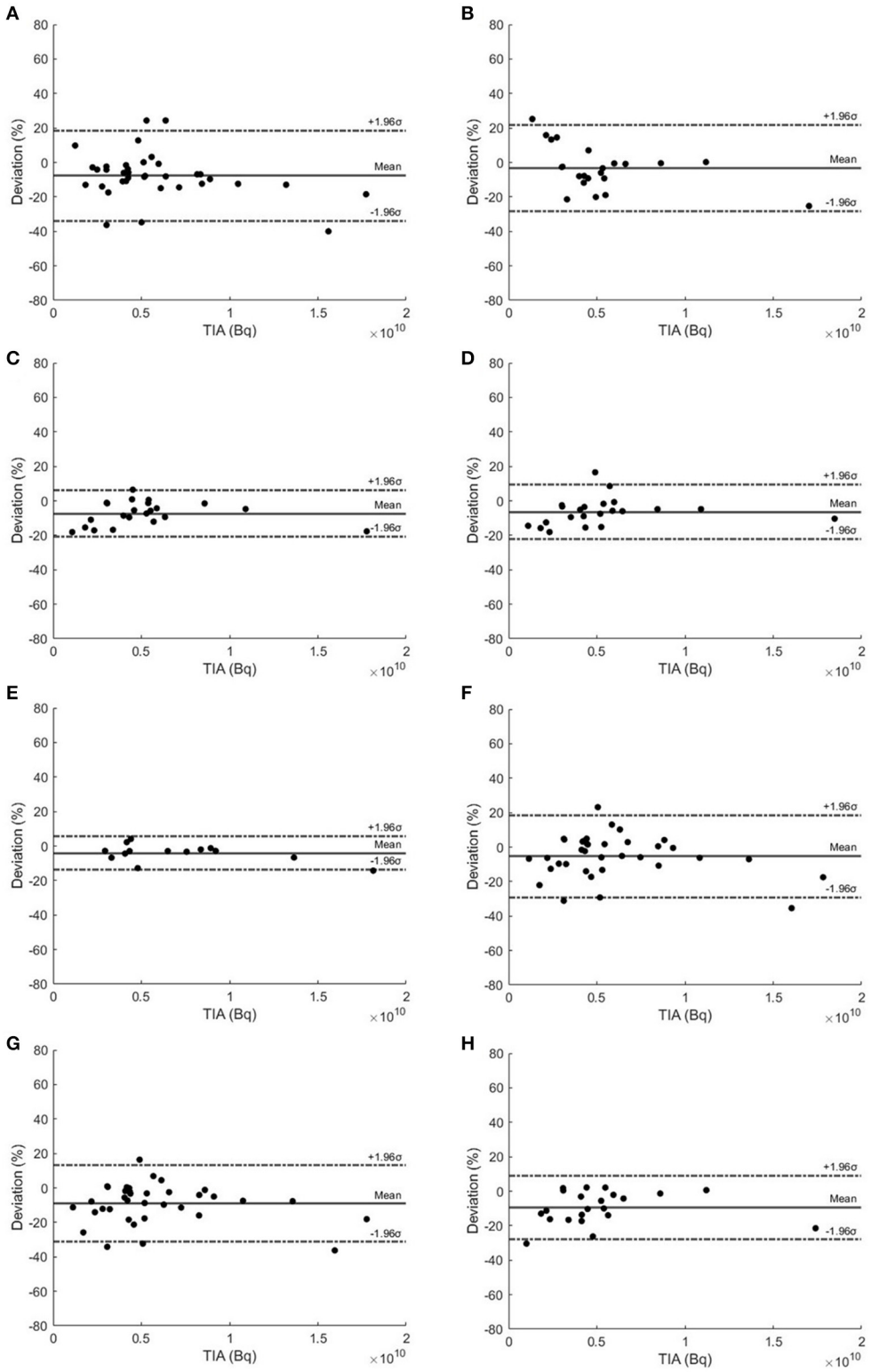

FIGURE 3
Bland–Altman plots of TTP methods using **(A)** 2–40 h, **(B)** 2–60 h, **(C)** 20–60 h, **(D)** 40–60 h, and **(E)** 40–200 h. **(F)** Madsen STP method at 40 h and Hänscheid STP method at **(G)** 40 h and **(H)** 60 h for kidneys.

The Bland–Altman plots of selected TTPs and selected STPs are depicted in Figure 3. TTP using 20–60 h and 40–200 h were recommended due to their narrowest 95% CIs, ranging from −20.90 to 6.25% and −13.76 to 5.66%, respectively. The Madsen method at 40 h had a 95% CI ranging from −29.21 to 18.60%., the Hänscheid method at 40 h had a 95% CI ranging from −31.11

TABLE 4 Comparison of TIA calculated by type I TTP methods with reference TIA for tumors.

| TIA error |	2–60 h	2–200 h	20–60 h	20–200 h	40–60 h	40–200 h
Mean±std (%)	64.84 ± 153.73	11.68 ± 12.16	6.14 ± 5.19	8.35 ± 16.73	23.25 ± 26.96	12.22 ± 4.44
[min, max] (%)	[1.70, 683.23]	[0.04, 44.85]	[0.07, 19.76]	[0.04, 55.67]	[1.69, 148.31]	[2.84,19.38]
>10%	16 (55.17 %)	5 (31.25%)	4 (13.79%)	2 (12.50%)	21 (72.41%)	11 (68.75%)
>20%	7 (24.14%)	3 (18.75 %)	0 (0.00%)	2 (12.50%)	12 (41.38%)	0 (0.00%)

TABLE 5 Comparison of TIA calculated by type II TTP methods with reference TIA for tumors.

| TIA error |	2–60 h	2– 200 h	20–60 h	20–200 h	40–60 h	40–200 h
Mean±std (%)	65.81 ± 153.59	12.45 ± 12.64	8.31 ± 7.16	16.89 ± 19.99	21.96 ± 29.68	4.48 ± 7.10
[min, max] (%)	[2.43,683.65]	[0.25,46.63]	[0.26,28.68]	[0.15,72.24]	[0.96,161.09]	[0.37,26.55]
>10%	17 (58.62%)	6 (37.50%)	11 (37.93%)	8 (50.00%)	20 (68.97%)	2 (12.50%)
>20%	9 (31.03%)	5 (31.25%)	5 (17.24%)	2 (12.50%)	16 (55.17%)	1 (6.25%)

TABLE 6 Comparison of TIA calculated by the STP methods with reference TIA for tumors.

| TIA error |	Madsen at 40 h	Madsen at 60 h	Madsen at 200 h	Hänscheid at 40 h	Hänscheid at 60 h	Hänscheid at 200 h
Mean ± std (%)	23.25 ± 16.62	21.83 ± 13.55	13.09 ± 6.35	24.47 ± 18.91	18.77 ± 14.80	14.69 ± 11.85
[min, max] (%)	[0.63, 66.07]	[1.73, 59.26]	[2.38, 22.49]	[0.27, 75.29]	[0.89, 62.28]	[0.44, 34.51]
>10%	34 (75.56%)	21 (79.31%)	10 (62.50%)	34 (75.56%)	21 (72.41%)	9 (56.25%)
>20%	22 (48.89%)	14 (55.17%)	2 (12.50%)	23 (51.11%)	9 (31.03%)	7 (43.75%)

to 12.99%, and at 60 h had a 95% CI ranging from −28.04 to 8.99%.

Comparison of tumor TIA

Two types of TTP methods for tumors compared with the reference 4TP TIA are shown in Tables 4, 5, respectively. In type I TTP, 20–60 h and 40–200 h had a mean absolute error <15% and STD <10%. In type II TTP, 20–60 h and 40–200 h also had a mean absolute error <15% and STD <10%. All STPs had a mean absolute error >10%, as shown in Table 6; therefore, they were not selected for further analysis.

Figure 4 shows the Bland–Altman plots of selected type I and type II TTP methods. Type I TTP using 20–60 h had the narrowest 95% CI ranging from −17.08 to 14.60% and from −24.06 to 1.42%, respectively. Type II TTP methods using 20–60 h and 40–200 h had the narrowest 95% CIs, ranging from −10.12 to 22.93% and from −11.93 to 18.52%, respectively. Type I and II TTPs using 20–60 h and 40–200 h were recommended with the narrowest 95% CIs.

Discussion

In this study, we compared the STP and TTP methods on kidneys and tumors with the reference 4TP TIA for Lu-177-PSMA-617. The STP methods could achieve better performance at 40 h, consistent with the results presented by Hou et al. (19), and better performance for tumors at >72 h, consistent with the conclusion presented by Jackson et al. (17). The accuracy of the STP methods can be improved by adding another suitable time point, i.e., TTP curve fitting, which was also reported by Peters et al. (23). The superior combination of time points was determined for kidneys and tumors based on a mono-exponential curve fitting in this study. TTP methods with 20–60 h and 40–200 h achieved better performance in kidneys and tumors, corresponding to two groups of patients with different last sampling time points. These two combinations are also implied in other studies based on Lu-177-PSMA-617 (22, 23). The proposed TTP methods could achieve an absolute 95% CI within 25% for kidneys and tumors, leading to a simplified dosimetry protocol.

Our bi-exponential model was effective for fitting all the referenced 4TP data with $R^2 > 0.93$. The resultant mean effective half-life for the slow washout phase of kidneys and tumors was 49.55 and 74.77 h, respectively, consistent with existing research (28). The time integral of the slow washout phase also accounts for a large proportion of the whole TIA (10) and should be better modeled by data at later time points. Therefore, TTP methods with combinations of later time points, i.e., 20–60 h or 40–200 h, were expected to provide superior performance. They provided a mean absolute error <8% and STD <7% as well as absolute 95% CIs <25% and are recommended in the clinical protocol. Similar time combinations were implied by Rinscheid et al. (18). Our results of the TTP method in kidneys indicated a slightly worse performance than other studies (16, 18, 22), which could be attributed to different patient cohorts.

For tumors, the type I TTP method had better performance at 20–60 h, while the type II TTP method achieved better performance

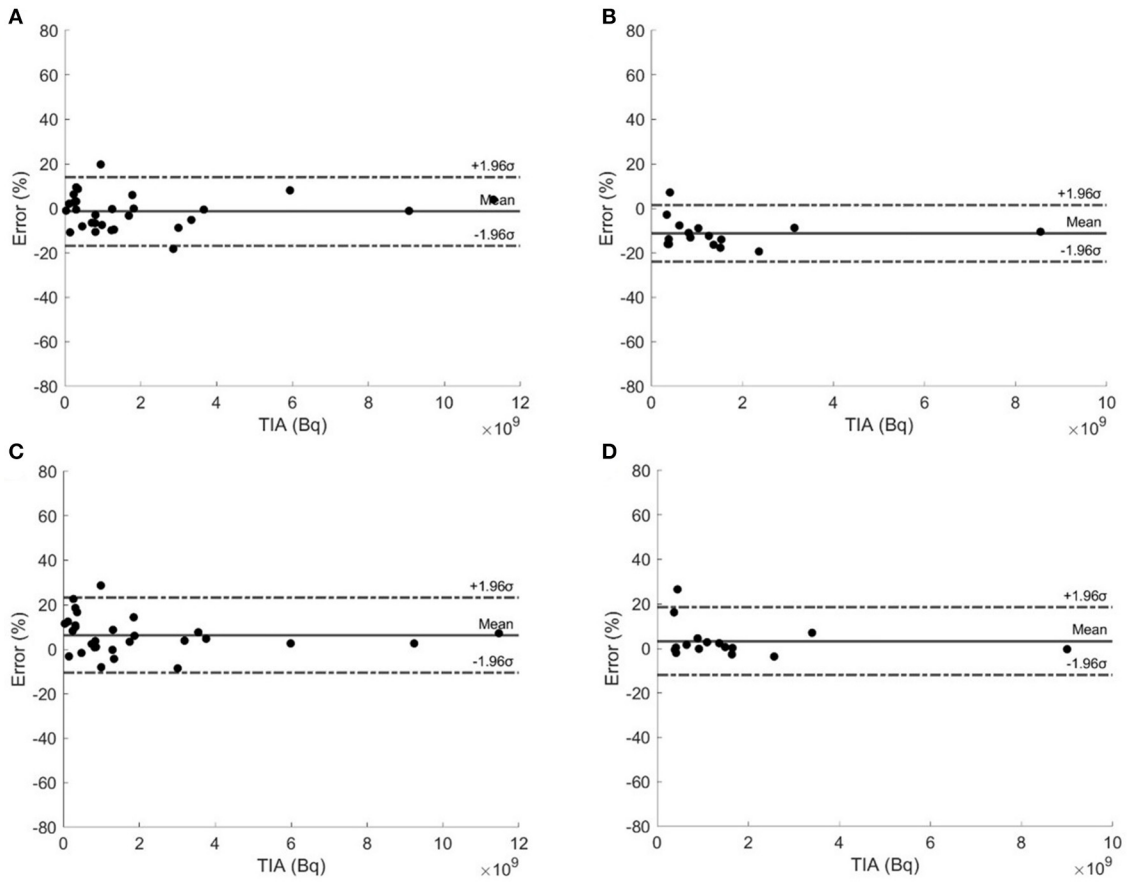

FIGURE 4
Bland–Altman plots of type I TTP methods using **(A)** 20–60 h and **(B)** 40–200 h, and type II TTP methods using **(C)** 20–60 h and **(D)** 40–200 h.

at 40–200 h. Our results showed better performance, with mean error <6% and STD <8%, than Resch et al. with 10 ± 14% (22). Peters et al. (23) only adopted the type II TTP method for tumors and achieved better performance with the last second time point at 168 h. The type I TTP method achieved better performance when the first time point was at 20 h, as it modeled the uptake phase better because the peak was expected to be approximately at 20 h. Therefore, the type II TTP method could overestimate the TIA for the uptake phase when the first time point was at 20 h. Therefore, in our study, the type II TTP method acquired better performance at 40–200 h.

The STP methods could achieve a mean error <10% when the selected imaging time point was within the optimal range derived from organ-specific effective half-life as proposed by Hänscheid et al. (10) and Madsen et al. (12). However, due to the high variability of the effective half-life in different patients and organs, the optimal range could vary for each patient. Moreover, the first washout phase of kidneys and the uptake phase of tumors were not modeled in the STP methods (10).

TTPs with 20–60 h and 40–200 h achieved superior performance in kidneys and tumors in this study. The 20–60 h combination could be a better choice considering the inpatient period for Lu-177-PSMA-617, as it may eliminate the need for patients to return for a second visit for the scans, allowing for a simplified dosimetry protocol. However, this study serves as a feasibility study, which was limited by a small cohort of retrospective patient data from a single center. Prospective evaluations with more patient data from different centers are warranted to validate the generalizability of our findings.

Conclusion

TTP methods using SPECT images acquired at 20–60 h and 40–200 h could simplify the current Lu-177-PSMA dosimetry procedures with errors <19% for kidneys and <20% for tumors based on this small patient cohort.

Data availability statement

The original contributions presented in the study are included in the article/supplementary material, further inquiries can be directed to the corresponding authors.

Ethics statement

The studies involving humans were approved by the Institutional Review Board of Bern University Hospital. The

studies were conducted in accordance with the local legislation and institutional requirements. The Ethics Committee/institutional review board waived the requirement of written informed consent for participation from the participants or the participants' legal guardians/next of kin because it's a retrospective study.

Author contributions

GC and GM are responsible for the implementation of the method, data evaluation, and paper writing. ZL is responsible for the data evaluation. HJ is responsible for image segmentation. AA-O and AR are responsible for the clinical evaluation and data support. KS and GM are responsible for supervising the whole project. All authors contributed to the article and approved the submitted version.

Funding

The project was supported by the Ministry of Education Frontiers Science Centre for Precision Oncology, University of Macau, Taipa, Macau SAR, China (SP2023–00001-FSCPO) and a research grant from Fundo para o Desenvolvimento das Ciências e da Tecnologia (FDCT 0099/2021/A).

Conflict of interest

The authors declare that the research was conducted in the absence of any commercial or financial relationships that could be construed as a potential conflict of interest.

Publisher's note

References

1. Sartor O, De Bono J, Chi KN, Fizazi K, Herrmann K, Rahbar K, et al. Lutetium-177–PSMA-617 for metastatic castration-resistant prostate cancer. *New Engl J Med.* (2021) 385:1091–103. doi: 10.1056/NEJMoa2107322

2. Kabasakal L, Toklu T, Yeyin N, Demirci E, Abuqbeitah M, Ocak M, et al. Lu-177-PSMA-617 prostate-specific membrane antigen inhibitor therapy in patients with castration-resistant prostate cancer: stability, bio-distribution and dosimetry. *Mol Imaging Radionucl Ther.* (2017) 26:62. doi: 10.4274/mirt.08760

3. Peters SM, Privé BM, de Bakker M, de Lange F, Jentzen W, Eek A, et al. Intra-therapeutic dosimetry of [177 Lu] Lu-PSMA-617 in low-volume hormone-sensitive metastatic prostate cancer patients and correlation with treatment outcome. *Eur J Nucl Med Mol Imaging.* (2021) 49:460–9. doi: 10.1007/s00259-021-05471-4

4. Siegel JA, Thomas SR, Stubbs JB, Stabin MG, Hays MT, Koral KF, et al. MIRD pamphlet no. 16: techniques for quantitative radiopharmaceutical biodistribution data acquisition and analysis for use in human radiation dose estimates. *J Nucl Med.* (1999) 40:37S—61S.

5. Ljungberg M, Celler A, Konijnenberg MW, Eckerman KF, Dewaraja YK, Sjögreen-Gleisner K, et al. pamphlet no. 26: joint EANM/MIRD guidelines for quantitative 177Lu SPECT applied for dosimetry of radiopharmaceutical therapy. *J Nucl Med.* (2016) 57:151–62. doi: 10.2967/jnumed.115.159012

6. Mok GS, Dewaraja YK. Recent advances in voxel-based targeted radionuclide therapy dosimetry. *Quant Imag Med Surg.* (2021) 11:483. doi: 10.21037/qims-20-1006

7. Merrill S, Horowitz J, Traino A, Chipkin S, Hollot C, Chait Y. Accuracy and optimal timing of activity measurements in estimating the absorbed dose of radioiodine in the treatment of Graves' disease. *Phys Med Biol.* (2011) 56:557. doi: 10.1088/0031-9155/56/3/003

8. Maaß C, Sachs JP, Hardiansyah D, Mottaghy FM, Kletting P, Glatting G. Dependence of treatment planning accuracy in peptide receptor radionuclide therapy on the sampling schedule. *EJNMMI Res.* (2016) 6:1–9. doi: 10.1186/s13550-016-0185-8

9. Heikkonen J, Mäenpää H, Hippeläinen E, Reijonen V, Tenhunen M. Effect of calculation method on kidney dosimetry in 177Lu-octreotate treatment. *Acta Oncol.* (2016) 55:1069–76. doi: 10.1080/0284186X.2016.1182642

10. Hänscheid H, Lapa C, Buck AK, Lassmann M, Werner RA. Dose mapping after endoradiotherapy with 177Lu-DOTATATE/DOTATOC by a single measurement after 4 days. *J Nucl Med.* (2018) 59:75–81. doi: 10.2967/jnumed.117.193706

11. Gosewisch A, Delker A, Tattenberg S, Ilhan H, Todica A, Brosch J, et al. Patient-specific image-based bone marrow dosimetry in Lu-177-[DOTA 0, Tyr 3]-Octreotate and Lu-177-DKFZ-PSMA-617 therapy: investigation of a new hybrid image approach. *EJNMMI Res.* (2018) 8:1–16. doi: 10.1186/s13550-018-0427-z

12. Madsen MT, Menda Y, O'Dorisio TM, O'Dorisio MS. Single time point dose estimate for exponential clearance. *Med Phys.* (2018) 45:2318–24. doi: 10.1002/mp.12886

13. Sundlöv A, Gustafsson J, Brolin G, Mortensen N, Hermann R, Bernhardt P, et al. Feasibility of simplifying renal dosimetry in 177Lu peptide receptor radionuclide therapy. *EJNMMI Phys.* (2018) 5:1–19. doi: 10.1186/s40658-018-0210-2

14. Willowson KP, Eslick E, Ryu H, Poon A, Bernard EJ, Bailey DL. Feasibility and accuracy of single time point imaging for renal dosimetry following 177Lu-DOTATATE ('Lutate') therapy. *EJNMMI Phys.* (2018) 5:1–9. doi: 10.1186/s40658-018-0232-9

15. Del Prete M, Arsenault F, Saighi N, Zhao W, Buteau F-A, Celler A, et al. Accuracy and reproducibility of simplified QSPECT dosimetry for personalized 177Lu-octreotate PRRT. *EJNMMI Phys.* (2018) 5:1–20. doi: 10.1186/s40658-018-0224-9

16. Zhao W, Esquinas PL, Frezza A, Hou X, Beauregard J-M, Celler A. Accuracy of kidney dosimetry performed using simplified time activity curve modelling methods: a 177Lu-DOTATATE patient study. *Phys Med Biol.* (2019) 64:175006. doi: 10.1088/1361-6560/ab3039

17. Jackson PA, Hofman MS, Hicks RJ, Scalzo M, Violet J. Radiation dosimetry in 177Lu-PSMA-617 therapy using a single posttreatment SPECT/CT scan: a novel methodology to generate time-and tissue-specific dose factors. *J Nucl Med.* (2020) 61:1030–6. doi: 10.2967/jnumed.119.233411

18. Rinscheid A, Kletting P, Eiber M, Beer AJ, Glatting G. Influence of sampling schedules on [177Lu] Lu-PSMA dosimetry. *EJNMMI Phys.* (2020) 7:1–14. doi: 10.1186/s40658-020-00311-0

19. Hou X, Brosch J, Uribe C, Desy A, Böning G, Beauregard J-M, et al. Feasibility of single-time-point dosimetry for radiopharmaceutical therapies. *J Nucl Med.* (2021) 62:1006–11. doi: 10.2967/jnumed.120.254656

20. Devasia TP, Dewaraja YK, Frey KA, Wong KK, Schipper MJ, A. novel time–activity information-sharing approach using nonlinear mixed models for patient-specific dosimetry with reduced imaging time points: Application in SPECT/CT after 177Lu-DOTATATE. *J Nucl Med.* (2021) 62:1118–25. doi: 10.2967/jnumed.120.256255

21. Hardiansyah D, Riana A, Beer AJ, Glatting G. Single-time-point dosimetry using model selection and nonlinear mixed-effects modelling: a proof of concept. *EJNMMI Phys.* (2023) 10:1–12. doi: 10.1186/s40658-023-00530-1

22. Resch S, Takayama Fouladgar S, Zacherl M, Sheikh GT, Liubchenko G, Rumiantcev M, et al. Investigation of image-based lesion and kidney dosimetry protocols for 177Lu-PSMA-I&T therapy with and without a late SPECT/CT acquisition. *EJNMMI Phys.* (2023) 10:11. doi: 10.1186/s40658-023-00529-8

23. Peters SM, Mink MC, Privé BM, de Bakker M, de Lange F, Muselaers CH, et al. Optimization of the radiation dosimetry protocol in Lutetium-177-PSMA therapy: toward clinical implementation. *EJNMMI Res.* (2023) 13:6. doi: 10.1186/s13550-023-00952-z

24. Gustafsson J, Taprogge J. Theoretical aspects on the use of single-time-point dosimetry for radionuclide therapy. *Phys Med Biol.* (2022) 67:025003. doi: 10.1088/1361-6560/ac46e0

25. Klein S, Staring M, Murphy K, Viergever MA, Pluim JP. Elastix: a toolbox for intensity-based medical image registration. *IEEE Trans Med Imag.* (2009) 29:196–205. doi: 10.1109/TMI.2009.2035616

26. Ao EC, Wu NY, Wang SJ, Song N, Mok GS. Improved dosimetry for targeted radionuclide therapy using nonrigid registration on sequential SPECT images. *Med Phys.* (2015) 42:1060–70. doi: 10.1118/1.4906242

27. Paganelli G, Sarnelli A, Severi S, Sansovini M, Belli ML, Monti M, et al. Dosimetry and safety of 177 Lu PSMA-617 along with polyglutamate parotid gland protector: Preliminary results in metastatic castration-resistant prostate cancer patients. *Eur J Nucl Med Mol Imag.* (2020) 47:3008–17. doi: 10.1007/s00259-020-04856-1

28. Peters SM, Hofferber R, Privé BM, de Bakker M, Gotthardt M, Janssen M, et al. [68 Ga] Ga-PSMA-11 PET imaging as a predictor for absorbed doses in organs at risk and small lesions in [177 Lu] Lu-PSMA-617 treatment. *Eur J Nucl Med Mol Imag.* (2021) 49:1101–12. doi: 10.1007/s00259-021-05538-2

29. Lu Z, Chen G, Jiang H, Sun J, Lin K-H, Mok GS, et al. and CT misregistration reduction in [99mTc] Tc-MAA SPECT/CT for precision liver radioembolization treatment planning. *Eur J Nucl Med Mol Imag.* (2023) 50:2319–30. doi: 10.1007/s00259-023-06149-9

Frontiers in Medicine

Translating medical research and innovation into improved patient care

A multidisciplinary journal which advances our medical knowledge. It supports the translation of scientific advances into new therapies and diagnostic tools that will improve patient care.

Discover the latest Research Topics

See more →

Frontiers

Avenue du Tribunal-Fédéral 34
1005 Lausanne, Switzerland
frontiersin.org

Contact us

+41 (0)21 510 17 00
frontiersin.org/about/contact